Ion Spectroscopy Studies of DNA Cation Radicals Generated from Electron Transfer and Collision-Induced Dissociations

Shu R. Huang

A dissertation

Submitted in partial fulfillment of the

Requirements for the degree of

Doctor of Philosophy

University of Washington

2021

Reading Committee:

Frantšek Tureček, Chair

Matthew F. Bush

Robert E. Synovec

Program Authorized to Offer Degree:

Department of Chemistry

University of Washington

University of Washington

Abstract

Ion Spectroscopy Studies of DNA Cation Radicals Generated from Electron Transfer and Collision-Induced Dissociations

Shu R. Huang

Chair of the Supervisory Committee:
Professor František Tureček
Department of Chemistry

This dissertation reports the UV/Vis spectroscopic investigations of transient DNA cation radical intermediates generated from collision-induced dissociation and electron transfer dissociation. To generate cation radicals using collision-induced dissociation, doubly-charged ternary Cu(II) complexes with auxiliary ligand 2,2';6',2''-terpyridine and a DNA nucleobase were first formed via electrospray ionization and upon collision-induced dissociation, the ternary Cu(II) complexes undergo intramolecular redox reaction and oxidize the nucleobase to generate the DNA cation radical. To generate the cation radical using electron transfer dissociation, a doubly-charged single-strand DNA sequence was first generated via electrospray ionization and upon electron-transfer dissociation, the one electron charge-reduction will generate the DNA cation radical containing an extra hydrogen adduct. These two methods approximate the mechanism on how these DNA cation radicals are suspected to be generated in nature via ionization. Briefly, the first method of utilizing the collision-induced dissociation with ternary Cu(II) complexes represents the direct ionization of DNA. The second method of utilizing electron-transfer dissociation on multiply-charged DNA represents the indirect ionization of DNA. This dissertation covers five projects involving these radical species.

The first project discusses the collision-induced dissociation of the ternary Cu(II)-2,2';6',2''-terpyridine-adenine complex to oxidize the adenine nucleobase. This spectroscopy investigation reveals the canonical 9-methyladenine cation radical is the dominant tautomer upon direct ionization of the nucleobase. Our high-level *ab initio* calculations also reveal the more stable 9-methylene-(1H)-adenine cation radical; unfortunately, this lower energy tautomer was not observed in the experimental action spectrum. As a follow-up, the second project is a targeted synthesis to generate the 9-methylene-(1H)-adenine tautomer. This elusive tautomer, generated in the gas-phase, also exhibited interesting gas-phase chemistry, where the primary dissociation proceeded with a hydrogen loss and a rearrangement to yield a protonated aminopteridine ion as the product. With deuterium labeling, reaction energetics and reaction kinetics, we propose an indirect mechanism for this rearrangement.

The third and fourth projects report the generation of the hachimoji DNA cation radicals from collision-induced dissociation of the Cu(II) ternary complexes. This investigation revealed that the canonical tautomers are formed upon intramolecular electron transfer for the two synthetic purine nucleobases, isoguanine and 5-aza-7-deazaguanine. The two synthetic pyrimidine nucleobases, however, offer different gas-phase chemistry from each other. Based on the action spectrum and our *ab initio* calculations on the 6-amino-5-nitro-(1H)-pyrid-2-one cation radical, we concluded that the canonical structure is the dominant form produced upon electron transfer. For 1-methylcytosine, oxidation was accompanied by isomerization of the canonical tautomer to form 1-methylene-2-hydroxy-4-aminopyrimidine cation radical as the dominant ion, as revealed by the action spectrum, our density functional theory calculations, and deuterium exchange experiments.

The last project discusses the one-electron transfer to a doubly-charged single strand DNA, GATC, to generate the cation radical moiety. The experimental spectrum and our density functional theory calculations reveal the cation radical isomerizes to a new 7,8-H-dihydroguanine cation radical.

Acknowledgement

First, I would like to thank my research advisor František Tureček for his years of support and guidance during my time here at the university. You showed me what it means to be a good teacher, a good mentor. More importantly, you have showed me what dedication to the craft means, what it means to produce consistent, high-quality science and lastly, the never-ending pursuit of knowledge. Thank you for that.

Next, I would like to thank my undergraduate mentors, and now friends, Peter T. Palmer and Cadapakam “CJ” Venkatramani, for taking a chance on me as an undergrad and the help along the way. Thank you.

Lastly, I would like to thank the members of the Tureček lab for your support, help, and guidance along the way. Thank you to the department and the university for providing me an environment to continue to learn and become better at my craft. And the NSF for funding throughout my time here.

Dedication

To my sister, my family members, and my tight-knit group of friends in San Francisco, CA.

Table of Content

Chapter 1—Introduction

1.1 DNA Ionization Damage

Ionization of DNA often leads to the transformation of the nucleobases to generate transient cation radicals in the process, often summarized as DNA damage from ionization.[1] There are two accepted mechanisms of DNA damage (Figure 1.1.1). One mechanism follows the oxidative pathway, involving the direct ionization of DNA by a high-energy particle (e.g., an electron, proton, alpha particle, or a cosmic ray) to produce cation radical intermediates, which can undergo further reactions (e.g., proton transfer from solvent).[1,2,3] These intermediates can then yield modified nucleobases or undergo nucleobase loss or strand break. The second mechanism, following the reductive pathway, is initiated by the capture of a low-energy electron to form transient anion radicals, which can spontaneously eliminate the nucleobase or quickly become protonated by solvent to form hydrogen radical adducts to nucleobases. Naturally, one would want to design clever experimental methods to investigate these radicals in solution. Some of the methods include direct ionization of DNA in solution,[4,5] and photooxidation of adducts with small molecules to observe hole-propagation and hole-transfer along the DNA double strand.[6,7] However, these methods did not investigate the primary cation radical intermediates generated from ionization. The challenge to investigate these cation radicals spectroscopically in solution is the propensity of the radical to undergo fast proton transfer with the solvent.[8,9] By generating and investigating these radical species in the gas-phase inside a mass spectrometer, we can eliminate their interactions with solvent or other protonation media. More importantly, we can use tandem mass spectrometry and photodissociation action spectroscopy to study the intrinsic and chemical properties of these intermediates.

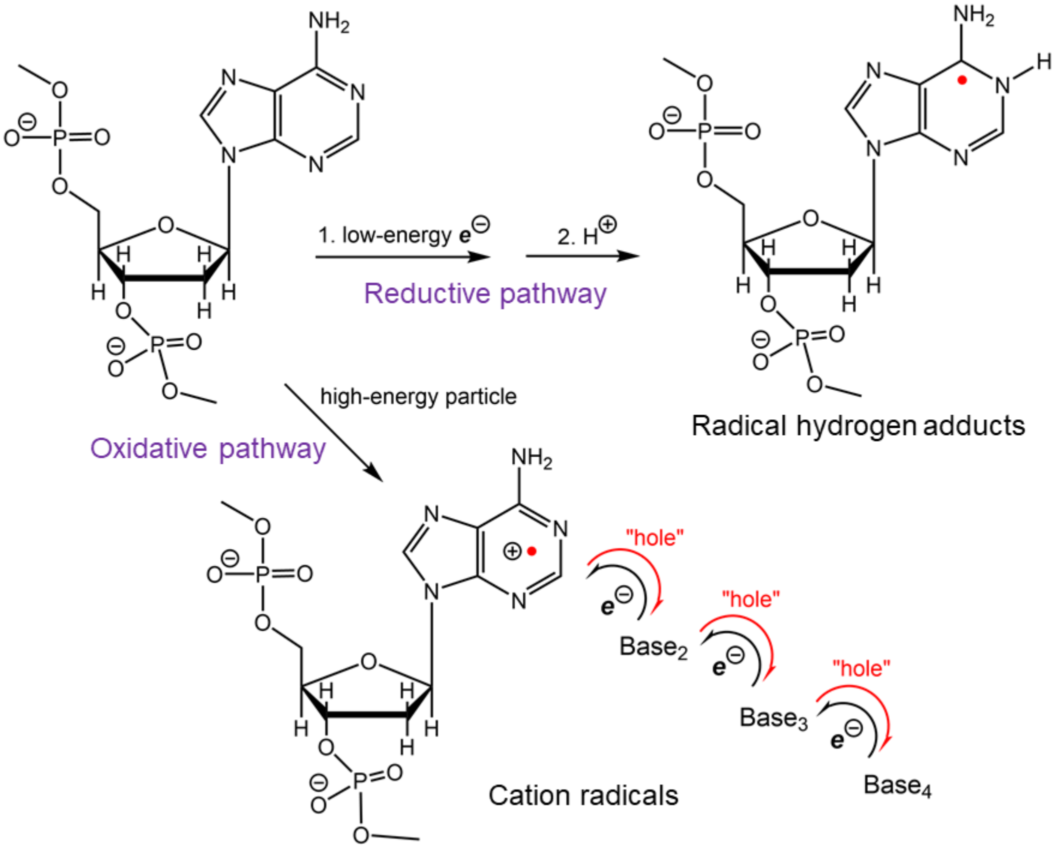

Figure 1.1.1. Schematic of the two mechanisms of DNA ionization. Source image: F. Turecek, J. Phys. Chem. B, 2021, in press.

1.2 A Brief Introduction to Mass Spectrometry

Mass spectrometry (MS) is an instrumentation method that is based on the measurement of mass-to-charge (m/z) ratios of a variety of analytes. The fundamental requirement of MS is that the ions be in the gas-phase before they can be separated according to their m/z values and detected.[10] The mass spectrometer consists of an ion source to generate ions, a mass analyzer to separate the ions, a detector to count the sorted ions, a vacuum system to increase the mean free path of the ions, and with modern mass spectrometers, a computer data acquisition and operational control system.[10]

1.3. Electrospray Ionization to Generate Biomolecular Ions

Electrospray ionization (ESI) is employed to generate ions from biomolecules, like DNA and peptides. In ESI, charged droplets are formed from a solution containing the analytes and a high electric field at the tip of the sample-containing capillary (Figure 1.3.1).[11,12] This high electric field is generated from a potential difference applied between the atmospheric inlet to the vacuum system and the tip of the sample-containing capillary. The field and forced flow supplied from a syringe pump or chromatography system expels the liquid to generate a Taylor cone at the end of the spraying nozzle. Charged microdroplets emerge from the tip of the Taylor cone in the form of an aerosol. As the solvent evaporates, the charged analytes are molecularly dispersed and de-solvated. Gas-phase ions are then introduced into the MS vacuum system via one or more interfaces.[11,12]

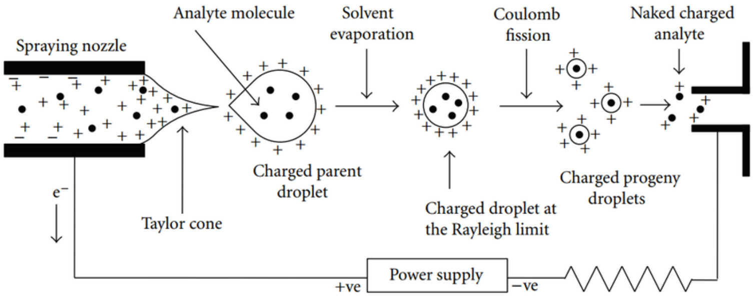

Figure 1.3.1. Electrospray ionization schematic to generate gas-phase ions. Image source: https://www.researchgate.net/figure/Schematic-representation-of-the-electrospray-ionization-process-Adopted-from-33_fig5_307606559

While there are other ionization methods that have been developed in the past, such as matrix-assisted laser desorption and atmospheric pressure chemical ionization, these methods were not used in my research and will not be discussed further.

1.4. The Quadrupole and the Quadrupole Ion Trap Mass Analyzers

In modern instruments, one of the most common types of analyzers is the quadrupole mass filter. A quadrupole analyzer consists of two pairs of rods, placed in the x, y plane opposite of each other, where AC and DC potentials of opposite polarity are applied (Figure

1.4.1). This combination of DC and RF potentials creates a region where trajectories of ions of selected m/z have bound amplitudes along the x and y axis and pass through the mass filter, while other m/z ions are rejected. By scanning the AC and DC potentials in a fixed ratio, ions are separated according to their m/z ratios to generate a mass spectrum.[13] Quadrupole mass analyzers are often used in many gas chromatography-mass spectrometry instruments; they are also coupled with other mass analyzers in tandem mass spectrometry.[13]

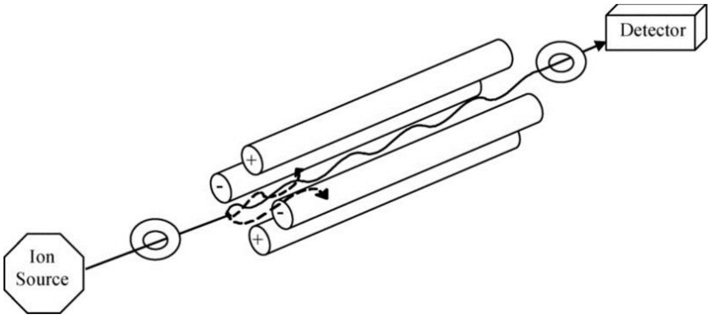

Figure 1.4.1. Schematic of a quadrupole mass analyzer. Image Source: A. El-Aneed et al., Appl. Spectrosc. Rev., 2009, 44, 210-230.

The quadrupole ion trap (also known as the 3-D trap or Paul trap, named after its inventor 1989 Nobel laureate Wolfgang Paul, or as a linear ion trap, LTQ) is related to the quadrupole mass filter, but contains additional functionality of ion trapping. To give a general overview, the 3D quadrupole ion trap consists of two endcaps and a center ring electrode of a hyperbolic cross section shape (Figure 1.4.2). Ions are typically formed in an external ion source, such as electrospray, and injected into the ion trap by a potential pulse. A wide range of ion m/z are confined in the ion trap by the quadrupolar field, following their trajectory stability.[14,15] Once the ion cloud within the trap has been focused for some time (usually between 1 to 30 ms), the amplitude of the radiofrequency potential applied to the trap is ramped up and the trapped ions are ejected through the endcaps. A mass spectrum is obtained by running the scan function (Figure 1.4.3) where ions of increasing m/z are sequentially ejected. The scans are usually repeated many times and the spectra are averaged.[14,15] The more detailed theory of ion trap operation, the ion trajectory stability calculations and related discussions of the Mathieu diagram and solutions are not the focus of this work; however, more information involving this discussion can be found here.[14,15]

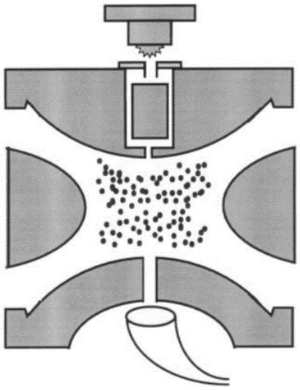

Figure 1.4.2. Schematic of a quadrupole ion trap. Image Source: R.E. March, *Journal of Mass Spectrometry*, 1997, 32, 351-369.

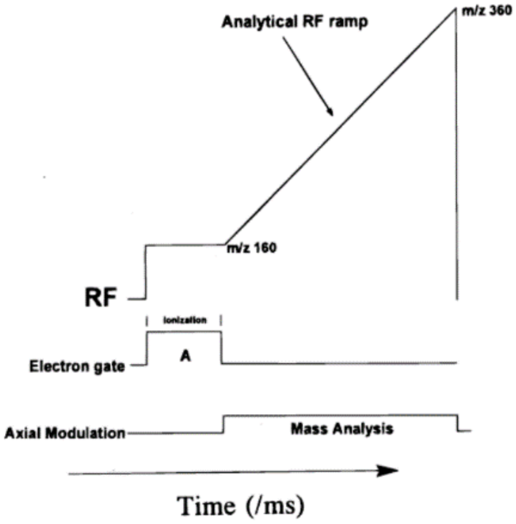

Figure 1.4.3. Schematic of a scan function to obtain an EI mass spectrum. The ionization period is followed by the analytical radiofrequency ramp, which concurrently occurs with the mass analysis. Image Source: R.E. March, *Journal of Mass Spectrometry*, 1997, 32, 351-369.

1.5. Tandem Mass Spectrometry

Tandem mass spectrometry is the process of carrying out consecutive ion mass selection and activation.[15] The objective of each mass-selective process is to first isolate the designated parent ion which is energized by an applied activation method to cause dissociation and generate product ions, with the goal of determining their m/z ratios that are used to characterize the parent ion.[19] In a quadrupole ion trap instrument, tandem mass spectrometry is achieved in a sequence in the same physical space. Briefly, a typical tandem mass spectrometry scan function begins with an increase in the RF amplitude to isolate the parent ion and eject ions that is above or below the designated m/z ratio (e.g., m/z 320 to m/z 322, see Figure 1.5.1).[15,20] The RF amplitude is then lowered, and a RF voltage is applied to the ring electrode to generate the product ions. The resultant product ions are trapped, ejected, and scanned with a RF ramp, like Figure 1.4.3.[15,20] The more detailed theory, explanation, and related on workings of tandem mass spectrometry in a quadrupole ion trap is not the focus of this work and related information can be found here.[15,20]

While tandem mass spectrometry is also commonly implemented in quadrupole-based or “beam”-type instruments, we did not use these instruments in this dissertation and will not be discussed further.

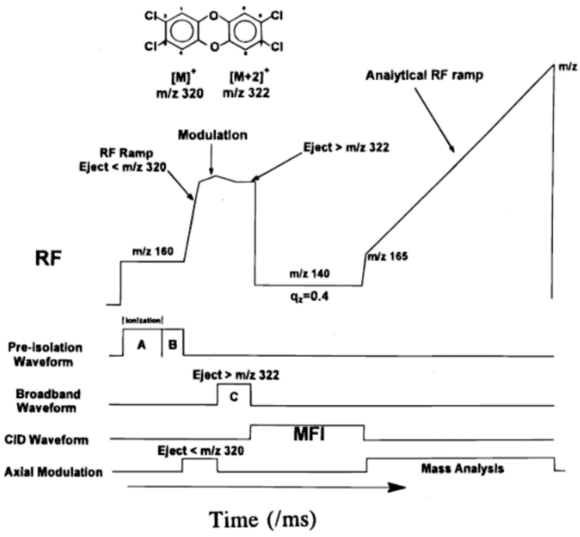

Figure 1.5.1. An example scan function for tandem MS using dioxin as the analyte. Image source: R.E. March, *Journal of Mass Spectrometry*, 1997, 32, 351-369.

1.6. Collision-Induced Dissociation and CID of Cu(II) Complexes

Collision-induced dissociation (CID) is one of the most common activation methods for ions stored inside ion traps. In CID, a RF voltage is applied to the ion trap ring electrode, causing an increase in the trapped ion kinetic energy. The translationally excited ions collide with the neutral bath gas in the ion trap and a portion of their kinetic energy is converted to internal energy which is distributed throughout the different vibrational modes of the ion. With enough collisions, the internal energy of this vibrationally hot trapped ion will exceed the energy threshold for bonds to dissociate and fragmentation occurs (Figure 1.6.1).[15,19,21] Because ions gain their internal energy in small increments in the course of multiple collisions, CID is called a slow-heating method.[19,21]

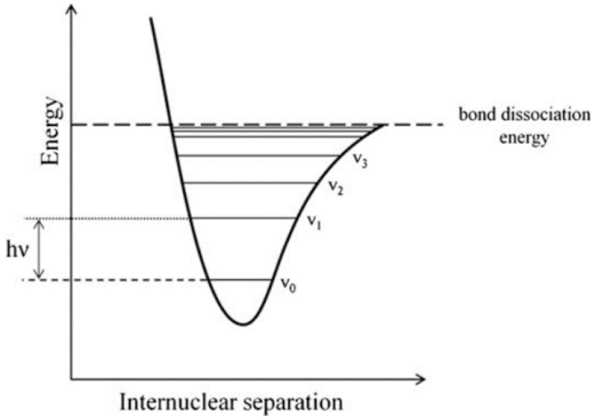

Figure 1.6.1. Potential energy curve of an anharmonic oscillator. Bond dissociation occurs when the ion internal energy crosses the bond dissociation energy threshold. Image source: N.C. Polfer et al., Laser Photodissociation and Spectroscopy of Mass-separated Biomolecular Ions. Springer: 2013; Vol. 83

In this work, CID is most frequently used on copper (II) complexes with DNA nucleobases to generate oxidized DNA cation radicals. Previous works established that collisionally-activated ternary Cu(II) complexes with auxiliary ligands, such as 2:2′,6′:2″-Terpyridine (terpy), and an amino acid displayed interesting gas-phase chemistry, including the formation of the molecular cation radical of pentapeptide sequences and related redox reactions.[22,23] Taking advantage of this phenomenon, we utilized this Cu(II) complex method to form the oxidized DNA nucleobases to generate its cation radical (eq 1.6.1).

$$[\text{CuTerpy(nucleobase)}]^{2+}\ (g) \rightarrow [\text{CuTerpy}]^{+}\ (g) + [\text{nucleobase}]^{+\bullet}\ (g) \qquad \text{(eq. 1.6.1)}$$

Details of this work will be explained in chapters three, five and six. Briefly and as an example, the $[Cu(terpy)adenine]^{2+\bullet}$ complex can be isolated and upon CID-MS^2, the complex undergoes intramolecular redox reaction to generate the adenine cation radical $A^{+\bullet}$ (m/z 135), which is the oxidized product, and the charged-reduced $Cu(terpy)^+$ complex (m/z 296, Figure 1.6.2).

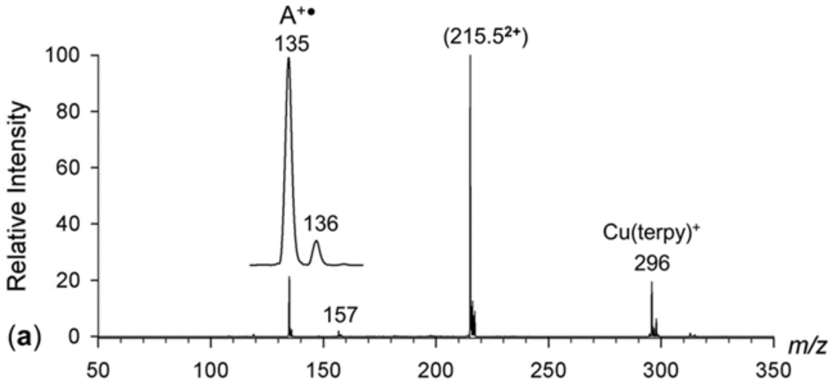

Figure 1.6.2. CID-MS^2 spectrum of $[Cu(terpy)adenine]^{2+\bullet}$ (m/z 215.5). Image source: S.R. Huang et al., J. Am. Soc. Mass Spectrom., 2020, 31, 1271-1281.

1.7. Electron Transfer Dissociation and Applied to Doubly-Charged DNA

Electron transfer dissociation (ETD) is an ion activation method that utilized an ion-ion reaction between a multiply charged cation and an anion radical, resulting in a charge reduction and the formation of a cation radical in the gas-phase.[24,25] This ion-ion reaction is a highly exothermic process that will ultimately induce dissociation. Negative mode chemical ionization is utilized to generate this anion radical (e.g., fluoranthene anion radical), In chemical ionization, an electron filament ion source is filled with a reagent gas, such as methane, at pressure of approx. 0.5 to 1 Torr. Under these conditions, the reagent gas is ionized by high-energy electrons to generate the methane cation radical ($CH_4^{+\bullet}$, eq. 1.7.1) and a secondary low-energy electron. Fluoranthene neutral gas, and other highly aromatic gases, can capture the secondary low-energy electron to generate the fluoranthene anion radical (eq. 1.7.2).[24,25]

$$CH_4\ (g) + e^-\ (\text{high eV}) \rightarrow CH_4^{+\bullet}\ (g) + e^-\ (\text{high eV}) + e^-\ (\text{thermal}) \qquad (\text{eq. } 1.7.1)$$

$$C_{16}H_{10}\ (g) + e^-\ (\text{thermal}) \rightarrow C_{16}H_{10}^{-\bullet}\ (g) \qquad (\text{eq. } 1.7.2)$$

Although ETD was initially used for peptide sequencing that preserved post-translational modifications in its fragments, it is also used to fragment DNA. In a tetranucleotide single strand DNA, ETD results in the formation of the DNA cation radical but also triggers dissociation to form the sequence d_3^+ ion (m/z 965) (Figure 1.7.1).[26] We will discuss the DNA fragmentation pattern later.

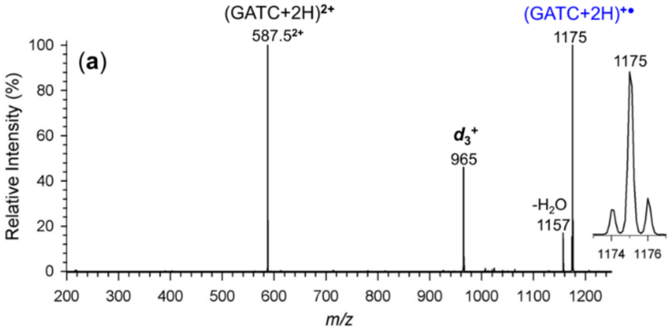

Figure 1.7.1. ETD-MS^2 spectrum of $(GATC+2H)^{2+}$. Image source: S.R. Huang et al., *J. Phys. Chem. B*, 2020, 124, 3505-3517.

1.8. Ultraviolet-Visible Light Photodissociation and UVPD Action Spectroscopy

Ultraviolet/visible light photodissociation (UVPD) utilizes UV and visible light in the electromagnetic spectrum to activate electronic transitions in ions and to induce dissociation (Figure 1.8.1).[21] Electronic transitions, relative to vibrational transitions, occur several orders of magnitude faster and can result in the following three dissociation pathways (Figure 1.8.2). The first pathway is the transition to an unbound vibrational level of the excited electronic state that is above the dissociation threshold. This results in dissociation from the excited electronic state. In the second pathway, the electronic transition is converted to a vibrationally hot state within the ground electronic state of the ion to drive the dissociation. The third mechanism is when the electronic transition crosses into a dissociative state (DS) and causes dissociation.[21] It is also worth noting that electronic transitions in the from 200 nm to 750 nm wavelength region are typically observed for molecules containing π- or non-bonding electrons undergoing *n* → π* and π → π* excitations.[21]

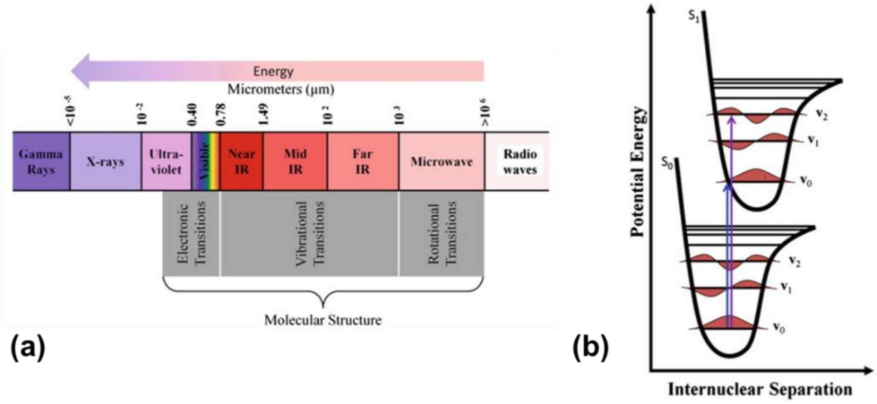

Figure 1.8.1. (a) The electromagnetic spectrum and its effect on chemical bonds depending on the photon wavelength. (b) Electronic transitions from the vibrational ground electronic state to a different vibrational level in the excited electronic state. Image source: N.C. Polfer et al., Laser Photodissociation and Spectroscopy of Mass-separated Biomolecular Ions. Springer: 2013; Vol. 83

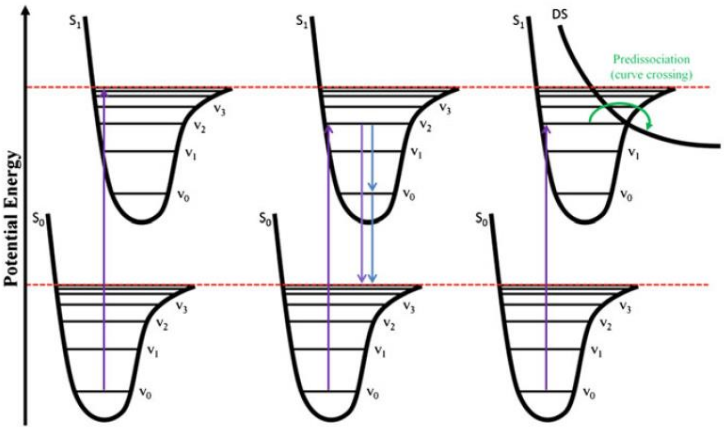

Figure 1.8.2. Three potential dissociation mechanisms for absorption of a UV/vis photon. Image source: N.C. Polfer et al., Laser Photodissociation and Spectroscopy of Mass-separated Biomolecular Ions. Springer: 2013; Vol. 83

Action spectroscopy, or consequence spectroscopy, measures the intensity of photodissociation product ions as a function of excitation wavelength inside a mass spectrometer (Figure 1.8.3).[21] This spectroscopy technique, analogous to its condensed-phase equivalent (e.g., UV/Vis absorption, FT-IR), allows one to acquire absorption spectra of optically thin samples, which are typically not feasible to obtain by absorbance measurements. Action spectroscopy utilizing IR photons typically requires multiple photon absorption to induce dissociation due to the low photon energies. Although infrared multi-photon dissociation (IRMPD) action spectroscopy has been used to determine the structures of guanine nucleobases,[27,28] IRMPD action spectra can be challenging to interpret, especially for larger ions having strong anharmonic vibrational modes because of the intramolecular hydrogen bonds.[29,30] Unlike IRMPD, action spectroscopy utilizing UV/Vis wavelengths relies on single-photon absorption to drive dissociation from the excited electronic state (see Figure 1.8.2). UVPD action spectroscopy also allows for the distinction between isomers of peptide cation radicals.[31] UVPD action spectroscopy is the primary spectroscopy technique used in this work.

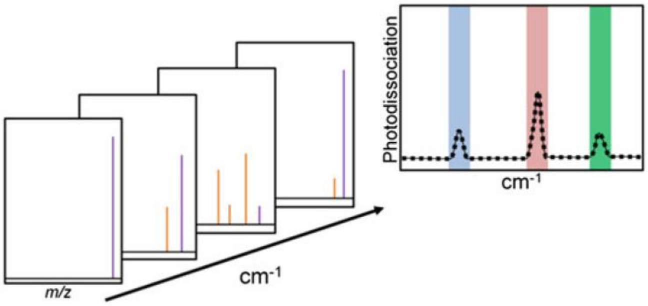

Figure 1.8.3. Schematic of a photodissociation action spectroscopy experiment, where the parent ion (purple) dissociations into the product ions (orange) as a function of wavelength. Image source: N.C. Polfer et al., Laser Photodissociation and Spectroscopy of Mass-separated Biomolecular Ions. Springer: 2013; Vol. 83.

1.9. Tandem MS DNA Fragmentation Pattern

Throughout the chapters ahead, we will utilize the ion activation methods listed above (e.g., CID, ETD, and UVPD) primarily on DNA sequences and DNA nucleobases. Therefore, a brief explanation of the DNA fragmentation pattern is warranted. Mass spectrometric fragmentation of DNA sequences typically proceeds along the sugar-phosphate backbone (Figure 1.9.1).[32] If the charging fragment or product ion contains the 5'- terminus, these fragments are denoted as the a, b, c, d-type ions. Similarly, if the charging fragments contain the 3'- terminus, they are denoted as the w, x, y, z-type ions. Other common dissociations that can be combined with the backbone cleavage include the loss of a nucleobase, the loss of water, and/or the loss of phosphoric acid.

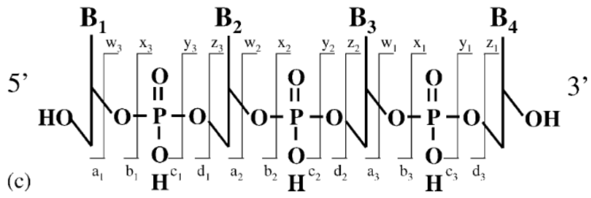

Figure 1.9.1. DNA oligonucleotide fragment ion nomenclature. Image source: J. Wu et al., Int. J. Mass Spectrom., 2004, 237, 197-241.

1.10. Ion Detection

Electron multipliers (EM) are one of the most common detectors in modern instruments. The underlying principle of electron multipliers is as a high energy (keV) particle first hits the wall of the EM, it ejects secondary electrons from the surface that are accelerated to keV kinetic energy by the applied field. Each successive collision between the burst of secondary electrons and the wall of the multiplier creates more secondary electrons, creating a cascade that amplifies the initial current. The electron current created by the cascade is collected on the collector electrode, converted to a voltage pulse, digitized, and stored by the data acquisition software (Figure 1.10.1).[33,34]

The electron multiplier is only a member in a family of ion detectors. Some of the other detectors are the Faraday cup and the photoplate detector.[33,35] While these other detectors are relevant, they will not be discussed moving forward in this work.

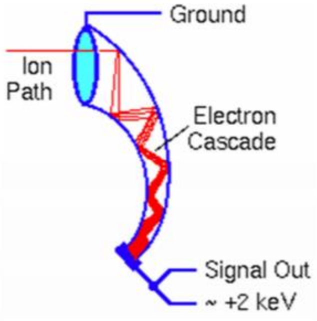

Figure 1.10.1. Schematic of an electron multiplier. Image source: S. Medhe, Chemical and Biomolecular Engineering, 2018, 3, 51-58.

1.11. References

1. C. von Sonntag, Free-Radical-Induced DNA Damage and Its Repair. A Chemical Perspective. Springer-Verlag: Berlin 2006

2. C. von Sonntag, *Adv. Quant. Chem.*, 2007, 52, 5-20.

3. X. Chen et al., *J. Phys. Chem. A*, 2005, 109, 8121-8132.

4. A. Banyasz et al., *J. Phys. Chem. Lett*., 2016, 7, 3949-3953.

5. E. Pluhařová et al., *Acc. Chem. Res*., 2015, 48, 1209-1217.

6. B. Giese et al., *Nature*, 2001, 412, 318−320.

7. B. Giese, *Top. Curr. Chem.*, 2004, 236, 27−44.

8. J. Choi et al., *Chem. Eur. J*., 2019, 25, 7711-7718.

9. J. Choi et al., *J. Phys. Chem. Lett*., 2015, 6, 5045-5050.

10. J. Throck Watson et al., Introduction to Mass Spectrometry, 4th Edition, Wiley, 2008, p.3-8.,

11. M. Wilm, *Mol. Cell. Proteomics*, 2011, 10, M111.009407

12. S. Banerjee et al., *Int. J. Anal. Chem.*, 2012, 1-40.

13. A. El-Aneed et al., *Appl. Spectrosc. Rev.*, 2009, 44, 210-230.

14. R.E. March et al., Quadrupole Ion Trap Mass Spectrometry. John Wiley & Sons: 2005; Vol. 165.

15. R.E. March, *Journal of Mass Spectrometry*, 1997, 32, 351-369.

19. L. Sleno et al., *J. Mass Spectrom.*, 2004, 39, 1091-1112.

20. J.V. Johnson et al., *Anal. Chem.*, 1990, 62, 2162-2172.

21. N.C. Polfer et al., Laser Photodissociation and Spectroscopy of Mass-separated Biomolecular Ions. Springer: 2013; Vol. 83

22. F. Tureček, *Mass Spectrom. Rev.*, 2007, 26, 563-582.

23. I.V. Chu et al., *J. Phys. Chem. B*, 2000, 104, 3393-3397.

24. J. Syka et al., *PNAS*, 2004, 101, 9528-9533.

25. R. Pepin et al., *J. Phys. Chem. B*, 2015, 119, 2818-2826.

26. S.R. Huang et al., *J. Phys. Chem. B*, 2020, 124, 3505-3517.

27. L. Feketeová et al., *Phys. Chem. Chem. Phys.*, 2015, 17, 25837-25844.

28. L. Feketeová et al., *Chem. Comm.*, 2013, 49, 7343-7345.

29. F. Tureček et al., *Int. J. Mass Spectrom.*, 2013, 354-355, 249-256.

30. C. Wolke et al., *Science*, 2016, 354, 1131-1335.

31. H.T. Nguyen et al., *J. Phys. Chem. B*, 2017, 121, 6557-6569.

32. J. Wu et al., *Int. J. Mass Spectrom.*, 2004, 237, 197-241.

33. S. Medhe, *Chemical and Biomolecular Engineering*, 2018, 3, 51-58.

34. L.A. Dietz, *Rev. Sci. Instrum.*, 1965, 36, 1763.

35. D.W. Koppenaal et al., Anal. Chem., 2005, 77, 418 A-427 A.

Chapter 2—Ground and Excited States of Gas-Phase DNA Nucleobase Cation-Radicals. A UV-Vis Photodissociation Action Spectroscopy and Computational Study of Adenine and 9-Methyladenine

Reproduced in part with permission from S.R. Huang, A. Dang, F. Tureček, *J. Am. Soc. Mass Spectrom.*, **2020**, 31, 1271-1281, DOI: 10.1021/jasms.0c00095.

2.1. Abstract

Cation radicals of adenine ($A^{\bullet+}$) and 9-methyladenine ($MA^{\bullet+}$) were generated in the gas phase by collision-induced intramolecular electron transfer in copper–terpyridine–nucleobase ternary complexes and characterized by collision-induced dissociation (CID) mass spectra and UV–vis photodissociation action spectroscopy in the 210–700 nm wavelength region. The action spectra of both $A^{\bullet+}$ and $MA^{\bullet+}$ displayed characteristic absorption bands in the near-UV and visible regions. Another tautomer of $A^{\bullet+}$ was generated as a minor product by multistep CID of protonated 9-(2-bromoethyl)adenine. Structure analysis by density functional theory and coupled-clusters ab initio calculations pointed to the canonical 9-H-tautomer $Ad1^{\bullet+}$ as the global energy minimum of adenine cation radicals. The canonical tautomer $MA1^{\bullet+}$ was also calculated to be a low-energy structure among methyladenine cation radicals. However, two new noncanonical tautomers were found to be energetically comparable to $MA1^{\bullet+}$. Vibronic absorption spectra were calculated for several tautomers of $A^{\bullet+}$ and $MA^{\bullet+}$ and benchmarked on equation-of-motion coupled-clusters excited-state calculations. Analysis of the vibronic absorption spectra of $A^{\bullet+}$ tautomers pointed to the canonical tautomer $Ad1^{\bullet+}$ as providing the best match with the action spectrum. Likewise, the canonical tautomer $MA1^{\bullet+}$ was the unequivocal best match for the $MA^{\bullet+}$ ion generated in the gas phase. According to potential-energy mapping, $MA1^{\bullet+}$ was separated from energetically favorable noncanonical cation radicals by a high-energy barrier that was calculated to be above the dissociation threshold for loss of a methyl hydrogen atom, thus preventing isomerization. Structures and energetics of all four DNA nucleobase cation radicals are compared and discussed.

2.2. Introduction

Ionization of DNA by impact of high energy particles creates random electron vacancies in the nucleobases, forming transient cation radicals.[1] The chemical processes triggered by DNA ionization involve electron transfer and formation of radical intermediates that have been studied extensively with a focus on downstream reaction intermediates and products.[2-4] In contrast, the primary cation radicals have not been characterized spectroscopically so far because of fast proton transfer reactions with solvent and other species present in the condensed phase environment.[5] Isolated nucleobase cation radicals have been produced by electron ionization of gaseous nucleobases, and their unimolecular dissociations have been characterized by mass spectrometry.[6] Thus, the rarefied gas phase provides a suitable environment for the generation of nucleobase cation radicals and spectroscopic investigations of their structure and electronic properties. Several previous computational studies of nucleobase cation radicals have been chiefly focused on the determination of ionization energies and electron density distribution.[7-11] In addition to direct ionization, DNA nucleobase cation radicals have been generated by collision-induced intramolecular electron transfer and dissociation of ternary metal complexes formed by electrospray ionization (Scheme 1).[12] This method, that was originally introduced to generate peptide cation radicals,[13] has been adapted by O’Hair and co-workers to provide a useful technique for nucleobase cation-radical generation.[14,15] Combined with mass separation and ion trapping, the Scheme 1 reaction allowed for structure studies of the synthesized nucleobase cation-radicals using methods of photodissociation action spectroscopy.[16-18] Guanine,[19] 9-methylguanine,[19,20] 2’-deoxyguanosine,[21] and guanosine[19] have been characterized by infrared multiphoton photodissociation (IRMPD)[20] and UV-vis photodissociation (UVPD)[19] action spectroscopy. IRMPD and UVPD differ in the mode of resonant ion photoexcitation. IRMPD requires multiple infrared photons to deliver energy via vibrational excitation, resulting in slow heating of the ion at the resonant wavelength. In contrast, UVPD relies on single-photon electronic excitation whereby the absorbed energy either drives dissociation starting from an excited electronic state,**[18]** or provides vibrational excitation after internal conversion to the ground electronic state. Despite these differences, the IRMPD and UVPD results were in accord that the guanine-based cation radicals all had canonical nucleobase structures (Scheme 1).**[19,20]**

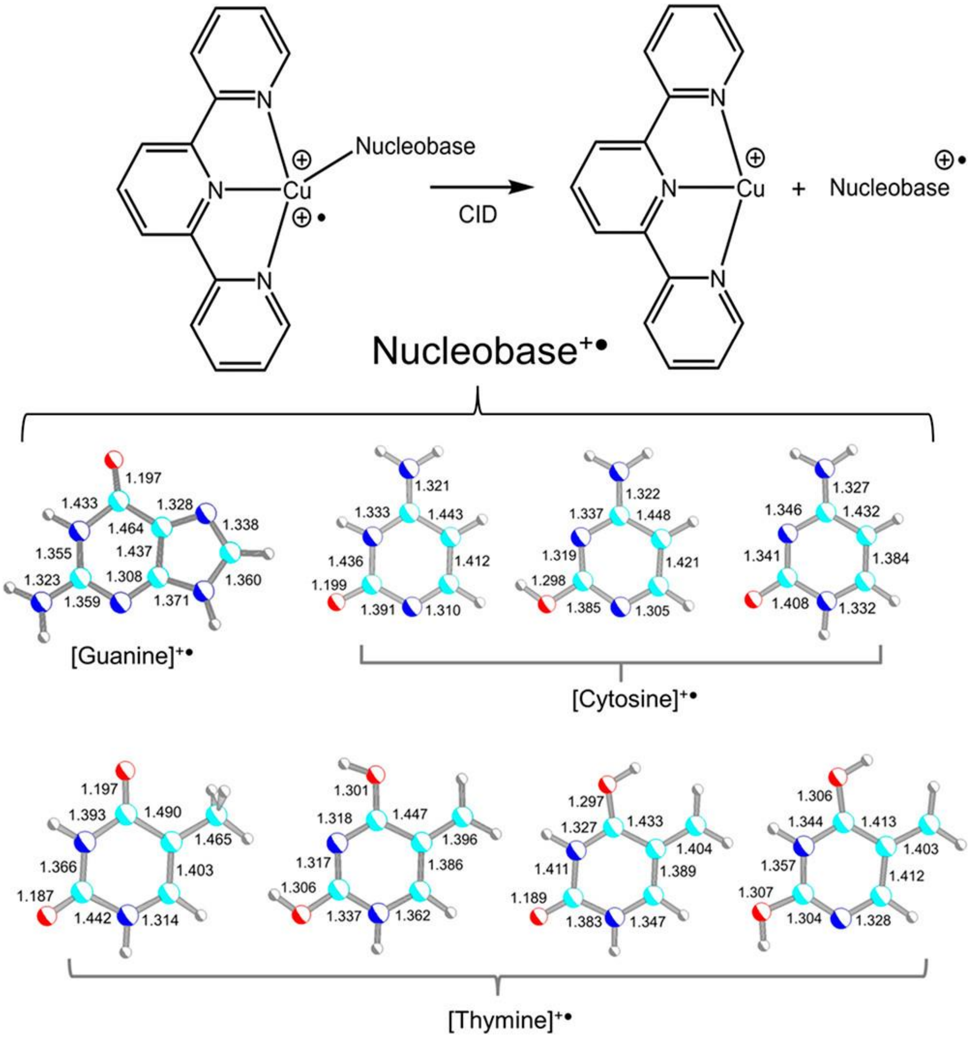

Scheme 1. Formation of nucleobase cation radicals from Cu complexes showing M06-2X/6-31+G(d,p) optimized geometries of low energy DNA nucleobase cation radicals generated previously by this technique. Atom color coding is as follows: cyan = C, blue = N, red = O, gray = H. Bond lengths are in angstroms.

In contrast to guanine, IRMPD and UVPD action spectroscopy of cytosine cation radicals pointed to a mixture of tautomers (Scheme 1) formed by collision-induced intramolecular transfer and dissociation of ternary copper complexes.[22] This promiscuous behavior of cytosine cation radicals parallels neutral cytosine which is known to exist as multiple tautomers in the gas phase.[23-26] A recent study of the thymine cation radical has brought surprising results in that the major species generated from a copper complex were noncanonical tautomers (Scheme 1) that represented 77% of the tautomer mixture, as characterized by UVPD action spectroscopy and ion–molecule reactions.[27] All these spectroscopic studies have been corroborated by extensive ab initio calculations of equilibrium structures, energies, vibrational frequencies, and excited electronic states to characterize the gas-phase nucleobase cation radicals.

Here, we report the generation and UVPD spectroscopic study of adenine-based cation radicals. This completes the series of DNA nucleobase cation radicals and at the same time provides reference structural and spectroscopic data that may be used in studies of more complex cation radicals derived from nucleosides,[28] oligonucleotides,[29] and duplex DNA.

2.3. Experimental

2.3.1. Materials

Adenine, 9-methyladenine, copper nitrate, and 2:2',6':2"-terpyridine (terpy) were purchased from Sigma-Aldrich (St. Louis, MO) and used as received. 9-(2-Bromoethyl)adenine was purchased from Combi-Blocks (San Diego, CA). To prepare the [Cu(terpy)(adenine)] or [Cu(terpy)(9-methyladenine)] complexes, 0.011 mmol of adenine or 9-methyladenine was dissolved in 1 mL of 0.01 M $Cu(NO_3)_2$ and terpy in acetonitrile–water. These stock solutions were diluted to 10 μM for infusion into the electrospray ion source.

2.3.2. Methods

Mass and photodissociation action spectra were measured on modified LTQ-XL ETD linear ion trap (Thermo Fisher, San Jose, CA) and amaZon Speed 3D ion trap tandem mass spectrometers (Bruker Daltonik, Bremen, Germany) equipped with an EKSPLA NL301G Nd:YAG laser (Altos Photonics, Bozeman, MT) working at 20 Hz frequency and 3 to 6 ns pulse width, as described previously.[30] The photon pulses were treated by a PG142C unit (Altos

Photonics, Bozeman, MT), which incorporated a third harmonic generator and optical parametric oscillator coupled with an optional second harmonic generator to enable wavelength tuning in the range of 210-700 nm. The laser beam (6 mm diameter) exiting the PG142C unit was aligned and focused into the ion trap. The laser pulse energies were measured at each experimental wavelength using an EnergyMax-USB J-10MB energy sensor (Coherent Inc., Santa Clara, CA) to calibrate the action spectra. The measured photofragment ion intensities were normalized to the number of photons per pulse. The action spectra were reproduced and are reported as averages of two measurements performed on different days. The action spectra obtained on the LTQ and Bruker ion traps were comparable; the Bruker spectra are reported and discussed here, the LTQ spectra are given as Supporting Information (Figure S1). Accurate mass-to-charge ratios were obtained from high-resolution mass spectra that were measured on an Orbitrap Velos mass spectrometer (Thermo Fisher, San Jose, CA) at a resolving power of 60000.

2.3.3. Calculations

Ab initio and density functional theory (DFT) calculations were performed with the Gaussian 16 (Revision A03) suite of programs.[31] Structures were first optimized with B3LYP/6-31+G(d,p)(32) and CAM-B3LYP/6-311+G(2d,p)(33) to obtain a preliminary ranking of the cation-radical tautomers by energy and evaluate local energy minima by adequate harmonic frequencies. Additional sets of optimized geometries were obtained with Møller–Plesset[34] (MP2, full) and coupled-clusters[35] (single and double excitations, CCSD)[36] calculations with the 6-31+G(d,p) basis set, as well as with M06-2X[37] and the 6-31+G(d,p) and 6-311++G(2d,p) basis sets. All these calculations were performed within the spin-unrestricted formalism. Higher spin states in the UMP2 calculations were treated with the spin projection method[38,39] using spin annihilation that reduced the total spin close to the theoretical value (0.75). The purpose of the multiple geometry optimizations was to find the best match between the CCSD/6-31+G(d,p) optimized geometries on one hand, and the DFT and MP2(FULL) optimized geometries on the other. The match was established on the basis of total single-point energies calculated using coupled clusters with single, double, and disconnected triple excitations, CCSD(T),[36] that were extrapolated to the complete basis set (CBS),[40] providing benchmark relative energies. The extrapolation used an exponential formula reported recently,[19] the coefficients are summarized in Table S1 (Supporting Information). From these benchmarking calculations we established that CCSD(T)/CBS total energies based on M06-2X/6-31+G(d,p) and M06-2X/6-311++G(2d,p) geometries provided a close match with those based on CCSD/6-31+G(d,p) optimized geometries within 0.7 and 1.0 millihartree, respectively. Thus, geometry optimizations with M06-2X/6-31+G(d,p) can provide an inexpensive and highly accurate access to nucleobase structures that rival that of CCSD. Transitions and oscillator strength for 10 excited electronic states were evaluated using equation-of-motion CCSD (EOM-CCSD) calculations[41] with the 6-31+G(d,p) basis set. This covered excitations down to 220 nm for all tautomers. The EOM-CCSD transitions were used to benchmark the time-dependent DFT (TD-DFT)(42) calculations that were carried out with M06-2X for 35–40 excited states in adenine and 9-methyladenine cation radicals, covering the wavelength range to below 180 nm. The M06-2X TD-DFT calculations with the 6-31+G(d,p) and 6-311++G(2d,p) basis sets gave very similar results in terms of excitation energies that showed a close correlation: ΔE_{exc}[M06-2X/6-31+G(d,p)] = 1.0043 × ΔE_{exc}[M06-2X/6-311++G(2d,p)], $r^2 = 0.9998$, and a root-mean square deviation of rmsd = 0.024 eV for $\mathrm{Ad1}^{\bullet+}$-$\mathrm{Ad679}^{\bullet+}$ (Table S2, Supporting Information). Likewise, the oscillator strengths calculated with M06-2X and the two basis sets showed rmsd = 0.0051 (Table S3, Supporting Information). Hence, the M06-2X/6-31+G(d,p) TD-DFT calculations were used to calculate all vibronic spectra at 310 K. The B3LYP/6-31+G(d,p) normal modes were used to generate vibrational configurations with the Newton X program,[43] that were ordered according to their Boltzmann factors at 310 K. Three hundred lowest-energy configurations were selected and submitted to TD-DFT M06-2X/6-31+G(d,p) calculations for 20 excited states to generate the vibronic spectra reported here.

2.4. Results & Discussion

2.4.1. Cation-Radical Generation

Electrospray ionization of solutions containing Cu^{2+} ions, terpy, and the nucleobase formed the respective [Cu(terpy)(adenine)] and [Cu(terpy)(9-methyladenine)] complexes as doubly charged ions at m/z 215.5 and 222.5 for ^{63}Cu, that were selected by mass and submitted to collision-induced dissociation (CID), yielding the respective $[adenine]^{\bullet+}$ (A•+, m/z 135) and $[9\text{-methyladenine}]^{\bullet+}$ ($MA^{\bullet+}$, m/z 149) cation radicals (Figure 1a,1b) together with the complementary $Cu(terpy)^{+}$ ions at m/z 296. The Cu-complex dissociations were clean and efficient, forming few side products and providing the nucleobase cation radicals in good yields. The $A^{\bullet+}$ and $MA^{\bullet+}$ ions were further investigated by CID-MS^3 (Figure 2a-2c). CID of $A^{\bullet+}$ led to loss of NH_2, HCN, CH_2N_2, and 2HCN (Figure 2a), which are standard dissociations also occurring upon electron ionization of adenine.[6] CID of $MA^{\bullet+}$ resulted in a dominant loss of a hydrogen atom and HCN (Figure 2b). CID of $MA^{\bullet+}$ labeled with deuterium in the ND_2 group showed a predominant loss of light hydrogen (Figure 2c, inset) and hydrogen migrations accompanying the elimination of HCN and DCN. The CID spectra further indicated the suitable fragment ions to be used in UVPD action spectra measurements.

In addition to the formation of cation radicals from the nucleobase metal complexes, we explored other methods (Scheme 2). Bromination of 9-methyladenine at C-8 followed by electrospray ionization produced $(MABr + H)^{+}$ ions which upon CID underwent loss of Br forming m/z 149 ions corresponding to $C_6H_7N_5^{\bullet+}$ by high resolution MS. In another approach, protonation of 9-(2-bromoethyl)adenine yielded the corresponding $(Br\text{-}C_2H_4\text{-}A + H)^{+}$ ion that upon CID-MS^2 eliminated C_2H_4, forming a bromoadenine ion, $(ABr + H)^{+}$, which afforded $C_5H_5N_5^{\bullet+}$ upon CID-MS^3. This fragment ion was characterized by its accurate mass (m/z 135.0525). The CID-MS^n spectra of thus generated $C_5H_5N_5^{\bullet+}$ and $C_6H_7N_5^{\bullet+}$ ions displayed the same fragment ions as the CID spectra of the respective $A^{\bullet+}$ and $MA^{\bullet+}$ that did not indicate any distinctive features.

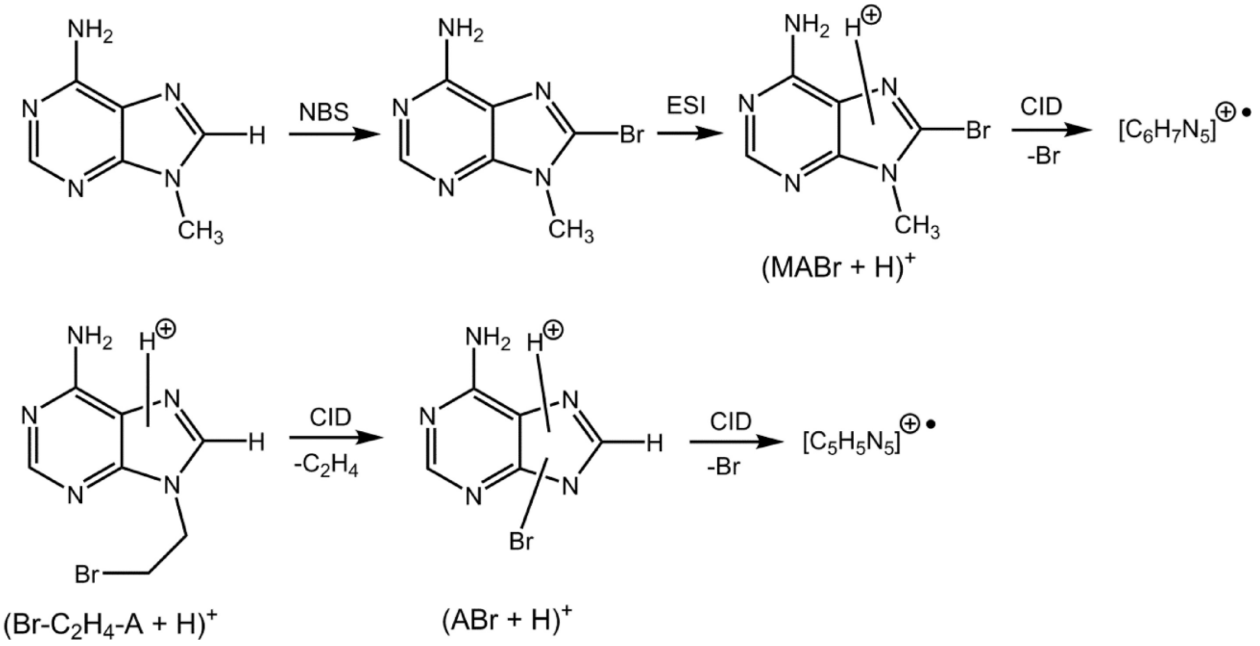

Scheme 2. Alternative formation of adenine cation radicals. NBS stands for bromination with N-bromosuccinimide in dichloromethane.

2.4.2. UVPD Action Spectra

To characterize the adenine cation radicals and explore their electronic structure, we obtained UVPD action spectra in the valence-electron excitation region of 210-700 nm (5.90 to 1.77 eV excitation energy range). The action spectrum of $A^{\bullet+}$ (Figure 3a) showed several bands that were distinguished by mass-resolved photofragmentation channels. The bands with maxima at 580, 330, and 290 nm were represented by the major m/z 108 fragment by loss of HCN. The bands at 480, 340, 270, and 225 nm were due to the m/z 81 fragment ion (loss of 2 HCN), while the m/z 93 fragment ion formed bands at 280 and 320 nm. It is noteworthy that neutral adenine,[44-46] as well as the protonated ion[47,48] do not have absorption bands above 280 nm, and thus the major bands in the action spectrum of $A^{\bullet+}$ are due to electron transitions in the radical chromophore.

The action spectrum of the $C_5H_5N_5^{\bullet+}$ ion from 9-(2-bromoethyl)adenine showed similar bands although at different photofragmentation intensities (Figure 3b). The main differences were in the diminished intensity of the 580 and 480 nm bands carried by the m/z 108 and 81 fragment ions and substantially increased intensities of the 300, 280, and 220 nm bands (Figure 3b). This indicated that the $C_5H_5N_5^{\bullet+}$ ion in question could be a mixture of tautomers. Subtraction of the normalized Figure 3a,b spectra furnished the difference spectrum (Figure 3c) which chiefly displayed bands in the 220–300 nm region.

Turning to $MA^{\bullet+}$, the action spectrum displayed overlapping bands of the m/z 148 (loss of H) and m/z 122 (loss of HCN) fragment ions giving rise to a maximum at 580 nm (Figure 4). Further absorption bands carried by these two major channels were found at 340, 320, 270, and 215 nm. Again, the major absorption bands at $\lambda > 300$ nm were associated with electron excitations in the cation-radical chromophore.

We attempted to generate isomeric $C_6H_7N_5^{\bullet+}$ ions by CID bromine loss from protonated bromomethyladenine (Scheme 2). However, the action spectrum of this $C_6H_7N_5^{\bullet+}$ ion (Figure S2, Supporting Information) was superimposable with that of $MA^{\bullet+}$ across the entire wavelength region, indicating that these ions were identical.

2.4.3. Adenine Ion Structures and Spectra Assignment

To assign the action spectra of adenine cation radicals, we used DFT and ab initio geometry optimizations to generate a number of $C_5H_5N_5^{\bullet+}$ tautomers (Figure 5) that were ranked by energy. Table 1 summarizes the 0 K relative energies obtained by the M06-2X and CCSD(T) calculations. Relative energies obtained by the other DFT and ab initio methods are given in Table S4. The canonical N-9-H tautomer $Ad1^{\bullet+}$ was the lowest energy tautomer among adenine cation radicals.[8] This followed the ranking of neutral adenine molecules in the gas phase, where the canonical form Ad1n is also the lowest energy tautomer (Figure S3, Table S5)[49] and prevails in the gas phase.[50] The CCSD(T)/CBS-calculated adiabatic ionization energy of Ad1n, IE_{adiab} = 8.32 eV, which was based on CCSD/6-31+G(d,p)-optimized geometries (Table S6), was in an agreement with previously calculated values (8.18–8.33 eV)[7-11] and also with the experimental values from photoionization measurements (8.2–8.3 eV).[51] The other cation-radical tautomers, $Ad3^{\bullet+}$-$Ad88^{\bullet+}$, that differed in the distribution of the five hydrogen atoms on the purine skeleton, had significantly higher energies (Table 1). The tautomers are labeled to indicate the proton positions.

Vibronic spectra were calculated by M06-2X/6-31+G(d,p) TD-DFT for 20 lowest excited states, including excitations from 300 vibrational configurations of the cation radicals populated at 310 K. The calculated spectra of the four lowest-energy tautomers Ad1•+–Ad7•+ are shown in Figure 6, and the spectra of the other, higher energy, tautomes are shown in Figure S4. The excited-state assignments were based on benchmark EOM-CCSD calculations that were used to align the M06-2X data and assign the excited states (Tables S2 and S3, Supporting Information). Excited states of very low oscillator strength or those falling outside the experimental wavelength region are not annotated in Figure 6. The absorption spectrum of Ad1•+ (Figure 6a) showed bands of the B and D states that upon vibronic broadening provided the absorption features at 400–650 nm. This region covered the broad bands at 380–650 nm in the action spectrum of [adenine]•+ (Figure 3a). The most characteristic features of Ad1•+ were transitions to the F and G states that gave rise to the dual band in the absorption spectrum (Figure 6a). This provided a close match with the 330 and 290 nm bands in the action spectrum. The higher energy excitations at 239, 231, and 215 nm merged into a band at 240 nm upon vibronic broadening (Figure 6a). This band was present in the action spectrum, although at a lower intensity.

2.4.4. 9-Methyladenine Ion Structures and Spectra Assignment

The presence of the 9-methyl group greatly reduced the number of cation-radical tautomers in this system (Figure 7). The canonical tautomer MA1$^{\bullet+}$ represented a low-energy structure followed by MA6$^{\bullet+}$ (Table 2). Other tautomers with an intact methyl group had substantially higher energies than MA1$^{\bullet+}$. However, additional, noncanonical, low-energy tautomers were generated in silico in which a methyl hydrogen atom was moved to N-1 (MA91$^{\bullet+}$), N-3 (MA93$^{\bullet+}$), or N-7 (MA97$^{\bullet+}$) (Table 2, Figure 7). The calculated vibronic spectrum of MA1$^{\bullet+}$ showed all of the features found in the action spectrum of MA$^{\bullet+}$. The broad band in the visible region of the action spectrum was represented by excitations to the B and C states of MA1$^{•+}$ at 605 and 482 nm, respectively (Figure 8a). The two action spectrum bands with maxima at 340 and 270 nm were assigned to excitations to the F and G states at 293 and 274 nm, respectively. In contrast, the noncanonical MA tautomers were calculated to have no absorption maxima above 350–360 nm, while the most prominent bands were in the 200–250 nm region where the action spectrum showed only weak absorption (Figure 8b,8c). Based on the match of the vibronic spectrum and the low relative energy, the action spectrum was assigned to the canonical tautomer MA1$^{•+}$.

2.4.5. Ion Dissociation Energies

The dissociative nature of the action spectra raised the question of the dissociation energetics of the lowest energy tautomers Ad1$^{•+}$ and MA1$^{•+}$. The most active dissociation channel of Ad1$^{•+}$ by loss of hydrogen cyanide can in principle involve any of the [adenine]$^{•+}$ nitrogen atoms and be associated with hydrogen atom migrations.[51-54] According to the analysis of threshold energies, formation of cation-radical fragment Af1$^{•+}$ by loss of N-1 and C-2 required the lowest energy threshold at 231 kJ mol^{-1} (Table 1, Scheme 3). Other, isomeric, fragment ions (Af2$^{•+}$, Af3$^{•+}$, Scheme S1, Supporting Information) were calculated to have substantially higher energy thresholds (Table 1). Although the elimination of HCN may involve intermediates and transition states of above-threshold energies, it is worth noting that the lowest threshold energy is accessible by single-photon absorption at wavelengths of up to 520 nm. The fact that photodissociation is seen at wavelengths up to 650 nm (184 kJ mol^{-1} photon energy) can be explained by an extremely fast internal conversion of the B excited electronic state (Figure 3a,b) to the vibrationally excited ground state.[55-57] If the conversion occurs early in the laser pulse (3-6 ns), the ground state can absorb a second photon from the same pulse to drive dissociation. The most prominent dissociation of MA1$^{•+}$ was a loss of a hydrogen atom. Out of several possible origins of the hydrogen atom we investigated, the loss of a methyl H was calculated to have the lowest threshold energy (292 kJ mol^{-1}, Table 1, Scheme 3). This can be delivered by a single photon with a wavelength of up to 424 nm. Again, the fact that photodissociation occurred with up to 650 nm photons indicated a sequential resonant absorption of two photons at these longer wavelengths. The action spectrum of $MA^{\bullet +}$ further indicated that the $MA1^{\bullet +}$ tautomer formed by CID of the Cu(terpy) complex did not isomerize to the thermodynamically favored ions $MA91^{\bullet +}$ and $MA93^{\bullet +}$. We investigated the possibility of an isomerization by a hydrogen migration from the methyl group to the sterically accessible N-3.

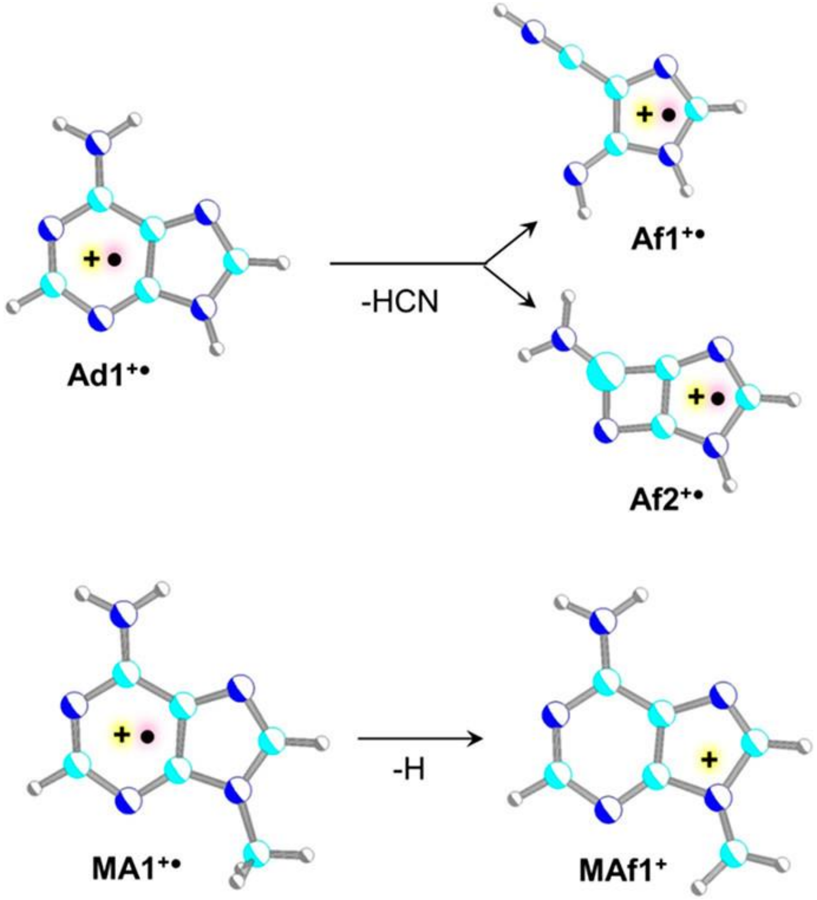

Scheme 3. Major Dissociations of $Ad1^{\bullet +}$ and $MA1^{\bullet +}$.

The potential energy surface for the migration (Figure S5, Supporting Information) showed a broad saddle at a large C-H separation (2.7 Å) whereby the N3-H bond at 1.85 Å was not yet formed. The in-plane migration forced the CH_2 group to be twisted out of the adenine ring plane, thus impairing π-electron interaction. Hence, the unfavorable geometry for the H atom migration was likely to prevent isomerization and formation of energetically favored tautomers. Both the C-

H separation and potential energy for the migration exceeded the threshold values for the simple H atom loss, where the C-H bond was essentially broken at 2.2 Å, and the H atom was departing at a 55° angle with respect to the adenine ring. This allowed the forming N═CH2 group to become planar and conjugated with the adenine π-electron system.

2.4.6. Comparison of Adenine with Other DNA Nucleobase Cation Radicals

The structure determination of the adenine and 9-methyladenine cation radicals as the respective canonical tautomers has completed the spectroscopic characterization of all four ionized DNA nucleobases. Energy calculations at the uniformly high level of theory indicate that the purine DNA nucleobases prefer the canonical forms. The stabilization of the canonical forms relative to the other tautomers, 14 and 2.8 kJ mol^{-1} for Ad1$^{\bullet+}$ and the guanine cation radical,[19] respectively, is relatively modest. The 9-methyl group has a mild effect on stabilizing tautomers of MA1$^{\bullet+}$ such as MA91$^{\bullet+}$, and the 6-OH tautomer of 9-methylguanine cation radical,[19] that are marginally more stable than the canonical forms. These global energy minima have not been yet observed experimentally and may require ingenious methods to be specifically generated in the gas phase. Importantly, however, UV-vis action spectra should provide unequivocal distinction of the isomeric adenine and guanine cation radicals, as evidenced by the current and previous studies.

Cation radicals derived from the pyrimidine nucleobases are more equivocal. The thymine cation radical has been shown to prefer noncanonical tautomers with OH groups produced by a hydrogen migration from the 6-methyl.[27] This is in a sharp contrast with neutral thymine which exists as the lowest energy canonical dioxo form.[58] Based on their relative energies,[59] cytosine cation radicals also represent a substantial departure from the neutral nucleobase. Neutral cytosine tautomers have been calculated to prefer the syn- and anti-2-OH tautomers over the canonical 2-oxo-N-1-H form.[60] In contrast, among cytosine cation radical tautomers, the lowest energy belongs to the 2-oxo-N-3-H tautomer, followed by the syn- and anti-2-OH tautomers.[59] In accord with theory, an experimental study using infrared multiphoton and UV-vis action spectroscopies has identified a mixture of cytosine cation radical tautomers being produced in the gas phase.[22] An important point of the nucleobase cation-radical properties is whether or not they extend to a more complex DNA building blocks such as nucleosides and nucleotides. Previous studies of 2'-deoxyriboguanosine[21] and riboguanosine[19] have indicated that ionized guanine maintains the canonical structure in gas-phase nucleosides. The properties of the other DNA nucleoside cation radicals remain to be investigated.

2.5. Conclusions

Cation radicals of adenine and 9-methyladenine are formed as their low-energy canonical tautomers by collision-induced oxidation in ternary copper-terpy complexes. The structures have been corroborated by UV-vis action spectra and matching calculated vibronic spectra. New low-energy noncanonical tautomers of the 9-methyladenine cation radical have been identified computationally that present a challenge to experimental verification and spectroscopic characterization. Comparison of the populations and relative energies of DNA cation radicals points to the ionized purine nucleobases preferring canonical tautomer structures in the gas phase. In contrast, the ionized pyrimidine nucleobases are equivocal, forming mixtures of several tautomers in the gas phase. In order to apply these data to ionized DNA, the nucleobase cation-radical properties have to be extended by studies of more complex nucleosides and nucleotides. Computational studies to this end are in progress in this laboratory.

2.6. References

1. Wagenknecht, H.-A., Ed. Charge Transfer in DNA; Wiley-VCH: Weinheim, Germany, 2005; pp 1– 23.
2. Schuster, G. B. Long-Range Charge Transfer in DNA: Transient Structural Distortions Control the Distance Dependence. Acc. Chem. Res. 2000, 33, 253– 260.

3. O’Neill, M. A.; Barton, J. K. Sequence-Dependent DNA Dynamics: The Regulator of DNA-Mediated Charge Transport. In Charge Transfer in DNA; Wagenknecht, H.-A., Ed.; Wiley-VCH: Weinheim, Germany, 2005; pp 27– 31.
4. Giese, B. Long-Distance Charge Transport in DNA: The Hopping Mechanism. Acc. Chem. Res. 2000, 33, 631– 636,
5. Steenken, S.; Jovanovic, S. V. How Easily Oxidizable Is DNA? One-Electron Reduction Potentials of Adenosine and Guanosine Radicals in Aqueous Solution. J. Am. Chem. Soc. 1997, 119, 617– 618,
6. NIST. Chemistry WebBook; Linstrom, P. J., Mallard, W. G., Eds.; NIST Standard Reference Database No. 69; National Institute of Standards and Technology: Gaithersburg, MD, 2019, http://webbook.nist.gov (retrieved July–December 2019)
7. Sevilla, M. D.; Besler, B.; Colson, A. O. Ab Initio Molecular Orbital Calculations of DNA Radical Ions. 5. Scaling of Calculated Electron Affinities and Ionization Potentials to Experimental Values. J. Phys. Chem. 1995, 99, 1060– 1063
8. Chen, X.; Syrstad, E. A.; Gerbaux, P.; Nguyen, M. T.; Tureček, F. Distonic Isomers and Tautomers of Adenine Cation Radical in the Gas Phase and Aqueous Solution. J. Phys. Chem. A 2004, 108, 9283– 9293
9. Crespo-Hernandez, C. E.; Arce, R.; Ishikawa, Y.; Gorb, J.; Leszczynski, J.; Close, D. M. Ab Initio Ionization Energy Thresholds of DNA and RNA Bases in Gas Phase and in Aqueous Solution. J. Phys. Chem. A 2004, 108, 6373– 6377
10. Cauet, E.; Dehareng, D.; Lievin, J. Ab Initio Study of the Ionization of the DNA Bases: Ionization Potentials and Excited States of the Cations. J. Phys. Chem. A 2006, 110, 9200– 9211
11. Cauet, E.; Lievin, J. Radical Cations of the Nucleic Acid Bases and Radiation Damage to DNA: Ab initio Study. Adv. Quantum Chem. 2007, 52, 121– 147,

12. Gatlin, C. L.; Tureček, F.; Vaisar, T. Gas-Phase Complexes of Amino Acids with Copper(II) and Diimine Ligands. Part II. Amino Acids with O, N and S Functional Groups in the Side-chain. J. Mass Spectrom. 1995, 30, 1617– 1627
13. Chu, I. K.; Rodriquez, C. F.; Lau, T. C.; Hopkinson, A. C.; Siu, K. W. M. Molecular Radical Cations of Oligopeptides. J. Phys. Chem. B 2000, 104, 3393– 3397
14. Wee, S.; O'Hair, R. A. J.; McFadyen, W. D. Can Radical Cations of the Constituents of Nucleic Acids Be Formed in the Gas Phase Using Ternary Transition Metal Complexes?. *Rapid Commun. Mass Spectrom.* **2005**, *19*, 1797– 1805
15. Lam, A. K.; Abrahams, B. F.; Grannas, M. J.; McFadyen, W. D.; O'Hair, R. A. J. Tuning the Gas Phase Redox Properties of Copper(II) Ternary Complexes of Terpyridines to Control the Formation of Nucleobase Radical Cations. *Dalton Trans.* **2006**, 5051– 5061
16. Dunbar, R. C. Photodissociation of Trapped Ions. *Int. J. Mass Spectrom.* **2000**, *200*, 571– 589
17. Antoine, R.; Dugourd, P. UV-Visible Activation of Biomolecular Ions. (Laser Photodissociation and Spectroscopy of Mass-Separated Biomolecular Ions). *Lect. Notes Chem.* **2013**, *83*, 93– 116
18. Polfer, N. C., Dugourd, P., Eds. Laser Photodissociation and Spectroscopy of Mass Separated Biomolecular Ions. *Lecture Notes in Chemistry*; Springer: Cham, 2013; Vol. 83, pp 13– 20
19. Dang, A.; Liu, Y.; Tureček, F. UV-Vis Action Spectroscopy of Guanine, 9-Methylguanine and 2′-Deoxyguanosine Cation Radicals in the Gas Phase. *J. Phys. Chem. A* **2019**, *123*, 3272– 3284
20. Feketeová, L.; Khairallah, G. N.; Chan, B.; Steinmetz, V.; Maître, P.; Radom, L.; O'Hair, R. A. J. Gas-Phase Infrared Spectrum and Acidity of the Radical Cation of 9-Methylguanine. *Chem. Commun.* **2013**, *49*, 7343– 7345,

21. Feketeova, L.; Yuriev, E.; Orbell, J. D.; Khairallah, G. N.; O’Hair, R. A. J. Gas-Phase Formation and Reactions of Radical Cations of Guanosine, Deoxyguanosine and Their Homodimers and Heterodimers. *Int. J. Mass Spectrom.* **2011**, *304*, 74– 82
22. Lesslie, M.; Lawler, J. T.; Dang, A.; Korn, J. A.; Bím, D.; Steinmetz, V.; Maitre, P.; Tureček, F.; Ryzhov, V. Cytosine Radical Cation: A Gas-Phase Study Combining IRMPD Spectroscopy, UVPD Spectroscopy, Ion–Molecule Reactions, and Theoretical Calculations. *ChemPhysChem* **2017**, *18*, 1293– 1301
23. Brown, R. D.; Godfrey, P. D.; McNaughton, D.; Pierlot, A. P. Tautomers of Cytosine by Microwave Spectroscopy. *J. Am. Chem. Soc.* **1989**, *111*, 2308– 2310
24. Dong, F.; Miller, R. E. Vibrational Transition Moment Angles in Isolated Biomolecules: A Structural Tool. *Science* **2002**, *298*, 1227– 1230
25. Nir, E.; Müller, M.; Grace, L. I.; de Vries, M. S. REMPI Spectroscopy of Cytosine. *Chem. Phys. Lett.* **2002**, *355*, 59– 64
26. Alonso, J. L.; Vaquero, V.; Pena, I.; Lopez, J. C.; Mata, S.; Caminati, W. All Five Forms of Cytosine Revealed in the Gas Phase. *Angew. Chem., Int. Ed.* **2013**, *52*, 2331– 2334
27. Dang, A.; Nguyen, H. T. H.; Ruiz, H.; Piacentino, E.; Ryzhov, V.; Tureček, F. Experimental Evidence for Non-Canonical Thymine Cation Radicals in the Gas Phase. *J. Phys. Chem. B* **2018**, *122*, 86– 97
28. Liu, Y.; Dang, A.; Urban, J.; Tureček, F. Charge-Tagged DNA Radicals I the Gas Phase Characterized by UV/Vis Photodisociation Action Spectroscopy. *Angew. Chem., Int. Ed.* **2020**,
29. Liu, Y.; Korn, J. A.; Dang, A.; Turecek, F. Hydrogen-Rich Cation Radicals of DNA Dinucleotides. Generation and Structure Elucidation by UV-Vis Action Spectroscopy. *J. Phys. Chem. B* **2018**, *122*, 9665– 9680

30. Dang, A.; Korn, J. A.; Gladden, J.; Mozzone, B.; Tureček, F. UV-Vis Photodissociation Action Spectroscopy on Thermo LTQ-XL ETD and Bruker amaZon Ion Trap Mass Spectrometers: A Practical Guide. *J. Am. Soc. Mass Spectrom.* **2019**, *30*, 1558– 1564
31. Frisch, M. J.; Trucks, G. W. et al. *Gaussian 16*, revision A03; Gaussian, Inc.: Wallingford, CT, 2016
32. Becke, A. D. New Mixing of Hartree-Fock and Local Density-Functional Theories. *J. Chem. Phys.* **1993**, *98*, 1372– 1377,
33. Yanai, T.; Tew, D. P.; Handy, N. C. A New Hybrid Exchange-Correlation Functional Using the Coulomb-Attenuating Method (CAM-B3LYP). *Chem. Phys. Lett.* **2004**, *393*, 51– 57,
34. Møller, C.; Plesset, M. S. A Note on an Approximation Treatment for Many Electron Systems. *Phys. Rev.* **1934**, *46*, 618– 622
35. Cížek, J. On the Use of the Cluster Expansion and the Technique of Diagrams in Calculations of Correlation Effects in Atoms and Molecules. *Adv. Chem. Phys.* **2007**, *14*, 35– 89
36. Purvis, G. D., III; Bartlett, R. J. A. Full Coupled-Cluster Singles and Doubles Model - the Inclusion of Disconnected Triples. *J. Chem. Phys.* **1982**, *76*, 1910– 1918
37. Zhao, Y.; Truhlar, D. G. The M06 Suite of Density Functionals for Main Group Thermochemistry, Thermochemical Kinetics, Noncovalent Interactions, Excited States, and Transition Elements: Two New Functionals and Systematic Testing of Four M06-Class Functionals and 12 Other Functionals. *Theor. Chem. Acc.* **2008**, *120*, 215– 241
38. Schlegel, H. B. Potential Energy Curves Using Unrestricted Møller-Plesset Perturbation Theory with Spin Annihilation. *J. Chem. Phys.* **1986**, *84*, 4530
39. Mayer, I. Spin-Projected UHF Method. IV. Comparison of Potential Curves Given by Different One-Electron Methods. *Adv. Quantum Chem.* **1980**, *12*, 189– 262,

40. Halkier, A.; Helgaker, T.; Jørgensen, P.; Klopper, W.; Koch, H.; Olsen, J.; Wilson, A. K. Basis Set Convergence in Correlated Calculations on Ne, N2, and H2O. *Chem. Phys. Lett.* **1998**, *286*, 243– 252

41. Comeau, D. C.; Bartlett, R. J. The Equation-of-Motion Coupled-Cluster Method. Applications to Open- and Closed-Shell Reference States. *Chem. Phys. Lett.* **1993**, *207*, 414– 423

42. Furche, F.; Ahlrichs, A. Adiabatic Time-Dependent Density Functional Methods for Excited State Properties. *J. Chem. Phys.* **2002**, *117*, 7433– 7447

43. Barbatti, M.; Ruckenbauer, M.; Plasser, F.; Pittner, J.; Granucci, G.; Persico, M.; Lischka, H. Newton-X: A Surface-Hopping Program for Nonadiabatic Molecular Dynamics. *Wiley Interdisciplinary Reviews: Comput. Mol. Sci.* **2014**, *4*, 26– 33

44. Broo, A.; Holmen, A. Calculations and Characterization of the Electronic Spectra of DNA Bases Based on ab Initio MP2 Geometries of Different Tautomeric Forms. *J. Phys. Chem. A* **1997**, *101*, 3589– 3600

45. Clark, L. B.; Peschel, G. G.; Tinoco, I., Jr. Vapor Spectra and Heat of Vaporization of Some Purine and Pyrimidine Bases. *J. Phys. Chem.* **1965**, *69*, 3615– 3618

46. Sapunar, M.; Domcke, W.; Doslic, N. UV Absorption Spectra of DNA Bases in the 350–190 nm Range: Assignment and State Specific Analysis of Solvation Effects. *Phys. Chem. Chem. Phys.* **2019**, *21*, 22782– 22793

47. Marian, C.; Nolting, D.; Weinkauf, R. The Electronic Spectrum of Protonated Adenine: Theory and Experiment. *Phys. Chem. Chem. Phys.* **2005**, *7*, 3306– 3316

48. Pedersen, S. O.; Stochkel, K.; Byskov, C. S.; Baggesen, L. M.; Nielsen, S. B. Gas-Phase Spectroscopy of Prootnated Adenine, Adenosine 5′-monophosphate and Monohydrated Ions. *Phys. Chem. Chem. Phys.* **2013**, *15*, 19748– 19752

49. Hanus, M.; Kabelac, M.; Rejnek, J.; Ryjacek, F.; Hobza, P. Correlated ab Initio Study of Nucleic Acid Bases and Their Tautomers in the Gas Phase, in a Microhydrated

Environment, and in Aqueous Solution. Part 3. Adenine. *J. Phys. Chem. B* **2004**, *108*, 2087– 2097

50. Brown, R. D.; Godfrey, P. D.; McNaughton, D.; Pierlot, A. P. A Study of the Major Gas-Phase Tautomer of Adenine by Microwave Spectroscopy. *Chem. Phys. Lett.* **1989**, *156*, 61– 63
51. Orlov, V. M.; Smirnov, A. N.; Varshavsky, Ya. M. Ionization Potentials and Electron-Donor Ability of Nucleic Acid Bases and Their Analogs. *Tetrahedron Lett.* **1976**, *17*, 4377– 4378
52. Bauer, C. Al.; Grimme, S. Elucidation of Electron Ionization Induced Fragmentations of Adenine by Semiempirical and Density Functional Molecular Dynamics. *J. Phys. Chem. A* **2014**, *118*, 11479– 11484
53. Nelson, C. C.; McCloskey, J. A. Collison-Induced Dissociation of Adenine. *J. Am. Chem. Soc.* **1992**, *114*, 3661– 3668
54. Dawley, M. M.; Tanzer, K.; Cantrell, W. A.; Plattner, P.; Brinkmann, N. R.; Scheier, P.; Denifl, S.; Ptasinska, S. Electron Ionization of the Nucleobases Adenine and Hypoxanthine Near the Threshold: a Combined Experimental and Theoretical study. *Phys. Chem. Chem. Phys.* **2014**, *16*, 25039– 25053
55. Luhrs, D. C.; Viallon, J.; Fischer, I. Excited-State Spectroscopy and Dynamics of Isolated Adenine and 9-Methyladenine. *Phys. Chem. Chem. Phys.* **2001**, *3*, 1827– 1831
56. Ullrich, S.; Schultz, T.; Zgierski, M. Z.; Stolow, A. Direct Observation of Electronic Relaxation Dynamics in Adenine via Time-Resolved Photoelectron Spectroscopy. *J. Am. Chem. Soc.* **2004**, *126*, 2262– 2263,
57. Kang, H.; Jung, B.; Kim, S. K. Mechanism for Ultrafast Internal Conversion of Adenine. *J. Chem. Phys.* **2003**, *118*, 6717– 6719,
58. Brown, R. D.; Godfrey, P. D.; McNaughton, D.; Pierlot, A. P. Microwave Spectrum of the Major Gas-Phase Tautomer of Thymine. *J. Chem. Soc., Chem. Commun.* **1989**, 37– 38

59. Wolken, J. K.; Yao, C.; Tureček, F.; Polce, M. J.; Wesdemiotis, C. Cytosine Neutral Molecules and Cation-Radicals in the Gas-Phase. Structures, Energetics, Ion Chemistry, and Neutralization-Reionization Mass Spectrometry. *Int. J. Mass Spectrom.* **2007**, *267*, 30– 42

60. Trygubenko, S. A.; Bogdan, T. V.; Rueda, M.; Orozco, M.; Lique, F. J.; Sponer, J.; Slavicek, P.; Hobza, P. Correlated ab Initio Study of Nucleic Acid Bases and Their Tautomers in the Gas Phase, in a Microhydrated Environment and in Aqueous Solution. Part 1. Cytosine. *Phys. Chem. Chem. Phys.* **2002**, *4*, 4192– 4203

2.7. Appendix

Table 1. Adenine Cation-Radical Relative and Dissociation Energies.

	Relative Energy^{a,b}			
Ion/ Reaction	M06-2X 6-31+G(d,p)	M06-2X 6-311++G(2d,p)	CCSD(T) aug-cc-pVTZ^{c}	CCSD(T) CBS^{d}
Ad1$^{+\bullet}$	0	0	0	0
Ad3$^{+\bullet}$	25	24	17	18
Ad6$^{+\bullet}$	21	21	22	22
Ad7$^{+\bullet}$	56	53	46	45
Ad367$^{+\bullet}$	42	43	45	46
Ad679$^{+\bullet}$	53	56	61	67
Ad10$^{+\bullet}$	68	66	66	58
Ad369$^{+\bullet}$	86	86	101	103
Ad79$^{+\bullet}$	130	133	132	-
Ad88$^{+\bullet}$	215	213	234	-
Ad1$^{+\bullet}$ → **F1**$^{+\bullet}$ + HCN	260	248	226	231
Ad1$^{+\bullet}$ → **F2**$^{+\bullet}$ + HCN	373	366	343	348

---

[a] In kJ mol^{-1}. [b] Including B3LYP/6-31+G(d,p) zero-point energies scaled with 0.975 and referring to 0 K in the gas phase. [c] Extrapolated to this basis set according to the linear formula: E[CCSD(T)/aug-cc-pVTZ] $\cong$ E[CCSD(T)/aug-cc-pVDZ] + E[MP2/aug-cc-pVTZ] – E[MP2/aug-cc-pVDZ]. [d] Single-point energies on CCSD/6-31+G(d,p) optimized geometries, extrapolated to the complete basis set, see Supporting Table S1.

Table 2. Relative and Dissociation Energies of Methyladenine Cation-Radicals.

Ion/ Reaction	Relative Energy[a,b] M06-2X 6-31+G(d,p)	M06-2X 6-311++G(2d,p)	CCSD(T) aug-cc-pVTZ[c]	CCSD(T) CBS[d]
MA1$^{+\bullet}$	0	0	0	0
MA6$^{+\bullet}$	23	23	19	22
MA67$^{+\bullet}$	49	52	-	-
MA18$^{+\bullet}$	79	81	86	85
MA36$^{+\bullet}$	90	90	-	-
MA91$^{+\bullet}$	–8	–6	–5	–8
MS93$^{+\bullet}$	4	4	5	2
MA97$^{+\bullet}$	22	24	25	23
MA98$^{+\bullet}$	82	81	83	87
MA1$^{+\bullet}$ → **MAf1**$^{+}$ + H	304	299	293	292
MA1$^{+\bullet}$ → TS(H-dis)	300	298	290	290

[a] In kJ mol^{-1}. [b] Including B3LYP/6-31+G(d,p) zero-point energies scaled with 0.975 and referring to 0 K in the gas phase. [c] Extrapolated to this basis set according to the linear formula: E[CCSD(T)/aug-cc-pVTZ] ≅ E[CCSD(T)/aug-cc-pVDZ] + E[MP2/aug-cc-pVTZ] – E[MP2/aug-cc-pVDZ]. [d] Single-point energies on CCSD/6-31+G(d,p) optimized geometries, extrapolated to the complete basis set, see Supporting Table S1.

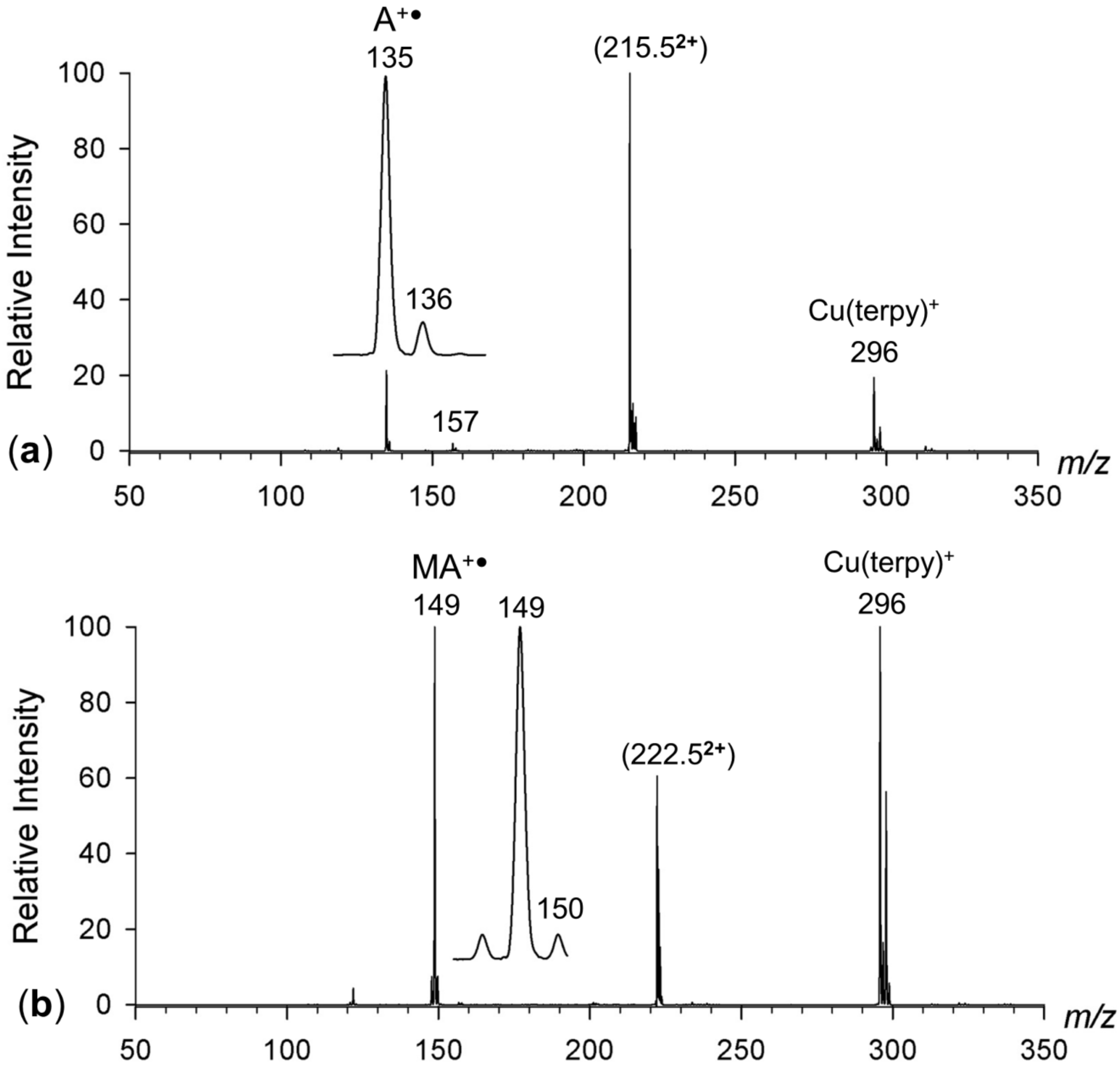

Figure 1. CID-MS^2 spectra of (a) [Cu(terpy)adenine]$^{2+\bullet}$ (m/z 215.5) and (b) [Cu(terpy)methyladenine]$^{2+\bullet}$ (m/z 222.5). Insets show the cation radical peak profiles.

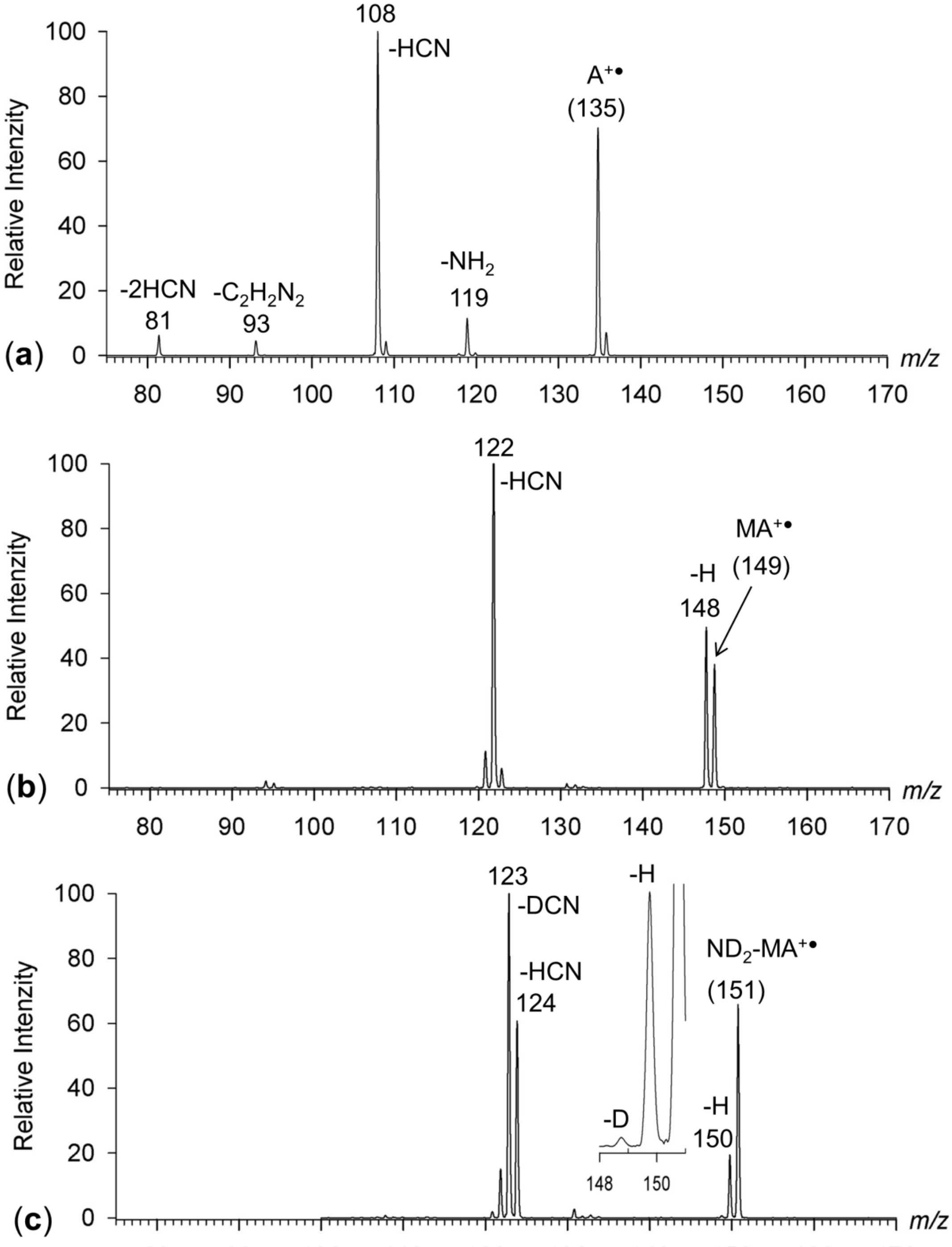

Figure 2. CID-MS^3 spectra of (a) [adenine]$^{+\bullet}$, (b) [9-methyladenine]$^{+\bullet}$, and (c) [ND$_2$-9-methyladenine]$^{+\bullet}$.

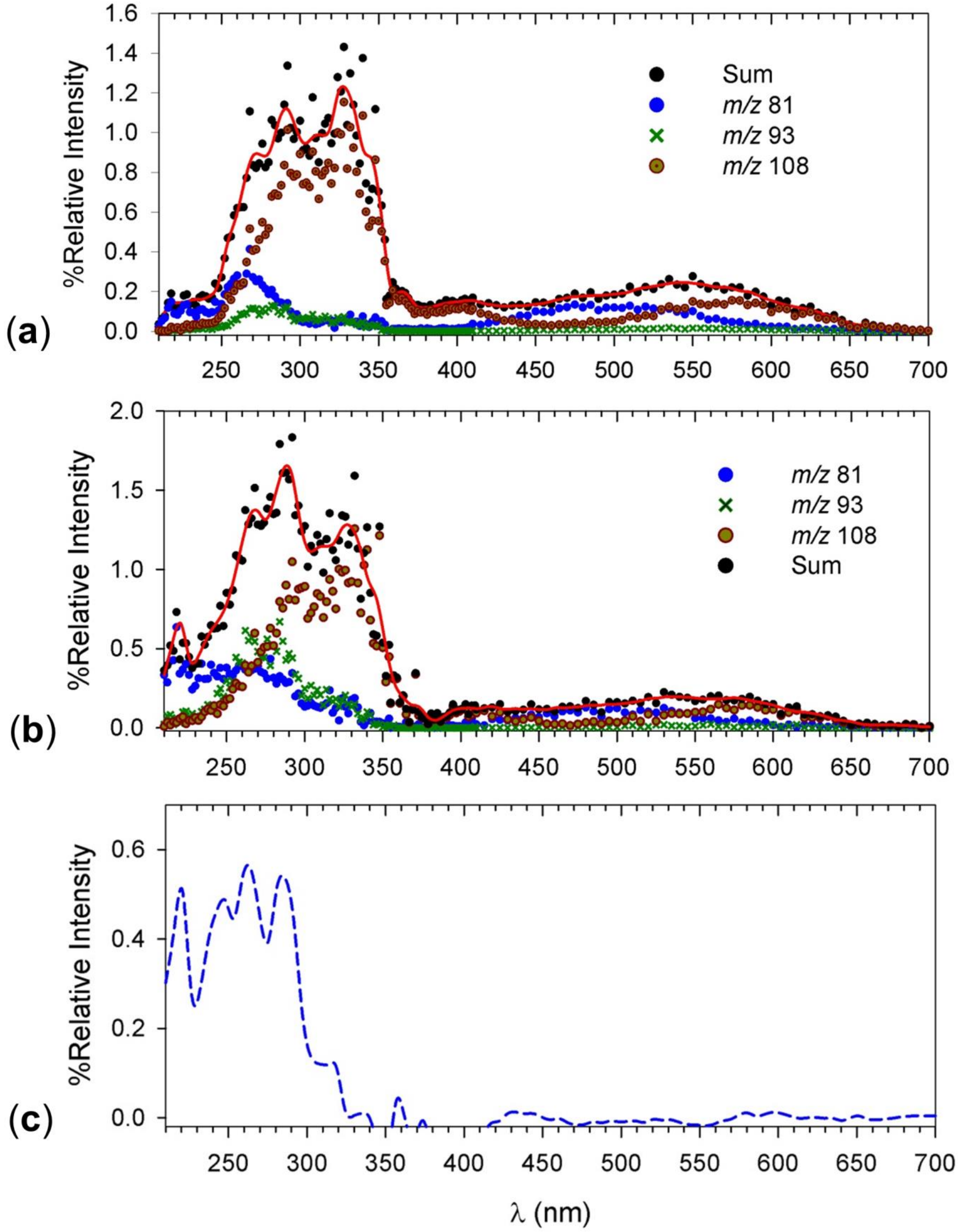

Figure 3. Action spectra of (a) [adenine]$^{+\bullet}$ and (b) m/z 135 ion from 9-(2-bromoethyl)adenine. (c) Difference spectrum of (a) and (b).

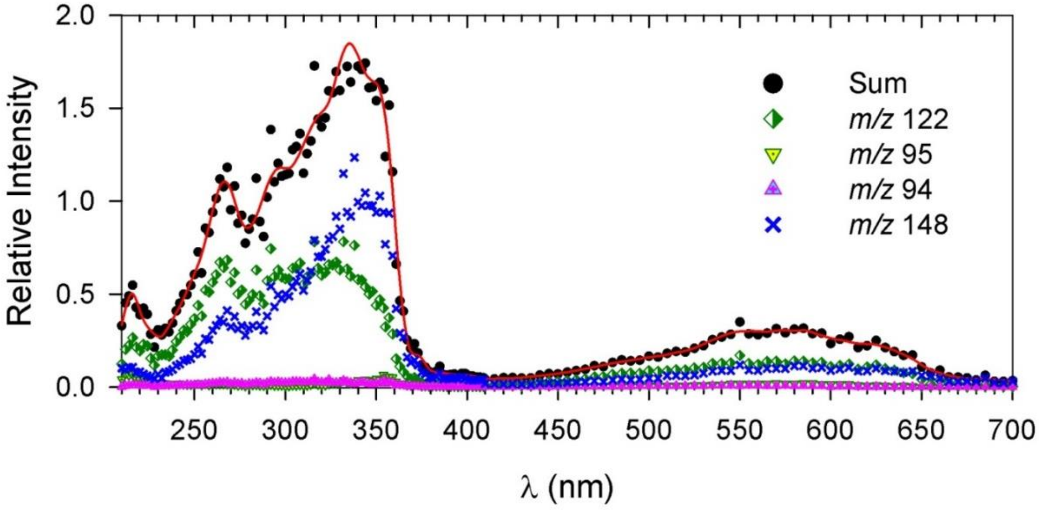

Figure 4. Action spectrum of [9-methyladenine]$^{+\bullet}$.

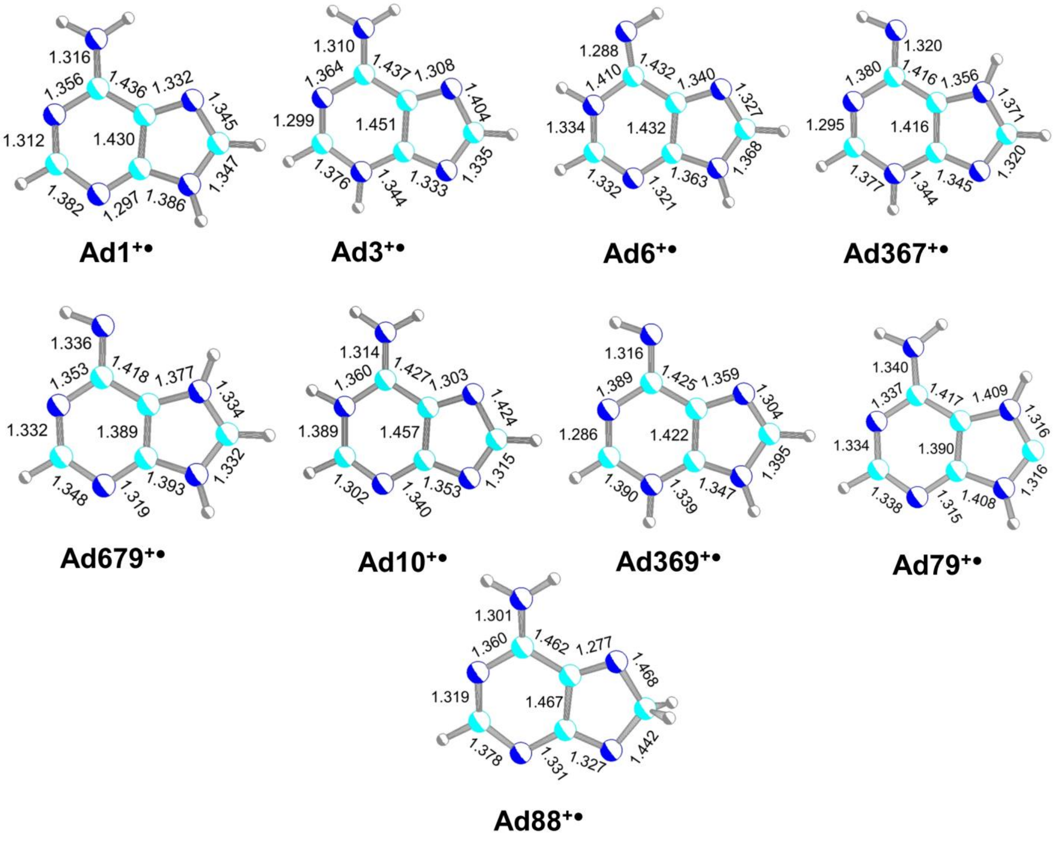

Ad1$^{+\bullet}$ **Ad3$^{+\bullet}$** **Ad6$^{+\bullet}$** **Ad367$^{+\bullet}$**

Ad679$^{+\bullet}$ **Ad10$^{+\bullet}$** **Ad369$^{+\bullet}$** **Ad79$^{+\bullet}$**

Ad88$^{+\bullet}$

Figure 5. M06-2X/6-31+G(d,p)-optimized geometries of low-energy adenine cation radicals. Atom color coding as in Figure 1. Bond lengths are in angstroms.

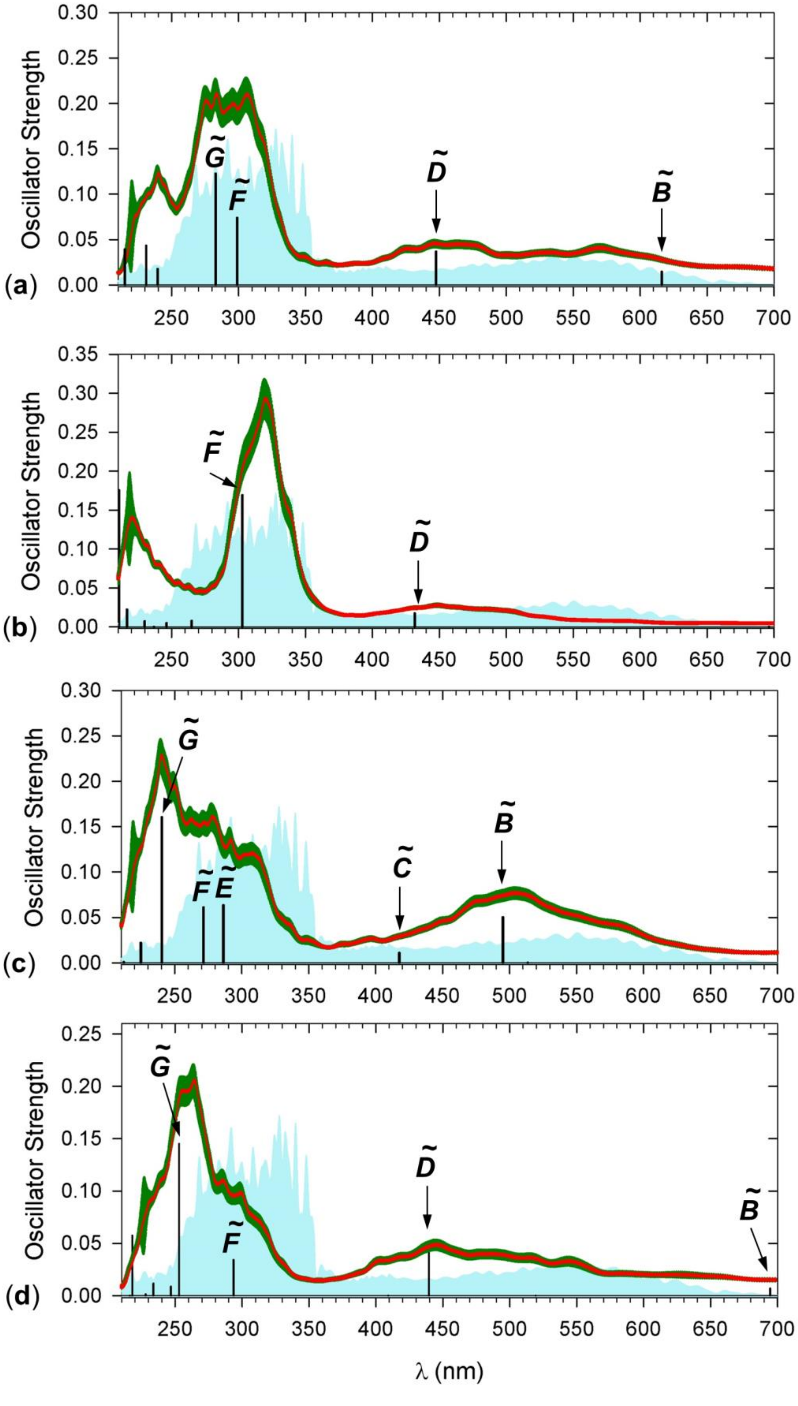

Figure 6. M06-2X/6-31+G(d,p) TD-DFT vibronic absorption spectra of (a) Ad1$^{•+}$, (b) Ad3$^{•+}$, (c) Ad6$^{•+}$, and (d) Ad7$^{•+}$. The blue shaded areas display the action spectrum presented as a sum of photofragment ion intensities and scaled for visual perusal.

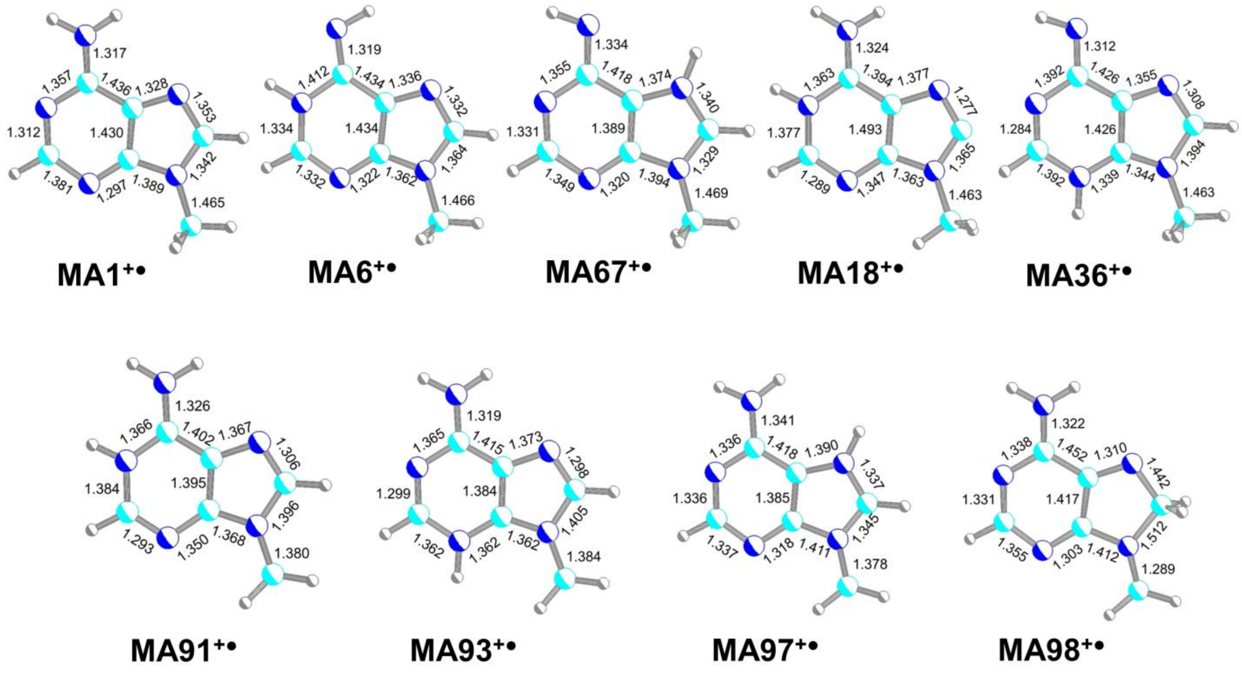

Figure 7. M06-2X/6-31+G(d,p)-optimized structures of low-energy MA$^{\bullet+}$ tautomers. Atom color coding as in Figure 1. Bond lengths are in angstroms.

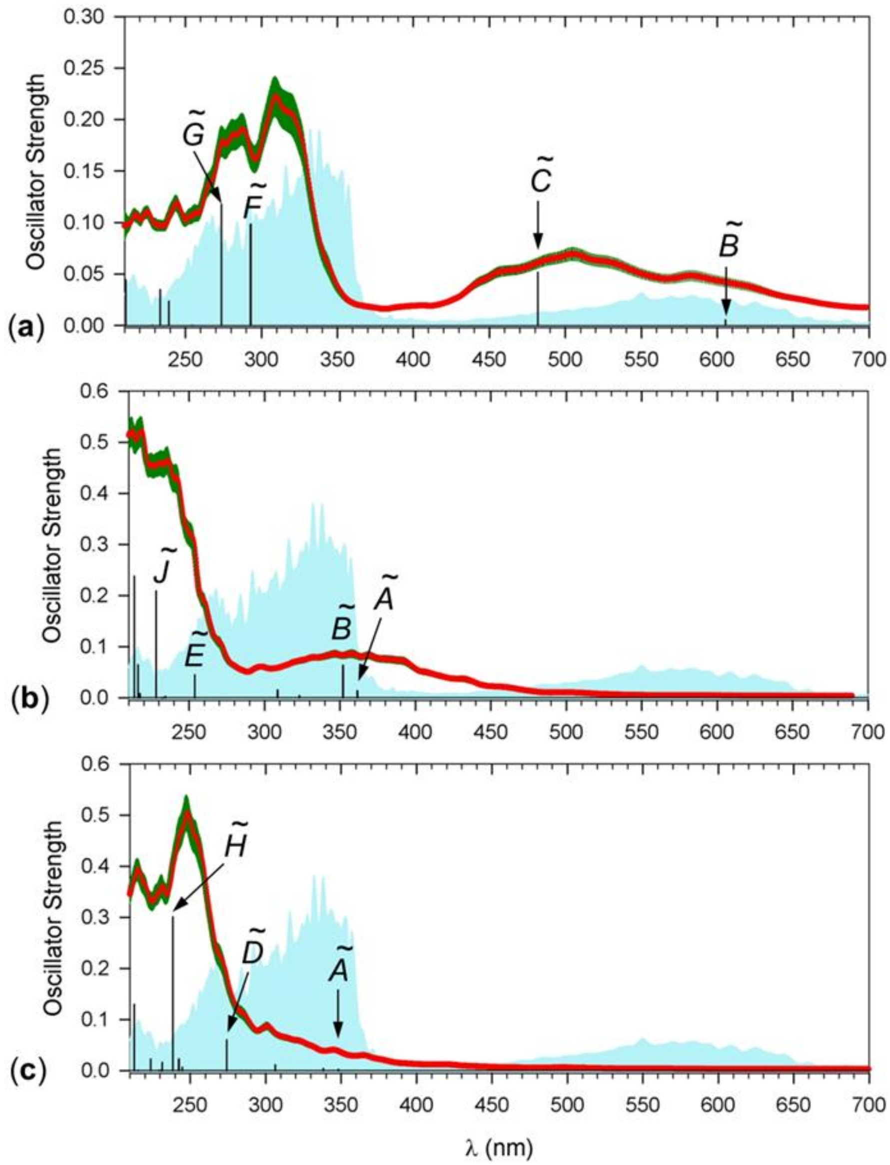

Figure 8. M06-2X/6-31+G(d,p) TD-DFT vibronic absorption spectra of (a) $MA1^{\bullet+}$, (b) $MA91^{\bullet+}$, and (c) $MA93^{\bullet+}$. The blue shaded areas are the action spectra presented as a sum of photofragment ion intensities and scaled for visual perusal.

Chapter 3—The Elusive Noncanonical Isomers of Ionized 9-Methyladenine and 2'-Deoxyadenosine

Reproduced in part with permission from S.R. Huang, G. Nováková, A. Marek, F. Tureček, *J. Phys. Chem. A*, **2021**, 125, 338-348, DOI: 10.1021/acs.jpca.0c10293.

3.1. Abstract

Noncanonical nucleobases and nucleosides represent newly discovered species of relevance for DNA ionization. We report a targeted synthesis of gas-phase 9-methylene(1H)adenine cation radical ($2^{+\bullet}$) as a low-energy isomer of ionized 9-methyladenine. Ion $2^{+\bullet}$ showed unique collision-induced dissociation and UV-vis photodissociation action spectra that distinguished it from other cation radical isomers. Ab initio energy calculations with coupled cluster theory extrapolated to the complete basis set limit, CCSD(T)/CBS, identified cation radical $2^{+\bullet}$ as the global energy minimum of the adenine-related $C_6H_7N_5^{+\bullet}$ isomers. The action spectrum of $2^{+\bullet}$ was assigned on the basis of vibronic absorption spectra that were calculated with time-dependent density functional theory for multiple vibrational configurations of thermal ions. The major dissociation of $2^{+\bullet}$ proceeded by hydrogen loss that was elucidated by deuterium labeling at the exchangeable N-1 and NH_2 positions and C-8 position and by kinetic analysis. The dissociation involved a reversible rearrangement to intermediate dihydropteridine structures, yielding a protonated aminopteridine as the product, which was identified by multistep UV-vis action spectroscopy. We also report a computational study of related noncanonical isomers of 2'-deoxyadenosine cation radical having the radical defect at C-1' that were found to be thermodynamically more stable than the canonical isomer in both the gas phase and aqueous solution. The noncanonical isomers were calculated to have extremely low ion-electron recombination energies of 4.42-5.10 eV that would make them dead-end hole traps if produced by DNA ionization.

3.2. Introduction

The DNA nucleobases represent chemically stable and biologically conserved heteroaromatic molecules of essential importance for terrestrial life forms. Ionization by high-energy particles or photons disrupts the nucleobase π-electronic system, rendering nucleobase cation radicals susceptible to fast electron and proton transfer reactions within DNA or with surrounding molecules. Previous experimental and theoretical investigations of nucleobase cation radicals have largely treated these reactive species within the paradigm of canonical structures produced by electron removal from neutral nucleobases.[1-13] However, this paradigm has been challenged recently by the generation of stable non-canonical isomers of the thymine[14] and 1-methylcytosine[15] cation radicals in the gas phase. Computational energy analysis of the non-canonical cation radicals of both thymine (4-hydroxy-5-methylene-(1,3*H*)pyrimid-2-one[14,16]) and 1-methylcytosine (1-methylene-2-hydroxy-4-aminopyrimidine[15]) revealed that they were substantially more stable than the pertinent canonical forms of oxidized DNA nucleobases. The discovery of non-canonical nucleobase cation radicals has been made possible by a combination of methods of gas-phase ion chemistry to generate such unusual species,[17,18] and UV-Vis photodissociation (UVPD) action spectroscopy[19-21] to characterize the ions and distinguish them from their canonical isomers and other protomers. Ion action spectroscopy relies on photodissociation of mass-selected gas-phase ions whereby the wavelength-dependent photofragment ion intensities are used to reconstruct the absorption profile of the precursor ion. Several variants of action spectroscopy have been developed working in the infrared or UV-Vis regions of the spectrum.[22-24] Multiphoton infrared photodissociation spectroscopy has been the most popular technique for small ions,[25] whereas its applications to strongly hydrogen bonded systems have faced difficulties with band assignment and spectra interpretation.[26,27] UV-Vis spectroscopy utilizing valence-electron excitation and single-photon dissociation largely avoids such issues and has been shown to provide structure information for larger biomolecular ions that display characteristic absorption bands, such as peptide and oligonucleotide cation radicals.[28-32]

The previously reported non-canonical nucleobase cation radicals have been generated by collision-induced oxidation of nucleobase ligands in metal ternary complexes[17,18] that relied on ion thermodynamics while not allowing one to have a mechanistic control over the produced ion structures.[14,15] We now report a combined experimental and ab initio computational study documenting a specific generation of a stable non-canonical isomer of 9-methyladenine cation radical that we complement with energy analysis of cation radicals of 2'-deoxyadenosine. Purine and pyrimidine nucleobases carrying a methyl group at N-9 or N-1, respectively, which are the linking positions to 2'-deoxyribose in DNA, have often been used as simplified models for nucleosides to limit the number of theoretical protomers while maintaining intact the π-electronic system of the nucleobase.[1,17,18]

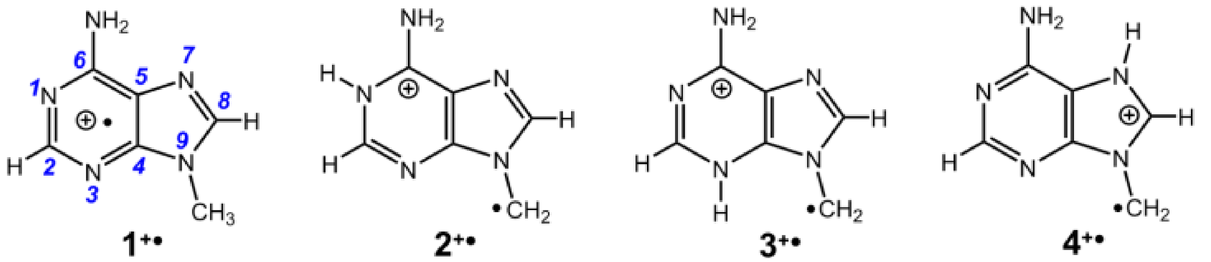

Scheme 1. Low-energy isomers of 9-methyladenine cation radical.

Two low-energy non-canonical isomers of 9-methyladenine cation radical (**1**$^{+\bullet}$) have recently been identified by ab initio calculations as 9-methylene-(*1H*)adenine (**2**$^{+\bullet}$) and 9-methylene-(*3H*)adenine (**3**$^{+\bullet}$) (Scheme 1).[33] However, synthetic pathways to generating ions **2**$^{+\bullet}$ and **3**$^{+\bullet}$ have not been established, especially in light of the energy analysis of the potential energy surface that has indicated large energy barriers separating the isomers and precluding unimolecular isomerization.[33] We reasoned that an adenine derivative carrying an N-9 CH$_2$-X group can be protonated, yielding a stable gas-phase ion in which a labile C–X bond, such as

C–I, could be homolytically cleaved upon collisional activation to form a ring-protonated 9-CH_2 radical, such as **$2^{+\bullet}$** (Scheme 2) or its N-3 (**$3^{+\bullet}$**) or N-7-protonated tautomers (**$4^{+\bullet}$**).

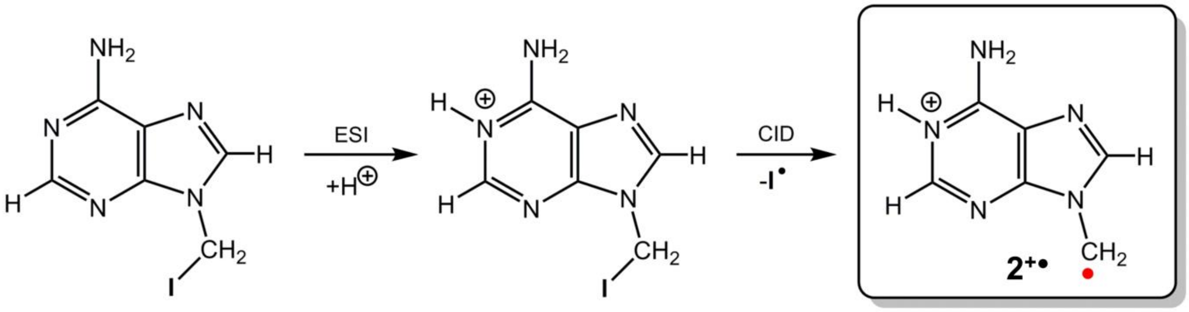

Scheme 2. Reaction sequence leading to ion **$2^{+\bullet}$** involving electrospray ionization (ESI) and collision-induced dissociation (CID).

A similar approach has been used by Kenttamaa and coworkers to generate σ-radicals in gas-phase distonic heteroaromatic ions.[34-37] According to our preliminary ab initio and density functional theory (DFT) calculations, thermodynamics favors N-1 in 9-alkylsubstituted adenines as the most basic position, possibly providing a pathway to generating **$2^{+\bullet}$**.

3.3. Experimental

3.3.1 Materials

Formaldehyde, adenine, thionylchloride, and deuterated solvents were obtained from Sigma-Aldrich (Milwaukee, WI). Solvents used in synthesis were purchased from Acros Organics (Geel, Belgium) or Penta Chemicals Unlimited (Prague, Czech Republic). N-Bromosucinimide was purchased from Fluka Chemie GmbH (Buchs, Switzerland), Pd/$CaCO_3$ (5%, type 405) was from Johnson Matthey (Prague, Czech Republic). Reagents and solvents were used without further purification. 9-Iodomethyladenine and [8-D]-9-iodomethyladenine were synthesized according to Scheme 3.

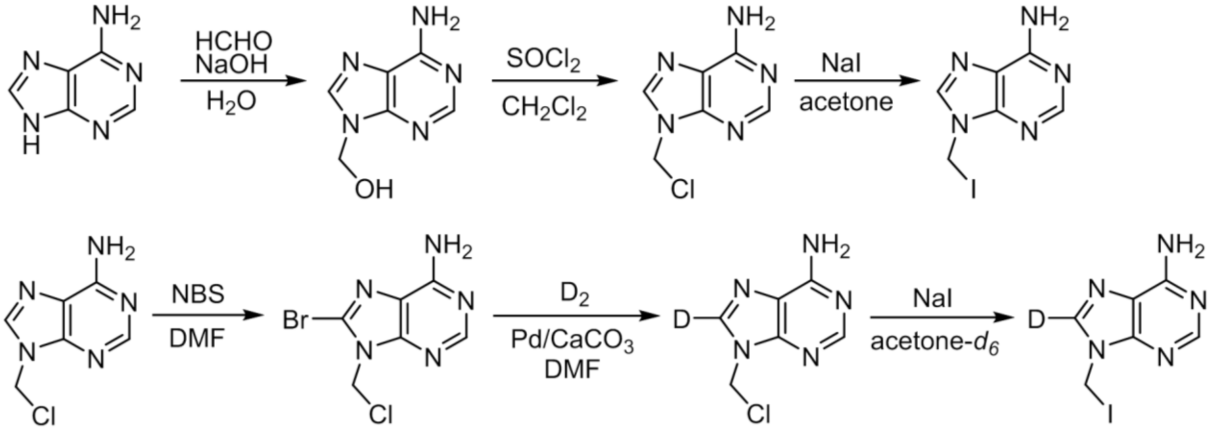

Scheme 3. Synthesis of 9-iodomethyladenine and [8-D]-9-iodomethyladenine.

A detailed description of the synthetic procedures and product spectroscopic characterization are provided in the Supporting Information (Scheme S1 and S2).

3.3.2. Methods

^{1}H and ^{13}C-NMR spectra were recorded on a Bruker Avance II spectrometer at 300 and 75 MHz, respectively at 25 °C. Experiments with tandem mass and photodissociation action spectra were performed on a modified amaZon Speed 3D ion trap tandem mass spectrometer (Bruker Daltonik, Bremen, Germany) equipped with an EKSPLA NL301G Nd-YAG laser (Altos Photonics, Bozeman, MT, USA) working at 20 Hz frequency and 3- to 6-ns pulse width, as described in detail previously.**[38]** Photofragment ion intensities were measured in three sections covering the 210-354 nm, 355-409 nm, and 410-700 nm ranges and normalized to the number of photons per pulse that were determined from laser pulse energy measurements at each experimental wavelength. The action spectra were reproduced on different days and are reported as averages of two measurements. Experiments involving H/D exchange were carried out in D_2O/CD_3CN solution that was used for electrospray ionization. The D content in gas-phase ions was maintained by feeding D_2O solvent vapor into the dry nitrogen stream flushing the enclosed electrospray interface volume. A high-resolution Orbitrap Velos mass spectrometer

(Thermo Fisher, San Jose, CA, USA) was used to measure accurate mass-to-charge ratios at a resolving power of 60000.

3.3.3. Calculations

We used the Gaussian 16 (Revision A03) suite of programs[39] to carry out ab initio and density functional theory (DFT) calculations of ions and neutral molecules of interest. Structures were first optimized using the hybrid B3LYP[40] and CAM-B3LYP[41] functionals and the 6-31+G(d,p) and 6-311+G(2d,p) basis sets, respectively, to obtain a preliminary ranking of the cation-radical tautomers. Harmonic frequencies were used to identify local energy minima as having all real frequencies and transition states as having one imaginary frequency. Based on our previous analysis and benchmarking of optimized geometries of nucleobase cation radicals,[15,33] we obtained additional sets of optimized geometries with M06-2X[42] and the 6-31+G(d,p) and 6-311++G(2d,p) basis sets to be used in single-point energy calculations. All these calculations were performed within the spin-unrestricted formalism. Solvation energies were calculated with full gradient optimization using the Polarizable Continuum Model (PCM)[43] and M06-2X/6-311++G(2d,p). Single-point energies were calculated using coupled clusters[44] with single, double, and disconnected triple excitations, CCSD(T),[45] and extrapolated to the complete basis set (CBS),[46] providing benchmark relative energies. We used the formula $E[\mathrm{CCSD(T)/CBS}] \approx E[\mathrm{CCSD(T)/aug\text{-}pVDZ}] - E[\mathrm{MP2/aug\text{-}pVDZ}] + E[\mathrm{HF/aug\text{-}pVQZ}] + E_{\mathrm{corr,CBS}}$, to extrapolate the basis set and obtain benchmark relative energies. The correlation energy at the complete basis set limit was calculated with least-squares fits to the standard two-parameter formula,[47] $E_{\mathrm{corr,CBS}} = \lim(X\rightarrow\infty)E_{\mathrm{corr,X}} = E[\mathrm{HF/aug\text{-}cc\text{-}pVXZ}] - E[\mathrm{MP2/aug\text{-}cc\text{-}pVXZ}] = A + BX^{-3}$, where X is the ζ split in the aug-cc-pVXZ basis set.[48] Higher spin states in the UMP2 calculations were treated with the spin projection method[49,50] using spin annihilation that reduced the total spin close to the theoretical value (0.75). Electronic excitations were evaluated using equation-of-motion CCSD (EOM-CCSD) calculations[51] with the 6-31+G(d,p) basis set for 16-18 excited electronic states, covering excitations down to 200 nm for all ions. WE used the

EOM-CCSD transitions to assign transitions in time-dependent DFT (TD-DFT)[52] calculations that were carried out with M06-2X. We found that 35-40 excited states in adenine and 9-methyladenine cation radicals were sufficient to cover the wavelength range to below 180 nm. The M06-2X TD-DFT calculations with the 6-31+G(d,p) and 6-311++G(2d,p) basis sets gave very similar results in terms of excitation energies and oscillator strength, as reported recently for other nucleobase cation radicals.[15,33] Therefore, the M06-2X/6-31+G(d,p) TD-DFT calculations were used to calculate all vibronic spectra at 310 K. The B3LYP/6-31+G(d,p) normal modes were used to generate Wigner distributions[53,54] of vibrational configurations of the ground electronics state. This was performed with the Newton X 16 program.[55] The configurations were ordered according to their Boltzmann factors at 310 K, and 300 lowest-energy configurations were selected and submitted to TD-DFT M06-2X/6-31+G(d,p) calculations for 20 excited states to generate the vibronic spectra reported here. To address the dissociation kinetics, we performed Rice-Ramsperger-Kassel-Marcus (RRKM) calculations of rate constants[56] using the QCPE program[57] that was recompiled and run under Windows 7, as described previously.[58] Born-Oppenheimer molecular dynamics (BOMD) trajectories were run with semiempirical all-valence-electron quantum chemistry calculations using the Berendsen thermostat algorithm.[59] Temperature was set at 310 K to approximate the experimental conditions in the ion trap. For each 2'-deoxyadenosine tautomer, several (> 5) initial structures were constructed from PM6-optimized adenosine cation radicals with different nucleobase-deoxyribose orientations and ring conformations. These structures were subjected to a preliminary BOMD using PM6[60] that was augmented by including dispersion interactions (D3H4).[61] These calculations were run by MOPAC[62] that was coupled to the Cuby4 framework.[63,64] Running trajectories with 1 fs steps for 20 ps furnished 20,000 snapshots per each initial structure from which 200 snapshots were extracted at 100 fs intervals. The extracted snapshot structures were fully gradient-optimized with PM6-D3H4 and sorted out by their secondary structural similarities to compact duplicates and reduce the size of the selection. This yielded 10–20 distinct structures whose geometries were fully gradient-optimized by B3LYP and M06-2X/6-31+G(d,p) calculations.

3.4. Results & Discussion

3.4.1. Ion Generation and Spectra

Electrospray ionization of 9-iodomethyladenine generated the protonated ion (*m/z* 276) that upon mass isolation and collision induced dissociation (CID) eliminated iodine, giving rise to the $C_6H_7N_5^{+\bullet}$ cation radical that was further characterized by its accurate *m/z* 149.0616 from a high-resolution CID-MS^2 spectrum (Figure 1a). Similarly, electrospray of 9-iodomethyladenine from a D_2O/CD_3CN solution generated an H/D-exchanged 9-iodomethyladenine ion at *m/z* 297 that produced a $C_6H_4D_3N_5$ ion (*m/z* 152) upon CID (Figure 1b). To further enhance adenine protonation selectivity,**[31,32]** we also considered protonated complexes of 9-methyladenine with 2,3:11,12-dibenzo-18-crown-6-ether (DBCE) where hydrogen bonding to the crown ether greatly favors conformers of the N-1-H protomer (Tables S1, S2, Figures S1, S2, Supporting Information). Electrospray ionization of 9-iodomethyladenine with DBCE produced the non-covalent complex ion (*m/z* 636) that was converted into $C_6H_7N_5^{+\bullet}$ in two consecutive CID steps, first eliminating DBCE and then iodine (Figure S3a,b, Supporting Information). Two steps with intermediate ion isolation were necessary to overcome the low-mass cutoff limit of the ion trap.

The $C_6H_7N_5^{+\bullet}$ ion was further characterized by its CID-MS^3 spectrum which showed a single dissociation by loss of H (Figure 2a). Loss of H upon CID was also prevalent (>98%) from the N-D_3-exchanged ion at *m/z* 152 and abundant from the [8-D] ion (*m/z* 150) which showed a 12/88 ratio for D and H loss (Figure 2a, insets). The CID spectrum of the $C_6H_7N_5^{+\bullet}$ ion was clearly distinct from that of the canonical isomer, $[\text{9-methyladenine}]^{+\bullet}$ (Figure 2b).**[33]** The latter showed a prominent fragment ion by elimination of HCN (*m/z* 122) that was absent in the Figure 2a CID spectrum. Loss of H was also the main photodissociation (UVPD) of $C_6H_7N_5^{+\bullet}$ where it was accompanied by a minor elimination of $C_2H_2N_2$ (*m/z* 95, Figure 2c) from both the unlabeled and [N-D_3] forms (Figure S4a,b, Supporting Information). The loss of D from the labeled ions showed a slightly increased D/H ratios, 7/93 and 14/86 for the [N-D_3] and [8-D] ions, respectively (Figure 2c, insets) The overall MS^3 results strongly indicated that the $C_6H_7N_5^{+\bullet}$ ion was different from the canonical [9-methyladenine]$^{+\bullet}$ isomer.

3.4.2. Action Spectra

The *m/z* 148 and *m/z* 95 fragment ions identified in the CID and UVPD spectra were selected to monitor the action spectra of the $C_6H_7N_5^{+\bullet}$ ions in the 210-700 nm region. We obtained action spectra for $C_6H_7N_5^{+\bullet}$ ions generated from both 9-iodomethyladenine (Figure 1a) and its complex with DBCE (Figure S3b, Supporting Information). The spectra were identical, as documented by comparing the Figure 3a and Figure S5 data, indicating that the same ions were generated by both methods. The action spectrum of $C_6H_7N_5^{+\bullet}$ showed a composite band with maxima at 220 and 260 nm, several bands in the 340-410 nm region, and a shoulder at 440 nm extending to 510 nm. These bands were represented in both mass-resolved photodissociation channels, with the *m/z* 95 fragment ion contributing more to the 220 nm band (Figure 3a). The action spectrum of $C_6H_7N_5^{+\bullet}$ markedly differed from the previously reported spectrum of $\mathbf{1}^{+\bullet}$,[33] which showed prominent bands with maxima at 335 and 580 nm (Figure 3b). These bands were not represented in the action spectrum of $C_6H_7N_5^{+\bullet}$.

3.4.3. Ion Structures and Action Spectra Assignment

To assign structure to the new $C_6H_7N_5^{+\bullet}$ ion, we considered several isomers for which we calculated theoretical vibronic absorption spectra for excitations in thermal ions at 310 K (Figure 4). Transitions were assigned on the basis of comparing the TD-DFT and EOM-CCSD excited-state calculations (Figure S6, Supporting Information). The calculated spectra unambiguously distinguished $\mathbf{2}^{+\bullet}$ from $\mathbf{1}^{+\bullet}$ and $\mathbf{3}^{+\bullet}$. In particular, excitation to the A and B states of $\mathbf{2}^{+\bullet}$ at 361 and 352 nm, respectively (Figure 4a), accounted for the near-UV band in the action spectrum, while $\mathbf{1}^{+\bullet}$ and $\mathbf{3}^{+\bullet}$ did not have adequate transitions in this wavelength region. The intense transitions of $\mathbf{2}^{+\bullet}$ at 200, 213, 216, and 228 nm accounted for the dominant composite band at 210-250 nm in the action spectrum. Conversely, transitions to the F and G excited states of **1**$^{+\bullet}$ (Figure 4b) and **3**$^{+\bullet}$ (Figure 4c) were outside the absorption region of **2**$^{+\bullet}$. Overall, the vibronic spectrum of **2**$^{+\bullet}$. provided the best match with the action spectrum of $C_6H_7N_5^{+\bullet}$ across the entire wavelength range. However, the calculated vibronic spectrum of the higher-energy tautomer **4**$^{+\bullet}$ also showed absorption bands matching the action spectrum, namely, for the 359 nm and 346 nm transitions to the ***A*** and ***B*** states, respectively (Figure 4d). The match for **4**$^{+\bullet}$ was poorer for the strong experimental band at 220 nm. Based on its unique CID-MS^2 and action spectrum, the $C_6H_7N_5^{+\bullet}$ ion was identified as having a non-canonical structure of a distonic ion represented by the global energy minimum of an N-1-protonated adenine radical **2**$^{+\bullet}$ or possibly the higher energy isomer **4**$^{+\bullet}$.

The electronic transitions in **2**$^{+\bullet}$ and **4**$^{+\bullet}$ were investigated by molecular orbital (MO) analysis of the low excited states (Figure S7, Supporting Information). In both ions, the first (***A***) excited state resulted in dipole-allowed electron transitions from the singly-occupied MO (SOMO39α) to the lowest unoccupied MO (LUMO40α) that were of the $\pi_z \rightarrow \pi_z^*$ type. Differences were apparent for the transitions within the β-orbital manifold, MO38β → MO39β, that corresponded to the ***D*** and ***B*** states at ΔE_{exc} = 4.02 and 3.58 eV for **2**$^{+\bullet}$ and **4**$^{+\bullet}$, respectively (Figure S7). In both **2**$^{+\bullet}$ and **4**$^{+\bullet}$, the SOMO had a large amplitude at the exocyclic CH_2 group, which was consistent with the high calculated atomic spin density at this carbon atom, 0.90 and 0.88 for **2**$^{+\bullet}$ and **4**$^{+\bullet}$, respectively. The electron transitions in **2**$^{+\bullet}$ and **4**$^{+\bullet}$ were fundamentally different from those in **1**$^{+\bullet}$ (Figure S8, Supporting Information). The four lowest excited states in the canonical cation radical (***A***-***D***) involved internal electron transitions within the β-orbital manifold, out of which only the ***B*** (MO37$\beta \rightarrow$ MO39β) and ***C*** (MO36$\beta \rightarrow$ MO39β) states were of the $\pi_z \rightarrow \pi_z^*$ type to have oscillator strength allowing detection in the action spectrum. This feature further underscored the difference between **1**$^{+\bullet}$ and its non-canonical isomers.

3.4.4. Ion Energies, Dissociation Mechanisms, and Product Ion Action Spectrum

We used ab initio calculations to establish the relative energies of cation radicals $\mathbf{1}^{+\bullet}$-$\mathbf{4}^{+\bullet}$ and to explore the parts of the potential energy surface that were relevant for the characteristic loss of hydrogen and competing dissociations. CCSD(T)/CBS relative energies are discussed in the text and schemes, energies obtained at other levels of theory are compiled in Table 1. Ion $\mathbf{2}^{+\bullet}$ was the global energy minimum of the adenine-related $C_6H_7N_5^{+\bullet}$ ions, closely followed by $\mathbf{1}^{+\bullet}$ and $\mathbf{3}^{+\bullet}$. The N-7-H isomer $\mathbf{4}^{+\bullet}$ was 30 kJ mol^{-1} less stable than $\mathbf{2}^{+\bullet}$. Threshold and transition-state (TS) energies were obtained for the loss of H from different positions of $\mathbf{2}^{+\bullet}$, $\mathbf{3}^{+\bullet}$, and $\mathbf{4}^{+\bullet}$; those for $\mathbf{2}^{+\bullet}$ are discussed here.

Loss of H from N-1, NH_2, C-2, and C-8 was calculated to require high threshold energies, forming fragment ions $\mathbf{2a}^{+}$, $\mathbf{2b}^{+}$, $\mathbf{2c}^{+}$ and $\mathbf{2d}^{+}$ respectively (Scheme 4). This was consistent with the labeling data that showed lack of D loss from exchangeable (N-1-D, ND_2) positions. However, the very high threshold energy for the loss of C-2-H, leading to a triplet ion $\mathbf{2c}^{+}$, did not provide a plausible explanation for the ion dissociation. The calculated threshold energies for loss of H are to be compared with the threshold energy for the ring cleavage and elimination of H_2C=N-CN, forming ion $\mathbf{5}^{+}$ that corresponds to the very minor *m/z* 95 ion in the CID-MS^3 spectrum. These results suggested that a direct loss of H from $\mathbf{2}^{+\bullet}$ was energetically unfavorable, and the dissociation must follow a different mechanistic pathway to outcompete the ring cleavage while being consistent with the labeling data.

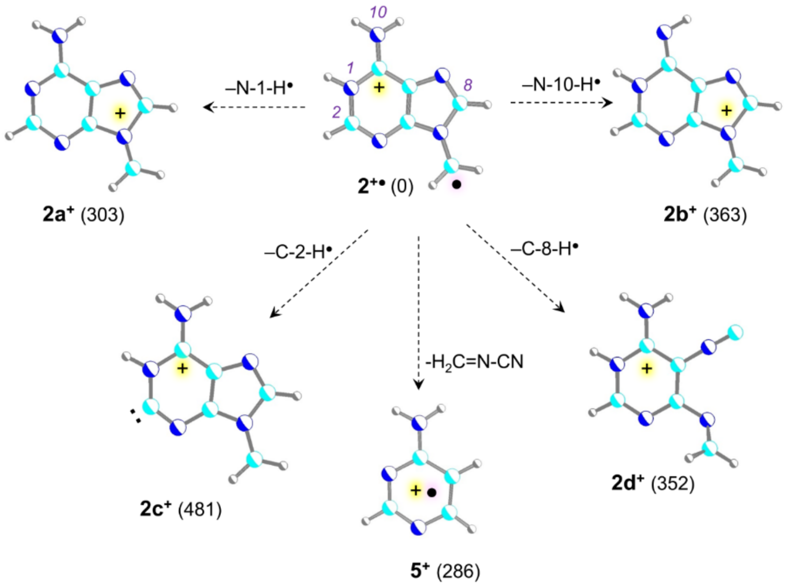

Scheme 4. High-energy dissociations of **2$^{+\bullet}$**. M06-2X/6-31+G(d,p) optimized structures with relative energies in kJ mol^{-1} from CCSD(T)/CBS + ZPVE calculations.

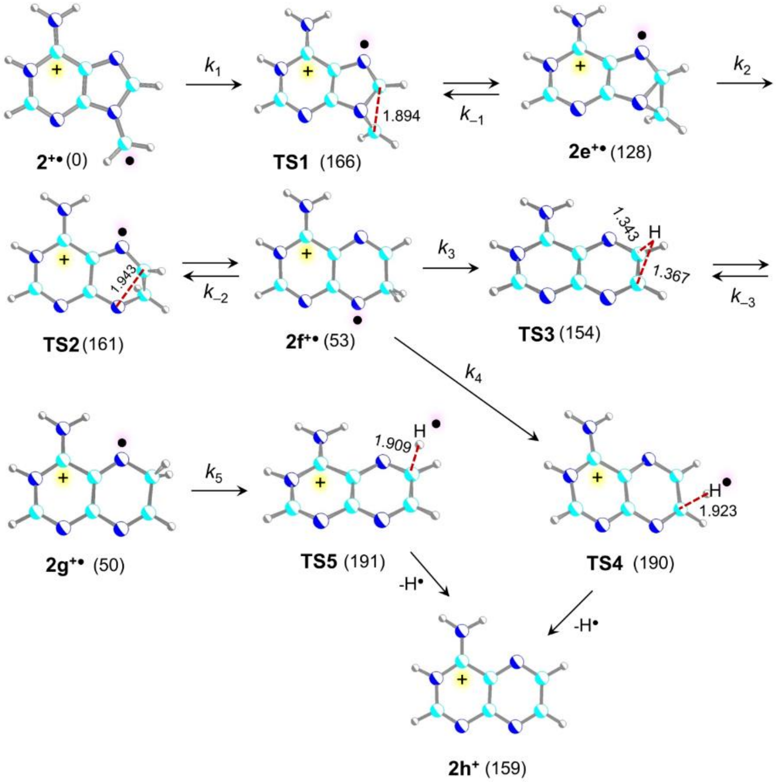

Scheme 5. Proposed mechanism for H-loss dissociation of **2$^{+\bullet}$**. M06-2X/6-31+G(d,p) optimized structures with relative energies in kJ mol^{-1} from CCSD(T)/CBS + ZPVE calculations.

We propose an indirect mechanism (Scheme 5) which is compatible with the labeling data, reaction energetics, and is supported by the reaction kinetics (*vide infra*). In the first step, the radical-carrying CH_2 group in $\mathbf{2}^{+\bullet}$ is assumed to cyclize to C-8, forming an aziridine ring in intermediate $\mathbf{2e}^{+\bullet}$ at 128 kJ mol^{-1} relative to $\mathbf{2}^{+\bullet}$. The cyclization proceeds through **TS1** at 166 kJ mol^{-1} relative to $\mathbf{2}^{+\bullet}$. The aziridine ring in $\mathbf{2e}^{+\bullet}$ is opened via **TS2** at 161 kJ mol^{-1} relative to $\mathbf{2}^{+\bullet}$ (33 kJ mol^{-1} relative to $\mathbf{2e}^{+\bullet}$), resulting in a ring expansion and forming the dihydropteridine intermediate $\mathbf{2f}^{+\bullet}$ at 53 kJ mol^{-1}. Ion $\mathbf{2f}^{+\bullet}$ can undergo facile reversible isomerization by 1,2-H atom shift between the CH_2 group and C-8, proceeding via **TS3** at 154 kJ mol^{-1} and forming dihydropteridine ion $\mathbf{2g}^{+\bullet}$ at 50 kJ mol^{-1} relative to $\mathbf{2}^{+\bullet}$. Finally, loss of H from the ring CH_2 groups in $\mathbf{2f}^{+\bullet}$ and $\mathbf{2g}^{+\bullet}$ required 190 and 191 kJ mol^{-1} in **TS4** and **TS5**, respectively, to form a common product, which is an N-1-protonated aminopteridine $\mathbf{2h}^{+}$ at 159 kJ mol^{-1} relative to $\mathbf{2}^{+\bullet}$. Note that we retain the adenine ring atom numbering for the aminopteridine dissociation products. The salient feature of the Scheme 5 mechanism was that all the TS and threshold energies were substantially lower than the threshold energy for the ring cleavage leading to elimination of $H_2C{=}N{-}CN$ (Table 1). Thus, the Scheme 5 mechanism was consistent with the CID-MS^3 spectrum. We also considered alternative mechanisms of H atom loss, but those required high TS energies (**TS6**-**TS9**), as described in detail in the Supporting Information (Schemes S3, S4). Loss of H from the N-7-H protomer $\mathbf{4}^{+\bullet}$ was also evaluated by its energetics and kinetics as visualized in Scheme S5 and Figures S9 and S10 (TS10-TS14, Supporting Information).

Experimental evidence for the proposed mechanism was sought by determining the structure of the *m/z* 148 product ion by CID-UVPD-MS^4 action spectroscopy. The action spectrum displayed two major photodissociation channels leading to loss of NH_3 (*m/z* 131) and HCN (*m/z* 121), forming bands with maxima at 285, 250, and 220 nm (Figure 5a). The spectrum of this ion was different from that obtained for the *m/z* 148 ion generated by CID-MS^3 from [9-methyladenine]$^{+\bullet}$ (Figure S11, Supporting Information). Significantly, the absorption bands in the action spectrum were matched by the calculated bands in the vibronic spectrum of $\mathbf{2h}^{+}$ (Figure 5b). The latter showed a weak transition to the A state at 351 nm, and more intense transitions to the ***C***, ***F***, and ***H*** states at 262, 225, and 196 nm, respectively. Upon vibronic red shift and broadening, these transitions gave rise to bands matching the prominent features in the action spectrum. In contrast, the spectrum of the N-7 protonated pteridine ion $\mathbf{4d}^{+}$ showed a major mismatch with the action spectrum. For example, the intense transitions to the ***B*** and ***G*** states at 348 and 228 nm, respectively (Figure 5c), did not match the bands in the action spectrum. In particular, the absence in the action spectrum of the 348-nm band excluded the N-7-protonated isomers for the *m/z* 148 and, by implication, also its precursor $\mathbf{4}^{+\bullet}$. Hence, UV-Vis action spectroscopy alone proved to be sufficient for resolving the protomeric forms and allowed us to assign structure $\mathbf{2}^{+\bullet}$ to the non-canonical adenine cation radical. It is fair to note that structures $\mathbf{2}^{+\bullet}$ and $\mathbf{4}^{+\bullet}$ are theoretically distinguishable by infrared spectra that show different bands for the N-1-H and N-7-H stretching and in-plane bending modes in the calculated spectra (Figure S12, Supporting Information). Structures $\mathbf{2}^{+\bullet}$ and $\mathbf{4}^{+\bullet}$ thus present a future challenge to be addressed by infrared action spectroscopies.

3.4.5. Dissociation Kinetics

To quantitatively evaluate the Scheme 5 mechanism, we utilized the CCSD(T)/CBS-calculated potential energy surface for the H-atom loss from $\mathbf{2}^{+\bullet}$ to calculate unimolecular rate constants, using the Rice-Ramsperger-Kassel-Marcus theory model.[56] The rate constants (log *k*) for the reversible reactions $\mathbf{2}^{+\bullet} \leftrightarrow \mathbf{TS1} \leftrightarrow \mathbf{2e}^{+\bullet}$ (k_1, k_{-1}), $\mathbf{2e}^{+\bullet} \leftrightarrow \mathbf{TS2} \leftrightarrow \mathbf{2f}^{+\bullet}$ (k_2, k_{-2}), $\mathbf{2f}^{+\bullet} \leftrightarrow \mathbf{TS3} \leftrightarrow \mathbf{2g}^{+\bullet}$ (k_3, k_{-3}), and the exit channels, $\mathbf{2f}^{+\bullet} \rightarrow \mathbf{TS4} \rightarrow \mathbf{2h}^{+} + \mathrm{H}^{\bullet}$ (k_4), and $\mathbf{2g}^{+\bullet} \rightarrow \mathbf{TS5} \rightarrow \mathbf{2h}^{+} + \mathrm{H}^{\bullet}$ (k_5), (Scheme 5) were plotted on a common energy scale and are shown in Figure 6a. The rate constants indicated that the rate-determining steps for the dissociation were the ring closure in $\mathbf{2}^{+\bullet}$ (k_1), and the C–H bond cleavages in $\mathbf{2f}^{+\bullet}$ (k_4) and $\mathbf{2g}^{+\bullet}$ (k_5), while the reversible interconversion of $\mathbf{2f}^{+\bullet}$ and $\mathbf{2g}^{+\bullet}$ (k_3, k_{-3}) was >2 orders of magnitude faster at all relevant internal energies of $\mathbf{2}^{+\bullet}$. Under these conditions, the populations of $\mathbf{2}^{+\bullet}$, $\mathbf{2f}^{+\bullet}$, and $\mathbf{2g}^{+\bullet}$ preceding dissociation can be considered to be close to a dynamic equilibrium to simplify the dissociation kinetics, where the energy-dependent mole fractions of **2f**$^{+\bullet}$ and **2g**$^{+\bullet}$ are functions of k_1, k_{-1}, k_2, k_{-2}, k_3, and k_{-3}. When combined with the rate constants for the rate-determining steps of H-atom loss, k_4 and k_5, respectively, we can calculate the energy-dependent mole fractions of the reactant (**2**$^{+\bullet}$) and products (**2h**$^+$ + H$^\bullet$) after 50 ms of the ion residence time in the ion trap (Figure 6b). The Figure 6b data indicated that >10% dissociation was achieved in ions having > 230 kJ mol^{-1} internal energy and the dissociation was complete in ions having 260 kJ mol^{-1}. These figures were reasonable considering the typical collisional excitation in 3D ion traps.**[66,67]** The calculated range of the kinetically-limited ion internal energies was also consistent with photoexcitation, allowing single-photon dissociation at laser wavelengths up to 520 nm. This was fully compatible with the UV-Vis action spectrum (Figure 3a).

3.4.6. Isotope Effects

We further used the equilibrium formation of **2f**$^{+\bullet}$ and **2g**$^{+\bullet}$ to address the isotope effects on the competitive loss of H and D from [8-D]-**2**$^{+\bullet}$ (Figure 2a). Equilibrium populations were calculated for intermediates A, B, A', and B' (Scheme 6), in which the D-atom (D15), originally placed at C-8, was distributed by reversible H and D migrations with rate constants k_{3A}, k_{-3A}, k_{3B}, k_{-3B}, k_{3C}, and k_{-3C}, (Figure 7a), followed by dissociation with rate constants $k_{4AH18} = k_{4AH16}$, k_{5BH18}, $k_{4A'H16}$, and $k_{5B'H18} = k_{5B'H16}$ for loss of H. The loss of D was analogously expressed by rate constants k_{5BD15} and $k_{4A'D15}$. All these rate constants were calculated including primary and secondary isotope effects with appropriate zero-point energies, vibrational frequencies, and moments of inertia of the D-containing intermediates and the pertinent transition states (**TS3**, **TS4** and **TS5**). The results are summarized as the energy-dependent k_D/k_H ratio, expressing the overall loss of D and H (Figure 7b). This showed that the fraction of D-loss increased with ion internal energy which was caused by a combination of kinetic factors, such as the increasing population of intermediate A' that can dissociate by D loss and the lower kinetic isotope effect affecting this dissociation. The experimental ratio for collisional activation (k_D/k_H = 12/88 = 0.136) was matched at the internal energy of 295 kJ mol^{-1}. The ratio for photoexcitation (14/86 = 0.163) was matched at 360 kJ mol^{-1}. This was less than the photon energy used to obtain the photodissociation spectrum (443 kJ mol^{-1}), but the difference can be accounted for by ion collisional cooling after photon absorption during the 50 ms ion storage time.[67,68]

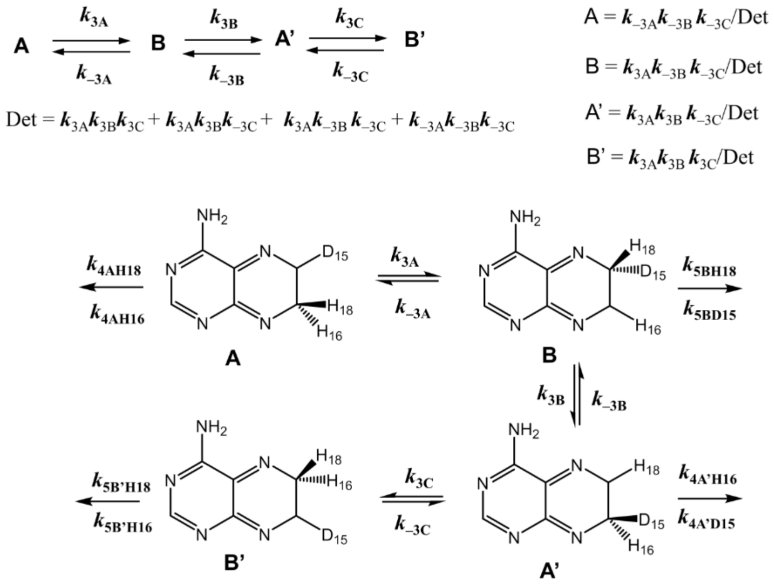

Scheme 6. Kinetic analysis of the distribution of D-labeled intermediates and rate constants for competitive loss of H and D.

3.4.7. Distonic Isomers of 2’-Deoxyadenosine Cation Radicals

The specific generation and stability of the elusive distonic isomer of 9-methyladenine cation radical, along with those of thymine[14] and methylcytosine,[15] indicated that non-traditional structures may play a role in DNA oxidation. To investigate this unusual aspect of nucleobase cation-radical chemistry, we investigated the structures and relative energies of 2'-deoxyadenosine isomers produced by H-atom migrations in the canonical structure **Ad1$^{+\bullet}$**. The lowest-energy 2'-deoxyribose conformers for each nucleobase tautomer were selected after Born-Oppenheimer Molecular Dynamics trajectory calculations and optimized by DFT calculations. Here we report CCSD(T)/CBS energies with zero-point corrections, and including enthalpies and entropies at 310 K. The calculated free energies (Table 2) indicated a substantial stabilization of the non-canonical isomers **Ad2**$^{+\bullet}$ and **Ad3**$^{+\bullet}$ relative to **Ad1**$^{+\bullet}$ in both the gas phase and including solvation by water. Structures **Ad2**$^{+\bullet}$-**Ad4**$^{+\bullet}$ have the protonation (N-1, N-3 or N-7) and radical (C-1') sites on separate atoms and thus represent stable distonic ions.[69,70] Their enhanced stability relative to that of **Ad1**$^{+\bullet}$ can be related to the difference in the N–H and C-1'–H bond dissociation energies in protonated adenosines. The available energy data placed the 298 K dissociation energy of the C-1'–H bond in 2'-deoxyribofuranose at 384 kJ mol^{-1}.[71] This is to be compared with the 298 K energies for homolytic dissociation of the N-1–H, N-3–H and N-7–H bonds in protonated 9-methyladenines that we calculated with CCSD(T)/CBS as 420, 412, and 395 kJ mol^{-1}, respectively. These energies indicated that a hydrogen atom transfer from C-1' to the adenine nitrogen positions was also exothermic in ionized **Ad1**$^{+\bullet}$, leading to the non-canonical structures **Ad2**$^{+\bullet}$-**Ad4**$^{+\bullet}$. The Table 2 data for 2'-deoxyadenosine further revealed that the stability of **Ad2**$^{+\bullet}$-**Ad4**$^{+\bullet}$ relative to **Ad1**$^{+\bullet}$ was retained after including solvation with water. Thus, the findings for gas-phase 9-methyladenine cation radicals can be extended to the case of nucleoside ions. The potential importance of the non-canonical nucleoside cation-radical isomers stems from their recombination energies that affect electron transfer in ionized DNA. For the canonical isomer **Ad1**$^{+\bullet}$ we calculated an adiabatic recombination energy (RE$_a$, given as an absolute value) of 7.82 eV which was between those of guanosine (7.49-7.51 eV),[72] thymidine (8.12 eV), and cytidine (8.14 eV). Thus, **Ad1**$^{+\bullet}$ can abstract an electron from guanosine and promote the ionization site moving along the DNA molecule. In contrast, the low-energy isomers **Ad2**$^{+\bullet}$ and **Ad3**$^{+\bullet}$ have very low RE$_a$, 4.41 and 4.73 eV, respectively. If formed in ionized DNA, these cation radicals would function as hole traps that would not engage in electron transfer along the backbone or in the Watson-Crick pairs.

3.5. Conclusions

In conclusion, non-canonical isomers of 9-methyladenine and adenosine cation radicals represent new low-energy species of distinct electronic properties. The non-canonical 9-methylene (*1H*) adenine cation radical was generated for the first time using targeted gas-phase ion chemistry and its structure was entirely characterized by UV-Vis photodissociation action spectroscopy. The discovery of stable non-canonical nucleobase and nucleoside cation radicals presents a challenge for future experimental and computational studies to search for the formation and role of such non-canonical intermediates in DNA ionization.

3.6. References

1. Yu, C.; O'Donnell, T. J.; LeBreton, P. R. Ultraviolet Photoelectron Studies of Volatile Nucleoside Models. Vertical Ionization Potential Measurements of Methylated Uridine, Thymidine, Cytidine, and Adenosine. *J. Phys. Chem.* **1981**, *85*, 3851-3855.
2. Improta, R.; Scalmani, G.; Barone, V. Radical Cations of DNA Bases: Some Insights on Structure and Fragmentation Patterns by Density Functional Methods. I*nt. J. Mass Spectrom.* **2000**, *201*, 321-336.
3. Crespo-Hernandez, C. E.; Arce, R.; Ishikawa, Y.; Gorb, L.; Leszczynski, J.; Close, D. M. Ab Initio Ionization Energy Thresholds of DNA and RNA Bases in Gas Phase and in Aqueous Solution. *J. Phys. Chem. A* **2004**, *108*, 6373-6377.
4. Blancafort, L.; Voityuk, A. A. CASSCF/CAS-PT2 Study of Hole Transfer in Stacked DNA Nucleobases *J. Phys. Chem. A* **2006**, *110*, 6426-6432.
5. Slavíček, P.; Winter, B.; Faubel, M.; Bradforth, S. E.; Jungwirth, P. Ionization Energies of Aqueous Nucleic Acids: Photoelectron Spectroscopy of Pyrimidine Nucleosides and ab Initio Calculations. *J. Am. Chem. Soc.* **2009**, *131*, 6460-6467.
6. Faber, C.; Attaccalite, C.; Olevano, V.; Runge, E.; Blase, X. First-Principles GW Calculations for DNA and RNA Nucleobases. *Phys. Rev. B: Condensed Matter and Materials Physics* **2011**, *83*, 115123/1-115123/5.
7. Pluhařová, E.; Jungwirth, P.; Bradforth, S. E.; Slavíček, P. Ionization of Purine Tautomers in Nucleobases, Nucleosides, and Nucleotides: From the Gas Phase to the Aqueous Environment. *J. Phys. Chem. B* **2011**, *115*, 1294-1305.

8. Tehrani, Z. A.; Javan, M. J.; Fattahi, A.; Hashemi, M. M. Effect of Cation Radical Formation on Reactivity and Acidity Enhancement of Cytosine Nucleobase: Natural Bond Orbital and Atom in Mol. Anal. *J. Theor. Comput. Chem.* **2012**, *11*, 313-327.
9. Pluhařová, E.; Schroeder, C.; Seidel, R.; Bradforth, S. E.; Winter, B.; Faubel, M.; Slavíček, P.; Jungwirth, P. Unexpectedly Small Effect of the DNA Environment on Vertical Ionization Energies of Aqueous Nucleobases. *J. Phys. Chem. Lett.* **2013**, *4*, 3766-3769.
10. Cadet, J.; Wagner, J. R.; Shafirovich, V.; Geacintov, N. E. One-Electron Oxidation Reactions of Purine and Pyrimidine Bases in Cellular DNA. *Int. J. Rad. Biol.* **2014**, *90*, 423-432.
11. Dawley, M. M.; Tanzer, K.; Cantrell, W. A.; Plattner, P.; Brinkmann, N. R.; Scheier, P.; Denifl, S.; Ptasinska, S. Electron Ionization of the Nucleobases Adenine and Hypoxanthine near the Threshold: A Combined Experimental and Theoretical Study. *Phys. Chem. Chem. Phys.* **2014**, *16*, 25039-25053.
12. Schroeder, C. A.; Pluhařová, E.; Seidel, R.; Schroeder, W. P.; Faubel, M.; Slavíček, P.; Winter, B.; Jungwirth, P.; Bradforth, S. E. Oxidation Half-Reaction of Aqueous Nucleosides and Nucleotides via Photoelectron Spectroscopy Augmented by Ab initio Calculations. *J. Am. Chem. Soc.* **2015**, *137*, 201-209.
13. Wang, Y.; Zhao, H.; Yang, C.; Jie, J.; Dai, X.; Zhou, Q.; Liu, K.; Song, D.; Su, H. Degradation of Cytosine Radical Cations in 2'-Deoxycytidine and in i-Motif DNA: Hydrogen-Bonding Guided Pathways. *J. Am. Chem. Soc.* **2019**, *141*, 1970-1979.
14. Dang, A.; Nguyen, H. T. H.; Ruiz, H.; Piacentino, E.; Ryzhov, V.; Tureček, F. Experimental Evidence for Non-Canonical Thymine Cation Radicals in the Gas Phase. *J. Phys. Chem. B*, **2018**, *122*, 86-97.
15. Huang, S. R.; Tureček, F. Cation Radicals of Hachimoji Nucleobases. Canonical Purine and Non-Canonical Pyrimidine Forms Generated in the Gas Phase and Characterized

by UV-Vis Photodissociation Action Spectroscopy. *J. Phys. Chem. A* **2020**, 124, 7101-7112.

16. Kim, N.-J. DFT Study of Water-Assisted Intramolecular Proton Transfer in the Tautomers of Thymine Radical Cation. *Bull. Korean Chem. Soc.* **2006**, *2*7, 1009−1014.
17. Lam, A. K.; Abrahams, B. F.; Grannas, M. J.; McFadyen, W. D.; O'Hair, R. A. J. Tuning the Gas Phase Redox Properties of Copper(II) Ternary Complexes of Terpyridines to Control the Formation of Nucleobase Radical Cations. *Dalton Trans.* **2006**, 5051−5061.
18. Feketeova, L.; Khairallah, G. N.; Chan, B.; Steinmetz, V.; Maitre, P.; Radom, L.; O'Hair, R. A. J. Gas-Phase Infrared Spectrum and Acidity of the Radical Cation of 9-Methylguanine. *Chem. Commun.* **2013**, 49, 7343−7345.
19. Antoine, R.; Dugourd, P. UV-Visible Activation of Biomolecular Ions. (Laser Photodissociation and Spectroscopy of Mass-Separated Biomolecular Ions). *Lect. Notes Chem*. **2013**, 83, 93−116.
20. Antoine, R.; Dugourd, P. In *Photophysics of Ionic Biochromophores*, Nielsen, S. B.; Wyer, J. A. Eds.; Springer: Heidelberg, **2013**, pp. 141-145.
21. Shaffer, C. J.; Pepin, R.; Tureček, F. Combining UV Photodissociation Action Spectroscopy with Electron Transfer Dissociation for Structure Analysis of Gas-Phase Peptide Cation-Radicals. *J. Mass Spectrom.* **2015**, 50, 1438-1442.
22. Dunbar, R. C. Photodissociation of Trapped Ions. *Int. J. Mass Spectrom.* **2000**, *200*, 571-589.
23. Baer, T.; Dunbar, R. C. Ion Spectroscopy: Where Did It Come From; Where Is It Now; and Where Is It Going? *J. Am. Soc. Mass Spectrom.* **2010**, *21*, 681-693.
24. Rizzo T. R., Stearns J. A., Boyarkin O. V. Spectroscopic Studies of Cold, Gas-Phase Biomolecular Ions. *Int. Rev. Phys. Chem.* **2009**, *28*, 481-515.
25. Polfer, N.; Sartakov, B. G.; Oomens, J. The Infrared Spectrum of the Adamantyl Cation. *Chem. Phys. Lett.* **2004**, *400*, 201-205.

26. Nizkorodov S. A.; Dopfer O.; Ruchti T.; Meuwly M.; Maier J. P.; Bieske E. J. Size Effects in Cluster Infrared Spectra: the ν_1 Band of Ar_n-HCO^+ (*n* = 1-13) *J. Phys. Chem.* **1995**, *99*, 17118-17129.

27. DeBlase, A. F., Bloom S., Lectka T., Jordan K. D., McCoy A. B., Johnson M. A. Origin of the Diffuse Vibrational Signature of a Cyclic Intramolecular Proton Bond: Anharmonic Analysis of Protonated 1,8-Disubstituted Naphthalene Ions. *J. Chem. Phys.* **2013**, *139*, 024301/1-9.

28. Nguyen, H. T. H.; Shaffer, C. J.; Pepin, R.; Tureček, F. UV Action Spectroscopy of Gas-Phase Peptide Radicals. *J. Phys. Chem. Lett.* **2015**, *6*, 4722-4727.

29. Viglino. E.; Shaffer, C. J.; Tureček, F.: UV-VIS Action Spectroscopy and Structures of Tyrosine Peptide Cation Radicals in the Gas Phase. *Angew. Chem. Int. Ed.* **2016**, *55*, 7469-7473.

30. Huang, S. R.; Liu, Y.; Tureček F. UV-Vis Photodissociation Action Spectroscopy Reveals Cytosine-Guanine Hydrogen Transfer in DNA Tetranucleotide Cation Radicals upon One-Electron Reduction. *J. Phys Chem. B* **2020**, *124*, 3505-3517.

31. Korn, J. A.; Urban, J.; Dang, A.; Nguyen, H. T. H.; Turecek, F. UV-Vis Action Spectroscopy Reveals a Conformational Collapse in Hydrogen-Rich Dinucleotide Cation Radicals. *J. Phys. Chem. Lett.* **2017**, *8*, 4100-4107.

32. Liu, Y.; Huang, S. R.; Tureček F. Guanine-Adenine Interactions in DNA Tetranucleotide Cation Radicals Revealed by UV/Vis Photodissociation Action Spectroscopy and Theory. *Phys. Chem. Chem. Phys.* **2020**, 22, 16831-16842.

33. Huang, S. R.; Dang, A.; Tureček, F. Ground and Excited States of Gas-Phase DNA Nucleobase Cation-Radicals. A UV-Vis Photodisociation Action Spectroscopy and Computational Study of Adenine and 9-Methyladenine. *J. Am. Soc. Mass Spectrom.* **2020**, *31*, 1271-1281.

34. Chyall, L. J.; Kenttämaa, H. I. Gas-Phase Reactions of the 4-Dehydroanilinium Ion and Its Isomers. *J. Mass Spectrom.* **1995**, *30*, 81-87.

35. Petzold, C. J.; Nelson, E. D.; Lardin, H. A.; Kenttämaa, H. I. Charge-Site Effects on the Radical Reactivity of Distonic Ions. *J. Phys. Chem. A* **2002**, *106*, 9767-9775.

36. Widjaja, F.; Jin, Z.; Nash, J. J.; Kenttämaa, H. I. Comparison of the Reactivity of the Three Distonic Isomers of the Pyridine Radical Cation Toward Tetrahydrofuran in Solution and in the Gas Phase. *J. Am. Soc. Mass Spectrom.* **2013**, *24*, 469-480.

37. Kotha, R. R.; Yerabolu, R.; Aqueel, M. S.; Riedeman, J. S.; Szalwinski, L.; Ding, D.; Nash, J. J.; Kenttämaa, H. I. Quinoline Triradicals: A Reactivity Study. *J. Am. Chem. Soc.* **2019**, *141*, 6672-6679.

38. Dang, A.; Korn, J. A.; Gladden, J.; Mozzone, B.; Tureček, F. UV-Vis Photodissociation Action Spectroscopy on Thermo LTQ-XL ETD and Bruker amaZon Ion Trap Mass Spectrometers: A Practical Guide. *J. Am. Soc. Mass Spectrom*. **2019**, *30*, 1558-1564.

39. Frisch, M. J.; Trucks, G. W.; Schlegel, H. B.; Scuseria, G. E.; Robb, M. A.; Cheeseman, J. R.; Scalmani, G.; Barone, V.; Petersson, G. A.; Nakatsuji, H.; et al. *Gaussian 16*, Revision A03; Gaussian, Inc.: Wallingford, CT, 2016.

40. Becke, A. D. New Mixing of Hartree-Fock and Local Density-Functional Theories. *J. Chem. Phys.* **1993**, *98*, 1372−1377.

41. Yanai, T.; Tew, D. P.; Handy, N. C. A New Hybrid Exchange-Correlation Functional Using the Coulomb-Attenuating Method (CAM-B3LYP). *Chem. Phys. Lett.* **2004**, *393*, 51−57.

42. Zhao, Y.; Truhlar, D. G. The M06 Suite of Density Functionals for Main Group Thermochemistry, Thermochemical Kinetics, Noncovalent Interactions, Excited States, and Transition Elements: Two New Functionals and Systematic Testing of Four M06-Class Functionals and 12 Other Functionals. *Theor. Chem. Acc.* **2008**, *120*, 215−241.

43. Tomasi, J.; Mennucci, B.; Cammi, R. Quantum Mechanical Continuum Solvation Models. *Chem. Rev.* **2005**, *105*, 2999−3093.

44. Čížek, J. On the Use of the Cluster Expansion and the Technique of Diagrams in Calculations of Correlation Effects in Atoms and Molecules. *Adv. Chem. Phys.* **1969**, *14*, 35−89.

45. Purvis, G. D., III; Bartlett, R. J. Full Coupled-Cluster Singles and Doubles Model−the Inclusion of Disconnected Triples. *J. Chem. Phys.* **1982**, *76*, 1910−1918.

46. Halkier, A.; Helgaker, T.; Jørgensen, P.; Klopper, W.; Koch, H.; Olsen, J.; Wilson, A. K. Basis Set Convergence in Correlated Calculations on Ne, N_2, and H_2O. *Chem. Phys. Lett.* **1998**, *286*, 243−252.

47. Helgaker, T.; Klopper, W.; Koch, H.; Noga, J. Basis-Set Convergence of Correlated Calculations on Water. *J. Chem. Phys.* **1997**, *106*, 9639−9646.

48. Dunning, T. H., Jr. Gaussian Basis Sets for Use in Correlated Molecular Calculations. I. The Atoms Boron through Neon and Hydrogen. *J. Chem. Phys.* **1989**, *90*, 1007−1023.

49. Schlegel, H. B. Potential Energy Curves Using Unrestricted Møller-Plesset Perturbation Theory with Spin Annihilation. *J. Chem. Phys.* **1986**, *84*, 4530.

50. Mayer, I. Spin-Projected UHF Method. IV. Comparison of Potential Curves Given by Different One-Electron Methods. *Adv. Quantum Chem.* **1980**, *12*, 189−262.

51. Comeau, D. C.; Bartlett, R. J. The Equation-of-Motion Coupled-Cluster Method. Applications to Open- and Closed-Shell Reference States. *Chem. Phys. Lett.* **1993**, *207*, 414−423.

52. Furche, F.; Ahlrichs, R. Adiabatic Time-Dependent Density Functional Methods for Excited State Properties. *J. Chem. Phys.* **2002**, *117*, 7433−7447.

53. Wigner, E. The Quantum Correction for Thermodynamic Equilibrium. *Phys. Rev.* **1932**, *40*, 749-759.

54. Bonacic-Koutecky, V.; Mitric, R. Theoretical Exploration of Ultrafast Dynamics in Atomic Clusters: Analysis and Control. *Chem. Rev.* **2005**, *105*, 11-65.

55. Barbatti, M.; Ruckenbauer, M.; Plasser, F.; Pittner, J.; Granucci, G.; Persico, M.; Lischka, H. Newton-X: A Surface-Hopping Program for Nonadiabatic Molecular Dynamics. *Wiley Interdiscip. Rev. Comput. Mol. Sci.* **2014**, *4*, 26−33.

56. Gilbert, R. G.; Smith, S. C. *Theory of Unimolecular and Recombination Reactions*; Blackwell Scientific Publications: Oxford, U.K., 1990; pp 52−132.

57. Zhu, L.; Hase, W. L. Quantum Chemistry Program Exchange; Indiana University: Bloomington, IN, 1994; Program no. QCPE 644.

58. Gregersen, J. A.; Tureček, F. Mass-Spectrometric and Computational Study of Tryptophan Radicals (Trp + H)• Produced by Collisional Electron Transfer to Protonated Tryptophan in the Gas Phase. *Phys. Chem. Chem. Phys.* **2010**, *12*, 13434−13447.

59. Berendsen, H. J.; Postma, J. V.; van Gunsteren, W. F.; DiNola, A. R. H. J.; Haak, J. R. Molecular dynamics with coupling to an external bath. *J. Chem. Phys.* **1984**, *81*, 3684–3690.

60. Stewart, J. J. P. Optimization of Parameters for Semi-Empirical Methods V: Modification of NDDO Approximations and Applications to 70 Elements. *J. Mol. Model.* **2007**, 13, 1173–1213.

61. Řezáč, J.; Fanfrlík, J.; Salahub, D.; Hobza, P. Semiempirical Quantum Chemical PM6 Method Augmented by Dispersion and H-bonding Correction Terms Reliably Describes Various Types of Noncovalent Complexes. *J. Chem. Theor. Comput.* **2009**, *5*, 1749–1760.

62. Stewart, J. J. P. MOPAC 16. Stewart Computational Chemistry, Colorado Springs, CO (2016).

63. Řezáč, J. Cuby: an Integrative Framework for Computational Chemistry. *J. Comput. Chem.* **2016**, *37*, 1230–1237.

64. Řezáč, J.: Cuby—ruby Framework for Computational Chemistry, Version 4, http://cuby4.molecular.cz

65. March, R. E.; Todd, J. F. J. Quadrupole Ion Trap Mass Spectrometry, 2nd Edition.; Wiley-Interscience: Hoboken, NJ, 2005. p. 123.

66. Danell, R. M.; Danell, A. S.; Glish, G. L.; Vachet, R. W. The Use of Static Pressures of Heavy Gases within a Quadrupole Ion Trap. *J. Am. Soc. Mass Spectrom.* **2003**, *14*, 1099-1109.

67. McLuckey, S. A.; Goeringer, D. E. Slow Heating Methods in Tandem Mass Spectrometry. *J. Mass Spectrom.* **1997**, *32*, 461-474.

68. Pepin, R.; Tureček, F. Kinetic Ion Thermometers for Electron Transfer Dissociation. *J. Phys. Chem. B*, **2015**, *119*, 2818-2826.

69. Yates, B. F.; Bouma, W. J.; Radom, L. Distonic Radical Cations. Guidelines for the Assessment of Their Stability *Tetrahedron* **1986**, *42*, 6225-6234.

70. Hammerum, S. Distonic Radical Cations in Gaseous and Condensed Phase. *Mass Spectrom. Rev.* **1988**, 7, 123-202.

71. Vannier, L. A.; Yao, C.; Tureček, F. 2-Deoxyribose Radicals in the Gas Phase and Aqueous Solution. Transient Intermediates of Hydrogen Atom Abstraction from 2-Deoxyribofuranose. *Coll. Czech. Chem. Commum.* **2005**, *70*, 1769-1786.

72. Dang, A.; Liu, Y., Tureček, F. UV-Vis Action Spectroscopy of Guanine, 9-Methylguanine and 2'-Deoxyguanosine Cation Radicals in the Gas Phase. *J. Phys. Chem. A* **2019**, *123*, 3272-3284.

3.7. Appendix

Table 1. Relative, Dissociation, and Transition-State Energies of Adenine Cation Radicals.

	relative energy^{a,b}			
species/reaction	M06-2X/ 6-311++G(2d,p)	CCSD(T)/^{c} aug-cc-pVTZ	CCSD(T)/^{c} aug-cc-pVQZ	CCSD(T)/^{d} CBS
1$^{+\bullet}$	6.0	5.3	6.7	6.4
2$^{+\bullet}$	0	0	0	0
3$^{+\bullet}$	10	10	9.8	9.9
4$^{+\bullet}$	30	31	30	30
2a^{+} + H$^{\bullet}$	305	298	300	303
2b^{+} + H$^{\bullet}$	371	358	360	363
2c^{+} + H$^{\bullet}$	468	474	478	481
2d^{+} + H$^{\bullet}$	348	346	348	352
5^{+} + H_2C=N-CN	293	281	284	286
2$^{+\bullet}$ → **TS1**	164	165	167	166
2e$^{+\bullet}$	124	128	130	128
2$^{+\bullet}$ → **TS2**	170	158	159	161
2f$^{+\bullet}$	49	51	53	53
2$^{+\bullet}$ → **TS3**	148	152	153	154
2g$^{+\bullet}$	44	48	50	50
2$^{+\bullet}$ → **TS4**	181	186	189	190
2$^{+\bullet}$ → **TS5**	182	187	190	191
2h^{+} + H$^{\bullet}$	160	158	160	159

[a] In kJ mol^{-1}. [b] Including B3LYP zero-point energies scaled by 0.975 and referring to 0 K. [c] From extrapolation: E[CCSD(T)/aug-cc-pVXZ)] ≈ E[CCSD(T)/aug-cc-pVDZ)] + E[PMP2/aug-cc-pVXZ)] – E[PMP2/aug-cc-pVDZ)]. [d] Extrapolated to the complete basis set: E[CCSD(T)/CBS)] = E[CCSD(T)/aug-cc-pVDZ)] – E[PMP2/aug-cc-pVDZ)] + E[HF/aug-cc-pVQZ] + $E_{\text{corr}, X \rightarrow \infty}$.

Table 2. Relative free energies, absolue adiabatic recombination energies and M06-2X optimized structures of adenosine cation radicals.

	relative energy[a,b]			
ion	M06-2X/6-311++G(2d,p)			CCSD(T)/CBS
Ad1$^{+\bullet}$	0 (0)[c]	(7.76)[d]	(6.26)[c,d]	0 (7.82)[d]
Ad2$^{+\bullet}$	–29 (–42)[c]	(4.12)[d]	(3.17)[c,d]	–23 (4.42)[d]
Ad3$^{+\bullet}$	–38 (–35)[c]	(4.65)[d]	(3.46)[c,d]	–39 (4.74)[d]
Ad4$^{+\bullet}$	–27 (–33)[c]	(4.88)[d]	(3.29)[c,d]	–19 (5.10)[d]

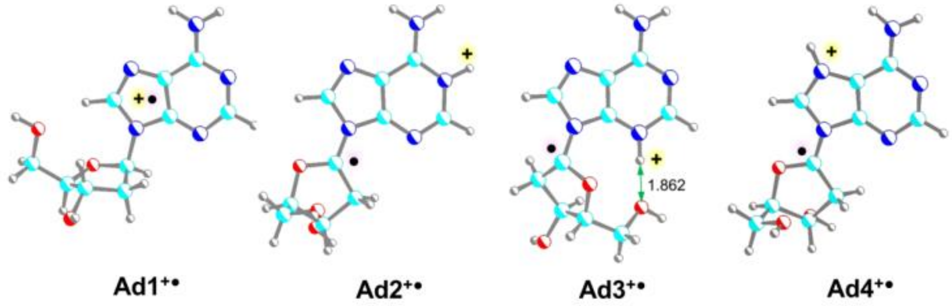

---

[a] In kJ mol^{-1} unless stated otherwise. [b] Including zero-point energies, enthalpies and entropies at 310 K. [c] Including solvation energies in water. [d] Absolute adiabatic recombination energies in eV.

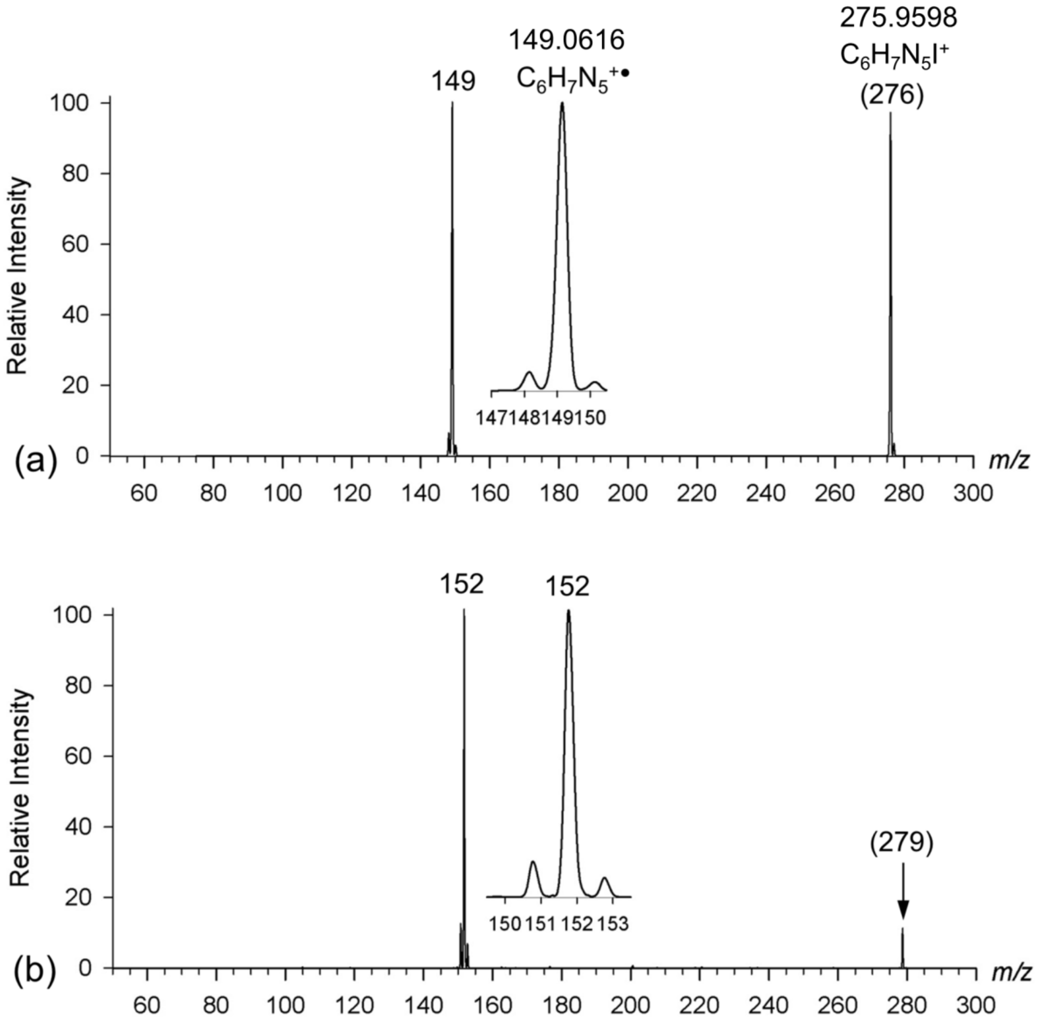

Figure 1. CID-MS^2 spectra of (a) protonated 9-iodomethyladenine ion, (b) [D_3]-9-iodomethyladenine ion. Insets show the cation-radical peak profiles.

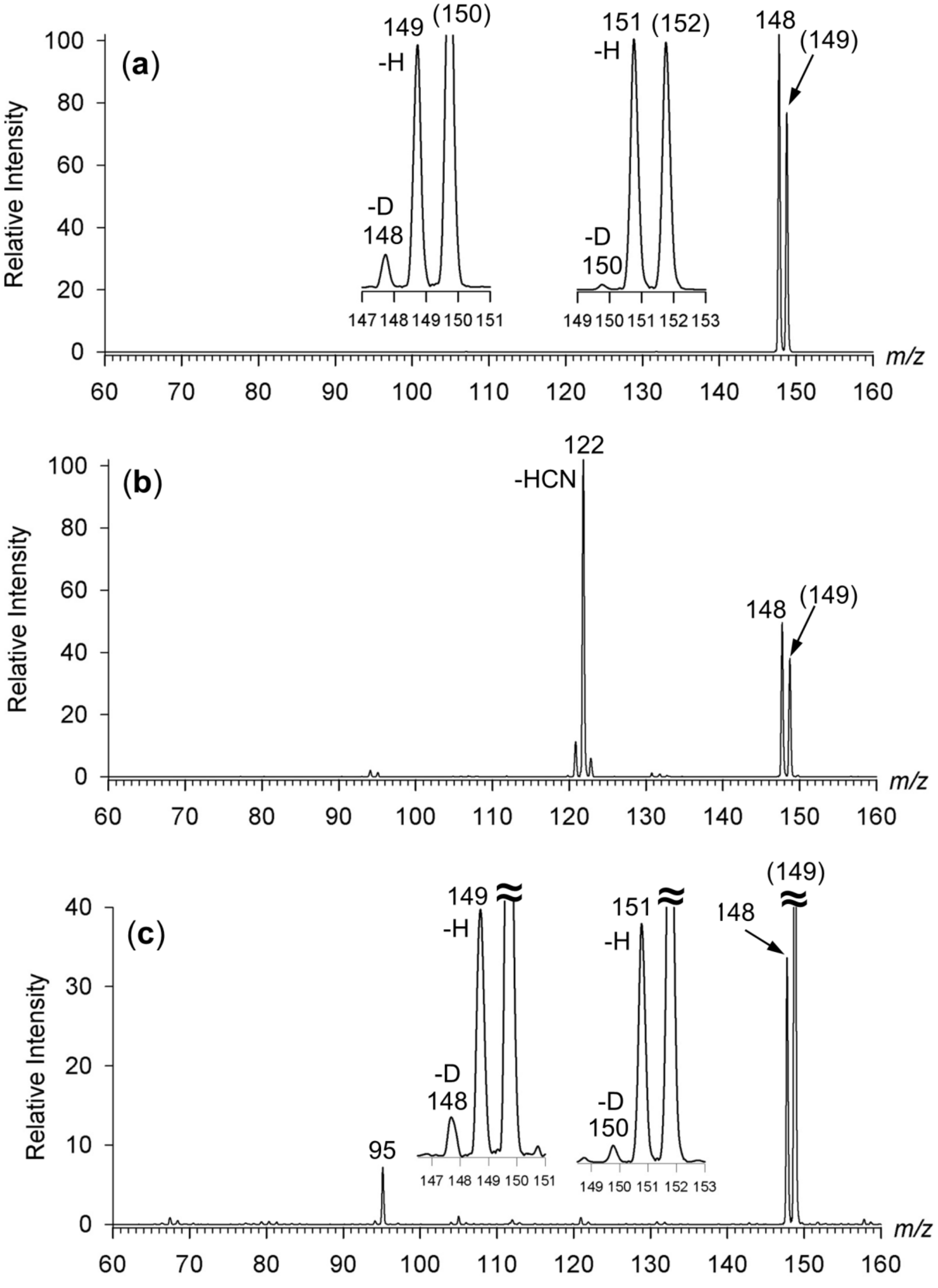

Figure 2. CID-MS3 spectra of (a) $C_6H_7N_5^{+\bullet}$ cation radical from 9-iodomethyladenine. (b) [9-methyladenine]$^{+\bullet}$ cation radical from [Cu(tpy)(9-methyladenine)]$^{2+\bullet}$ complex (ref.33). (c) UVPD-MS^3 (250 nm) spectrum of the $C_6H_7N_5^{+\bullet}$ cation radical from 9-iodomethyladenine. Insets in (a) and (c) show the loss of H/D from the [8-D] (m/z 150) and [N-D_3] (m/z 152) ions.

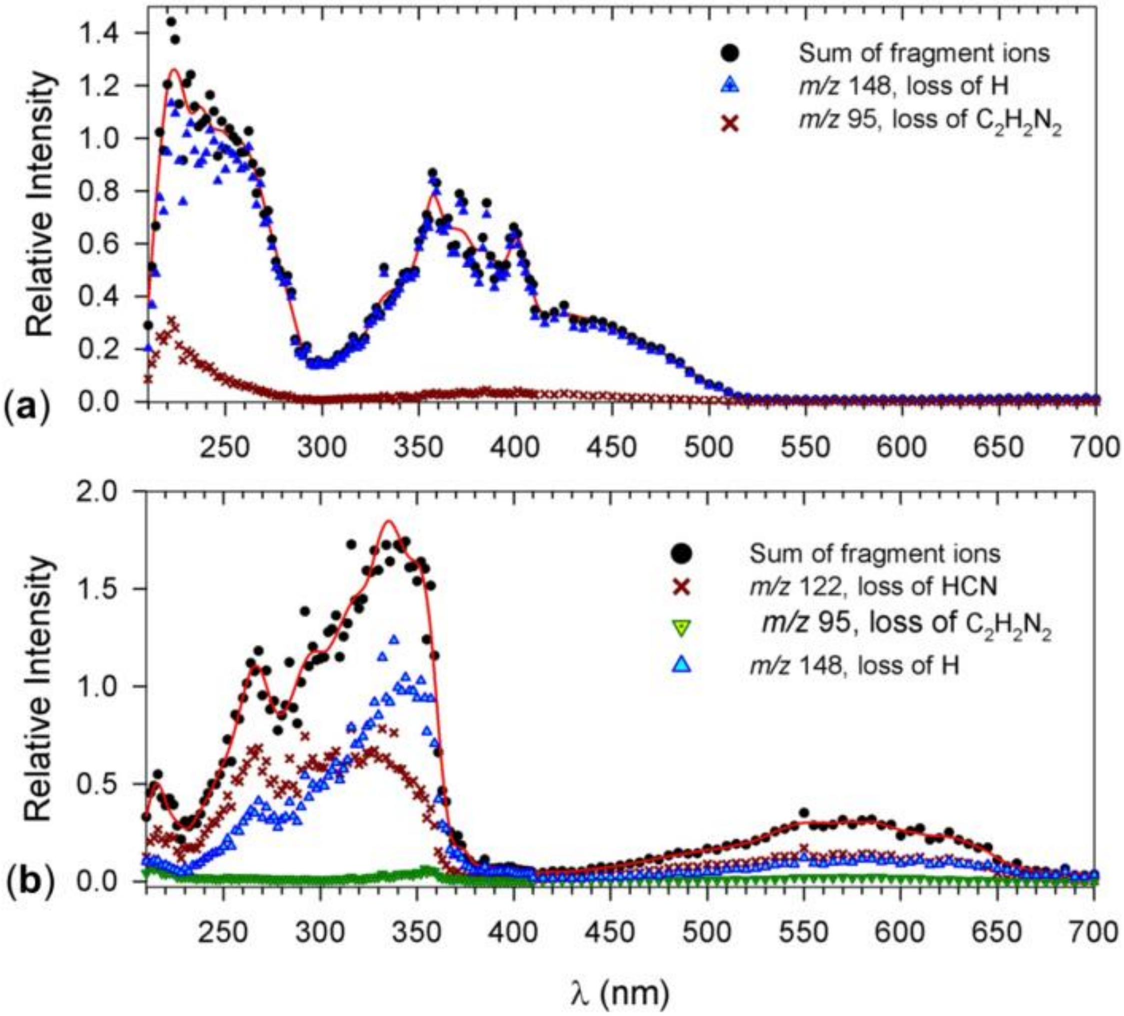

Figure 3. UV-Vis photodissociation action spectra of (a) $C_6H_7N_5^{+\bullet}$ from 9-iodomethyladenine. (b) Canonical 9-methyladenine cation radical $1^{+\bullet}$ (ref.33).

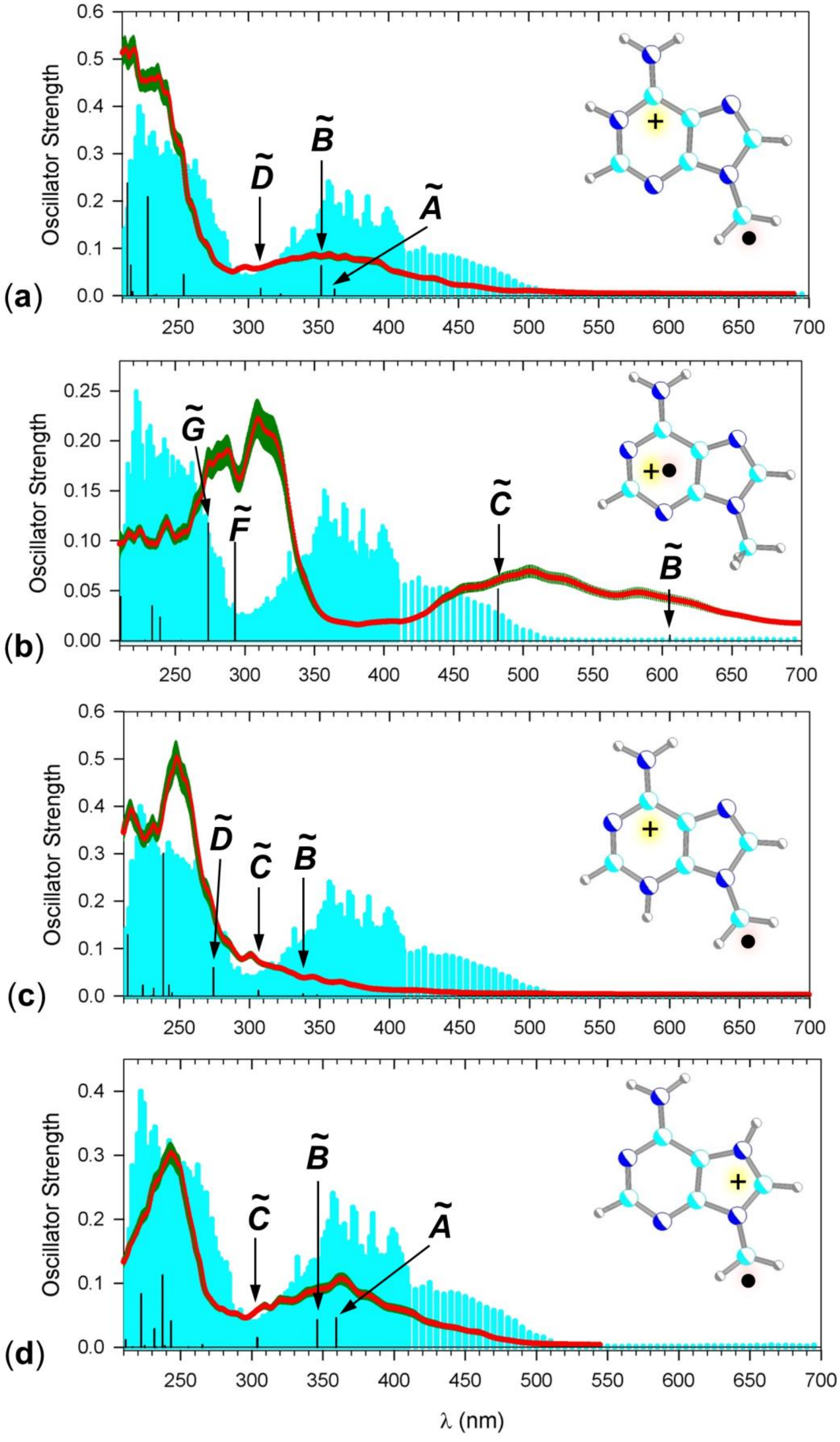

Figure 4. M06-2X/6-31+G(d,p) calculated vibronic spectra (310 K) of (a) $2^{+\bullet}$ (b) $1^{+\bullet}$, (c) $3^{+\bullet}$, and (d) $4^{+\bullet}$. The cyan background is an overlay of the action spectrum of $C_6H_7N_5^{+\bullet}$. The excited states were assigned from the comparison of M06-2X TD-DFT and EOMCCSD calculations.

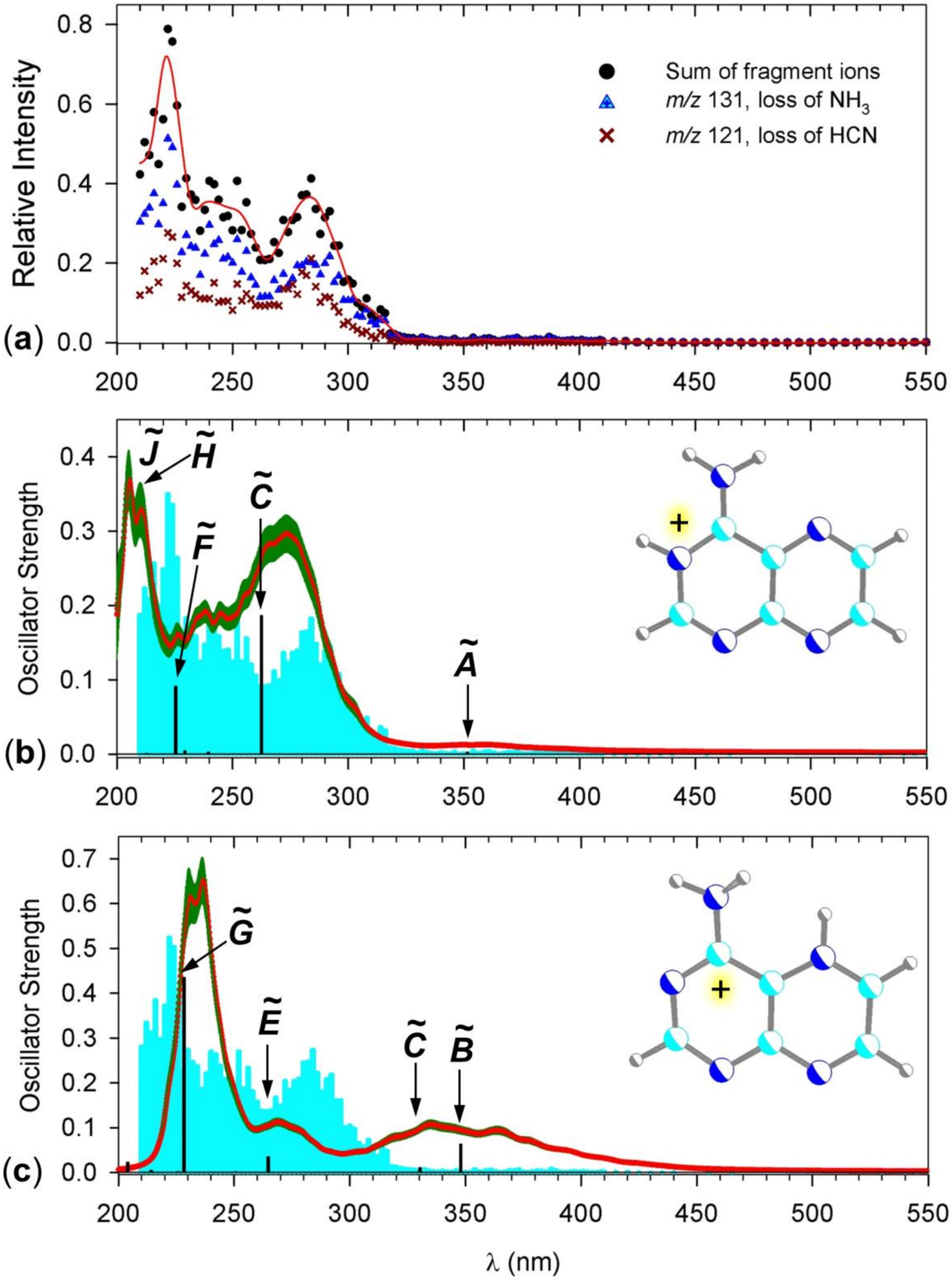

Figure 5. (a) UV-Vis action spectrum of *m/z* 148 ($C_6H_6N_5^+$) ion by loss of H from $2^{+\bullet}$. M06-2X/6-31+G(d,p) calculated vibronic spectra (310 K) of (b) $2h^+$ and (c) $4d^+$. The cyan background is an overlay of the action spectrum of $C_6H_6N_5^+$.

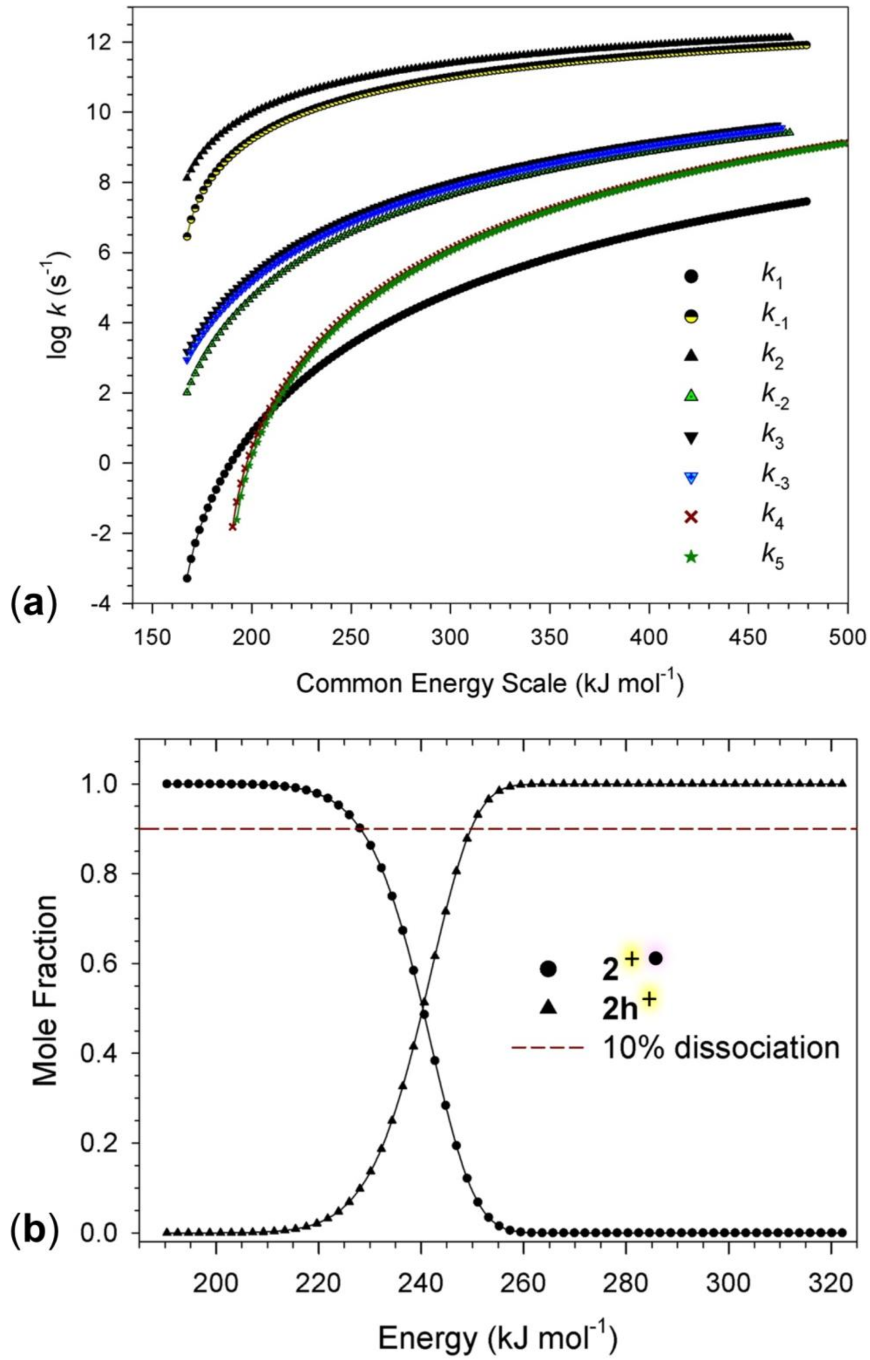

Figure 6. (a) RRKM rate constants pertinent to Scheme 5 reactions plotted on a common energy scale relative to $2^{+\bullet}$. (b) Calculated mole fractions of the $2^{+\bullet}$ reactant and $2h^+$ product after 50 ms in the ion trap.

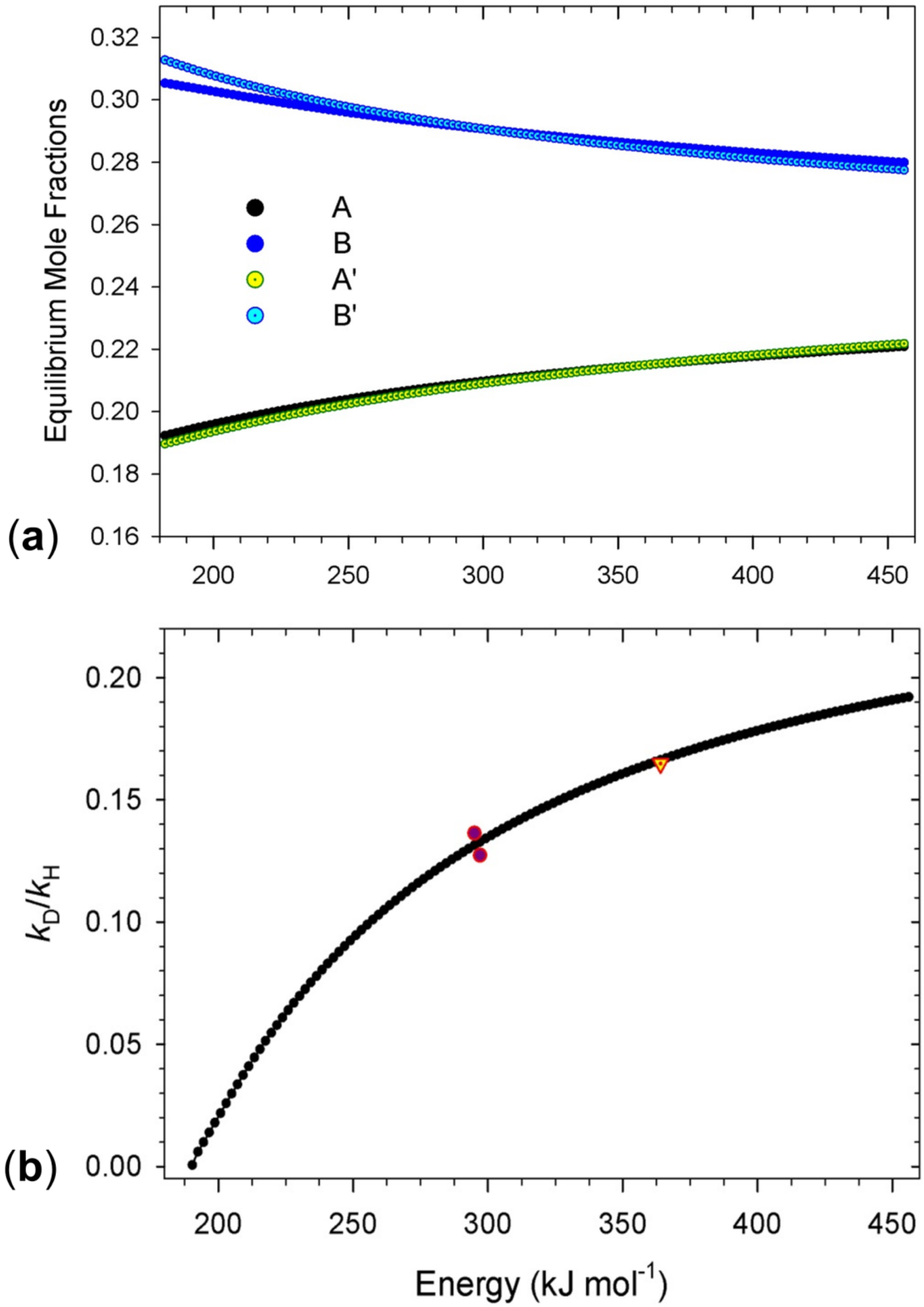

Figure 7. (a) Equilibrium populations of $2f^{+\bullet}$ and $2g^{+\bullet}$ isotopologues A, A', B, and B'. (b) Calculated ratio of rate constants for loss of H (k_{H}) and D (k_{D}) from an equilibrium mixture of $2f^{+\bullet}$ and $2g^{+\bullet}$ isotopologues A, A', B, and B' according to Scheme 6. The experimental data are shown as circles (CID) and upside triangle (UVPD at 270 nm).

Chapter 4—Cation Radicals of Hachimoji Nucleobases. Canonical Purine and Noncanonical Pyrimidine Forms Generated in the Gas Phase and Characterized by UV–Vis Photodissociation Action Spectroscopy

Reproduced in part with permission from S.R. Huang, F. Tureček, *J. Phys. Chem. A*, **2020**, 124, 7101-7112, DOI: 10.1021/acs.jpca.0c06227.

4.1. Abstract

Oxidation of nontraditional nucleobases 1-methylcytosine (hachimoji base S) and isoguanine (hachimoji base B) in gas-phase ternary complexes with Cu^{II}(terpyridine)$^{2+}$ formed cation radicals that were characterized by tandem mass spectrometry, UV-vis photodissociation action spectroscopy in the 210-700 nm region, and ab initio calculations up to the CCSD(T)/complete basis set level of theory. Oxidation of S was accompanied by exothermic isomerization in the 1-methylcytosine ion ($1^{+\bullet}$), forming 1-methylene-2-hydroxy-4-aminopyrimidine cation radical ($9^{+\bullet}$) as a noncanonical distonic isomer of the nucleobase. Ion $9^{+\bullet}$ was characterized by deuterium exchange experiments and provided a matching UV-vis action spectrum with the vibronic absorption spectrum from time-dependent density functional theory calculations. Oxidation of B resulted in the formation of a canonical isoguanine cation radical ($12^{+\bullet}$) as judged from the match of the experimental action spectrum with the calculated vibronic absorption spectrum. The calculated adiabatic ionization energies of canonical S and B, 8.51 and 7.76 eV, respectively, indicated exothermic electron transfer from B to $S^{+\bullet}$ to proceed in an ionized base pair. Contrasting this, the lowest energy tautomer of ionized S ($9^{+\bullet}$) had a low adiabatic recombination energy, RE_{adiab} = 5.70 eV, that would prevent it from oxidizing other nucleobases. Recombination energies of several nucleobase tautomers are reported and discussed.

4.2. Introduction

The information capacity of DNA, given by 4n where n is the number of coding nucleobases, has recently been expanded by combining the four standard nucleobases, adenine (A), guanine (G) cytosine (C), and thymine (T) with nonstandard nucleobases isoguanine (B), 2-aminoimidazo[1,2-a]-s-triazin-4-one (5-aza-7-deazaguanine, P), 1-methylcytosine (S), 1-methyl-2-amino-1H-pyrimidin-4-one (1-methylisocytosine), and 6-amino-5-nitro-1H-pyridin-2-one (Z).[1] These nucleobases have been incorporated into the so-called hachimoji DNA and RNA as the corresponding nucleotides and found to form hydrogen-bonding S/B and Z/P patterns that were analogous to standard Watson–Crick pairing (Scheme 1).[2] Considering the potential of using the hachimoji nucleobases for expanded DNA information storage and computing, it has become of interest to investigate their stability with respect to degradation processes resulting from ionization. Ionization damage during long-term storage would disrupt the embedded nucleobase code and result in readout malfunction and information loss. This could be particularly pernicious, because as opposed to living organisms, DNA computers are unlikely to have intrinsic mechanisms for damage repair. DNA damage is known to proceed via direct and indirect mechanisms out of which direct ionization by high-energy photons or elementary particles is the most prevalent one.[3] Nonselective DNA ionization primarily affects the nucleobases, forming reactive cation radicals that undergo fast electron[4,5] and proton transfers[6-10] among the nucleobases or by interactions with the environment.[11,12]

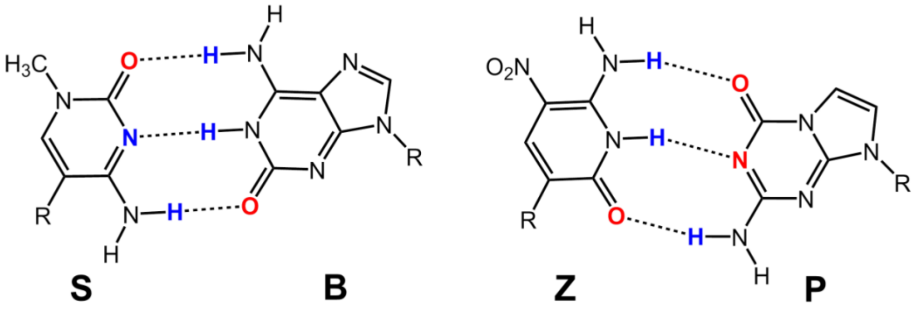

Scheme 1. Nontraditional Nucleobases S, B, Z, and P for Hachimoji DNA

In contrast to nonselective DNA ionization and side reactions occurring in the condensed phase, the rarefied gas phase offers an inert medium where nucleobase, nucleoside, and oligonucleotide cation radicals can be generated site-specifically and analyzed by tandem mass spectrometry combined with ion spectroscopy methods. Besides direct ionization of gas-phase nucleobases, the generation of gas-phase nucleobase cation radicals relies on intramolecular electron transfer in doubly charged ternary transition-metal complexes, such as those composed of a nucleobase, 2:2',6':2"-terpyridine (terpy), and Cu^{II}. The complexes are formed by electrospray ionization (ESI), stored in an ion trap, and the nucleobase oxidation is induced by collisional activation which drives complex dissociation (Scheme 2). This approach to nucleobase cation radicals has been pioneered by O'Hair and co-workers,[13] following earlier studies of peptide cation radicals by Chu, Siu, and co-workers,[14] and the first generation of amino acid and peptide complexes and cation radicals in the author's laboratory.[15,16] The gas-phase cation radicals have been characterized by methods of multiphoton infrared and single-photon UV-vis photodissociation action spectroscopy. Action spectroscopy utilizes wavelength-dependent photodissociation to plot the fragment ion yield and thus construct a spectrum profile in the wavelength domain that is representative of the active chromophore bands in the gas-phase ion.[17,18] By switching from absorbance measurements to monitoring photofragment ions, action spectroscopy achieves highly sensitive detection of photon absorption even for extremely optically thin samples, such as the 10^4 to 10^5 populations of ions stored in the ion trap. Previous studies of gas-phase DNA nucleobase cation radicals revealed a diversity of structures. The purine bases adenine,[19] guanine,[20,21] and their methyl derivatives have been shown by action spectroscopy to form canonical tautomers of the nucleobase cation radicals, contrasting cytosine cation radicals that were produced as a mixture of tautomers.[22] Perhaps the most intriguing result has stemmed from the generation of thymine cation radicals that have been shown by action spectroscopy to predominantly assume noncanonical ion structures.[23] Here, we report the generation of nucleobase cation radicals derived from hachimoji nucleobases S and

B. Using UV-vis action spectroscopy and ab initio theory, we wish to show that the purine nucleobase B prefers a canonical structure, whereas the gas-phase pyrimidine nucleobase S is formed as a stable noncanonical isomer.

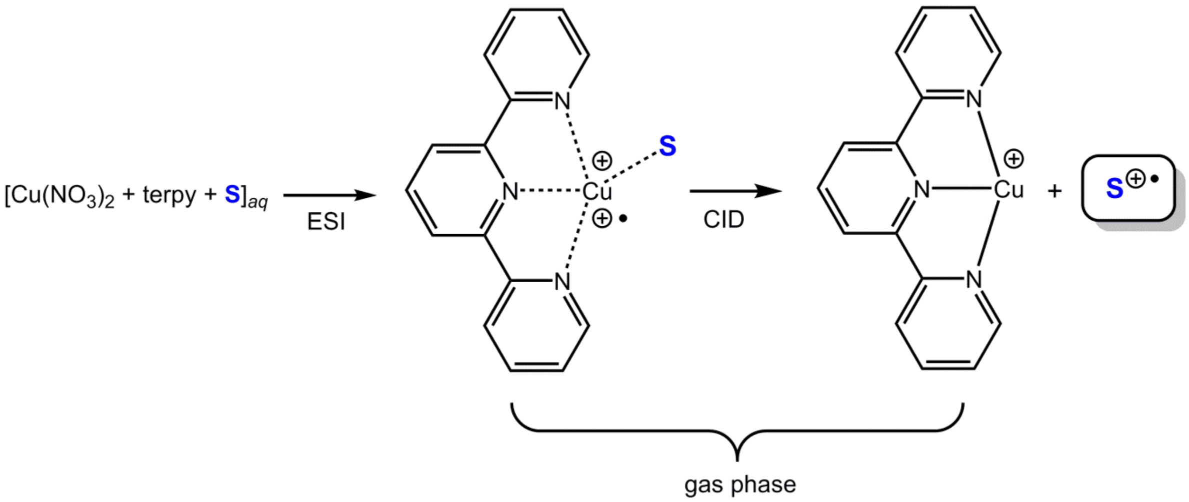

Scheme 2. Formation of Hachimoji Cation Radical $S^{+\bullet}$ from a Ternary Cu(terpy) Complex.

4.3. Experimental

4.3.1. Materials and Methods

Isoguanine (Cayman Chemical, Ann Arbor, MI, USA), 1-methylcytosine, copper nitrate, and 2:2’,6’:2”-terpyridine (Sigma-Aldrich, St. Louis, MO, USA) were purchased from the suppliers and used as received. Complexes were made in situ from equimolar concentrations of the components in 50:50 acetonitrile/water, and the solutions were electrosprayed into a modified Bruker Daltonik (Bremen, Germany) amaZon Speed 3D ion trap mass spectrometer. H/D exchange was accomplished in D_2O/CD_3CN solution and the D content in gas-phase ions was maintained by feeding D_2O solvent vapor into the dry nitrogen stream, flushing the enclosed electrospray interface volume. The ion trap was furnished with windows, lenses, and mirrors to allow irradiation of trapped ions with a laser beam.[24] The beam was generated by an EKSPLA NL301G (Altos Photonics, Bozeman, MT, USA) Nd:YAG laser working at a 20 Hz frequency that was equipped with a PG142C optical parametric oscillator, as described previously for a similar setup using a linear ion trap.[25] The laser pulse energies were measured at each experimental wavelength with an EnergyMax-USB J-10MB energy sensor (Coherent Inc., Santa Clara, CA, USA) and used to calibrate the action spectra. Photofragment ion intensities were measured in three sections covering the 210–700 nm range and normalized to the number of photons per pulse. The action spectra were reproduced and are reported as averages of two measurements performed on different days. Accurate mass measurements were made on an Orbitrap Velos mass spectrometer (Thermo Fisher, San Jose, CA, USA) at a resolving power of 60,000 to assign elemental compositions to ions of interest.

4.3.2. Calculations

Ab initio and density functional theory (DFT) calculations were performed with the Gaussian 16 (Revision A03) suite of programs.[26] Initial structure guesses were first fully gradient-optimized with B3LYP/6-31+G(d,p)[27] and CAM-B3LYP/6-311+G(2d,p)[28] to obtain a preliminary ranking by energy of the doublet-state cation-radical tautomers and to evaluate local energy minima by adequate harmonic frequencies. The B3LYP/6-31+G(d,p) frequencies, scaled by 0.975, were then used to calculate zero-point vibrational energy corrections, enthalpies, and entropies. Additional sets of optimized geometries were obtained with M06-2X[29] and the 6-31+G(d,p) and 6-311++G(2d,p) basis sets as well as with coupled clusters[30] (single and double excitations, CCSD) calculations with the 6-31+G(d,p) basis set. Quartet-state energies were examined with M06-2X/6-31+G(d,p) and 6-311++G(2d,p) gradient optimizations for methylcytosine cation-radicals $1^{+\bullet}$ and $9^{+\bullet}$. The quartet-state energies for these tautomers were 3.5-3.6 eV higher than the corresponding doublet-state energies and so the quartet potential energy surface (PES) was not explored for the other isomers. All these calculations were performed within the spin-unrestricted formalism. The goal of the multiple geometry optimizations was to find the best match between the CCSD/6-31+G(d,p) optimized geometries on one hand and the DFT optimized geometries on the other. The match was established on the basis of total single-point energies calculated using coupled clusters with single, double, and disconnected triple excitations, CCSD(T),[31] that were extrapolated to the complete basis set

(CBS)[32] using the formula E[CCSD(T)/CBS] ≅ E[CCSD(T)/aug-pVDZ] – E[MP2/aug-pVDZ] + E[HF/aug-pVQZ] + $E_{corr,CBS}$, providing benchmark relative energies. The extrapolations for calculating the correlation energy at the CBS limit used least-squares fits to both the standard two-parameter formula,[33] $E_{corr,CBS} = A + BX^{-3}$, where X is the ζ split in the aug-cc-pVXZ basis set,[34] and a three-parameter exponential formula, $E_{corr,CBS} = a + b*e^{-cX}$, reported recently.[35] The coefficients for both fits are summarized in Table S1 (Supporting Information). Single-point energies based on these two kinds of fits gave very similar relative energies for most species, reactions, and transition states (TSs), although deviations on the order of 10 kJ mol-1 were observed for a few structures when using the three-parameter exponential fit. Therefore, energies based on the X^{-3} fits are used in text. Higher spin states in the UMP2 calculations were treated with the spin projection method[36,37] using spin annihilation that reduced the total spin close to the theoretical value (0.75). These benchmarking calculations pointed to a close match between the CCSD(T)/CBS total energies when based on M06-2X/6-31+G(d,p), M06-2X/6-311++G(2d,p), and CCSD/6-31+G(d,p) geometries that were within 0.3 millihartree (0.8 kJ mol^{-1}) absolute deviation. Transitions and oscillator strength for 13-14 excited electronic states were evaluated using equation-of-motion CCSD (EOM-CCSD) calculations[38] with the 6-31+G(d,p) basis set. This covered excitations down to below 200 nm for all tautomers. The EOM-CCSD transitions were used to assign excited states from the time-dependent DFT (TD-DFT)[39] calculations that were carried out with M06-2X for 35-40 excited states, covering the wavelength range to below 180 nm. The EOMCCSD- and TD-DFT-calculated excitation wavelengths and oscillator strength are compared in Tables S2–S5 and Figures S1a–d and S2a–d (Supporting Information). The M06-2X TD-DFT calculations with the 6-31+G(d,p) and 6-311++G(2d,p) basis sets gave very similar results in terms of excitation energies that differed by root-mean-square deviation rmsd = 0.026–0.062 eV. Similarly, the oscillator strengths calculated with M06-2X and the two basis sets showed rmsd = 0.004–0.007. Hence, the M06-2X/6-31+G(d,p) TD-DFT calculations were deemed to be sufficient to be used in calculations of all vibronic spectra at 310 K. The B3LYP/6-31+G(d,p) normal modes were used to generate vibrational configurations with the Newton X program,[40] which were ordered according to their Boltzmann factors at 310 K. Three hundred lowest energy configurations were selected and submitted to TD-DFT M06-2X/6-31+G(d,p) calculations for 20 excited states to generate the vibronic spectra reported here.

TSs for isomerizations were located by stepwise M06-2X/6-31+G(d,p) and 6-311++G(2d,p) calculations to map the PES along the reaction coordinate. The TSs were characterized by harmonic frequency analysis as having a zero gradient along the reaction coordinate and one imaginary frequency. The TS geometries were used for single-point CCSD(T) calculations. CCSD/6-31+G(d,p) step-wise geometry optimizations were used to locate the TS for the isomerization of $1^{+\bullet}$ to $8^{+\bullet}$, see Figure S3a–c and discussion therein (Supporting Information) for a detailed description of this difficult case.

Rice–Ramsperger–Kassel–Marcus calculations (RRKM)[41] of rate constants for unimolecular isomerizations were carried out with a direct count of vibrational quantum states using TS energies from CCSD(T)/CBS single-point energy calculations. The RRKM calculations used the QCPE program[42] that was recompiled and run under Windows 7.[43] Rotational states were treated adiabatically, and the microcanonical rate constants, *k(E, J)*, were Boltzmann-averaged over the rotational state distribution at 310 K.

4.4. Results & Discussion

4.4.1. Generation of $S^{+\bullet}$ and D_2-$S^{+\bullet}$

ESI of solutions containing $Cu(NO_3)_2$, terpy, and 1-methylcytosine produced doubly charged complexes of $[^{63}Cu(terpy)S]2^{+\bullet}$ at m/z 210 that were isolated by mass and subjected to collision-induced dissociation (CID-MS^2). This yielded cation radicals $S^{+\bullet}$ (m/z 125) together with the complementary $Cu(terpy)^+$ ions at m/z 296 (Figure 1a). Analogously, ESI of the same components from D_2O/CD_3CN formed $[^{63}Cu(terpy)(D_2\text{-}S)]2^{+\bullet}$ ions at m/z 211 by H/D exchange of the methylcytosine NH_2 protons. CID-MS^2 of $[^{63}Cu(terpy)\ (D_2\text{-}S)]2^{+\bullet}$ then produced isotopically labeled cation radicals D_2-$S^{+\bullet}$ (Figure 1b). The nucleobase cation radicals were further characterized by CID-MS^3 to identify the dissociation channels for UV photodissociation (UVPD) action spectroscopy. CID-MS^3 of $S^{+\bullet}$ chiefly proceeded by ring-cleavage dissociations, forming the m/z 96 (loss of COH) and m/z 83 (loss of NCO) fragment ions that were assigned according to their accurate mass measurements (Figure 2a). UVPD-MS^3 of $S^{+\bullet}$ at 270 nm resulted in the same dissociations (m/z 96 and m/z 83, Figure 2b), so both channels were suitable for action spectroscopy measurements. CID-MS^3 of D_2-$S^{+\bullet}$ (Figure 2c) indicated retention of two deuterium atoms in both the m/z 98 and m/z 85 fragment ions; hence, the ND_2 group did not undergo intramolecular H/D exchange with the other hydrogen atoms in the course of ring fragmentation.

4.4.2. Action Spectra of $S^{+\bullet}$ and D_2-$S^{+\bullet}$

The action spectra were recorded in the 210–700 nm region using the dissociation channels identified by CID-MS^3. The spectrum of $S^{+\bullet}$ displayed a composite band with maxima at 240, 270, 319, and 355 nm that were chiefly represented by the m/z 96 and m/z 83 channels (Figure 3a). In addition, the spectrum of $S^{+\bullet}$ showed two weaker bands in the visible region, one with a maximum at 470 nm and a very weak one extending between 540 and 650 nm. The action spectrum of D_2-$S^{+\bullet}$ (Figure 3b) was remarkably similar to that of $S^{+\bullet}$. The similarities included the structure of the UV band that showed maxima at 240, 270, 318, and 355 nm for D_2-$S^{+\bullet}$. Also, the shapes of absorption bands for the corresponding channels, m/z 96 and m/z 98 and m/z 83 and m/z 85 for $S^{+\bullet}$ and D_2-$S^{+\bullet}$, respectively, were similar. The action spectrum of D_2-$S^{+\bullet}$ also showed two bands in the visible region, one at 465 nm and a broad weak band at 570 nm. In contrast to the Figure 3a,b action spectra, the reported absorption spectra of both cytosine and 3-methylcytosine taken in the gas phase and aqueous solution at pH 7 have not displayed bands above ca. 270 nm.[44] Hence, the prominent bands at $\lambda > 300$ nm in the Figure 3a,b spectra are associated with absorption by a radical-related chromophore in $S^{+\bullet}$.

4.4.3. Cation Radical Structures and Action Spectra Assignment

To assign the action spectra to methylcytosine cation-radical structures, we obtained optimized geometries and relative energies of several tautomers (Table 1). The canonical 1-methylcytosine structure $1^{+\bullet}$ was nearly isoenergetic with the N-3-H, 4-imine tautomer $2^{+\bullet}$ (for the ring position numbering see Figure 4). The 2-OH, 4-imine tautomers $3^{+\bullet}$ and $4^{+\bullet}$ were 18 and 31 kJ mol^{-1}, respectively, less stable than $1^{+\bullet}$. Tautomers protonated at N-1 ($5^{+\bullet}$, $6^{+\bullet}$) and C-5 ($7^{+\bullet}$) had substantially higher energies than $1^{+\bullet}$, whereas an isomer initially protonated at C-6 collapsed to $7^{+\bullet}$ upon gradient optimization with M06-2X. The optimized structures of these higher-energy ions are shown in Figure S4 (Supporting Information). In addition to structures of $S^{+\bullet}$ that preserved the N-1 methyl group, we obtained low-energy structures in which a methyl H moved to other positions. Ions $8^{+\bullet}$ and $9^{+\bullet}$ in which a methyl H atom moved to O-2 (Figure 4) were low-energy tautomers, with $9^{+\bullet}$ being the global energy minimum at -59 kJ mol^{-1} relative to $1^{+\bullet}$ (Table 1). The related ion $10^{+\bullet}$ was a nearly isoenergetic N-3-H tautomer of $9^{+\bullet}$, whereas another tautomer with a proton at N-4 ($11^{+\bullet}$) was less stable at 60 kJ mol^{-1} above 1.

Ions $9^{+\bullet}$ and $10^{+\bullet}$ substantially differed from the canonical isomer $1^{+\bullet}$ in their atomic spin density distributions according to natural population analysis[45] (NPA) of the M06-2X/6-31+G(d,p) wave functions (Figure S5). Ion $1^{+\bullet}$ showed NPA spin densities delocalized among positions N-1, O-2, N-3, and C-5 with spin polarization reversing the α and β electron density population at C-2, C-4, and C-6. In contrast, ions $9^{+\bullet}$ and $10^{+\bullet}$ showed high spin densities at the CH_2 group, 88 and 85%, respectively, much less spin polarization, and <10% spin density in the other ring positions and the NH_2 group. Because of this spin density localization at CH_2, ions $9^{+\bullet}$ and $10^{+\bullet}$ can be qualified as distonic ions[46,47] in which the spin and charge are located at separate atoms.

The calculated vibronic absorption spectra of four low-energy tautomers $1^{+\bullet}$, $2^{+\bullet}$, $9^{+\bullet}$, and $10^{+\bullet}$ of $S^{+\bullet}$ are shown in Figure 5a-d where they are overlaid on a scaled action spectrum plotted as the green shading in the background. The absorption spectrum of the canonical isomer $1^{+\bullet}$

(Figure 5a) did not match the action spectrum. In particular, the absorption spectrum indicated a strong band at the edge of the experimental wavelength range (210 nm) that was absent in the action spectrum. Moreover, the absorption spectrum lacked the composite band at 270–330 nm. A mismatch was also revealed for the absorption spectrum of $2^{+\bullet}$ (Figure 5b) that was dominated by a split band at 250-260 nm that was less prominent in the action spectrum. We found the best match for the absorption spectrum of noncanonical isomer $9^{+\bullet}$ that reproduced most of the salient features of the action spectrum, namely, showing a composite band because of several transitions at 210–350 nm and a 420 nm band in the visible region (Figure 5c). We note that, compared to the action spectrum, the calculated spectrum showed a blue shift for all bands. This may be due to a combination of overestimated excitation energies from TD-DFT calculations by 0.2–0.3 eV and a higher ion temperature in the ion trap. The assignment of the electron excitation transitions in $9^{+\bullet}$ (Table S3, Supporting Information) revealed that the transition at 393 nm corresponded to the first (A) excited state that was vibronically shifted to 420 nm. However, this could not explain the presence in the action spectrum of another weak band at 570–580 nm (Figure 3a,b) for which we did not find an excited state. This band can be accounted for by the presence of $10^{+\bullet}$ as a minor component of the gas-phase ions. Indeed, the absorption spectrum of $10^{+\bullet}$ (Figure 5d) displayed an intense band at 490 nm for the transition to the A state that was broadened and vibronically shifted to 530 nm. Considering the blue shift of the TD-DFT excitation energies, excitation to the A state of $10^{+\bullet}$ could explain the presence of the 570–580 nm band in the action spectrum. We did not attempt to compose an absorption spectrum of a mixture of $9^{+\bullet}$ and $10^{+\bullet}$ from different combinations of their absorption spectra, and thus the theoretical fractions of $9^{+\bullet}$ and $10^{+\bullet}$ remain uncertain, although $9^{+\bullet}$ appears to be the dominant component.

The formation of $9^{+\bullet}$ and possibly also $10^{+\bullet}$ was further corroborated by H/D exchange experiments. Ions $1^{+\bullet}$-$6^{+\bullet}$ have only two exchangeable protons, contrasting $8^{+\bullet}$-$11^{+\bullet}$ in which the initially nonexchangeable methyl hydrogen becomes exchangeable. We generated D_2-$S^{+\bullet}$ ions by ESI and stored the mass-selected ions in the ion trap for a prolonged time where they were exposed to D_2O vapor. This showed a slow progressive H/D exchange whereby 25% of D_2-$S^{+\bullet}$ was converted to D_3-$S^{+\bullet}$ after 8 s (Figure S6, Supporting Information). Thus, a substantial fraction of $S^{+\bullet}$ existed as species with three exchangeable protons, out of which $9^{+\bullet}$ and $10^{+\bullet}$ were the energetically most favorable isomers. An exponential fit of the time-dependent H/D exchange data gave the pseudo-first-order rate constant as 0.036 ± 0.02 s^{-1} (rmsd).

4.4.4. Formation of Noncanonical Cation Radicals $9^{+\bullet}$ and $10^{+\bullet}$

To explain the formation of the noncanonical isomers, we analyzed the reaction sequence from the $[Cu(tpy)S]^{2+\bullet}$ complexes to the gas-phase $S^{+\bullet}$. Fully optimized structures of complexes in which the nucleobase ligand was represented by neutral analogues 1, 2, 3, and 9 were obtained by CAM-B3LYP/6-311+G(2d,p) (Figure 6) that also provided relative free enthalpies in the gas phase and water dielectric (Table 2). From these calculations, it was clear that not only was the complex of 1 by far most stable in both solution and the gas phase, but also it was the only one that was bound ($\Delta G_{310,\mathrm{diss}}$ = 72 kJ mol^{-1}) in the gas phase. Hence, nucleobase 1 should predominate in the $[Cu(tpy)S]^{2+\bullet}$ complexes under equilibrium conditions, and the formation of gas phase $9^{+\bullet}$ and $10^{+\bullet}$ must occur as a result of collisional activation breaking the complex and accomplishing nucleobase ionization.

The PES for unimolecular interconversions of $1^{+\bullet}$, $2^{+\bullet}$, $8^{+\bullet}$, $9^{+\bullet}$, and $10^{+\bullet}$ was explored by finding the respective TSs, TS1–TS4, for hydrogen migrations and TS_{rot} for OH group rotation in $8^{+\bullet}$ (Figure 7). For fully optimized TS structures, see Figure S7 (Supporting Information). The PES is represented by CCSD(T)/CBS energies at 0 K relative to $1^{+\bullet}$. Ions $1^{+\bullet}$ and $2^{+\bullet}$ were separated by an energy barrier for hydrogen migration in TS1 at 174 kJ mol^{-1} relative to $1^{+\bullet}$. This was similar to the barrier for an analogous hydrogen migration in cytosine cation radicals (161 kJ mol^{-1}).[48] In contrast, H atom migration from the $1^{+\bullet}$ methyl required only 90 kJ mol^{-1} in TS2, forming $8^{+\bullet}$ at −25 kJ mol^{-1}, which can further undergo a facile OH rotation via TS_{rot}, forming in turn the lowest energy isomer $9^{+\bullet}$. The latter was separated from the nearly isoenergetic $10^{+\bullet}$ by a somewhat higher energy barrier in TS3 at 155 kJ mol^{-1} relative to 9$^{+\bullet}$. A further hydrogen migration from N-3 to the NH$_2$ group to form 11$^{+\bullet}$ required a still higher energy in TS4 at 201 kJ mol^{-1} relative to 10$^{+\bullet}$. The exothermic migration of the methyl hydrogen in 1$^{+\bullet}$ (TS2) was reminiscent of the analogous isomerization of the canonical form of the thymine cation radical, where the pertinent energy barrier was at 107 kJ mol^{-1} and allowed fast exothermic isomerization to occur upon ion formation.[23]

We used the TS energies to estimate the isomerization kinetics. TS theory (TST) calculations gave thermal rate constants for the 1$^{+\bullet}$ → 8$^{+\bullet}$ (k_1) and 9$^{+\bullet}$ → 10$^{+\bullet}$ (k_2) isomerizations shown in Figure S8a (Supporting Information). These indicated that for a thermal 1$^{+\bullet}$ → 8$^{+\bullet}$ isomerization to occur on the time scale of ion storage in the trap (0.15 s), the ions would have had to be heated to > 390 K. This is beyond the typical range of trapped-ion effective temperatures (300–350 K),[49–52] suggesting that thermal isomerization would be slow. Similarly, a thermally driven 9$^{+\bullet}$ → 10$^{+\bullet}$ isomerization was calculated to be too slow to proceed at typical ion trap temperatures (Figure S8a). In contrast, upon excitation by collisions, ions 1$^{+\bullet}$ were calculated to undergo fast isomerization, as illustrated by the RRKM rate constants (k_1, Figure S8b). Even at internal energies within 10 kJ mol^{-1} above TS2, ion 1$^{+\bullet}$ was expected to isomerize to 8$^{+\bullet}$ with $k_1 > 10^3$ s^{-1}. The OH bond rotation in 8$^{+\bullet}$, which requires only 6 kJ mol^{-1} in TS$_{rot}$, was considered to be very fast, so that the formation of 8$^{+\bullet}$ should be followed by exothermic isomerization to 9$^{+\bullet}$. The reversible interconversion of 9$^{+\bullet}$ and 10$^{+\bullet}$ with rate constants k_2 and k_{-2} was calculated to require ca. 14 kJ mol^{-1} above TS3 to achieve 50% conversion (Figure S8b). The k_2/k_{-2} ratio that determines the equilibrium population of 9$^{+\bullet}$ and 10$^{+\bullet}$ was 0.86-0.89 over the entire range of kinetically relevant internal energies (Figure S8b), indicating a 46/54 ratio of 9$^{+\bullet}$ to 10$^{+\bullet}$. Hence, the concomitant formation of 10$^{+\bullet}$ along with 9$^{+\bullet}$ was kinetically possible at elevated internal energies.

4.4.5. Generation and Action Spectra of Isoguanine Cation Radical $B^{+\bullet}$

The isoguanine cation radical $B^{+\bullet}$ was generated by the CID of the mass-selected [^{63}Cu(tpy)B]$^{2+\bullet}$ complex (m/z 223.5, Figure S9, Supporting Information) in a manner analogous to the formation of $S^{+\bullet}$ (Scheme 2). We note that the formation of the gas phase [^{63}Cu(tpy)B]$^{2+\bullet}$ complex by an electrospray was hampered by the very low solubility of isoguanine in electrospray-compatible solvents, so that the ESI spectrum contained the [63Cu(tpy)B]2+• ions at ca. 1% relative intensity (Figure S9a). However, cation radical $B^{+\bullet}$ (m/z 151.0435, $C_5H_5N_5O$) was successfully generated (Figure S9b) and characterized by the CID-MS^3 and UVPD-MS^3 (310 nm) spectra (Figure 8a,b). Both spectra showed common dissociation channels by loss of NH_2 (m/z 135), NH_3 (m/z 134), HCN (m/z 124), NCO (m/z 109), and HNCO (m/z 108) that were assigned according to accurate mass measurements and used to monitor the action spectra.

The action spectrum of $B^{+\bullet}$ displayed bands with maxima at 215, 263, 330, and 355 nm, with a shoulder showing a maximum at 400 nm and extending to 550 nm (Figure 9a). The mass-resolved channels (m/z 108, 124, 134, and 135, Figure 9b) followed the same trend, each contributing to the bands in the spectrum. We note that the action spectrum of $B^{+\bullet}$ differs from the spectra of guanine ($G^{+\bullet}$) and 9-methylguanine ($MG^{+\bullet}$) cation radicals.[21] In particular, the spectra of $G^{+\bullet}$ and $MG^{+\bullet}$ show only a weak band at 220 nm and a strong band at 290 nm, whereas the latter is absent in the spectrum of $B^{+\bullet}$.

4.4.6. Isoguanine Cation Radical Structures, Relative Energies and Action Spectra Assignment

To sort out ion isomers and assign the action spectrum, we obtained several tautomeric structures for $B^{+\bullet}$ in which the exchangeable proton locations were varied among the N-1, O-2, N-3, N-6, N-7, and N-9 positions. Six lowest-energy isomers $12^{+\bullet}$-$17^{+\bullet}$ are shown in Figure 10, the other, higher-energy isomers $18^{+\bullet}$-$22^{+\bullet}$ are compiled in Figure S10 (Supporting Information). The canonical 2-oxo isomer ($12^{+\bullet}$) and the *syn* and *anti* enols ($13^{+\bullet}$ and $14^{+\bullet}$, respectively) represented the lowest-energy ions of close relative energies according to DFT and correlated calculations (Table 3). The relative energies extrapolated to the aug-cc-pVTZ, aug-cc-pVQZ, and complete basis sets showed a gradually smaller gap between $12^{+\bullet}$ and the enol isomers $13^{+\bullet}$ and $14^{+\bullet}$ so that the tautomers became virtually isoenergtic at our highest level of theory (Table 3). This effect was not observed for the relative energies of neutral isoguanine tautomers (Table S6) which converged at calculations with the aug-cc-pVTZ basis set, and further expansions had only a small effect. The N-3, N-9 tautomer $15^{+\bullet}$ and enol-imine $16^{+\bullet}$ were 39 and 28 kJ mol^{-1} higher in energy than $12^{+\bullet}$, respectively, while the other isomers were still less stable (Table 3). The energy ordering of isoguanine cations radicals differed from that calculated for neutral gas-phase molecules by Orozco et al. where neutral tautomers 13 and 14 had 31-32 kJ mol^{-1} lower energies relative to neutral 12 at the CCSD(T)/aug-cc-pVTZ level of theory[53] (see also Table S6 data). The leveling off of the energies for the 2-oxo form $12^{+\bullet}$ and enols $13^{+\bullet}$ and $14^{+\bullet}$ (0.5 and 1.5 kJ mol^{-1}, respectively, at the CCSD(T)/CBS level of theory) indicated relative stabilization of the oxo-form upon ionization. This was unusual, because ionized enols are often stabilized relative to oxo forms upon ionization, reversing the order of stability for the neutral molecules.[54-56] In contrast to the neutral species, where tautomer 15 has been reported to be virtually isoenergetic with 12[53] (cf. also Table S6 data), we found ionized $15^{+\bullet}$ to be substantially less stable than $12^{+\bullet}$-$14^{+\bullet}$ (Table 3).

The electronic structure of $12^{+\bullet}$-$15^{+\bullet}$ was scrutinized by atomic spin densities based on natural population analysis of the M06-2X/6-311++G(2d,p) wave functions (Figure S11, Supporting Information). All these tautomers displayed substantial spin density at C-8, ranging from 0.19 to 0.31 for $12^{+\bullet}$ and $15^{+\bullet}$, respectively. These oxo-forms also showed spin density on O-2 (0.20 and 0.18 for $12^{+\bullet}$ and $15^{+\bullet}$, respectively), indicating polarization of the carbonyl C=O bond. The other locations of high spin density were at N-3 and C-5 that were common for $12^{+\bullet}$-$15^{+\bullet}$.

The calculated vibronic spectra of $12^{+\bullet}$-$15^{+\bullet}$ displayed differences in the 0 K excitation energies as well as in the band shapes upon vibronic thermal broadening. Starting with $12^{+\bullet}$, transitions to the ***A*** and ***B*** states at 632 and 518 nm, respectively, were dipole disallowed (Table

S4) and did not appear in the spectrum. The major calculated bands corresponded to transitions to the ***C***, ***D***, ***E***, ***G***. ***H***, ***I***, and ***L*** states at 409, 375, 330, 302, 236, 227, and 207 nm, respectively (Figure 11a). Enol hydroxyl rotamers $13^{+\bullet}$ and $14^{+\bullet}$ gave very similar spectra (Figure 11b, c), showing transitions to the ***B***, ***C***, ***E***, ***G***, ***I***, ***J***, ***K***, and ***L*** states at 550, 425, 326, 278, 235, 225, 212, and 205 nm. The other 2-oxo tautomer ($15^{+\bullet}$) showed transitions to the ***A***, ***D***, ***F***, ***H***, ***I***, ***J***, and ***M*** states at 786, 398, 323, 248, 234, 226, and 201 nm, respectively (Figure 11d). The band pattern in the vibronic spectrum of $12^{+\bullet}$ was similar to that in the action spectrum, allowing for an overall blue shift of the calculated bands. A discrepancy was observed for the band of the ***C*** state at 409 nm that was apparent only as a shoulder at 400 nm in the action spectrum. The vibronic spectra of the other isoguanine tautomers showed a more substantial mismatch with the action spectrum. The strong band of the G state (279 nm) for $13^{+\bullet}$ and $14^{+\bullet}$ is not represented in the action spectrum. Likewise, the very strong band of the M state of $15^{+\bullet}$ was weak in the action spectrum, which in turn showed a strong band at 330-360 nm which was weak in the calculated vibronic spectrum. We also calculated the vibronic spectra at 360 K in an effort to achieve an improved match with the action spectrum. However, the changes in the band maxima and intensities from 310 to 360 K were relatively minor and did not result in an improved match. We note that the calculated absorption spectra of several higher-energy $B^{+\bullet}$ ion tautomers ($16^{+\bullet}$-$22^{+\bullet}$. Figure S12) showed bands that did not appear in the action spectrum and made them incompatible with the experimental data.

To shed further light on the $B^{+\bullet}$ ion formation, we analyzed the relative energies of the precursor $[Cu(tpy)B]^{2+\bullet}$ complexes for different tautomers of the neutral B ligand (Figure S13, Table S7). The data indicated that the 2-oxo-tautomer 12 formed the lowest-energy gas-phase Cu(tpy) complexes in which bonding to Cu^{2+} was realized by coordination with O-2 or N-3, as in $[Cu(tpy)12a]^{2+\bullet}$ and $[Cu(tpy)12b]^{2+\bullet}$, respectively. Solvation with water brought the energies of complexes of the other 2-oxo-tautomers 15 and 18 close to those of 12 (Table S7). In contrast, the complexes of the enol tautomers 13 and 14 were less stable in both the gas phase and water. Solvation also affected the relative free energies of neutral B tautomers. Table S6 data indicated a substantial relative stabilization of solvated 12, 15, and 18 compared to the lowest gas-phase enol tautomers 13 and 14. The thermodynamic data for solvated 12-18 allowed us to obtain pair-wise equilibrium constants, e.g. $K_B = x_{12}/x_B = e^{-\Delta G(B)/RT}$, B = 13-18, expressing the relative mole fractions of neutral isoguanine tautomers in solution (Table S8). These were combined with the equilibrium constants for solvated complexes, $K_{CutpyB} = e^{-\Delta G(CutpyB)/RT}$, to calculate the equilibrium mole fractions ($x_{complex}$) of the complexes in solution (Table S8). The data indicated that complexes of 13 and 14 should be disfavored and present at levels <1%. Complexes of 12 and 15 were the dominant components, although the calculated mole fractions differed, depending on the DFT method used to calculate the Δ*G*(B) and Δ*G*(CutpyB) (Table S8). A large mole fraction of $[Cu(tpy)15]^{2+\bullet}$ complexes at 0.60-0.85 was indicated. However, this result was incompatible with the vibronic spectra analysis that excluded major contribution of $15^{+\bullet}$ in the gas-phase ion population (vide supra).

Since the gas-phase $B^{+\bullet}$ are formed by intramolecular ionization in the complexes, we examined the adiabatic ionization energies (IE_{adiab}) of lowest-energy isoguanine tautomers to gauge their propensity for oxidation. The IE_{adiab} ranged from 7.76 eV to 8.16 eV for 12 through 15, respectively, (Table S9). The recombination energy for $Cu(tpy)^{2+\bullet} + e^- \rightarrow Cu(tpy)^+$ was calculated by both M06-2X and CAM-B3LYP as $|RE_{adiab}|$ = 10.30 eV. This implied that intramolecular electron transfer in all $[Cu(tpy)B]^{2+\bullet}$ complexes was substantially exothermic, and the redox energy differences among the B tautomers were too minor to affect the formation of the cation radicals. Hence, the formation of $12^{+\bullet}$ led us to the conclusion that the $[Cu(tpy)12]^{2+\bullet}$ complex also was a major species produced from solution and serving as a precursor for the cation-radical formation in the gas phase.

4.4.7. Comparison of Recombination Energies and the Propensity for Electron Transfer between Nucleobases

Incorporation of hachimoji nucleobases S and B into chimeric DNA raises the question of inter-base electron transfer following a random ionization event. We addressed this question by comparing the adiabatic recombination energies (REadiab) of hachimoji and standard nucleobase cation radicals obtained at the uniform CCSD)(T)/CBS level of theory. Note that when expressed as absolute values, | RE_{adiab} (nucleobase$^{+\bullet}$) | = | IE_{adiab}(nucleobase) |, and the enthalpy for the electron transfer reaction, (nucleobase)$_1$ + (nucleobase$^{+\bullet}$)$_2$ → (nucleobase$^{+\bullet}$)$_1$ + (nucleobase)$_2$, is given by ΔH_{ET} = | IE_{adiab} (nucleobase)$_1$ | – | RE_{adiab} (nucleobase$^{+\bullet}$)$_2$ | with $\Delta H_{ET} < 0$ indicating spontaneous electron transfer. Considering the ionized S-B pair, electron transfer from isoguanine tautomer 12 (IE_{adiab} = 7.76 eV) to the canonical S$^{+\bullet}$ tautomer 1$^{+\bullet}$ of RE_{adiab} = 8.51 eV (Table 4) is 0.75 eV exothermic and therefore energetically favored. In contrast, the non-canonical S$^{+\bullet}$ tautomer 9$^{+\bullet}$ (RE_{adiab} = 5.70 eV) has a low recombination energy and, if directly ionized or formed by low-energy isomerization of 1$^{+\bullet}$, it would trap the electron defect in the methylcytosine base. Table 4 data allow one to consider other (nucleobase)$_1$ + (nucleobase$^{+\bullet}$)$_2$ combinations. As expected on the basis of experimental[57-63] and calculated ionization energies,[64,65] the canonical tautomer of [thymine]$^{+\bullet}$ (RE_{adiab} = 8.98 eV, Table 4) is able to abstract an electron from all the other nucleobases. In contrast, the more stable 2,4-OH-5-CH_2 [thymine]$^{+\bullet}$ tautomer could abstract an electron only from the non-canonical methyl cytosine tautomer 9. The recombination energies of the enol tautomers of guanine and isoguanine cation radicals were similar, whereas the oxo-form of ionized guanine showed a greater recombination energy (7.91 eV) than did the isoguanine oxo form 12$^{+\bullet}$ (7.76 eV, Table 4). For these close matches, the direction of electron transfer is expected to be affected by the local environment of the ionized and neutral nucleobase. This includes not only the N-9 or N-1 deoxyribose substituents that overall decrease the nucleoside recombination energies, but also the presence of additional charges, hydrogen bonding and solvation of oligonucleotides and DNA.[66-71]

4.5. Conclusions

The experimental and computational results reported here allow us to arrive at the following conclusions. Intramolecular electron transfer in 1-methylcytosine complexes with Cu(terpy) produces the 1-methylene-2-hydroxy-4-aminopyrimidine cation radical $9^{+\bullet}$ as the major product. Ion $9^{+\bullet}$, which is the global energy minimum of 1-methylcytosine ions in the gas phase, represents another low-energy, non-canonical nucleobase isomer that can be formed by exothermic isomerization of ionized canonical nucleobases. Cation radical $9^{+\bullet}$ has an extremely low recombination energy that is expected to prevent it from oxidizing other nucleobases. In contrast to pyrimidine nucleobases, we find that the canonical form of isoguanine ($12^{+\bullet}$) is formed upon intramolecular electron transfer of isoguanine Cu(terpy) complexes. The dominant formation of $12^{+\bullet}$, as opposed to two other low-energy isoguanine cation-radical enol tautomers, is conditioned on the stability of its complexes in solution. These findings set the groundwork for future investigations of canonical and non-canonical nucleosides and nucleotides to further examine their potential role in electron and proton transfer reactions triggered by DNA ionization.

4.6. References

1. Hutter, D.; Benner, S. A. Expanding the Genetic Alphabet: Non-Epimerizing Nucleoside with the pyDDA Hydrogen-Bonding Pattern. *J. Org. Chem.* **2003**, *68*, 9839– 9842, DOI: 10.1021/jo034900k
2. Hoshika, S.; Leal, N. A.; Kim, M.-J.; Kim, M.-S.; Karalkar, N. B.; Kim, H.-J.; Bates, A. M.; Watkins, N. E., Jr.; SantaLucia, H. A.; Meyer, A. J.Hachimoji DNA and RNA: A genetic system with eight building blocks. *Science* **2019**, *363*, 884– 887, DOI: 10.1126/science.aat0971
3. Kanvah, S.; Joseph, J.; Schuster, G. B.; Barnett, R. N.; Cleveland, C. L.; Landman, U. Oxidation of DNA: Damage to Nucleobases. *Acc. Chem. Res.* **2010**, *43*, 280– 287, DOI: 10.1021/ar900175a

4. O’Neill, M. A.; Barton, J. K. Sequence-Dependent DNA Dynamics: The Regulator of DNA-mediated Charge Transport. In *Charge Transfer in DNA: From Mechanism to Application*; Wagenknecht, H.-A., Ed.; Wiley-VCH: Weinheim, 2005; pp 27– 77
5. Meggers, E.; Dussy, A.; Schäfer, T.; Giese, B. Electron Transfer in DNA from Guanine and 8-Oxoguanine to a Radical Cation of the Carbohydrate Backbone. *Chem.—Eur. J.* **2000**, *6*, 485– 492, DOI: 10.1002/(sici)1521-3765(20000204)6:3<485::aid-chem485>3.0.co;2-a
6. Steenken, S.; Jovanovic, S. V. How Easily Oxidizable Is DNA? One-Electron Reduction Potentials of Adenosine and Guanosine Radicals in Aqueous Solution. *J. Am. Chem. Soc.* **1997**, *119*, 617– 618, DOI: 10.1021/ja962255b
7. Kobayashi, K.; Tagawa, S. Direct Observation of Guanine Radical Cation Deprotonation in Duplex DNA Using Pulse Radiolysis. *J. Am. Chem. Soc.* **2003**, *125*, 10213– 10218, DOI: 10.1021/ja036211w
8. Morozova, O. B.; Saprygina, N. N.; Fedorova, O. S.; Yurkovskaya, A. V. Deprotonation of Transient Guanosyl Cation Radical Catalyzed by Buffer in Aqueous Solution: TR-CIDNP Study. *Appl. Magn. Reson.* **2011**, *41*, 239– 250, DOI: 10.1007/s00723-011-0252-2
9. Morozova, O. B.; Fishman, N. N.; Yurkovskaya, A. V. Indirect NMR Detection of Transient Guanosyl Radical Protonation in Neutral Aqueous Solution. *Phys. Chem. Chem. Phys.* **2017**, *19*, 21262– 21266, DOI: 10.1039/c7cp03797j
10. Choi, J.; Yang, C.; Fujitsuka, M.; Tojo, S.; Ihee, H.; Majima, T. Proton Transfer of Guanine Radical Cations Studied by Time- Resolved Resonance Raman Spectroscopy Combined with Pulse Radiolysis. *J. Phys. Chem. Lett.* **2015**, *6*, 5045– 5050, DOI: 10.1021/acs.jpclett.5b02313

11. Bachler, V.; Hildenbrand, K. EPR-Detection of the Guanosyl Radical Cation in Aqueous Solution. Quantum Chemically Supported Assignment of Nitrogen and Proton Hyperfine Couplings. *Radiat. Phys. Chem.* **1992**, *40*, 59– 68, DOI: 10.1016/1359-0197(92)90141-2
12. Barnett, R. N.; Joseph, J.; Landman, U.; Schuster, G. B. Oxidative Thymine Mutation in DNA: Water-Wire-Mediated Proton-Coupled Electron Transfer. *J. Am. Chem. Soc.* **2013**, *135*, 3904– 3914, DOI: 10.1021/ja311282k
13. Wee, S.; O'Hair, R. A. J.; McFadyen, W. D. Can Radical Cations of the Constituents of Nucleic Acids Be Formed in the Gas Phase Using Ternary Transition Metal Complexes?. *Rapid Commun. Mass Spectrom.* **2005**, *19*, 1797– 1805, DOI: 10.1002/rcm.1988
14. Chu, I. K.; Rodriquez, C. F.; Lau, T.-C.; Hopkinson, A. C.; Siu, K. W. M. Molecular Radical Cations of Oligopeptides. *J. Phys. Chem. B* **2000**, *104*, 3393– 3397, DOI: 10.1021/jp994487d
15. Gatlin, C. L.; Turecek, F.; Vaisar, T. Copper(II) Amino Acid Complexes in the Gas Phase. *J. Am. Chem. Soc.* **1995**, *117*, 3637– 3638, DOI: 10.1021/ja00117a043
16. Gatlin, C. L.; Rao, R. D.; Tureček, F.; Vaisar, T. Carboxylate and Amine Terminus Directed Fragmentations in Gaseous Dipeptide Complexes with Copper(II) and Diimine Ligands Formed by Electrospray. *Anal. Chem.* **1996**, *68*, 263– 270, DOI: 10.1021/ac950884i
17. Dunbar, R. C. Photodissociation of Trapped Ions. *Int. J. Mass Spectrom.* **2000**, *200*, 571– 589, DOI: 10.1016/s1387-3806(00)00368-7
18. Laser Photodissociation and Spectroscopy of Mass Separated Biomolecular Ions. *Lecture Notes in Chemistry*; Polfer, N. C., Dugourd, P., Eds.; Springer: Cham, 2013; Vol. 83, pp 13– 20.
19. Huang, S. R.; Dang, A.; Tureček, F. Ground and Excited States of Gas-Phase DNA Nucleobase Cation-Radicals. A UV-Vis Photodisociation Action Spectroscopy and

Computational Study of Adenine and 9-Methyladenine. *J. Am. Soc. Mass Spectrom.* **2020**, *31*, 1271– 1281, DOI: 10.1021/jasms.0c00095

20. Feketeová, L.; Khairallah, G. N.; Chan, B.; Steinmetz, V.; Maître, P.; Radom, L.; O'Hair, R. A. J. Gas-Phase Infrared Spectrum and Acidity of the Radical Cation of 9-Methylguanine. *Chem. Commun.* **2013**, *49*, 7343– 7345, DOI: 10.1039/c3cc43244k
21. Dang, A.; Liu, Y.; Tureček, F. UV-Vis Action Spectroscopy of Guanine, 9-Methylguanine and 2'-Deoxyguanosine Cation Radicals in the Gas Phase. *J. Phys. Chem. A* **2019**, *123*, 3272– 3284, DOI: 10.1021/acs.jpca.9b01542
22. Lesslie, M.; Lawler, J. T.; Dang, A.; Korn, J. A.; Bím, D.; Steinmetz, V.; Maître, P.; Tureček, F.; Ryzhov, V. Cytosine Radical Cation: a Gas-Phase Study Combining IRMPD Spectroscopy, UV-PD Spectroscopy, Ion-Molecule Reactions, and Theoretical Calculations. *ChemPhysChem* **2017**, *18*, 1293– 1301, DOI: 10.1002/cphc.201700281
23. Dang, A.; Nguyen, H. T. H.; Ruiz, H.; Piacentino, E.; Ryzhov, V.; Tureček, F. Experimental Evidence for Non-Canonical Thymine Cation Radicals in the Gas Phase. *J. Phys. Chem. B* **2018**, *122*, 86– 97, DOI: 10.1021/acs.jpcb.7b09872
24. Dang, A.; Korn, J. A.; Gladden, J.; Mozzone, B.; Tureček, F. UV-Vis Photodissociation Action Spectroscopy on Thermo LTQ-XL ETD and Bruker amaZon Ion Trap Mass Spectrometers: A Practical Guide. *J. Am. Soc. Mass Spectrom.* **2019**, *30*, 1558– 1564, DOI: 10.1007/s13361-019-02229-z
25. Nguyen, H. T. H.; Shaffer, C. J.; Pepin, R.; Tureček, F. UV Action Spectroscopy of Gas-Phase Peptide Radicals. *J. Phys. Chem. Lett.* **2015**, *6*, 4722– 4727, DOI: 10.1021/acs.jpclett.5b02354
26. Frisch, M. J.; Trucks, G. W.; Schlegel, H. B.; Scuseria, G. E.; Robb, M. A.; Cheeseman, J. R.; Scalmani, G.; Barone, V.; Petersson, G. A.; Nakatsuji, H. et al.; *Gaussian 16*, Revision A03; Gaussian, Inc.: Wallingford, CT, 2016.

27. Becke, A. D. New Mixing of Hartree-Fock and Local Density-Functional Theories. *J. Chem. Phys.* **1993**, *98*, 1372– 1377, DOI: 10.1063/1.464304

28. Yanai, T.; Tew, D. P.; Handy, N. C. A New Hybrid Exchange-Correlation Functional Using the Coulomb-Attenuating Method (CAM-B3LYP). *Chem. Phys. Lett.* **2004**, *393*, 51– 57, DOI: 10.1016/j.cplett.2004.06.011

29. Zhao, Y.; Truhlar, D. G. The M06 Suite of Density Functionals for Main Group Thermochemistry, Thermochemical Kinetics, Noncovalent Interactions, Excited States, and Transition Elements: Two New Functionals and Systematic Testing of Four M06-Class Functionals and 12 Other Functionals. *Theor. Chem. Acc.* **2008**, *120*, 215– 241, DOI: 10.1007/s00214-007-0310-x

30. Cížek, J. On the Use of the Cluster Expansion and the Technique of Diagrams in Calculations of Correlation Effects in Atoms and Molecules. *Adv. Chem. Phys.* **1969**, *14*, 35– 89, DOI: 10.1002/9780470143599.ch2

31. Purvis, G. D., III; Bartlett, R. J. Full Coupled-Cluster Singles and Doubles Model–the Inclusion of Disconnected Triples. *J. Chem. Phys.* **1982**, *76*, 1910– 1918, DOI: 10.1063/1.443164

32. Halkier, A.; Helgaker, T.; Jørgensen, P.; Klopper, W.; Koch, H.; Olsen, J.; Wilson, A. K. Basis Set Convergence in Correlated Calculations on Ne, N_2, and H_2O. *Chem. Phys. Lett.* **1998**, *286*, 243– 252, DOI: 10.1016/s0009-2614(98)00111-0

33. Helgaker, T.; Klopper, W.; Koch, H.; Noga, J. Basis-Set Convergence of Correlated Calculations on Water. *J. Chem. Phys.* **1997**, *106*, 9639– 9646, DOI: 10.1063/1.473863

34. Dunning, T. H., Jr. Gaussian Basis Sets for Use in Correlated Molecular Calculations. I. The Atoms Boron through Neon and Hydrogen. *J. Chem. Phys.* **1989**, *90*, 1007– 1023, DOI: 10.1063/1.456153

35. Liu, Y.; Dang, A.; Urban, J.; Tureček, F. Charge-Tagged DNA Radicals in the Gas Phase Characterized by UV-Vis Photodissociation Action Spectroscopy. *Angew. Chem., Int. Ed.* **2020**, *59*, 7772– 7777, DOI: 10.1002/anie.201916493
36. Schlegel, H. B. Potential Energy Curves Using Unrestricted Møller-Plesset Perturbation Theory with Spin Annihilation. *J. Chem. Phys.* **1986**, *84*, 4530, DOI: 10.1063/1.450026
37. Mayer, I. Spin-Projected UHF Method. IV. Comparison of Potential Curves Given by Different One-Electron Methods. *Adv. Quantum Chem.* **1980**, *12*, 189– 262, DOI: 10.1016/s0065-3276(08)60317-2
38. Comeau, D. C.; Bartlett, R. J. The Equation-of-Motion Coupled-Cluster Method. Applications to Open- and Closed-Shell Reference States. *Chem. Phys. Lett.* **1993**, *207*, 414– 423, DOI: 10.1016/0009-2614(93)89023-b
39. Furche, F.; Ahlrichs, R. Adiabatic Time-Dependent Density Functional Methods for Excited State Properties. *J. Chem. Phys.* **2002**, *117*, 7433– 7447, DOI: 10.1063/1.1508368
40. Barbatti, M.; Ruckenbauer, M.; Plasser, F.; Pittner, J.; Granucci, G.; Persico, M.; Lischka, H. Newton-X: A Surface-Hopping Program for Nonadiabatic Molecular Dynamics. *Wiley Interdiscip. Rev. Comput. Mol. Sci.* **2014**, *4*, 26– 33, DOI: 10.1002/wcms.1158
41. Gilbert, R. G.; Smith, S. C. *Theory of Unimolecular and Recombination Reactions*; Blackwell Scientific Publications: Oxford, U.K., 1990; pp 52– 132
42. Zhu, L.; Hase, W. L. *Quantum Chemistry Program Exchange*; Indiana University: Bloomington, IN, 1994; Program no. QCPE 644.
43. Gregersen, J. A.; Tureček, F. Mass-Spectrometric and Computational Study of Tryptophan Radicals (Trp + H)• Produced by Collisional Electron Transfer to Protonated Tryptophan in the Gas Phase. *Phys. Chem. Chem. Phys.* **2010**, *12*, 13434– 13447, DOI: 10.1039/c0cp00597e

44. Clark, L. B.; Peschel, G. G.; Tinoco, I., Jr. Vapor Spectra and Heats of Vaporization of Some Purine and Pyrimidine Bases. *J. Phys. Chem.* **1965**, *69*, 3615– 3618, DOI: 10.1021/j100894a063
45. Reed, A. E.; Weinstock, R. B.; Weinhold, F. Natural Population Analysis. *J. Chem. Phys.* **1985**, *83*, 735– 746, DOI: 10.1063/1.449486
46. Yates, B. F.; Bouma, W. J.; Radom, L. Distonic radical cations. Guidelines for the assessment of their stability. *Tetrahedron* **1986**, *42*, 6225– 6234, DOI: 10.1016/s0040-4020(01)88084-4
47. Hammerum, S. Distonic Radical Cations in Gaseous and Condensed Phase. *Mass Spectrom. Rev.* **1988**, *7*, 123– 202, DOI: 10.1002/mas.1280070202
48. Wolken, J. K.; Yao, C.; Tureček, F.; Polce, M. J.; Wesdemiotis, C. Cytosine Neutral Molecules and Cation-Radicals in the Gas Phase. Structure, Energetics, Ion Chemistry, and Neutralization-Reionization Mass Spectrometry. *Int. J. Mass Spectrom.* **2007**, *267*, 30– 42, DOI: 10.1016/j.ijms.2007.02.016
49. Goeringer, D. E.; McLuckey, S. A. Evolution of Ion Internal Energy during Collisional Excitation in the Paul Ion Trap: A Stochastic Approach. *J. Chem. Phys.* **1996**, *104*, 2214– 2221, DOI: 10.1063/1.471812
50. Gronert, S. Estimation of Effective Ion Temperatures in a Quadrupole Ion Trap. *J. Am. Soc. Mass Spectrom.* **1998**, *9*, 845– 848, DOI: 10.1016/s1044-0305(98)00055-5
51. Lovejoy, E. R.; Wilson, R. R. Kinetic Studies of Negative Ion Reactions in a Quadrupole Ion Trap: Absolute Rate Coefficients and Ion Energies. *J. Phys. Chem. A* **1998**, *102*, 2309– 2315, DOI: 10.1021/jp973391l
52. Donald, W. A.; Khairallah, G. N.; O'Hair, R. A. J. The Effective Temperature of Ions Stored in a Linear Quadrupole Ion Trap Mass Spectrometer. *J. Am. Soc. Mass Spectrom.* **2013**, *24*, 811– 815, DOI: 10.1007/s13361-013-0625-x

53. Blas, J. R.; Luque, F. J.; Orozco, M. Unique Tautomeric Properties of Isoguanine. *J. Am. Chem. Soc.* **2004**, *126*, 154– 164, DOI: 10.1021/ja036806r

54. Guthrie, J. P. Thermodynamics of Enols. In *The Chemistry of Enols*; Rappoport, Z.; Ed.; John Wiley and Sons: Chichester, 1990; Chapter 2, pp 75– 94

55. Turecek, F. The Chemistry of Ionized Enols in the Gas Phase. In *The Chemistry of Enols*; Rappoport, Z., Ed.; John Wiley and Sons: Chichester, 1990; Chapter 3, pp 95– 146.

56. Turecek, F.; Cramer, C. J. Thermochemistry of Simple Enols and Enol Cation-Radicals Revisited. A G2(MP2) ab Initio Study. *J. Am. Chem. Soc.* **1995**, *117*, 12243– 12253, DOI: 10.1021/ja00154a026

57. Dougherty, D.; Wittel, K.; Meeks, J.; McGlynn, S. P. Photoelectron Spectroscopy of Carbonyls. Ureas, Uracils, and Thymine. *J. Am. Chem. Soc.* **1976**, *98*, 3815– 3820, DOI: 10.1021/ja00429a013

58. Orlov, V. M.; Smirnov, A. N.; Varshavsky, Y. M. Ionization Potentials of the Nitrogen Bases of Nucleic Acids and Some of Their Analogs. *Tetrahedron Lett.* **1976**, *17*, 4377, DOI: 10.1016/0040-4039(76)80120-7

59. Dougherty, D.; Younathan, E. S.; Voll, R.; Abdulnur, S.; McGlynn, S. P. Photoelectron Spectroscopy of Some Biological Molecules. *J. Electron Spectrosc. Relat. Phenom.* **1978**, *13*, 379– 393, DOI: 10.1016/0368-2048(78)85042-7

60. Choi, K.-W.; Lee, J.-H.; Kim, S. K. Ionization Spectroscopy of a DNA Base: Vacuum-Ultraviolet Mass-Analyzed Threshold Ionization Spectroscopy of Jet-Cooled Thymine. *J. Am. Chem. Soc.* **2005**, *127*, 15674– 15675, DOI: 10.1021/ja055018u

61. Trofimov, A. B.; Schirmer, J.; Kobychev, V. B.; Potts, A. W.; Holland, D. M. P.; Karlsson, L. Photoelectron Spectra of the Nucleobases Cytosine, Thymine and Adenine. *J. Phys. B: At., Mol. Opt. Phys.* **2006**, *39*, 305– 329, DOI: 10.1088/0953-4075/39/2/007

62. Fulfer, K. D.; Hardy, D.; Aguilar, A. A.; Poliakoff, E. D. High- Resolution Photoelectron Spectra of the Pyrimidine-Type Nucleobases. *J. Chem. Phys.* **2015**, *142*, 224310, DOI: 10.1063/1.4922310
63. Majdi, Y.; Hochlaf, M.; Pan, Y.; Lau, K.-C.; Poisson, L.; Garcia, G. A.; Nahon, L.; Al-Mogren, M. M.; Schwell, M. Theoretical and Experimental Photoelectron Spectroscopy Characterization of the Ground State of Thymine Cation. *J. Phys. Chem. A* **2015**, *119*, 5951– 5958, DOI: 10.1021/jp510716c
64. Crespo-Hernández, C. E.; Arce, R.; Ishikawa, Y.; Gorb, L.; Leszczynski, J.; Close, D. M. Ab Initio Ionization Energy Thresholds of DNA and RNA Bases in Gas Phase and in Aqueous Solution. *J. Phys. Chem. A* **2004**, *108*, 6373– 6377, DOI: 10.1021/jp049270k
65. Roca-Sanjuan, D.; Rubio, M.; Merchan, M.; Serrano-Andres, L. Ab initio Determination of the Ionization Potentials of DNA and RNA Nucleobases. *J. Chem. Phys.* **2006**, *125*, 084302, DOI: 10.1063/1.2336217
66. Colson, A. O.; Besler, B.; Sevilla, M. D. Ab initio Molecular Orbital Calculations on DNA Base Pair Radical Ions: Effect of Base Pairing on Proton-Transfer Energies, Electron Affinities, and Ionization Potentials. *J. Phys. Chem.* **1992**, *96*, 9787– 9794, DOI: 10.1021/j100203a039
67. Bertran, J.; Oliva, A.; Rodríguez-Santiago, L.; Sodupe, M. Single versus Double Proton-Transfer Reactions in Watson-Crick Base Pair Radical Cations. A Theoretical Study. *J. Am. Chem. Soc.* **1998**, *120*, 8159– 8167, DOI: 10.1021/ja9804417
68. Li, X.; Cai, Z.; Sevilla, M. D. Energetics of the Radical Ions of the AT and AU Base Pairs: A Density Functional Theory (DFT) Study. *J. Phys. Chem. A* **2002**, *106*, 9345– 9351, DOI: 10.1021/jp021322n
69. Ghosh, D.; Isayev, O.; Slipchenko, L. V.; Krylov, A. I. Effect of Solvation on the Vertical Ionization Energy of Thymine: From Microhydration to Bulk. *J. Phys. Chem. A* **2011**, *115*, 6028– 6038, DOI: 10.1021/jp110438c

70. Pluhařová, E.; Jungwirth, P.; Bradforth, S. E.; Slavíček, P. Ionization of Purine Tautomers in Nucleobases, Nucleosides, and Nucleotides: From the Gas Phase to the Aqueous Environment. *J. Phys. Chem. B* **2011**, *115*, 1294– 1305, DOI: 10.1021/jp110388v

71. Zhang, Y.; Xie, P.; Yang, S.; Han, K. Ionization and Electron Attachment for Nucleobases in Water. *J. Phys. Chem. B* **2019**, *123*, 1237– 1247, DOI: 10.1021/acs.jpcb.8b09435

4.7. Appendix

Table 1. Relative Energies of Methylcytosine Cation Radicals.

	Relative energy^{a,b}				
Ion/reaction	M06-2X/ 6-31+G(d,p)	M06-2X/ 6-311++G(2d,p)	CCSD(T)^{c,d}/ aug-cc-pVTZ	CCSD(T)^{c,d}/ aug-cc-pVQZ	CCSD(T)^{c,e}/ CBS
1$^{+\bullet}$	0	0	0	0	0
2$^{+\bullet}$	3.1	5.5	–1.4	–1.1	–1.2
3$^{+\bullet}$	13	18	18	19	18
4$^{+\bullet}$	29	31	31	32	31
5$^{+\bullet}$	220	219			
6$^{+\bullet}$	200	200			
7$^{+\bullet}$	132	133	122	126	125
8$^{+\bullet}$	–26	–26	–22	–24	–25
9$^{+\bullet}$	–66	–62	–55	–58	–59
10$^{+\bullet}$	–63	–59	–53	–56	–56
11$^{+\bullet}$	57	59	61	60	60
1$^{+\bullet}$ → **TS1**	180	183	174	174	174
1$^{+\bullet}$ → **TS2**	90	94	90	90	90
9$^{+\bullet}$ → **TS3**	162	163	157	157	155
9$^{+\bullet}$ → **TS**$_{\mathbf{rot}}$	42	40	39	40	40
10$^{+\bullet}$ → **TS4**	202	203	200	202	201

[a] In kJ mol^{-1}. [b] Including B3LYP/6-31+G(d,p) zero-point energies and referring to 0 K. Single-point energies on M06-2X/6-31+G(d,p) optimized geometries. [c] Single-point calculations on M06-2X/6-31+G(d,p) optimized geometries. [d] Extrapolated to the larger basis set according to the formula: E[CCSD(T)/aug-cc-pVXZ] ≅ E[CCSD(T)/aug-cc-pVDZ] + E[MP2/aug-cc-pVXZ] – E[MP2/aug-cc-pVDZ]. [e] Extrapolated to the complete basis set according to the formula: E[CCSD(T)/CBS] ≅ E[CCSD(T)/aug-cc-pVDZ] – E[MP2/aug-cc-pVDZ] + E[HF/aug-cc-pVQZ] + $E_{\mathrm{corr}}(\mathrm{HF}, X \rightarrow \infty)$.

Table 2. Binding energies of [Cu(tpy)**S**]$^{2+\bullet}$ complexes in the gas phase.

	Binding energy^{a,b}	
Complex	ΔH_0	ΔG_{310}
[Cu(tpy)**1**]$^{2+\bullet}$ → **1**$^{+\bullet}$ + [Cu(tpy)]$^{+}$	129 (258)^{c}	72 (201)^{c}
[Cu(tpy)**2**]$^{2+\bullet}$ → **2**$^{+\bullet}$ + [Cu(tpy)]$^{+}$	–25	–79
[Cu(tpy)**3**]$^{2+\bullet}$ → **3**$^{+\bullet}$ + [Cu(tpy)]$^{+}$	21	–29
[Cu(tpy)**9**]$^{2+\bullet}$ → **9**$^{+\bullet}$ + [Cu(tpy)]$^{+}$	–199	–249

[a] In kJ mol^{-1}. [b] Including CAM-B3LYP/6-311+G(2d,p) zero-point energies (ΔH_0), and 310 K enthalpies and entropies (ΔG_{310}). [c] Including solvation energies in water dielectric.

Table 3. Relative Energies of Isoguanine Cation Radicals.

	Relative energy^{a,b}				
Ion	M06-2X/ 6-31+G(d,p)	M06-2X/ 6-311++G(2d,p)	CCSD(T)/ aug-cc-pVTZ	CCSD(T)/ aug-cc-pVQZ	CCSD(T)/ CBS
12$^{+\bullet}$	0	0	0	0	0
13$^{+\bullet}$	–2.2	–3.2	0.0	–2.0	0.5
14$^{+\bullet}$	1.0	–0.6	2.5	0.6	1.5
15$^{+\bullet}$	43	40	39	36	36
16$^{+\bullet}$	29	29	28		
17$^{+\bullet}$	56	52	49		
18$^{+\bullet}$	67	64	62		
19$^{+\bullet}$	53	49	49		
20$^{+\bullet}$	50	46	45		
21$^{+\bullet}$	60	57			
22$^{+\bullet}$	76	78			
23$^{+\bullet}$	110	107			

[a] In kJ mol^{-1}. [b] Including B3LYP/6-31+G(d,p) zero-point energies and referring to 0 K. Single-point energies on M06-2X/6-31+G(d,p) optimized geometries. [c] Single-point calculations on M06-2X/6-31+G(d,p) optimized geometries. [d] Extrapolated to the larger basis set according to the formula: E[CCSD(T)/aug-cc-pVXZ] ≅ E[CCSD(T)/aug-cc-pVDZ] + E[MP2/aug-cc-pVXZ] – E[MP2/aug-cc-pVDZ]. [e] Extrapolated to the complete basis set according to the formula: E[CCSD(T)/CBS] ≅ E[CCSD(T)/aug-cc-pVDZ] – E[MP2/aug-cc-pVDZ] + E[HF/aug-cc-pVQZ] + $E_{\mathrm{corr}}(\mathrm{HF}, X \rightarrow \infty)$.

Table 4. Adiabatic Recombination Energies of Selected Nucleobase Cation Radicals.

	Recombination Energy^{a,b}			
Ion	M06-2X/ 6-311++G(2d,p)	CCSD(T)/ aug-cc-pVTZ	CCSD(T)/ aug-cc-pVQZ	CCSD(T)/ CBS
1$^{+\bullet}$	8.48	8.42	8.49	8.51
2$^{+\bullet}$	8.41	8.33	8.40	8.42
9$^{+\bullet}$	5.57	5.63	5.67	5.70
10$^{+\bullet}$	5.73	5.85	5.89	5.92
12$^{+\bullet}$	7.69	7.65	7.74	7.76
13$^{+\bullet}$	7.99	7.97	8.05	8.10
14$^{+\bullet}$	8.01	8.00	8.07	8.10
15$^{+\bullet}$	8.13	8.08	8.14	8.16
Adenine$^{+\bullet}$	8.25^{c}	8.28	8.33	8.32
Guanine$^{+\bullet}$	7.82^{d}	7.90	7.95	7.91
	7.85^{e}	7.90	7.95	7.97
Thymine$^{+\bullet}$	8.88^{f}	8.91	8.94	8.98
	5.71^{g}	5.77	5.77	5.80

---

[a] Absolute values in electron volts. [b] Including zero-point energies and referring to 0 K. [c] Most stable N-9-H tautomer (ref. 19). [d] 6-oxo-N-1-H tautomer. [e] 6-OH tautomer. [f] 2,4-dioxo-5-methyl tautomer. [g] 2,4-OH-5-CH_2 tautomer.

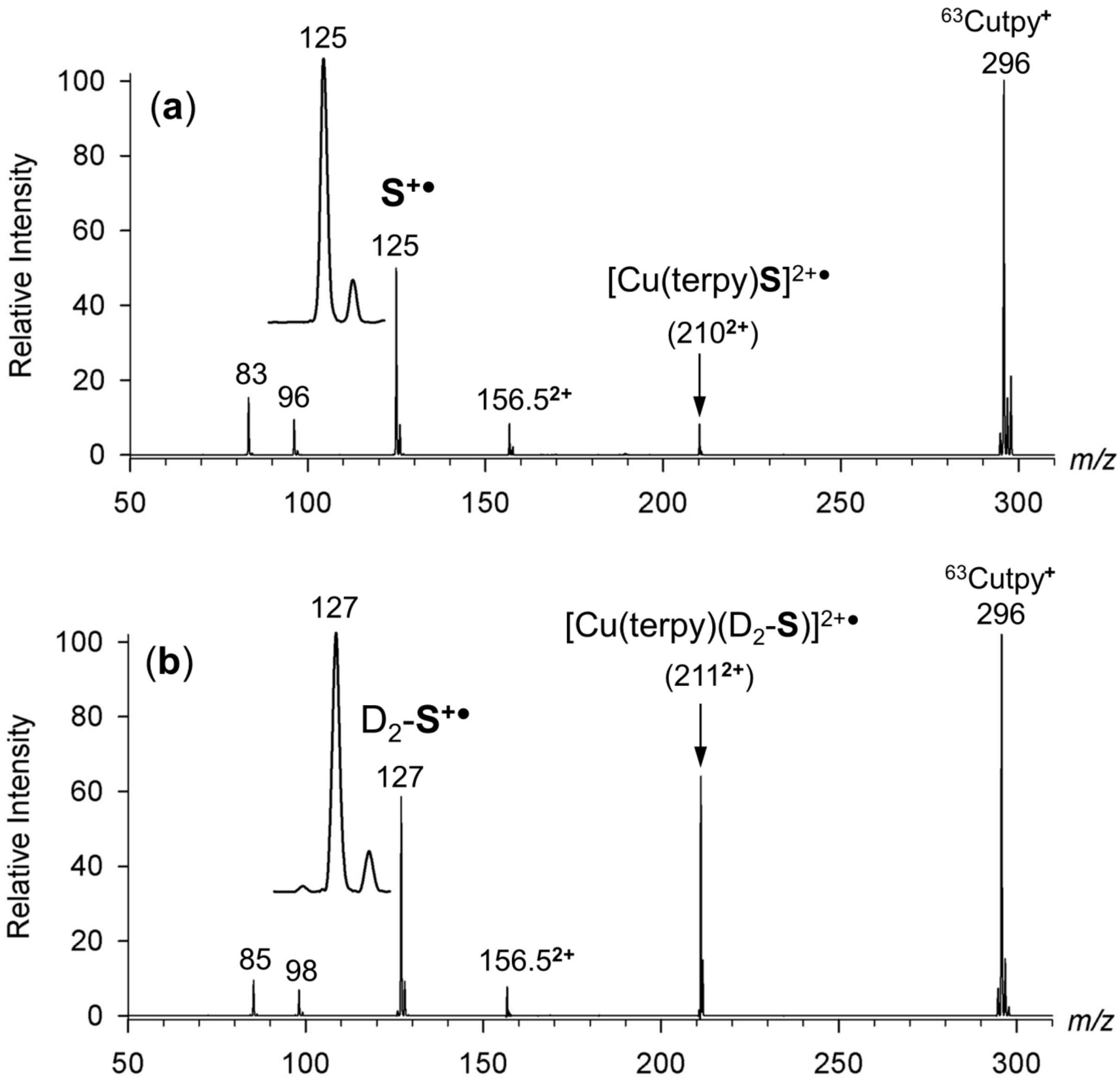

Figure 1. CID-MS^2 spectra of (a) [^{63}Cu(tpy)S]$^{2+•}$ (m/z 210) and (b) [^{63}Cu(tpy)D$_2$-S]$^{2+•}$ (m/z 211). Insets show the cation-radical peak profiles.

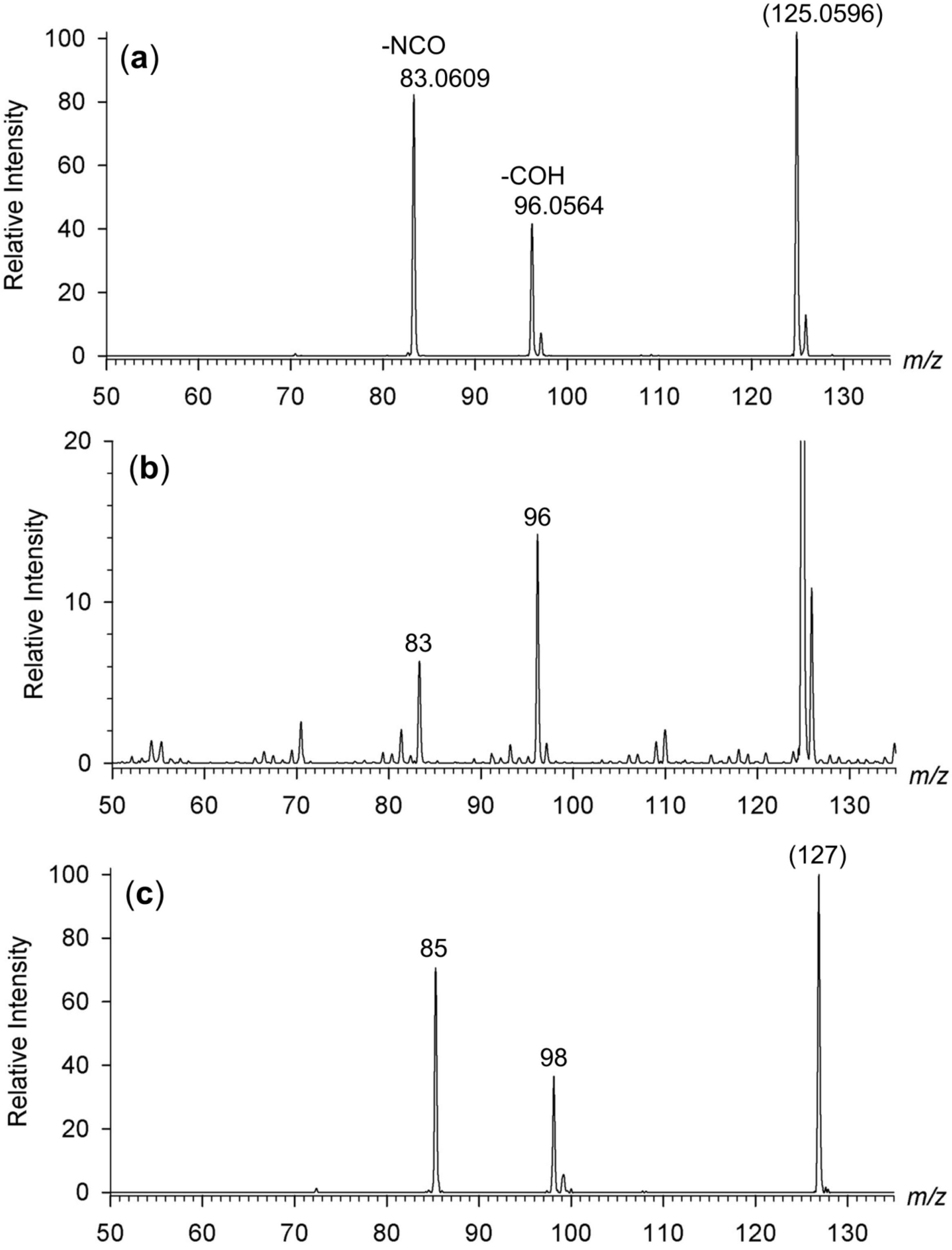
(a)
Relative Intensity
100
80
60
40
20
0
-NCO
83.0609
-COH
96.0564
(125.0596)
50
60
70
80
90
100
110
120
130
m/z
(b)
Relative Intensity
20
10
0
83
96
50
60
70
80
90
100
110
120
130
m/z
(c)
Relative Intensity
100
80
60
40
20
0
85
98
(127)
50
60
70
80
90
100
110
120
130
m/z

Figure 2. (a) CID-MS3 spectrum of $S^{+\bullet}$ (m/z 125) with accurate m/z values from high-resolution mass measurements. (b) UVPD spectrum of $S^{+\bullet}$ at 270 nm; (c) CID-MS^3 spectrum of D_2-$S^{+\bullet}$ (m/z 127).

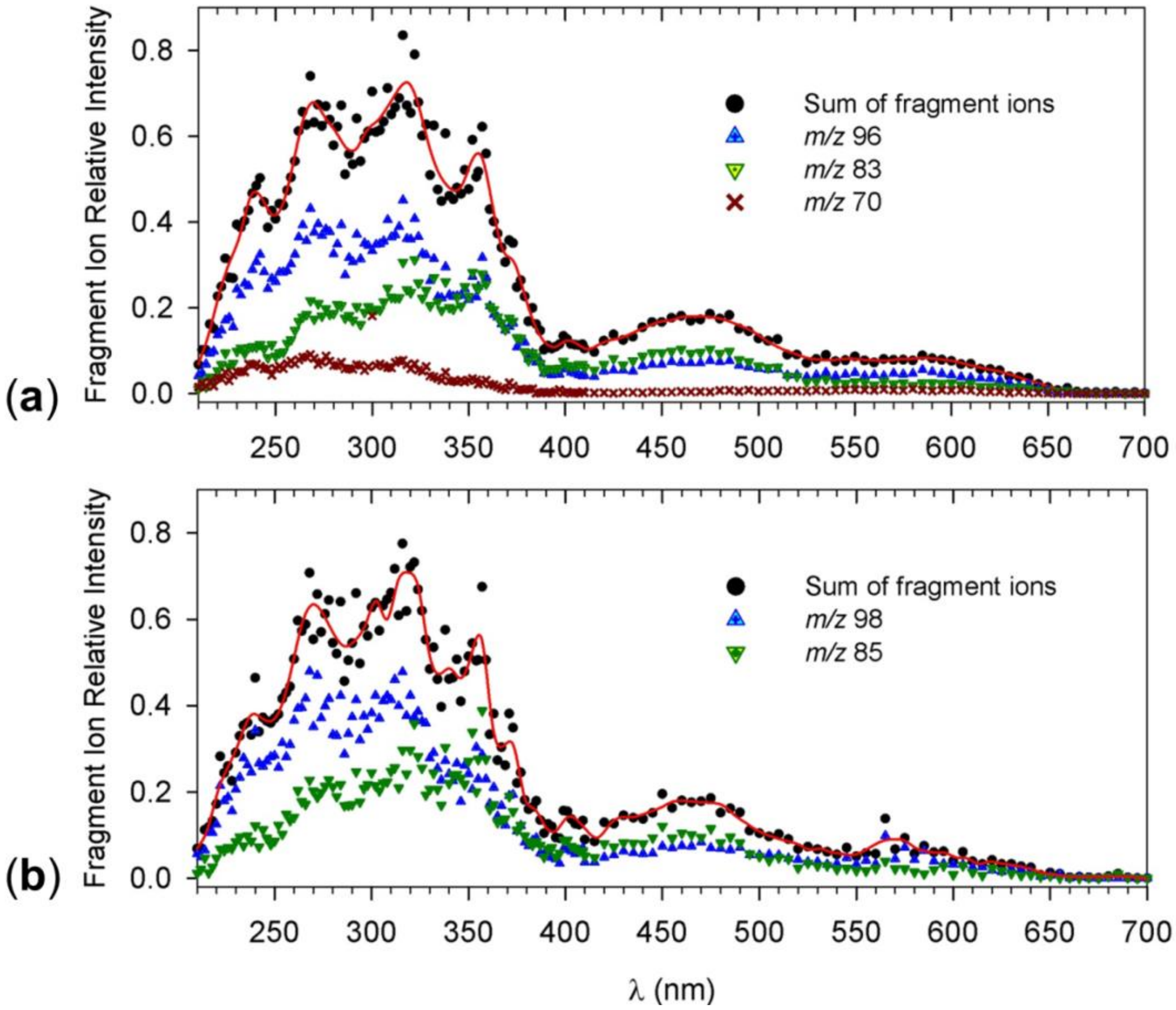

Figure 3. Mass-resolved UVPD action spectra of (a) $S^{+\bullet}$; (b) D_2-$S^{+\bullet}$.

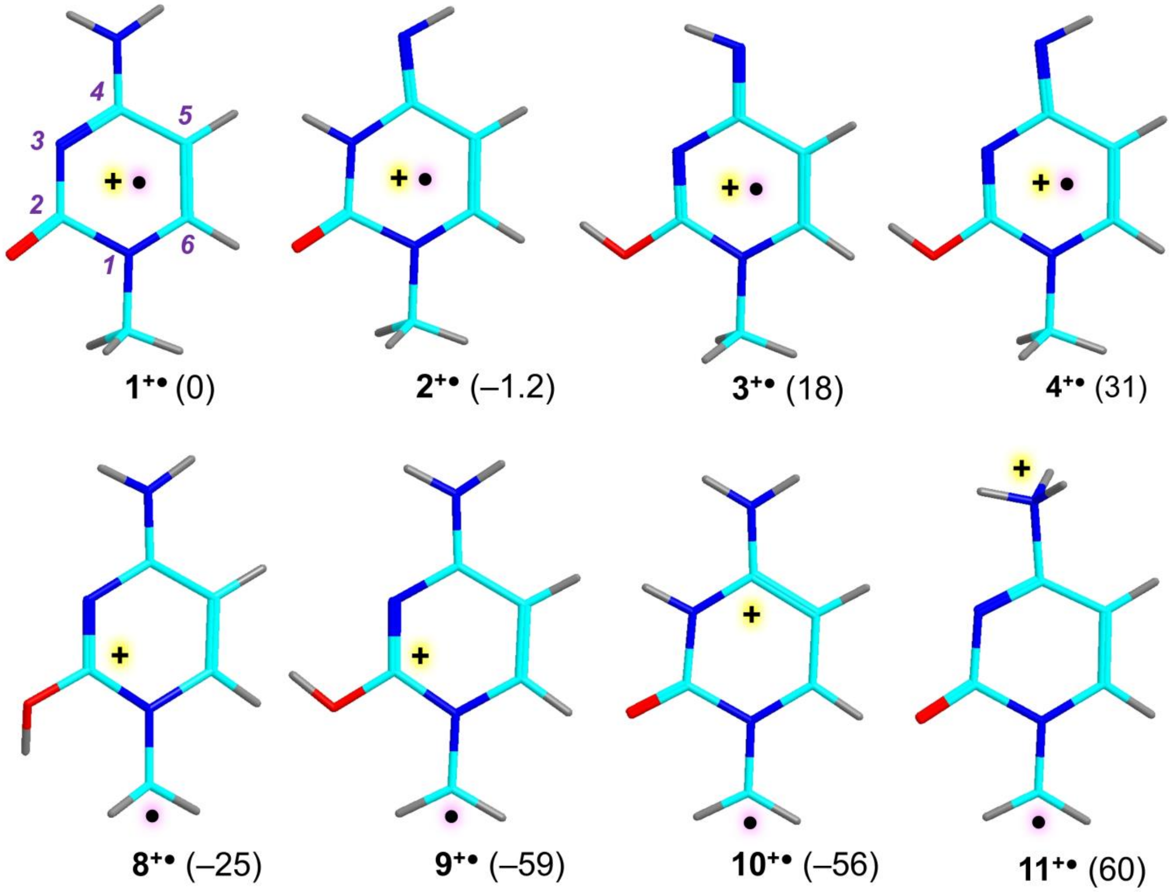

1$^{+\bullet}$ (0) **2**$^{+\bullet}$ (–1.2) **3**$^{+\bullet}$ (18) **4**$^{+\bullet}$ (31)

8$^{+\bullet}$ (–25) **9**$^{+\bullet}$ (–59) **10**$^{+\bullet}$ (–56) **11**$^{+\bullet}$ (60)

Figure 4. M06-2X/6-31+G(d,p) optimized structures of isomeric S$^{+\bullet}$ ions. Atom color coding is as follows: cyan = C, blue = N, red = O, gray = H. Values in parentheses are relative energies (ΔH_0, kJ mol^{-1}) from CCSD(T)/CBS single-point calculations.

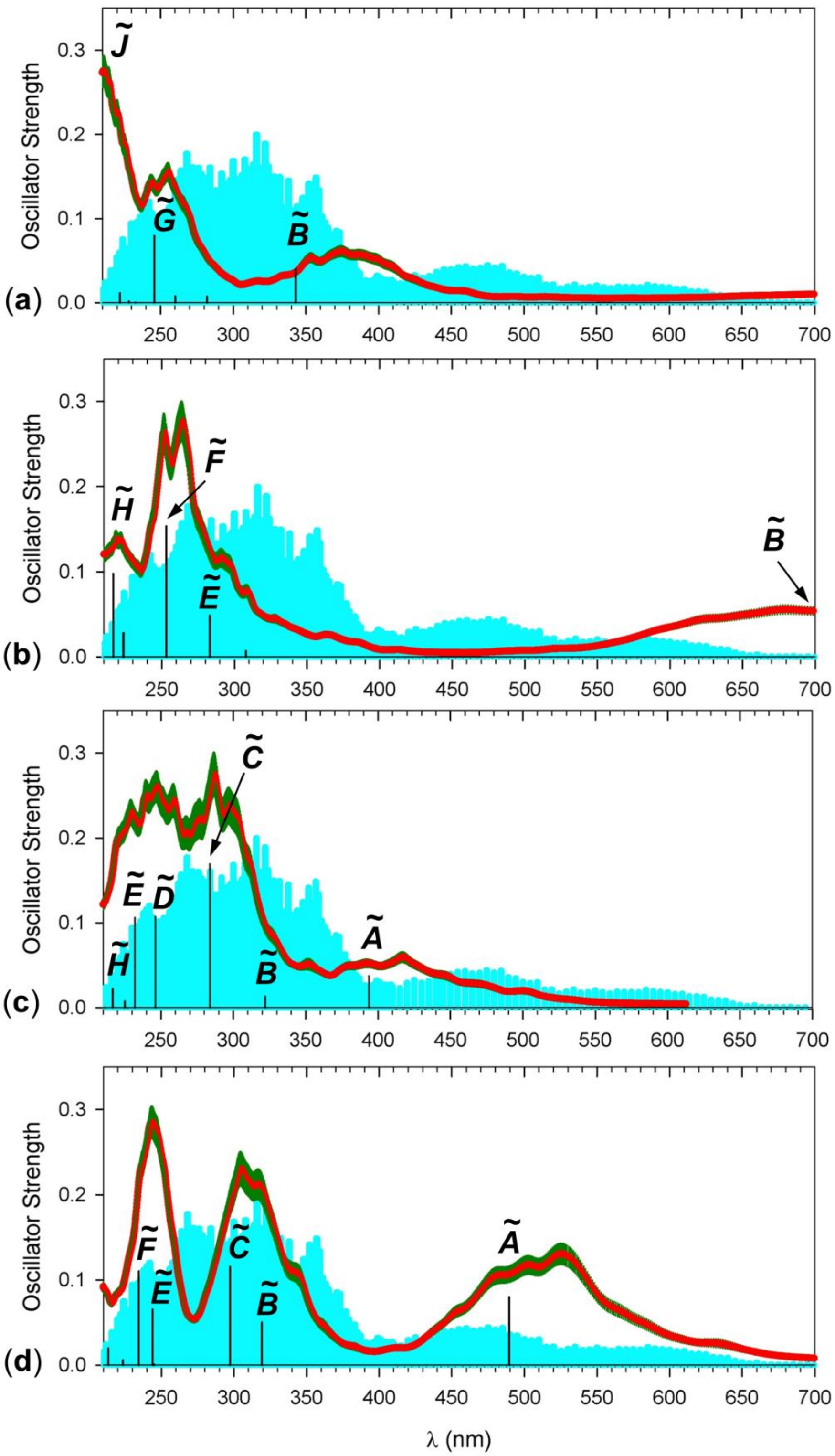

Figure 5. Calculated vibronic absorption spectra of (a) $1^{+\bullet}$, (b) $2^{+\bullet}$, (c) $9^{+\bullet}$, and (d) $10^{+\bullet}$ from TD-DFT M06-2X/6-31+G(d,p) calculations of 300 ground-state configurations. Black vertical bars

show the 0 K transitions. The cyan background shows the overlaid action spectrum of S$^{+\bullet}$ that was scaled to fit the format.

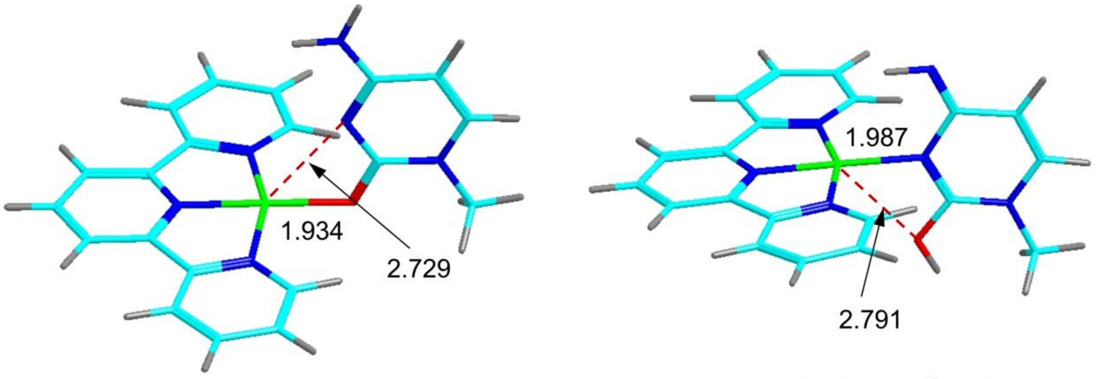

[Cu(tpy)**1**]$^{2+\bullet}$ (0, *0*)

[Cu(tpy)**2**]$^{2+\bullet}$ (172, *128*)

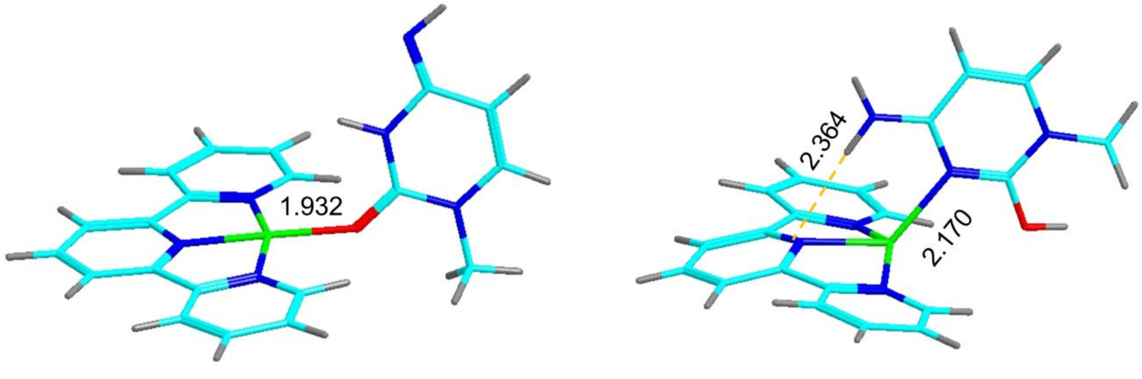

[Cu(tpy)**3**]$^{2+\bullet}$ (101, *61*)

[Cu(tpy)**9**]$^{2+\bullet}$ (264, *228*)

Figure 6. CAM-B3LYP/6-311+G(2d,p) optimized structures of [Cu(tpy)S]$^{2+\bullet}$ complexes. Atom color coding is as follows: cyan = C, blue = N, red = O, gray = H, light green = Cu. The Cu–N and Cu–O bond lengths are in Angstrøms. Values in parentheses are relative free energies (ΔG_{310}, kJ mol^{-1}) in the gas phase (roman characters) and aqueous solution (italics) from CAM-B3LYP/6-311+G(2d,p) calculations.

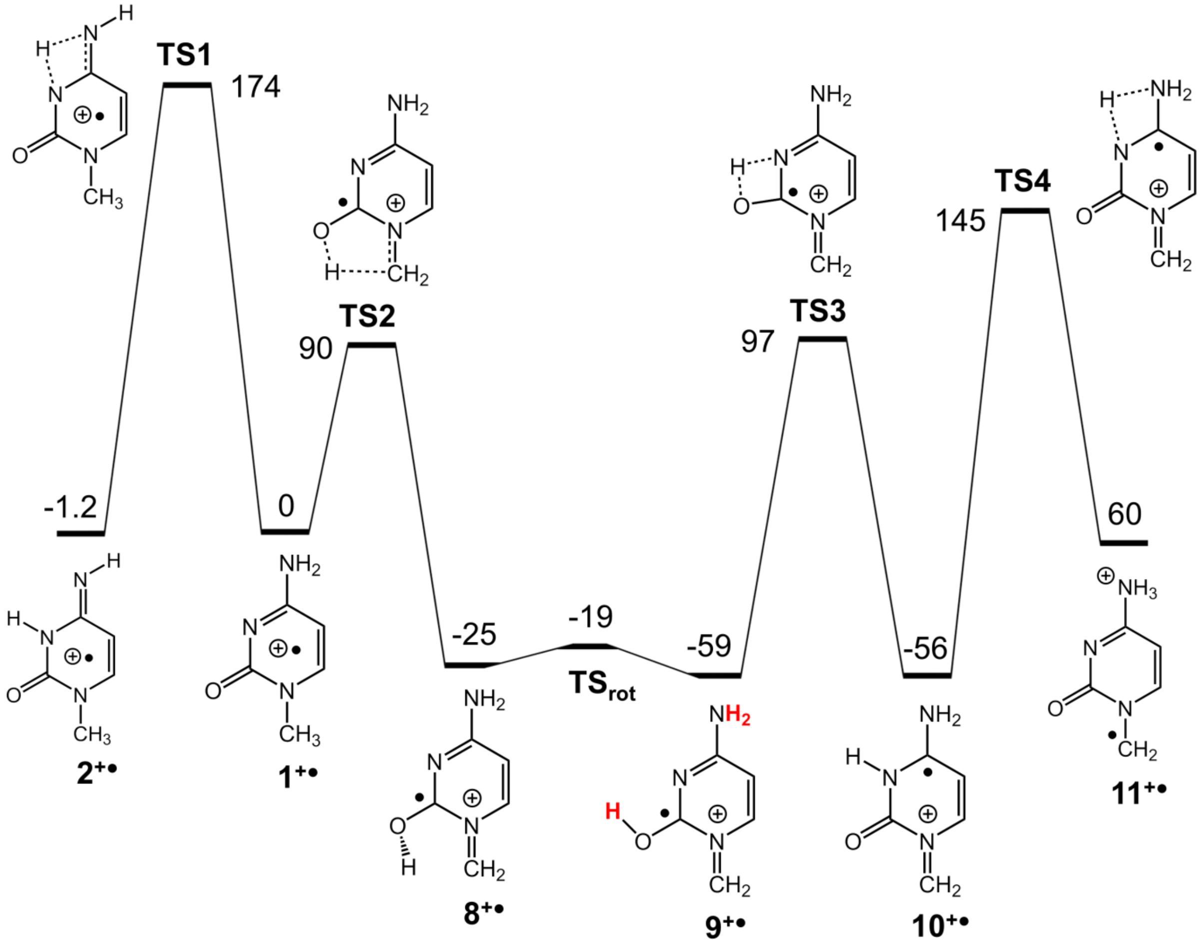

Figure 7. CCSD(T)/CBS PES for isomerizations of S$^{+•}$. The energies, ΔH_0 in kJ mol^{-1}, are relative to that of 1$^{+•}$.

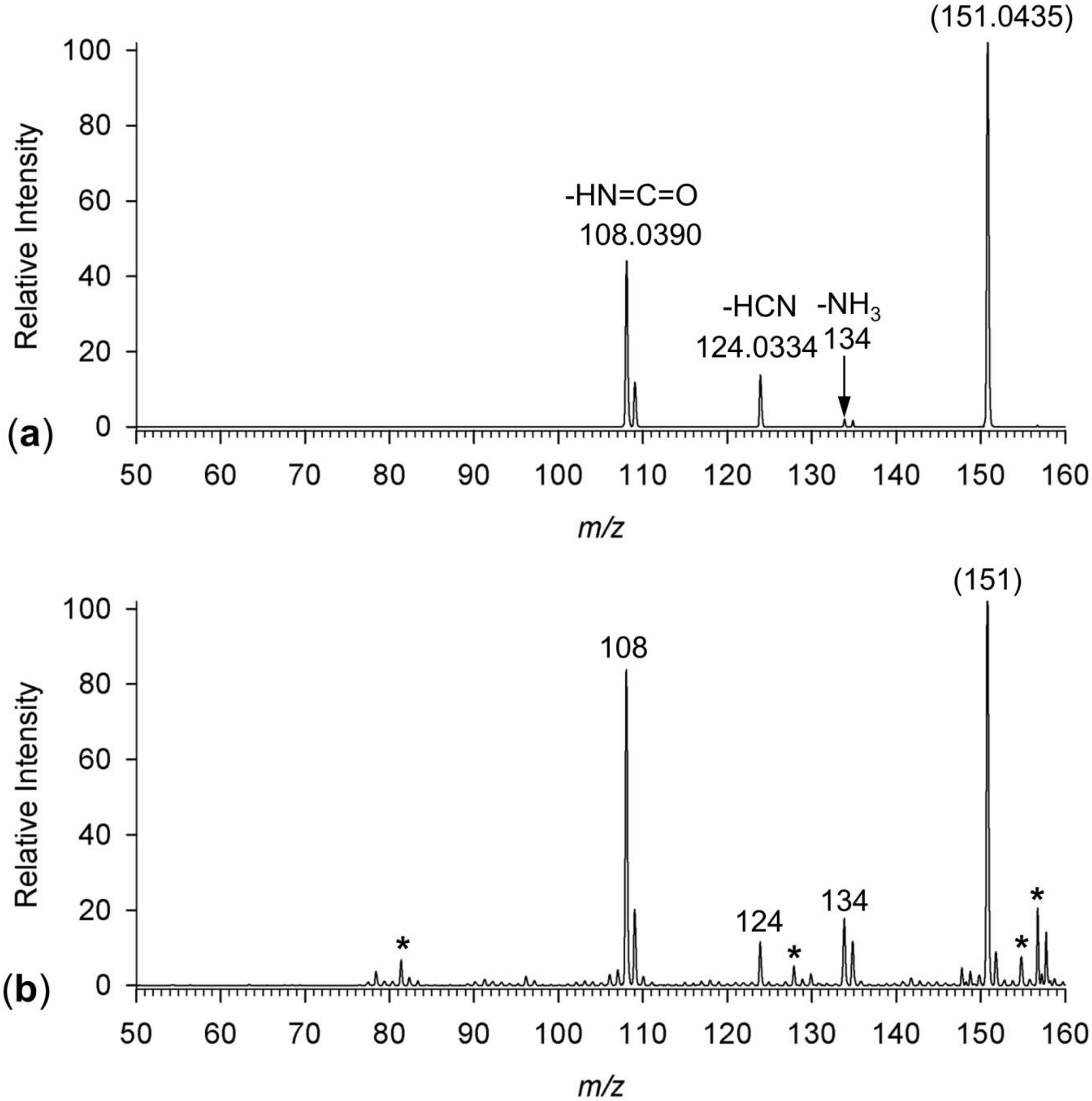

Figure 8. (a) CID-MS^3 spectrum of $B^{+\bullet}$ (m/z 151) with accurate m/z values from high-resolution mass measurements. (b) UVPD spectrum of $B^{+\bullet}$ at 310 nm. Asterisks denote background peaks from photodesorption/ionization.

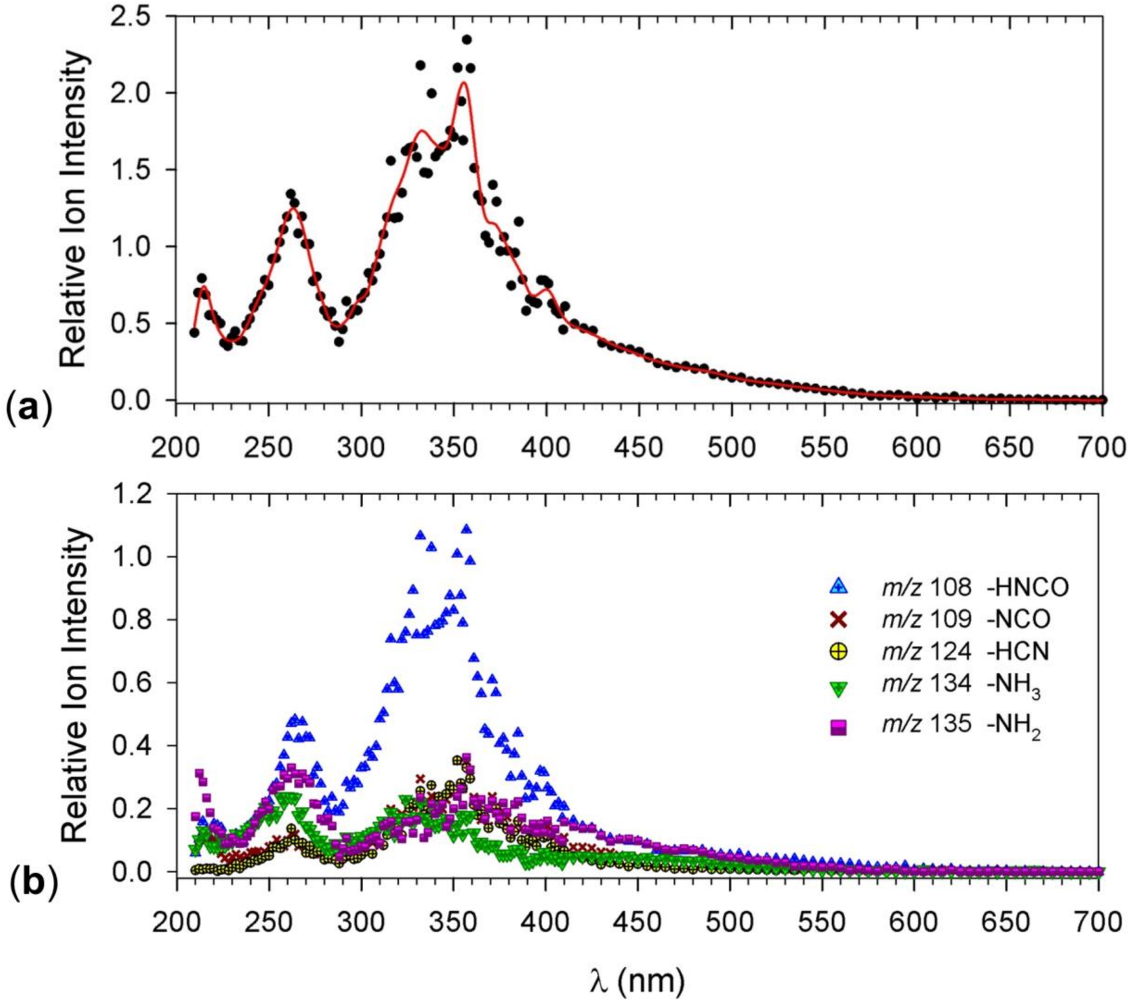

Figure 9. UVPD action spectra of $B^{+\bullet}$. (a) Overall profile of the sum of fragment ion intensities. (b) Mass-resolved fragment ion channels.

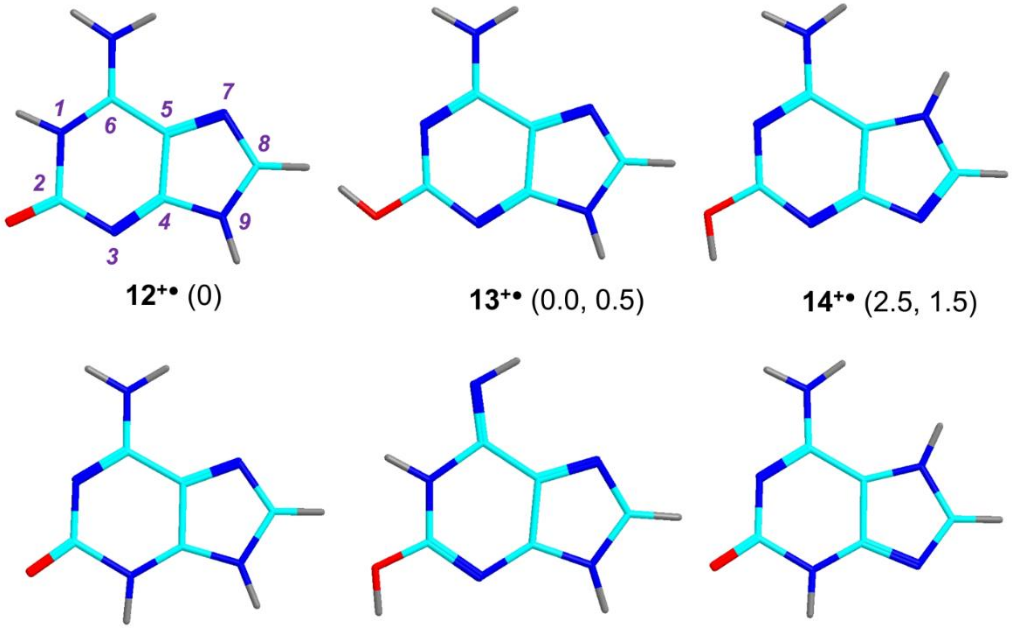

$12^{+\bullet}$ (0)

$13^{+\bullet}$ (0.0, 0.5)

$14^{+\bullet}$ (2.5, 1.5)

$15^{+\bullet}$ (39, 36)

$16^{+\bullet}$ (28)

$17^{+\bullet}$ (49)

Figure 10. M06-2X/6-31+G(d,p) optimized structures of isoguanine cation radicals $12^{+\bullet}$-$17^{+\bullet}$. Atom color coding is as in Figure 4. Values in parentheses are relative energies (ΔH_0, kJ mol^{-1}) from effective CCSD(T)/aug-cc-pVTZ and CBS-extrapolated single-point calculations.

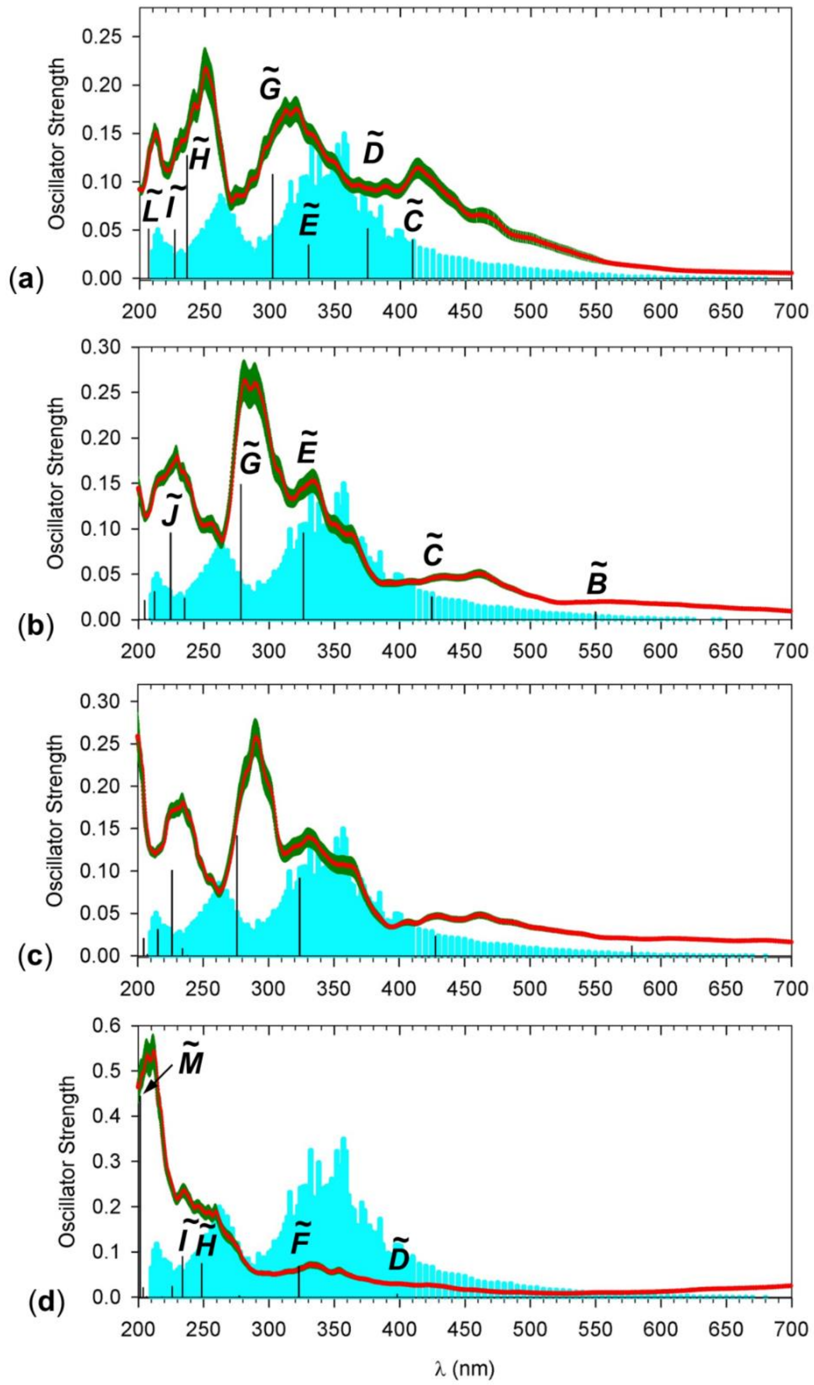

Figure 11. M06-2X/6-31+G(d,p) vibronic absorption spectra of (a) $12^{+\bullet}$, (b) $13^{+\bullet}$, (c) $14^{+\bullet}$, and (d) $15^{+\bullet}$ from TD-DFT M06-2X/6-31+G(d,p) calculations of 300 ground-state configurations. Black vertical bars show the 0 K transitions. Cyan background shows the overlaid action spectrum of $B^{+\bullet}$ that was scaled to fit the format.

Chapter 5—Cation Radicals of Hachimoji Nucleobase P and Z: Generation in the Gas Phase and Characterization by UV-Vis Photodissociation Action Spectroscopy and Theory

Reproduced in part with permission from S.R. Huang, F. Tureček, *J. Am. Soc. Mass Spectrom.*, **2021**, 32, 373-386, DOI: 10.1021/jasms.0c00381.

5.1. Abstract

We report the generation of gas-phase cation radicals of unusual nucleobases 5-aza-7-deazaguanine (P) and 6-amino-5-nitro-(1H)pyrid-2-one (Z) that have been used as building blocks of base-expanded (hachimoji) DNA. The cation radicals were generated by collision-induced intramolecular electron transfer and dissociation of ternary copper-terpyridine complexes. The cation radicals were characterized by deuterium labeling and tandem mass spectrometry including MS3 collision-induced dissociation, UV–vis photodissociation, and action spectroscopy. Vibronic absorption UV-vis spectra were calculated by time-dependent density functional theory (TD-DFT) and compared with the action spectra to unequivocally assign the most closely matching structures for the gas-phase cation radicals. Ab initio calculations up to the coupled clusters–complete basis set (CCSD(T)/CBS) level of theory were used to rank by energy the P and Z neutral molecules and cation-radical isomers and provided transition-state and dissociation energies. The 5-aza-7-deazaguanine cation radicals were determined to have the canonical N-1-H, 6-oxo structure (**P1**$^{+\bullet}$) that was the global energy minimum within this group of isomers. The Z cation radicals were found to have the 1H-pyrid-2-one structure (**Z1**$^{+\bullet}$). The formation of **P1**$^{+\bullet}$ and **Z1**$^{+\bullet}$ was shown to be controlled by the solution thermodynamics of the Cu-terpyridine complexes and the kinetics of their dissociations. We also report and compare CCSD(T)/CBS-calculated adiabatic recombination energies of cation radicals for the entire hachimoji set of eight nucleobases, **P**$^{+\bullet}$ (7.92 eV), **Z**$^{+\bullet}$ (8.51 eV), **S**$^{+\bullet}$ (8.51 eV), **B**$^{+\bullet}$ (7.76 eV), **T**$^{+\bullet}$ (8.98 eV), **C**$^{+\bullet}$ (8.62 eV), **A**$^{+\bullet}$ (8.32 eV), and **G**$^{+\bullet}$ (7.97 eV), to assess the thermodynamics of base-to-base electron transfer following random ionization.

5.2. Introduction

Structurally modified DNA and RNA nucleobases[1,2] have a long history of development and use as components of cytotoxic antimetabolites for treating cancer[3] and as potent antivirals,[4-7] that extends back to the late 1950's when Prusoff[8] and Kaufman and Heidelberger[9] reported the synthesis of biologically active modified deoxyuridines. Modified nucleobases have also been recognized as having anti-parasite activity.[10] A novel application of modified DNA nucleobases has been pursued by Benner and coworkers in the development of artificially expanded genetic information systems.[11] The artificial nucleobases are designed to be orthogonal to the natural ones, adenine (A), guanine (G), cytosine (C) and thymine (T), in that they pair by specific hydrogen bonds with each other without pairing with A, G, C, and T. The expanded portfolio of nucleobases in DNA chimeras incorporating five, six or even eight letters is thought to have applications in information storage, low-noise microarrays, multiplexed PCR, etc.

The development of new DNA for information storage raises the question of long-term stability of such constructs. In particular, DNA damage by ionizing radiation has to be considered because artificial DNA is not likely to possess the ability of self-repair which is inherent to DNA in living cells. Recently, we have investigated the formation and properties of cation radicals produced from the so-called hachimoji S and B nucleobases,[12] which have been designed to form an orthogonal Watson-Crick pair.[13] Hachimoji S and B are, respectively, analogs of cytosine and guanine that have traditional heterocyclic skeletons while differing from the natural nucleobases by the position of substituents. Here, we address cation radicals of the other pair of hachimoji nucleobases, **P** and **Z**, that have substantially altered heterocyclic rings (Scheme 1). Nucleobase **P** is based on imidazo[1,2-*a*]-1,3,5-triazine which is the 5-aza-7-deaza analogue of guanine (Scheme 1, where we retain the guanine ring numbering in **P**). Hachimoji **P** pairs with nucleobase **Z** which is 6-amino-5-nitro-(*1H*)pyrid-2-one.[11,13] Our goal was to generate cation radicals of both hachimoji P and Z as isolated species in the gas phase. We use collision-induced dissociation (CID), deuterium labeling, and UV-Vis photodissociation action spectroscopy to investigate the cation-radicals' stability, dissociations, and electronic properties in the ground and excited states. Ab initio calculations are used to provide a theoretical framework for structure assignment, dissociation energetics, and vibronic spectra interpretation. The present study has completed the structure elucidation of non-traditional nucleobase cation radicals and allowed us to compare ionization and electron transfer energetics for the entire set of eight nucleobases used to build hachimoji DNA.

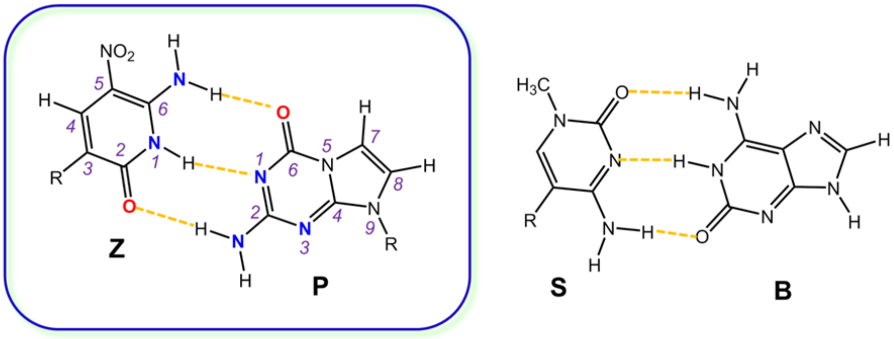

Scheme 1. Non-traditional nucleobases for hachimoji DNA.

5.3. Experimental

5.3.1. Materials and Methods

Imidazo[1,2-*a*]-1,3,5-triazine (nucleobase P) and 6-amino-5-nitro-1H pyrid-2-one (nucleobase Z) were purchased from BOC Sciences (Shirley, NY, USA) and used as received. Copper nitrate and 2:2',6':2"-terpyridine were purchased from Sigma-Aldrich (St. Louis, MO, USA). Complexes were prepared in situ from equimolar concentrations of the components in 50:50 acetonitrile/water and diluted for electrospray ionization.[14-16] Mass spectra were measured on a modified Bruker Daltonik (Bremen, Germany) amaZon Speed 3D ion trap mass spectrometer that was furnished with windows for laser beam entrance, as described previously.[17] The laser beam was produced by an EKSPLA NL301G (AltosPhotonics, Bozeman, MT, USA) Nd:YAG laser working at a 20 Hz frequency that was equipped with a PG142C optical parametric oscillator. The laser pulse energies were measured at each wavelength with an EnergyMax- USB J-10MB energy sensor (Coherent Inc., Santa Clara, CA, USA) and used to calibrate the action spectra. Photofragment ion intensities were measured in three sections covering the 210−700 nm range and normalized to the number of photons per pulse. The action spectra were reproduced on different days and are reported as averages of two measurements. Accurate mass measurements were made on an Orbitrap Velos mass spectrometer (Thermo Fisher, San Jose, CA, USA) at a resolving power of 60,000 to assign elemental compositions to ions of interest. H/D exchange was accomplished in D_2O/CD_3CN solution and the deuterium content in gas-phase ions was maintained by feeding D_2O solvent vapor into the dry nitrogen stream flushing the enclosed electrospray interface volume.

5.3.2. Calculations

Ab initio and density functional theory (DFT) calculations were performed with the Gaussian 16 (Revision A03) suite of programs.[18] Initial structure guesses were first fully gradient-optimized with B3LYP/6-31+G(d,p)[19] and CAM-B3LYP/6-311+G(2d,p)[20] to evaluate local energy minima by adequate harmonic frequencies. The B3LYP/6-31+G(d,p) frequencies, scaled by 0.975, were then used to calculate zero-point vibrational energy (ZPVE) corrections, enthalpies, and entropies. Additional sets of optimized geometries were obtained with M06-2X[21] and the 6-31+G(d,p) and 6-311++G(2d,p) basis sets, and are available from the corresponding author upon request. These were used to obtain single-point energies that were calculated using coupled clusters[22] with single, double, and disconnected triple excitations, CCSD(T),[23] that were extrapolated to the complete basis set (CBS)[24] using the formula $E[\text{CCSD(T)/CBS}] \cong E[\text{CCSD(T)/aug-cc-pVDZ}] - E[\text{MP2/aug-cc-pVDZ}] + E[\text{HF/aug-cc-pVQZ}] + E_{\text{corr,CBS}}$, providing benchmark relative energies. The extrapolations for calculating the MP2 correlation energy at the CBS limit used least-squares fits to the standard two-parameter formula,[25] $E_{\text{corr,CBS}} = E[\text{MP2/aug-cc-pVXZ}] - E[\text{HF/aug-cc-pVXZ}] = a + bX^{-3}$, where X is the ζ split in the aug-cc-pVXZ basis set.[26] Higher spin states in the UMP2 calculations were treated with the spin projection method[27, 28] using spin annihilation that reduced the total spin close to the theoretical value (0.75). Excited electronic states were evaluated by calculating electronic transitions and oscillator strength for 10 excited states using equation-of-motion CCSD (EOM-CCSD) calculations[29] with the 6-31+G(d,p) basis set. This extended to excitations down to 240 nm for all tautomers. The EOM-CCSD transitions were used to assign excited states from the time-dependent DFT (TD-DFT)[30] calculations that were carried out with M06-2X for 30 excited states, covering the wavelength range to below 180 nm. The EOMCCSD and TD-DFT-calculated excitation wavelengths and oscillator strength are compared in Figures S1a,b and S2a,b (Supporting Information). The high-level EOMCCSD-calculated transitions were used to assign the excited states and sort out artifacts that tend to occur in TD-DFT calculations of open-shell systems. The M06-2X TD-DFT calculations with the 6-31+G(d,p) and 6-311++G(2d,p) basis sets gave very similar results in terms of excitation energies and oscillator strengths, as reported previously.[12, 31] Thus, the M06-2X/6-31+G(d,p) TD-DFT calculations were considered to be sufficiently accurate to be used in calculations of all vibronic spectra at 350 K. The B3LYP/6-31+G(d,p) normal modes were used within the Newton X program[32] to generate Wigner distributions of vibrational configurations[33, 34] which were ordered according to their Boltzmann factors at 350 K. Typically, three hundred lowest energy configurations were selected and submitted to TD-DFT M06-2X/6-31+G(d,p) calculations for 20 excited states to generate the vibronic spectra reported here. Rice-Ramsperger-Kassel-Marcus (RRKM) calculations of rate constants[35] were carried out with the QCPE program[36] that was recompiled and run under Windows 7, as described previously.[37]

5.4. Results & Discussion

5.4.1. Generation of $P^{+\bullet}$ and $Z^{+\bullet}$

Cation radicals $\mathbf{P}^{+\bullet}$ and $\mathbf{Z}^{+\bullet}$ were generated in the gas phase from the respective complexes with Cu^{II} and 2:2',6':2"-terpyridine (tpy), according to O'Hair *et al*.[38] Electrospray ionization of solutions containing $Cu(NO_3)_2$, tpy, and P or Z yielded mixtures of complexes (Figure S3a,b, Supporting Information) from which the doubly charged $[Cu(tpy)P]^{2+\bullet}$ and

[Cu(tpy)Z]$^{2+\bullet}$ ions at the respective *m/z* 223.5 and 225.5 for the ^{63}Cu isotope were isolated by mass and stored in the ion trap. The identity of the complexes was further supported by accurate mass measurements, *m/z* 223.5355 and *m/z* 225.5273 for [Cu(tpy)P]$^{2+\bullet}$ and [Cu(tpy)Z]$^{2+\bullet}$, respectively (Table S1, Supporting Information). Collision-induced dissociation (CID-MS^2) of the mass-selected complexes resulted in nucleobase ionization and complex break up, forming **P**$^{+\bullet}$ and **Z**$^{+\bullet}$ at *m/z* 151 and 155, respectively (Figure 1). The ion composition was established by accurate mass measurements, 151.0480 ($C_5H_5N_5O^{+\bullet}$) and 155.0316 ($C_5H_5N_3O_2^{+\bullet}$) for **P**$^{+\bullet}$ and **Z**$^{+\bullet}$, respectively (Table S1, Supporting Information). The CID spectra of [Cu(tpy)P]$^{2+\bullet}$ and [Cu(tpy)Z]$^{2+\bullet}$ ions displayed an interesting difference. The dissociation of [Cu(tpy)Z]$^{2+\bullet}$ proceeded solely by electron transfer, producing the [Cu(tpy)]$^{+}$ (*m/z* 296) and **Z**$^{+\bullet}$ ions as the only primary products. The *m/z* 125 ions seen in the Figure 1b spectrum probably resulted from secondary dissociations of **Z**$^{+\bullet}$, as established by CID-MS^3 experiments (see below). In contrast, CID of [Cu(tpy)P]$^{2+\bullet}$ gave complementary [Cu(tpy)]$^{+}$ and **P**$^{+\bullet}$ ions from electron transfer but also complementary [Cu(tpy)NCO]$^{+\bullet}$ (*m/z* 338) and $C_4H_5N_4^{+}$ ions (*m/z* 109) ions, resulting from the dissociation of the P ligand in the complex. This ligand dissociation in [Cu(tpy)P]$^{2+\bullet}$, which has not been observed for other nucleobase complexes,[39-42] indicated that the P ligand was susceptible to ring-cleavage dissociations.

The **P**$^{+\bullet}$ and **Z**$^{+\bullet}$ ions were further characterized by CID-MS^3 and UVPD spectra at 270 nm. Upon CID, ion **P**$^{+\bullet}$ underwent ring cleavage by loss of HOCN and C_2N_2O, (*m/z* 108 and 83, respectively, Figure 2a) as established by accurate mass measurements (Table S1, Supporting Information). UVPD of **P**$^{+\bullet}$ gave additional *m/z* 109 (loss of CH_2N_2) and *m/z* 81 fragment ions (Figure 2b) that were also used to monitor action spectra. CID and UVPD-MS^3 of ions D_3-**P**$^{+\bullet}$ (*m/z* 154), produced after H/D exchange in solution, showed the expected mass shifts, which were *m/z* 108 → *m/z* 110 for loss of DOCN, *m/z* 109 → *m/z* 110 (loss of CD_2N_2), and *m/z* 83 → *m/z* 86 (loss of C_2N_2O, Figure S4a,b, Supporting Information). CID-MS^3 of ion **Z**$^{+\bullet}$ resulted in a dominant loss of NO (*m/z* 125, Figure 2c), which is a typical dissociation of aromatic nitro groups.[43-46] UVPD at 270 nm gave additional fragments at *m/z* 98, 97, and 81, presumably by consecutive dissociations of the *m/z* 125 ion by loss of HCN, CO, and NH_3 (Figure 2d), as supported by the pertinent fragment ion mass shifts in the UVPD-MS^3 spectrum of the H/D exchanged D_3-$\mathbf{Z}^{+\bullet}$ (*m/z* 158, Figure S4c,d).

5.4.2. UV-Vis Action Spectra

The dissociation channels identified by CID and UVPD were used to monitor wavelength-dependent dissociations and obtain UV-Vis action spectra in the 210-700 nm range, covering valence bond electronic excitations in the cation radicals. The action spectrum of $\mathbf{P}^{+\bullet}$ was monitored at the *m/z* 109, 108, and 83 channels that provided matching absorption bands with maxima at 300 and 360 nm (Figure 3a). Further bands can be distinguished as shoulders at 275 and 400 nm, and a broad weak band extending to ca. 500 nm. The action spectrum of $\mathbf{Z}^{+\bullet}$ (Figure 3b) was monitored at the *m/z* 125, 98, 81, and 54 channels (Figure 3c). These mass-resolved channels showed maxima at different wavelengths presumably because of energy-dependent competitive dissociations. The loss of NO channel (*m/z* 125) was the dominant component of the absorption bands with the 400 and 450 nm maxima, but also contributed to the band at 290 nm (Figure 3c). The formation of the *m/z* 125 at the low-energy end of the spectrum was consistent with the CID spectrum where this fragment ion was formed as a dominant product by slow collisional heating in the ion trap. The *m/z* 98 (loss of NO + HCN) and *m/z* 81 (loss of NO + HCN + NH_3) fragment ions showed major band maxima at 270 and 290 nm. The minor *m/z* 54 ion, possibly formed by a consecutive loss of HCN from the *m/z* 81 ion, became more intense at higher photon energies in the 220-300 nm region.

The CID, UVPD, and action spectra of the cation radicals were distinctly different from those of their closed-shell analogues, represented by $(P + H)^+$ and $(Z + H)^+$ ions (Figure S5a-c, S6a-c, Supporting Information). The action spectrum of $(P + H)^+$ (Figure S5a), which was obtained by monitoring the *m/z* 109 (loss of HNCO) and *m/z* 82 (combined loss of HNCO and HCN) channels, did not display any bands at $\lambda > 260$ nm. The action spectrum of $(Z + H)^+$

(Figure S6a) showed two absorption bands with maxima at 250 and 320 nm that were monitored at the intense *m/z* 139 and *m/z* 96 channels. However, there was no absorption in the visible region for this even-electron ion. We note that the UVPD and CID spectra of $(Z + H)^+$ differed in that the former (Figure S6b) displayed a prominent fragment ion by loss of ammonia (*m/z* 139) combined with loss of HNCO (*m/z* 96), whereas the latter (Figure S6c) showed a loss of water (*m/z* 138) again combined with loss of HNCO (*m/z* 95).

5.4.3. Ion Structures and Action Spectra Assignment

To assign the action spectra, we calculated structures for several isomers of the nucleobase cation radicals and determined their relative energies and details of electronic structure. These are discussed separately for the **P**$^{+\bullet}$ and **Z**$^{+\bullet}$ systems.

The nucleobase **P**$^{+\bullet}$ isomers were represented by tautomeric structures **P1**$^{+\bullet}$**- P6**$^{+\bullet}$ (Figure 4) with relative energies summarized in Table 1. The lowest-energy tautomer **P1**$^{+\bullet}$ had a proton at N-1 (according to a guanine ring numbering) and the spin density[47] distributed among C-7 (major), N-3 and N-9. The enol isomer **P2**$^{+\bullet}$ was the second lowest-energy structure with the spin density distribution resembling that in **P1**$^{+\bullet}$. The other N-protonated tautomers, **P3**$^{+\bullet}$ and **P4**$^{+\bullet}$, were less stable than **P1**$^{+\bullet}$ and **P2**$^{+\bullet}$. Finally, the NH_3 (**P5**$^{+\bullet}$) and C-8 (**P6**$^{+\bullet}$) tautomers were high-energy species (Table 1). A conspicuous feature of the optimized structures was the length of the N-5–C-6 bond that ranged from 1.373 Å in **P2**$^{+\bullet}$ to 1.542 Å in **P6**$^{+\bullet}$.

We used the structures of **P1**$^{+\bullet}$**- P6**$^{+\bullet}$ for TD-DFT calculations of electronic transitions and oscillator strength relevant to their absorption spectra. For the lowest-energy isomers **P1**$^{+\bullet}$ **- P4**$^{+\bullet}$ we also obtained theoretical vibronic spectra at 350 K to be compared with the action spectrum of **P**$^{+\bullet}$. Figure 5 shows the calculated vibronic spectra vis-à-vis the action spectrum outlined as a cyan background.

The vibronic spectrum of **P1**$^{+\bullet}$ (Figure 5a) showed an excellent match between the thermally broadened bands of the transitions to the ***B*** and ***D*** excited states and the bands in the action spectrum at 404 and 358 nm. Transition to the first excited state (***A***) at 530 nm was dipole disallowed (oscillator strength *f* = 0.0002) and gave rise to a low intensity band upon vibronic broadening. A close match with the experimental action spectrum was also obtained for the intense band of thermally broadened transitions to the ***G*** and ***H*** states at 276 and 251 nm (Figure 5a). The other **P$^{+\bullet}$** isomers exhibited various degrees of mismatch with the action spectrum. For example, the vibronic absorption spectra of ions **P3$^{+\bullet}$** and **P4$^{+\bullet}$** (Figure 5c and 5d) displayed strong bands at 200-250 nm that had no equivalents in the action spectrum of **P$^{+\bullet}$**. The absorption spectrum of the enol isomer **P2$^{+\bullet}$** (Figure 5b), albeit similar to that of **P1$^{+\bullet}$**, showed a poorer match between the strong band from transition to the ***G*** state at 255 nm and the band in the action spectrum (300 nm). Similarly, the calculated bands of the ***B*** and ***D*** states (424 nm and 388 nm, respectively) showed a substantial vibronic red shift and broadening that extended to 550 nm. On the basis of the theoretical absorption spectra, we conclude that the **P$^{+\bullet}$** ion had structure **P1$^{+\bullet}$**. However, judged by the vibronic spectra alone, a minor contribution of structure **P2$^{+\bullet}$** cannot be excluded. We provide additional evidence for structure **P1$^{+\bullet}$** later in the paper that was obtained on the basis of energy analysis of [Cu(tpy)P]$^{2+\bullet}$ complexes.

The nature of the excited states in **P1$^{+\bullet}$** was visualized with molecular orbital (MO) diagrams (Figure S7, Supporting Information). These revealed that most of the low-energy transitions were inner-electron excitations within the β-orbital manifold that promoted the electron to the semi-vacant MO39. This is a specific feature of open-shell systems where it leads to low-energy excited states providing absorption bands in the near UV and visible regions of the spectrum. The A and C states (ΔE_{exc} = 2.34 and 3.45 eV, respectively) were due to dipole-disallowed $\pi_{x,y} \rightarrow \pi_z$ transitions of very low oscillator strength. The bright ***B*** and ***D*** states involved dipole allowed β-electron transitions of the $\pi_z \rightarrow \pi_z$ type (Figure S7).

The nucleobase **Z$^{+\bullet}$** isomers were represented by structures **Z1$^{+\bullet}$-Z6$^{+\bullet}$** (Figure 6). Out of these, only **Z1$^{+\bullet}$-Z4$^{+\bullet}$** corresponded to standard valence-bond structures whereas **Z5$^{+\bullet}$** and **Z6$^{+\bullet}$** were ionized heterocyclic Wheland intermediates[48, 49] in which the aromatic π-electron system was interrupted by an sp^3 carbon. The pyridone (**Z1**$^{+\bullet}$) and hydroxypyridine (**Z2**$^{+\bullet}$) tautomers clearly represented the two lowest-energy covalent structures (Table 2). The calculated vibronic spectra of **Z1**$^{+\bullet}$ and **Z2**$^{+\bullet}$ (Figure 7a and 7b, respectively) displayed bands that matched those in the action spectrum of **Z**$^{+\bullet}$. In particular, the long-wavelength bands at 400 and 450 nm were represented by excitations to the ***B***, ***D***, and ***F*** states of **Z1**$^{+\bullet}$ as well as the ***B*** and ***E*** states of **Z2**$^{+\bullet}$. The calculated spectrum of **Z1**$^{+\bullet}$ showed a closer match with the action spectrum for the 270 and 290 nm bands that are represented by the J and K states, and even matched the 240 nm shoulder for excitation to the ***O*** state (Figure 7a). Structure **Z2**$^{+\bullet}$ displayed major mismatch with the action spectrum in the 220-250 nm region where it had intense transitions to the ***M***, ***N***, and ***P*** states (Figure 7b) that were weak in the action spectrum. On the basis of UV-Vis action spectra alone, we conclude that nucleobase ion **Z**$^{+\bullet}$ chiefly consists of the 2-pyridone isomer **Z1**$^{+\bullet}$. However, a minor admixture of **Z2**$^{+\bullet}$, co-formed with **Z1**$^{+\bullet}$, could not be excluded on the basis of action spectra alone.

The nature of electron transitions in **Z1**$^{+\bullet}$ was elucidated with MO diagrams (Figure S7). These showed prominent excitations of inner β electrons to the semivacant MO40. The A state (ΔE_{exc} = 1.79 eV) was dark (*f* = 0.000) as it corresponded to a dipole disallowed $\pi_{x,y} \rightarrow \pi_z$ transition, while excitation to the B state ($\pi_z \rightarrow \pi_z$, ΔE_{exc} = 2.24 eV) was weak.

5.4.4. Ion Dissociations

We analyzed the potential energy surfaces of **P**$^{+\bullet}$ and **Z**$^{+\bullet}$ to address the energetics and kinetics of the most prominent ion dissociations. The relative energies discussed in text are from CCSD(T)/CBS + ZPVE single-point calculations that were based on M06-2X/6-31+G(d,p) optimized geometries of stable ions, intermediates, transition states and products. Energies obtained by other methods are presented in Tables 1 and 2. Starting with **Z**$^{+\bullet}$, the 2-pyridone (**Z1**$^{+\bullet}$) and hydroxypyridine (**Z2**$^{+\bullet}$) isomers are interconnected via **TS1**$_Z$ for proton 1,3-migration (Scheme 2). The **TS1**$_Z$ energy relative to **Z1**$^{+\bullet}$ was calculated as 150 kJ mol^{-1} (Table 2). RRKM calculations of unimolecular rate constants for the reversible **Z1$^{+\bullet}$** ↔ **Z2$^{+\bullet}$** isomerization (k_1, and k_{-1}, Figure S8a, Supporting Information) indicated a rapid rise of both rate constants, reaching k = 13.9 s^{-1} for 50% conversion on the 50 ms experimental time scale within 20 kJ mol^{-1} above **TS1$_Z$**. This threshold is shown as a dotted line in Figure S8a. The isomerization resulted in a 48:52 equilibrium composition of **Z1$^{+\bullet}$** and **Z2$^{+\bullet}$** that showed less than 1% change within the 180-360 kJ mol^{-1} range of internal energies. Interconversion of thermal **Z1$^{+\bullet}$** and **Z2$^{+\bullet}$** was substantially slower, showing $k_1 < 10^{-4}$ s^{-1} at $T < 450$ K even when including a correction for tunneling through **TS1$_Z$** (Figure S8b). This led us to conclude that **Z1$^{+\bullet}$** and **Z2$^{+\bullet}$** cannot isomerize when stored in the ion trap under standard conditions (310-350 K)[50-53] and without collisional excitation.

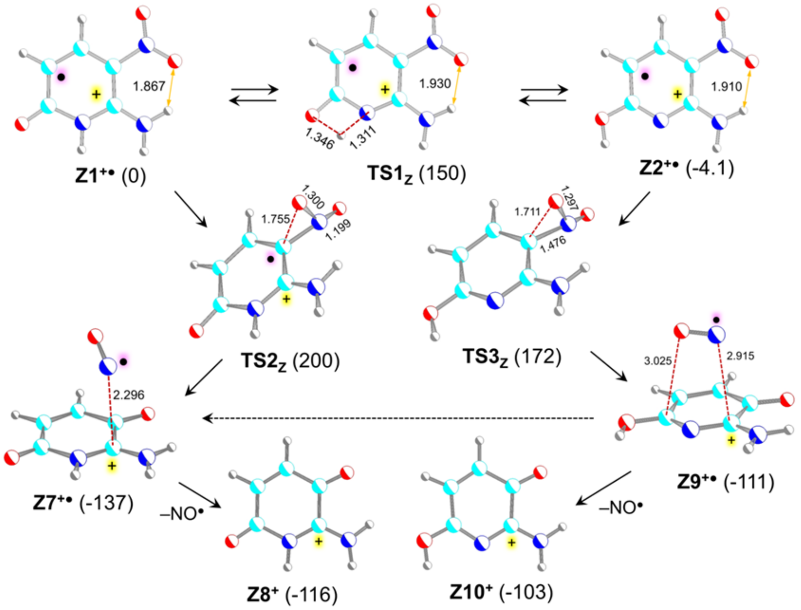

Scheme 2. Proposed mechanisms for NO loss from **Z1$^{+\bullet}$**. The energies in parentheses (kJ mol^{-1}) are from CCSD(T)/CBS + ZPVE calculations (Table 1) relative to **Z1$^{+\bullet}$**. Bond lengths are in Ångstrøms

The loss of NO from **Z1$^{+\bullet}$** and **Z2$^{+\bullet}$** proceeded via separate transition states, **TS2$_Z$** and **TS3$_Z$**, respectively (Scheme 2). Both **TS2$_Z$** and **TS3$_Z$** indicated initial pathways to a rearrangement of the nitro group to a nitrite, proceeding via simultaneous NO_2 out-of-plane rotation, C–N bond elongation and formation of the C–O bond. However, the putative nitrite cation-radical intermediates were unbound and exothermically dissociated to nitric oxide complexes $\mathbf{Z7}^{+\bullet}$ and $\mathbf{Z9}^{+\bullet}$, respectively. The $\mathbf{TS2}_{\mathrm{Z}}$ and $\mathbf{TS3}_{\mathrm{Z}}$ energies, 200 and 172 kJ mol^{-1} relative to $\mathbf{Z1}^{+\bullet}$, respectively, (Scheme 2, Table 2) were both above $\mathbf{TS1}_{\mathrm{Z}}$, indicating that dissociating $\mathbf{Z}^{+\bullet}$ can reversibly isomerize to follow the lower energy path via $\mathbf{TS3}_{\mathrm{Z}}$. The product formation can be kinetically controlled by the $\mathbf{TS2}_{\mathrm{Z}}$ and $\mathbf{TS3}_{\mathrm{Z}}$ energies or by dissociation thermodynamics, whereby the 2-pyridone complex ($\mathbf{Z7}^{+\bullet}$) had a lower energy than the complex of the hydroxypyridine fragment ion with NO ($\mathbf{Z9}^{+\bullet}$). The hydroxypyridine complex $\mathbf{Z9}^{+\bullet}$ can undergo prototropic isomerization to the more stable 2-pyridone complex $\mathbf{Z7}^{+\bullet}$, similar to internally catalyzed isomerizations that have been previously reported to proceed in ion-molecule complexes, forming lower energy isomers.[54-56] Overall, the dissociation was exothermic, with $\Delta H_{\mathrm{rxn},0}$ = –116 and –103 kJ mol^{-1} for the formation of $\mathbf{Z8}^{+}$ + NO and $\mathbf{Z10}^{+}$ + NO, respectively. This was consistent with the facile dissociation of $\mathbf{Z}^{+\bullet}$ upon formation and CID-MS^3.

To further address the fragment ion structure, we obtained an action spectrum of the *m/z* 125 ion produced by CID-MS^3 loss of NO from $\mathbf{Z}^{+\bullet}$ (Figure S9, Supporting Information). The action spectrum indicated a closer match with the calculated vibronic absorption spectrum of the more stable pyridone tautomer $\mathbf{Z8}^{+}$, as judged by the band at 280 nm that matched an absorption band at the same wavelength in the vibronic spectrum. The hydroxypyridine tautomer $\mathbf{Z10}^{+}$ was expected to show a band at 330 nm which, however, was only very weakly represented in the action spectrum. The action spectrum indicated that the *m/z* 125 ion chiefly consisted of the lower energy $\mathbf{Z8}^{+}$ tautomer, correlating to complex $\mathbf{Z7}^{+\bullet}$.

To investigate the dissociations of $\mathbf{P}^{+\bullet}$ we first addressed the transition states for isomerizations of the low energy isomers $\mathbf{P1}^{+\bullet}$-$\mathbf{P4}^{+\bullet}$ (Scheme S1, Supporting Information) N-1-H migration in $\mathbf{P1}^{+\bullet}$ forming $\mathbf{P2}^{+\bullet}$ can proceed via $\mathbf{TS1}_{\mathrm{P}}$ which was at 178 kJ mol^{-1} relative to $\mathbf{P1}^{+\bullet}$ (Table 1). Although this was a relatively low-energy TS for collision-driven isomerization, the TST rate constants (Figure S10a, Supporting Information) were too low ($<10^{-4}$ s) for the isomerization to proceed thermally in trapped ions without collisional activation. The calculated equilibrium constant, when expressed by mole fractions, $K_{eq} = x(\mathbf{P2}^{+\bullet})/x(\mathbf{P1}^{+\bullet})$, was <0.006 for the temperature range of 290-460 K (Figure S10b). This indicated that even in the presence of isomerization, the amide isomer $\mathbf{P1}^{+\bullet}$ would be preferred by >99%. Ions $\mathbf{P3}^{+\bullet}$ and $\mathbf{P4}^{+\bullet}$ were separated by high-energy barriers for 1,2-H migration, as exemplified by $\mathbf{TS2}_{\mathbf{P}}$ for N-9-H migration to C-4, which was at 339 kJ mol^{-1} relative to $\mathbf{P1}^{+\bullet}$ (Scheme S1). Another isomerization pathway for 1,2-H migration from N-9 to C-8 in $\mathbf{P4}^{+\bullet}$ also required a high energy in $\mathbf{TS3}_{\mathbf{P}}$ (296 kJ mol^{-1}, Table 1).

Elimination of HOCN was a major dissociation of $\mathbf{P}^{+\bullet}$ upon CID and UVPD (Figure 2a,b). We considered two logical pathways for this dissociation starting from $\mathbf{P1}^{+\bullet}$ (Scheme 3). Pathway ***a*** was a direct elimination of hydrogen isocyanate, involving N-1 and C-6 and forming fragment ion $\mathbf{P9}^{+\bullet}$ and HN=C=O with a 288 kJ mol^{-1} threshold energy. This could proceed by initial ring opening by cleavage of the N-1–C-2 or N-5–C-6 bonds. However, the lower-energy TS for the triazine ring opening by N-5–C-6 bond cleavage ($\mathbf{TS4}_{\mathbf{P}}$) was accompanied by a concomitant rotation about the N-1–C-2 bond and led to a migration of N-1-H onto N-5 of the imidazole ring, forming an isocyanate intermediate ($\mathbf{P7}^{+\bullet}$) at 68 kJ mol^{-1} above $\mathbf{P1}^{+\bullet}$ (route ***b***, Scheme 3). The further course of the dissociation comprised a transfer of the N-2 amine proton onto the oxygen atom of the NCO$^{\bullet}$ fragment ($\mathbf{TS5}_{\mathbf{P}}$), resulting in the formation of a weakly bound complex ($\mathbf{P8}^{+\bullet}$) of hydroxycyanide (HO–C≡N) with the final product $\mathbf{P10}^{+\bullet}$. The $\mathbf{TS5}_{\mathbf{P}}$ energy (316 kJ mol^{-1}) was lower than the threshold energy for the elimination of NCO$^{\bullet}$ (331 kJ mol^{-1}). This was consistent with the CID and UVPD dissociations where elimination of HOCN dominated at low (CID) excitations to be outcompeted by loss of NCO$^{\bullet}$ following excitations with 270 nm (4.59 eV) photons. It is worth noting that the TS energies in path ***b*** were higher that that of $\mathbf{TS1}_{\mathbf{P}}$, suggesting that the dissociating $\mathbf{P}^{+\bullet}$ can reversibly isomerize between the $\mathbf{P1}^{+\bullet}$ and $\mathbf{P2}^{+\bullet}$ structures.

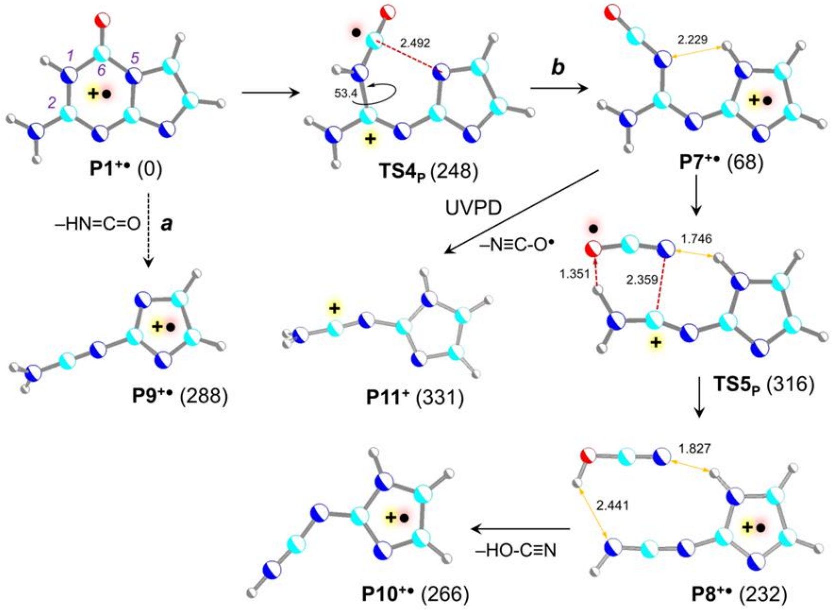

Scheme 3. Proposed mechanisms for HOCN and OCN loss from **P1**$^{+\bullet}$. The energies (kJ mol^{-1}) are from CCSD(T)/CBS + ZPVE calculations relative to **P1**$^{+\bullet}$.

Because of the possibility of a **P1**$^{+\bullet}$ ↔ **P2**$^{+\bullet}$ isomerization preceding the loss of HOCN, we also investigated the triazine ring cleavage in **P2**$^{+\bullet}$ (Scheme S2, Supporting Information). However, the TS energies for the ring opening in **P2**$^{+\bullet}$ (**TS6**$_{\mathbf{P}}$, 285 kJ mol^{-1}) and subsequent loss of HOCN (**TS7**$_{\mathbf{P}}$, 374 kJ mol^{-1}, Table 1,) were substantially higher than those for the respective **TS4**$_{\mathbf{P}}$ and **TS5**$_{\mathbf{P}}$ in the dissociation starting from **P1**$^{+\bullet}$. These TS energies, as well as the high threshold energy for the formation of **P9**$^{+\bullet}$ + HOCN (389 kJ mol^{-1}, Table 1) made the direct dissociation in **P2**$^{+\bullet}$ non-competitive with the path ***b*** reaction starting from **P1**$^{+\bullet}$.

5.4.5. Ion Recombination Energies

Having the ion structures and energies at a high level of theory, we can now compare the propensity for electron transfer between a neutral nucleobase and a cation radical within the complete set of eight hachimoji nucleobases. This tendency is expressed by adiabatic recombination energies (RE$_{\mathrm{ad}}$, Table 3) which, as absolute values, are equal to neutral nucleobase ionization energies. The calculated RE$_{\mathrm{ad}}$ indicated that in a P…Z pair, electron transfer from **P** to **Z**$^{+\bullet}$ would be uniformly exothermic by 0.31-0.70 eV, depending on the combination of the $\mathbf{P}^{+\bullet}$ and $\mathbf{Z}^{+\bullet}$ isomers. Within the entire set of eight nucleobases, the RE_{ad} ranking was $\mathbf{T}^{+\bullet}$ > $\mathbf{C}^{+\bullet}$ > $\mathbf{S}^{+\bullet} \approx \mathbf{Z}^{+\bullet}$ > $\mathbf{A}^{+\bullet}$ > $\mathbf{G}^{+\bullet} \approx \mathbf{P}^{+\bullet}$ > $\mathbf{B}^{+\bullet}$. Thus, the purine ($\mathbf{B}^{+\bullet}$ and $\mathbf{G}^{+\bullet}$) and $\mathbf{P}^{+\bullet}$ nucleobase cation radicals were the ones least capable of abstracting an electron and promoting electron transfer in hachimoji DNA. Conversely, these neutral nucleobases are the most susceptible ones to be ionized by electron abstraction by another ionized nucleobase. This comparison has to take into account the effect on the RE_{ad} of the 2'-deoxyribose substituent. For $\mathbf{T}^{+\bullet}$, $\mathbf{C}^{+\bullet}$, $\mathbf{A}^{+\bullet}$, and $\mathbf{G}^{+\bullet}$, the RE_{ad} of the ionized nucleosides are uniformly 0.5-0.9 eV lower than those of the nucleobase cation radicals,[41] and a similar shift can be expected for nucleosides of $\mathbf{S}^{+\bullet}$, $\mathbf{Z}^{+\bullet}$, $\mathbf{P}^{+\bullet}$ and $\mathbf{B}^{+\bullet}$. Another feature to be taken into account is that different nucleobase tautomers may be preferred in nucleosides, as opposed to free nucleobases. For example, structure $\mathbf{P4}^{+\bullet}$ cannot exist in a nucleoside where the deoxyribose blocks N-9. Similarly, structure $\mathbf{P3}^{+\bullet}$ may be stabilized by N-3-hydrogen bonding to the sugar, thus altering its stability and recombination energy.

5.4.6. Structures and Energies of neutral Nucleobases and Cu Complexes

The identification of gas-phase $\mathbf{P1}^{+\bullet}$ and $\mathbf{Z1}^{+\bullet}$ as the major components of cation radicals produced from Cu(tpy) complexes was based on their action spectra that displayed features that were characteristic for these structures. To be formed in the gas phase as cation radicals, the P and Z tautomers must have existed as neutral components of the Cutpy complexes to be formed in solution and transferred to the gas phase. Thus, it was of interest to investigate the structures and relative energies of relevant neutral P and Z, as well as their $[\mathrm{Cu(tpy)}\mathbf{P}]^{2+\bullet}$ and $[\mathrm{Cu(tpy)}\mathbf{Z}]^{2+\bullet}$ complexes to align the formation of the gas-phase nucleobase cation radicals with the distribution of the complexes in solution and the gas phase.

Starting with Z, the two lowest-energy nucleobase tautomers **Z1** and **Z2** (Figure S11, Supporting Information) showed a strong solvation effect on their relative free energies. Judged by M06-2X/6-311++G(2d,p) relative free energies at 310 K, the hydroxypyridine tautomer **Z2** was 15 kJ mol^{-1} more stable than the 2-pyridone isomer **Z1** in the gas phase. The CCSD(T)/CBS relative free energies were similar, showing **Z2** at 14 kJ mol^{-1} below **Z1** in the gas phase. Solvation with water, assessed with M06-2X/6-311++G(2d,p) and the polarizable continuum model,[58] reversed the relative free energies, showing solvated **Z1** at 7.4 kJ mol^{-1} below solvated **Z2**. Hence, neutral **Z1** is expected to constitute 95% of the isomer mixture at equilibrium in aqueous solution.

Neutral **Z1** and **Z2** can be bound in the [Cu(tpy)**Z**]$^{2+\bullet}$ complexes in the form of coordination isomers [Cu(tpy)**Z1a**]$^{2+\bullet}$, [Cu(tpy)**Z1b**]$^{2+\bullet}$, [Cu(tpy)**Z2a**]$^{2+\bullet}$, and [Cu(tpy)**Z2b**]$^{2+\bullet}$ (Figure 8). The complexes differed in the coordinating nucleobase functional groups, which were C=O, N-1, or the NO_2 group. In all these complexes, the nucleobase was essentially monodentate with a weak coordination by an adjacent N or O atom. Coordination by the NO_2 group was preferred in the gas-phase complexes, whereby [Cu(tpy)**Z2b**]$^{2+\bullet}$ was the lowest free-energy structure (Table 4). However, this was reversed by solvation with water, where the carbonyl-coordinated complex of the N-1-H tautomer, [Cu(tpy)**Z1a**]$^{2+\bullet}$, was the most stable isomer. Based on the CAM-B3LYP/6-311+G(2d,p) calculated free enthalpies for complex dissociation to Z and [Cu(tpy)]$^{2+\bullet}$, we obtained the stability constants as 1.1×10^{11} mol L^{-1} (from $\Delta G_{\mathrm{dis},298}$ = 63 kJ mol^{-1}), 6.8×10^{8} mol L^{-1} (from $\Delta G_{\mathrm{dis},298}$ = 49.9 kJ mol^{-1}) and 5.6×10^{8} mol L^{-1} (from $\Delta G_{\mathrm{dis},298}$ = 50.4 kJ mol^{-1}) for [Cu(tpy)**Z1a**]$^{2+\bullet}$, [Cu(tpy)**Z1b**]$^{2+\bullet}$, and [Cu(tpy)**Z2b**]$^{2+\bullet}$, respectively. When combined with the prevalence of neutral **Z1** in aqueous solution, the energy data strongly suggested that the complexes produced from solution contained the 2-pyridone **Z1** ligand. We calculated the TS energy for the gas-phase isomerization of [Cu(tpy)**Z1b**]$^{2+\bullet}$ to [Cu(tpy)**Z2b**]$^{2+\bullet}$ which was at 142 kJ mol^{-1} relative to [Cu(tpy)**Z1b**]$^{2+\bullet}$ Table 4, Figure 8). However, the TST rate constants for this isomerization (Figure S12, Supporting Information) were too low to allow it to proceed in thermal trapped ions. All this was consistent with our conclusion, based on the action spectrum, that the cation radical produced from the complex had structure **Z1**$^{+\bullet}$**.**

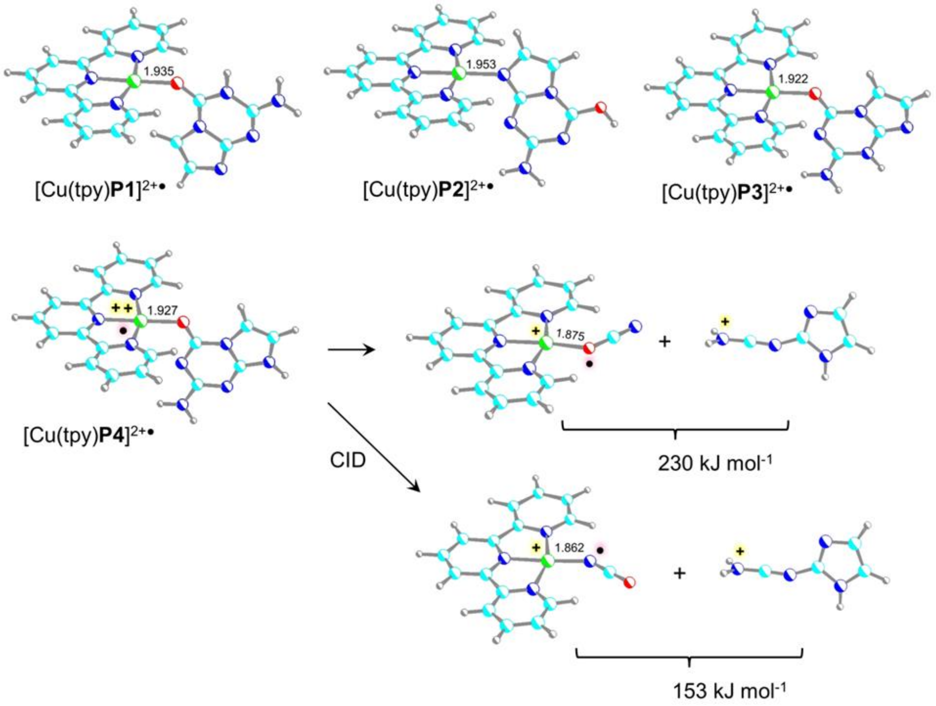

Scheme 4. Optimized structures and dissociation of [Cu(tpy)**P**]$^{+\bullet}$ complexes. The relative energies with respect to [Cu(tpy)**P4**]$^{2+\bullet}$ are from CAM-B3LYP/6-311+G(2d,p) + ZPVE calculations.

Moving to P, the relative free energies of neutral **P1**-**P4** (Figure S11, Supporting Information) indicated the N-9-H tautomer to be the lowest-energy species in both the gas phase and aqueous solution (Table 1). The pertinent [Cu(tpy)**P**]$^{2+\bullet}$ complexes ranked similarly in the gas phase where [Cu(tpy)**P4**]$^{2+\bullet}$ was the lowest-energy structure (Table 5). It is noteworthy that the P tautomers showed different coordination to Cu(tpy). **P1**, **P3** and **P4** were coordinated by the amide carbonyl oxygen while **P2** was coordinated by N-9 of the imidazole ring. However, the energy ranking of the complexes was overturned by solvation that made [Cu(tpy)**P1**]$^{2+\bullet}$ the lowest-free energy complex in aqueous solution (Table 5). Nevertheless, the stability of **P4** indicated that both [Cu(tpy)**P1**]$^{2+\bullet}$ and [Cu(tpy)**P4**]$^{2+\bullet}$ could be present in solution and transferred into the gas phase by electrospray whereas the higher-energy complexes of the less stable neutral **P2** and **P3** should not be formed. To resolve the question of gas-phase [Cu(tpy)**P**]$^{2+\bullet}$ complexes, we referred to the action spectrum of **P**$^{+\bullet}$ that showed a major mismatch with the vibronic spectrum of tautomer **P4**$^{+\bullet}$, indicating that this ion was not produced in the gas phase. In addition to the formation of **P**$^{+\bullet}$, CID-MS^2 of the [Cu(tpy)**P**]$^{2+\bullet}$ complexes was accompanied by loss of NCO radical from the ligand that amounted to ca. 45% of dissociation products (Figure 1a). This dissociation can directly occur in **P4** which contains the N-C=O moiety. This was corroborated by the calculated dissociation energies of [Cu(tpy)**P4**]$^{2+\bullet}$ that furthermore favored a nitrogen-ligated dissociation product, [Cu(tpy)NCO]$^{+\bullet}$, over the oxygen-ligated one, [Cu(tpy)OCN]$^{+\bullet}$ (Scheme 4). Thus, CID of [Cu(tpy)**P1**]$^{2+\bullet}$ and [Cu(tpy)**P4**]$^{2+\bullet}$ leaves **P1**$^{+\bullet}$ as the dominant stable nucleobase isomer, while the formation of **P4**$^{+\bullet}$ is hampered by competitive dissociations of the nucleobase ligand in the complex.

5.5. Conclusions

Gas-phase ion chemistry offers a unique and flexible tool for generating nucleobase cation radicals to be investigated by tandem mass spectrometry,[38] especially when combined with UV-Vis photodissociation action spectroscopy. The combination of action spectroscopy and high-level theory allowed us to assign structures to non-traditional ionized nucleobases hachimoji **P1**$^{+\bullet}$ and **Z1**$^{+\bullet}$. These are the same as the nucleobase tautomer forms appearing in synthetic hachimoji DNA, and their electronic properties and recombination energies are relevant to DNA ionization. The ranking of nucleobase recombination energies places the electron affinity of **P1**$^{+\bullet}$ close to that of [guanine]$^{+\bullet}$, indicating that P can become ionized by exothermic electron transfer to another nucleobase cation radical, such as its Watson-Crick counterpart **Z**$^{+\bullet}$, but also to **A**$^{+\bullet}$, **C**$^{+\bullet}$, **S**$^{+\bullet}$, and **T**$^{+\bullet}$. Nucleobase Z ranks in the middle of the ionization energy range, and its electron-transfer interactions with **A**$^{+\bullet}$, **C**$^{+\bullet}$, and **S**$^{+\bullet}$ are likely to be modulated by the solvent and DNA environment. Further studies of nucleoside ionization are needed to address this topic.[59,60]

5.6. References

1. Seley-Radtke, K. L.; Yates, M. K. The Evolution of Nucleoside Analogue Antivirals: A Review for Chemists and Non-Chemists. Part 1: Early structural modifications to the nucleoside scaffold. *Antiviral. Res*. **2018**, *154*, 66-86.
2. Tsesmetzis, N.; Paulin, C. B. J.; Rudd, S. G.; Herokt, N. Nucleobase and Nucleoside Analogues: Resistance and Re-Sensitisation at the Level of Pharmacokinetics, Pharmacodynamics and Metabolism. *Cancers* **2018**, *10*, 240-278.
3. Galmarini, C. M.; Mackey, J. R.; Dumontet, C. Nucleoside Analogues and Nucleobases in Cancer Treatment. *Lancet Oncol.* **2002**, *3*, 415-424.
4. Perigaud, C.; Gosselin, G.; Imbach, J. L. Nucleoside Analogues as Chemotherapeutic Agents: a Review. *Nucleoside Nucleotides* **1992**, *11*, 903–945.
5. De Clercq, E. Strategies in the Design of Antiviral Drugs. *Nat. Rev. Drug Discov*. **2002**, *1*, 13–25.
6. De Clercq, E. Historical Perspectives in the Development of Antiviral Agents against Pox Viruses. *Viruses* **2010**, *2*, 1322–1339.
7. Jordheim, L. P.; Durantel, D.; Zoulim, F.; Dumontet, C. Advances in the Development of Nucleoside and Nucleotide Analogues for Cancer and Viral Diseases. *Nat. Rev. Drug Discov.* **2013**, *12*, 447–464.
8. Prusoff, W. H. Synthesis and Biological Activities of Iododeoxyuridine, an Analog of Thymidine. *Biochim. Biophys. Acta* **1959**, *32*, 295–296.
9. Kaufman, H. E.; Heidelberger, C. Therapeutic Antiviral Action of 5-Trifluoromethyl-2'-deoxyuridine in Herpes simplex Keratitis. *Science* **1964**, *145*, 585–586.
10. Wataya, Y.; Hiraoka, O.; Sonobe, Y.; Yoshioka, A.; Matsuda, A.; Miyasaka, T.; Saneyoshi, M.; Ueda, T. Anti-Parasite Activity of Nucleoside Analogues in Leishmania tropica Promastigotes. *Nucleic Acids Symp. Ser.* **1984**, 69–71.
11. Sismour, A. M.; Benner, S. A. Synthetic Biology. *Nat. Rev. Genet.* **2005**, *6*, 533.

12. Huang, S. R.; Tureček, F. Cation Radicals of Hachimoji Nucleobases. Canonical Purine and Noncanonical Pyrimidine Forms Generated in the Gas Phase and Characterized by UV-Vis Photodissociation Action Spectroscopy. *J. Phys. Chem. A* **2020**, *124*, 7101-7112.
13. Hoshika, S.; Leal, N. A.; Kim, M.-J.; Kim, M.-S.; Karalkar, N. B.; Kim, H.-J.; Bates, A. M.; Watkins, N. E., Jr.; SantaLucia, H. A.; Meyer, A. J.; DasGupta, S.; Piccirilli, J. A.; Ellington, A. D.; SantaLucia, J., Jr.; Georgiadis, M. M.; Benner, S. A. Hachimoji DNA and RNA: A Genetic System with Eight Building Blocks. *Science* **2019**, *363*, 884−887.
14. Gatlin, C. L.; Turecek, F.; Vaisar, T. Copper(II) Amino Acid Complexes in the Gas Phase. *J. Am. Chem. Soc.* **1995**, *117*, 3637−3638.
15. Gatlin, C. L.; Rao, R. D.; Tureček, F.; Vaisar, T. Carboxylate and Amine Terminus Directed Fragmentations in Gaseous Dipeptide Complexes with Copper(II) and Diimine Ligands Formed by Electrospray. *Anal. Chem.* **1996**, *68*, 263−270.
16. Chu, I. K.; Rodriquez, C. F.; Lau, T.-C.; Hopkinson, A. C.; Siu, K. W. M. Molecular Radical Cations of Oligopeptides. *J. Phys. Chem. B* **2000**, *104*, 3393−3397.
17. Dang, A.; Korn, J. A.; Gladden, J.; Mozzone, B.; Tureček, F. UV-Vis Photodissociation Action Spectroscopy on Thermo LTQ-XL ETD and Bruker amaZon Ion Trap Mass Spectrometers: A Practical Guide. *J. Am. Soc. Mass Spectrom.* **2019**, *30*, 1558−1564.
18. Robb, M. A.; Cheeseman, J. R.; Scalmani, G.; Barone, V.; Petersson, G. A.; Nakatsuji, H.; Caricato, M.; Marenich, A. V.; Bloino, J.; Janesko, B. G.; Gomperts, R.; Mennucci, B.; Hratchian, H. P.; Ortiz, J. V.; Izmaylov, A. F.; Sonnenberg, J. L.; Williams-Young, D.; Ding, F.; Lipparini, F.; Egidi, F.; Goings, J.; Peng, B.; Petrone, A.; Henderson, T.; Ranasinghe, D.; Zakrzewski, V. G.; Gao, J.; Rega, N.; Zheng, G.; Liang, W.; Hada, M.; Ehara, M.; Toyota, K.; Fukuda, R.; Hasegawa, J.; Ishida, M.; Nakajima, T.; Honda, Y.; Kitao, O.; Nakai, H.; Vreven, T.; Throssell, K.; Montgomery, Jr., J. A.; Peralta, J. E.; Ogliaro, F.; Bearpark, M. J.; Heyd, J. J.; Brothers, E. N.; Kudin, K. N.; Staroverov, V. N.;

Keith, T. A.; Kobayashi, R.; Normand, J.; Raghavachari, K.; Rendell, A. P.; Burant, J. C.; Iyengar, S. S.; Tomasi, J.; Cossi, M.; Millam, J. M.; Klene, M.; Adamo, C.; Cammi, R.; Ochterski, J. W.; Martin, R. L.; Morokuma, K.; Farkas, O.; Foresman, J. B.; Fox, D. J.. *Gaussian 16*, Revision A03; Gaussian, Inc.: Wallingford, CT, 2016.

19. Becke, A. D. New Mixing of Hartree-Fock and Local Density-Functional Theories. J. *Chem. Phys.* **1993**, *98*, 1372−1377.
20. Yanai, T.; Tew, D. P.; Handy, N. C. A New Hybrid Exchange- Correlation Functional Using the Coulomb-Attenuating Method (CAM-B3LYP). *Chem. Phys. Lett.* **2004**, *393*, 51−57.
21. Zhao, Y.; Truhlar, D. G. The M06 Suite of Density Functionals for Main Group Thermochemistry, Thermochemical Kinetics, Noncovalent Interactions, Excited States, and Transition Elements: Two New Functionals and Systematic Testing of Four M06-Class Functionals and 12 Other Functionals. *Theor. Chem. Acc.* **2008**, *120*, 215−241.
22. Čížek, J. On the Use of the Cluster Expansion and the Technique of Diagrams in Calculations of Correlation Effects in Atoms and Molecules. *Adv. Chem. Phys.* **1969**, *14*, 35−89.
23. Purvis, G. D., III; Bartlett, R. J. Full Coupled-Cluster Singles and Doubles Model−the Inclusion of Disconnected Triples. *J. Chem. Phys.* **1982**, *76*, 1910−1918.
24. Halkier, A.; Helgaker, T.; Jørgensen, P.; Klopper, W.; Koch, H.; Olsen, J.; Wilson, A. K. Basis Set Convergence in Correlated Calculations on Ne, N_2, and H_2O. *Chem. Phys. Lett.* **1998**, *286*, 243−252.
25. Helgaker, T.; Klopper, W.; Koch, H.; Noga, J. Basis-Set Convergence of Correlated Calculations on Water. *J. Chem. Phys.* **1997**, *106*, 9639−9646.
26. Dunning, T. H., Jr. Gaussian Basis Sets for Use in Correlated Molecular Calculations. I. The Atoms Boron through Neon and Hydrogen. *J. Chem. Phys.* **1989**, *90*, 1007−1023.

27. Schlegel, H. B. Potential Energy Curves Using Unrestricted Møller-Plesset Perturbation Theory with Spin Annihilation. *J. Chem. Phys.* **1986**, *84*, 4530.

28. Mayer, I. Spin-Projected UHF Method. IV. Comparison of Potential Curves Given by Different One-Electron Methods. *Adv. Quantum Chem.* **1980**, *12*, 189−262.

29. Comeau, D. C.; Bartlett, R. J. The Equation-of-Motion Coupled-Cluster Method. Applications to Open- and Closed-Shell Reference States. *Chem. Phys. Lett.* **1993**, *207*, 414−423.

30. Furche, F.; Ahlrichs, R. Adiabatic Time-Dependent Density Functional Methods for Excited State Properties. *J. Chem. Phys.* **2002**, *117*, 7433−7447.

31. Liu, Y.; Dang, A.; Urban, J.; Tureček, F. Charge-Tagged DNA Radicals in the Gas Phase Characterized by UV-Vis Photodissociation Action Spectroscopy. *Angew. Chem., Int. Ed.* **2020**, *59*, 7772−7777.

32. Barbatti, M.; Ruckenbauer, M.; Plasser, F.; Pittner, J.; Granucci, G.; Persico, M.; Lischka, H. Newton-X: A Surface-Hopping Program for Nonadiabatic Molecular Dynamics. *Wiley Interdiscip. Rev. Comput. Mol. Sci.* **2014**, *4*, 26−33.

33. Wigner, E. The Quantum Correction for Thermodynamic Equilibrium. *Phys. Rev.* **1932**, *40*, 749-759.

34. Bonacic-Koutecky, V.; Mitric, R. Theoretical Exploration of Ultrafast Dynamics in Atomic Clusters: Analysis and Control. *Chem. Rev.* **2005**, *105*, 11-65.

35. Gilbert, R. G.; Smith, S. C. *Theory of Unimolecular and Recombination Reactions*; Blackwell Scientific Publications: Oxford, U.K., 1990; pp 52−132.

36. Zhu, L.; Hase, W. L. Quantum Chemistry Program Exchange; Indiana University: Bloomington, IN, 1994; Program no. QCPE 644.

37. Gregersen, J. A.; Tureček, F. Mass-Spectrometric and Computational Study of Tryptophan Radicals (Trp + H)• Produced by Collisional Electron Transfer to Protonated Tryptophan in the Gas Phase. *Phys. Chem. Chem. Phys.* **2010**, *12*, 13434−13447.

38. Wee, S.; O'Hair, R. A. J.; McFadyen, W. D. Can Radical Cations of the Constituents of Nucleic Acids Be Formed in the Gas Phase Using Ternary Transition Metal Complexes? *Rapid Commun. Mass Spectrom.* **2005**, *19*, 1797−1805.
39. Lesslie, M.; Lawler, J. T.; Dang, A.; Korn, J. A.; Bím, D.; Steinmetz, V.; Maitre, P.; Tureček F.; Ryzhov, V. Cytosine Radical Cation: a Gas-Phase Study Combining IRMPD Spectroscopy, UV-PD Spectroscopy, Ion-Molecule Reactions, and Theoretical Calculations. *ChemPhysChem* **2017**, *18*, 1293-1301.
40. Dang, A.; Nguyen, H. T. H.; Ruiz, H.; Piacentino, E.; Ryzhov, V.; Tureček, F. Experimental Evidence for Non-Canonical Thymine Cation Radicals in the Gas Phase. *J. Phys. Chem. B*, **2018**, *122*, 86-97.
41. Dang, A.; Liu, Y., Tureček, F. UV-Vis Action Spectroscopy of Guanine, 9-Methylguanine and 2'-Deoxyguanosine Cation Radicals in the Gas Phase. *J. Phys. Chem. A* **2019**, *123*, 3272-3284.
42. Huang, S. R.; Dang, A.; Tureček, F. Ground and Excited States of Gas-Phase DNA Nucleobase Cation-Radicals. A UV-Vis Photodisociation Action Spectroscopy and Computational Study of Adenine and 9-Methyladenine. *J. Am. Soc. Mass Spectrom.* **2020**, *31*, 1271-1281.
43. McLafferty, F. W.; Turecek, F. *Interpretation of Mass Spectra*, 4th Edn. University Science Book, SMill Valley, CA, 1993, p. 278.
44. Karni, M.; Mandelbaum, A. The Even-Electron Rule. *Org. Mass Spectrom.* **1980**, *15*, 53-64.
45. Yinon, J. Mass Spectrometry of Explosives: Nitro Compounds, NitrateEsters and Nitramines. *Mass Spectrom. Rev.* **1982**, *1*, 257-307.
46. Yinon, J. Mass Spectral Fragmentation Pathways in Some Dinitroaromatic Compounds Studied by Collision-Induced Dissociation and Tandem Mass Spectrometry. *Org. Mass Spectrom.* **1992**, *27*, 689-694.

47. Reed, A. E.; Weinstock, R. B.; Weinhold, F. Natural Population Analysis. *J. Chem. Phys*. **1985**, *83*, 735−746.
48. Benson, H. G.; Murrell, J. N. Benzenoid-Quinonoid Resonance. 1. General Theory and Applications to the Structure of the Pyridones and to the Stability of Wheland Intermediates. *J. Chem. Soc., Faraday Trans. 2: Molecular and Chemical Physics* **1972**, *68*, 129-136.
49. Polasek, M.; Turecek, F. Hydrogen Atom Adducts to Nitrobenzene: Formation of the Phenylnitronic Radical in the Gas Phase and Energetics of Wheland Intermediates. *J. Am. Chem. Soc.* **2000**, *122*, 9511-9524.
50. Goeringer, D. E.; McLuckey, S. A. Evolution of Ion Internal Energy during Collisional Excitation in the Paul Ion Trap: A Stochastic Approach. *J. Chem. Phys.* **1996**, *104*, 2214−2221.
51. Gronert, S. Estimation of Effective Ion Temperatures in a Quadrupole Ion Trap. *J. Am. Soc. Mass Spectrom.* **1998**, *9*, 845−848.
52. Lovejoy, E. R.; Wilson, R. R. Kinetic Studies of Negative Ion Reactions in a Quadrupole Ion Trap: Absolute Rate Coefficients and Ion Energies. J*. Phys. Chem. A* **1998**, *102*, 2309−2315.
53. Donald, W. A.; Khairallah, G. N.; O'Hair, R. A. J. The Effective Temperature of Ions Stored in a Linear Quadrupole Ion Trap Mass Spectrometer. *J. Am. Soc. Mass Spectrom.* **2013**, *24*, 811−815.
54. Tureček, F.; Drinkwater, D. E.; McLafferty, F. W. The Stepwise Nature of the γ-Hydrogen Rearrangement in Unsaturated Ions. *J. Am. Chem. Soc.* **1990**, *112*, 993-997.
55. Audier, H. E.; Mourgues, P.; van der Rest, G.; Chamot-Rooke, J.; Nedev, H. Catalyzed Isomerizations of Ions in the Gas Phase. *Adv. Mass Spectrom*. **2001**, *15*, 101-121.
56. Mourgues, P.; Chamot-Rooke, J.; van der Rest, G.; Nedev, H.; Audier, H. E.; McMahon, T. B. Catalyzed Keto-Enol Tautomerism of Ionized Acetone: a Fourier Transform Ion

Cyclotron Resonance Mass Spectrometry Study of Proton Transport Isomerization. *Int. J. Mass Spectrom.* **2001**, *210/211*, 429-446.

57. Wolken, J. K.; Yao, C.; Tureček, F.; Polce, M. J.; Wesdemiotis, C. Cytosine Neutral Molecules and Cation-Radicals in the Gas-Phase. Structures, Energetics, Ion Chemistry, and Neutralization-Reionization Mass Spectrometry. *Int. J. Mass Spectrom.* **2007**, *267*, 30-42.
58. Tomasi, J.; Mennucci, B.; Cammi, R. Quantum Mechanical Continuum Solvation Models. *Chem. Rev.* **2005**, *105*, 2999−3093.
59. Slavicek, P.; Winter, B.; Faubel, M.; Bradforth, S. E.; Jungwirth, P. Ionization Energies of Aqueous Nucleic Acids: Photoelectron Spectroscopy of Pyrimidine Nucleosides and ab Initio Calculations. *J. Am. Chem. Soc.* **2009**, *131*, 6460-6467.
60. Schroeder, C. A.; Pluharova, E.; Seidel, R.; Schroeder, W. P.; Faubel, M.; Slavicek, P.; Winter, B.; Jungwirth, P.; Bradforth, S. E. Oxidation Half-Reaction of Aqueous Nucleosides and Nucleotides via Photoelectron Spectroscopy Augmented by Ab initio Calculations. *J. Am. Chem. Soc.* **2015**, *137*, 201-209.

5.7. Appendix

Table 1. Relative Energies of Nucleobase P Cation Radicals and Neutral Molecules.

	Relative Energy[a,b]			
Species/ reaction	M06-2X/ 6-311++G(2d,p)	CCSD(T)/[c] aug-ccc-pVTZ	CCSD(T)/[c] aug-cc-pVQZ	CCSD(T)/[d] CBS
Ions				
P1$^{+\bullet}$	0	0	0	0
P2$^{+\bullet}$	16	19	19	19
P3$^{+\bullet}$	48	47	46	46
P4$^{+\bullet}$	32	30	30	30
P5$^{+\bullet}$	109	103	104	103
P6$^{+\bullet}$	200	186	190	190
TS1$_{\mathbf{P}}$	181	178	179	178
TS2$_{\mathbf{P}}$	343	336	339	339
TS3$_{\mathbf{P}}$	296	294	296	296
TS4$_{\mathbf{P}}$	259	245	247	248
TS5$_{\mathbf{P}}$	323	314	316	316
TS6$_{\mathbf{P}}$	288	286	286	285
TS7$_{\mathbf{P}}$	378	372	373	374
P7$^{+\bullet}$	67	68	68	68
P8$^{+\bullet}$	229	230	232	232
P9$^{+\bullet}$ + HN=C=O	291	285	287	288
P9$^{+\bullet}$ + HO–CN	394	386	388	389
P10$^{+\bullet}$ + HO–CN	268	265	265	266
P11^{+} + O–CN$^{\bullet}$	335	327	330	331
Neutral Molecules				
P1	0	0	0	0
P2	27 (39)[e]	31	31	30
P3	13 (5.3)	14	13	13
P4	–10 (–14)	–8	–8.8	–8.4

---

[a] In kJ mol^{-1}. [b] Including scaled B3LYP/6-31+G(d,p) zero-point energies and referring to 0 K. [c] From basis set expansion: E[CCSD(T)/aug-cc-pVXZ] ≈ E[CCSD(T)/aug-cc-pVDZ] + E[PMP2/aug-cc-pVXZ] – E[PMP2/aug-cc-pVDZ]. [d] From expansion to the complete basis set: E[CCSD(T)/CBS] ≈ E[CCSD(T)/aug-cc-pVDZ] – E[PMP2/aug-cc-pVDZ] + E[HF/aug-cc-pVQZ] + E_{corr}[MP2, X $\rightarrow\infty$]. [e] Relative free energies in parentheses include solvation energies in water dielectric and refer to 298 K.

Table 2. Relative Energies of Nucleobase Z Cation Radicals.

	Relative Energy[a,b]			
Species/ reaction	M06-2X/ 6-311++G(2d,p)	CCSD(T)/[c] aug-ccc-pVTZ	CCSD(T)/[c] aug-cc-pVQZ	CCSD(T)/[d] CBS
Z1$^{+\bullet}$	0	0	0	0 (0)[e]
Z2$^{+\bullet}$	–5.0	–2.9	–3.5	–4.1 (–3.8)
Z3$^{+\bullet}$	109	106	110	110
Z4$^{+\bullet}$	123	139	141	141
Z5$^{+\bullet}$	173			
Z6$^{+\bullet}$	173			
Z7$^{+\bullet}$	–137	–157	–154	–157
Z8^{+} + NO	–113	–120	–118	–116
Z9$^{+\bullet}$	–121	–115	–113	–111
Z10^{+} + NO	–106	–106	–106	–103
TS1$_{\mathrm{Z}}$	157	150	151	150
TS2$_{\mathrm{Z}}$	196	183	186	200
TS3$_{\mathrm{Z}}$	175	171	172	172

---

[a] In kJ mol^{-1}. [b] Including scaled B3LYP/6-31+G(d,p) zero-point energies and referring to 0 K unless stated otherwise. [c] From basis set expansion: E[CCSD(T)/aug-cc-pVXZ] ≈ E[CCSD(T)/aug-cc-pVDZ] + E[PMP2/aug-ccpVXZ] – E[PMP2/aug-cc-pVDZ]. [d] From expansion to the complete basis set: E[CCSD(T)/CBS] ≈ E[CCSD(T)/aug-cc-pVDZ] – E[PMP2/aug-cc-pVDZ] + E[HF/aug-cc-pVQZ] + E_{corr}[MP2, X →∞]. [e] Values in parentheses are relative free energies at 310 K including B3LYP/6-31+G(d,p) enthalpies and entropies.

Table 3. Recombination Energies of Nucleobase P and Z Cation Radicals

Ion	Recombination Energy[a]			
	M06-2X/ 6-311++G(2d,p)	CCSD(T)/[b] aug-ccc-pVTZ	CCSD(T)/[b] aug-cc-pVQZ	CCSD(T)/[c] CBS
P1$^{+\bullet}$	7.85	7.85	7.90	7.92
P2$^{+\bullet}$	7.74	7.73	7.78	7.81
P3$^{+\bullet}$	8.24	8.19	8.24	8.26
P4$^{+\bullet}$	8.29	8.24	8.29	8.32
Z1$^{+\bullet}$	8.58	8.44	8.49	8.51
Z2$^{+\bullet}$	8.70	8.56	8.61	8.63
S$^{+\bullet}$	8.48	8.42	8.49	8.51
B$^{+\bullet}$	7.69	7.65	7.74	7.76
T$^{+\bullet}$	8.88[d]	8.91	8.94	8.98
C$^{+\bullet}$		8.62-8.71[e]		
A$^{+\bullet}$	8.25[f]	8.28	8.33	8.32
G$^{+\bullet}$	7.82[g]	7.90	7.95	7.97

[a] Absolute adiabatic values in electron volts including zero-point energy corrections and referring to 0 K. [b] From single-point energy calculations extrapolated to expanded basis set. [c] Extrapolated to the complete basis set limit. [d] 2,4-dioxo-5-methyl [thymine]$^{+\bullet}$ tautomer (ref.[40]). [e] Lowest-energy [cytosine]$^{+\bullet}$ 2-oxo-N-1-H, and 2-OH tautomers (ref[57]). [f] Most stable N-9-H [adenine]$^{+\bullet}$ tautomer (ref[42]). [g] 6-oxo-N-1-H [guanine]$^{+\bullet}$ tautomer (ref.[41]).

Table 4. Relative Energies of [Cu(tpy)Z]$^{2+\bullet}$ Complexes.

Complex/ Reaction	Relative Energy[a,b]	
	Gas Phase	Solvated[c]
[Cu(tpy)**Z1a**]$^{2+\bullet}$	0 (0)[d]	0 (0)[e]
[Cu(tpy)**Z1b**]$^{2+\bullet}$	–4.7 (–0.5)	13 (12)
[Cu(tpy)**Z2a**]$^{2+\bullet}$	37 (41)	29 (30)
[Cu(tpy)**Z2b**]$^{2+\bullet}$	–18 (–14)	32 (27)
TS{[Cu(tpy)**Z1b**]$^{2+\bullet}$ → [Cu(tpy)**Z2b**]$^{2+\bullet}$}	142	
[Cu(tpy)**Z1a**]$^{2+\bullet}$ → **Z1**$^{+\bullet}$ + [Cu(tpy)]$^{+}$	49 (–8.4)	
[Cu(tpy)**Z1b**]$^{2+\bullet}$ → **Z1**$^{+\bullet}$ + [Cu(tpy)]$^{+}$	53 (–7.9)	
[Cu(tpy)**Z2b**]$^{2+\bullet}$ → **Z2**$^{+\bullet}$ + [Cu(tpy)]$^{+}$	68 (6.5)	

[a] In kJ mol^{-1}. [b] From full optimization with CAM-B3LYP/6-311+G(2d,p) including scaled zero-point energies and referring to 0 K unless stated otherwise. [c] Including solvation energies calculated with the polarization continuum model for complexes fully optimized in water dielectric. [d] Relative free energies of gas-phase ions at 310 K including CAM-B3LYP/6-311+G(2d,p) enthalpies and entropies. [e] Relative free energies of solvated ions at 298 K including CAM-B3LYP/6-311+G(2d,p) enthalpies and entropies.

Table 5. Relative Energies of [Cu(tpy)P]$^{2+\bullet}$ Complexes.

Complex/ Reaction	Relative Energy[a,b]	
	Gas Phase	Solvated[c]
[Cu(tpy)**P1**]$^{2+\bullet}$	0 (0)[d]	0[e]
[Cu(tpy)**P2**]$^{2+\bullet}$	20 (30)	47
[Cu(tpy)**P3**]$^{2+\bullet}$	33 (42)	41
[Cu(tpy)**P4**]$^{2+\bullet}$	–25 (–16)	8
[Cu(tpy)**P4**]$^{2+\bullet}$ → **P11**$^{+}$ + [Cu(tpy)OCN]$^{+\bullet}$	230	
[Cu(tpy)**P4**]$^{2+\bullet}$ → **P11**$^{+}$ + [Cu(tpy)NCO]$^{+\bullet}$	153	

[a] In kJ mol^{-1}. [b] From full optimization with CAM-B3LYP/6-311+G(2d,p) including scaled zero-point energies and referring to 0 K unless stated otherwise. [c] Including solvation energies calculated with the polarization continuum model for complexes fully optimized in water dielectric. [d] Relative free energies of gas-phase ions at 310 K including CAM-B3LYP/6-311+G(2d,p) enthalpies and entropies. [e] Relative free energies of solvated ions at 298 K including CAM-B3LYP/6-311+G(2d,p) enthalpies and entropies.

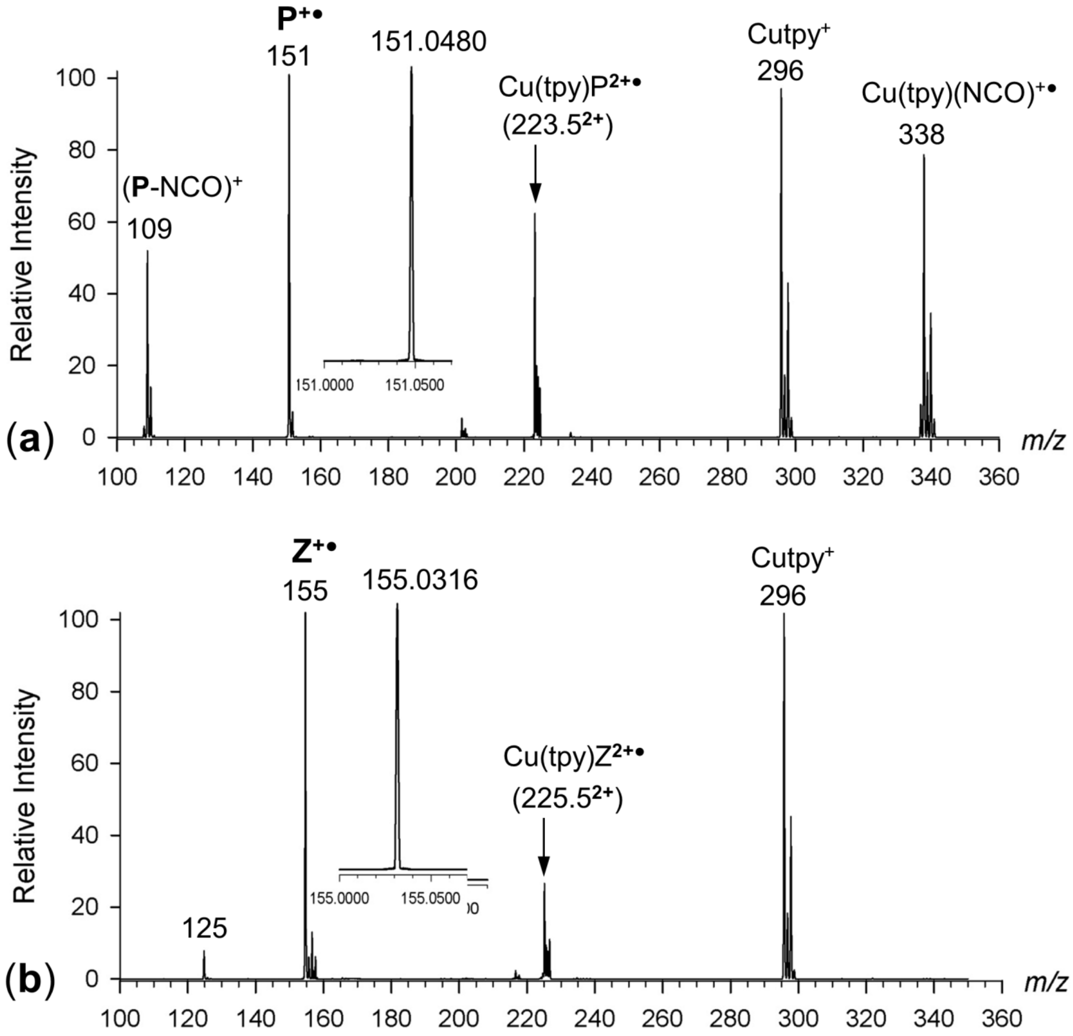

Figure 1. CID-MS^2 spectra of complexes (a) [Cu(tpy)P]$^{2+\bullet}$ and (b) [Cu(tpy)Z]$^{2+\bullet}$. Insets show the **P**$^{+\bullet}$ and **Z**$^{+\bullet}$ peak profiles and accurate *m/z* values from high-resolution CID-MS^2 mass spectra.

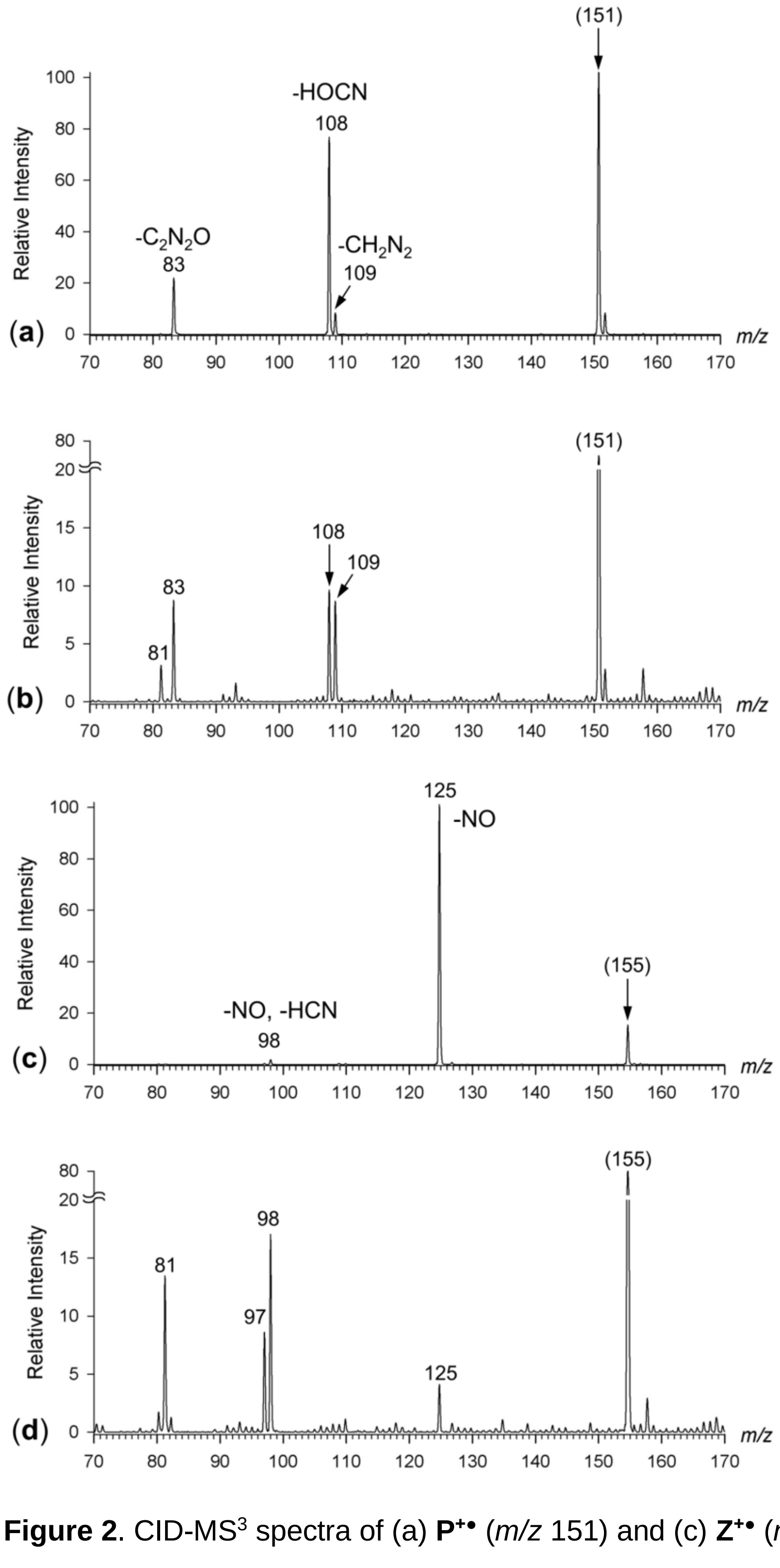

Figure 2. CID-MS^3 spectra of (a) $\mathbf{P^{+\bullet}}$ (*m/z* 151) and (c) $\mathbf{Z^{+\bullet}}$ (*m/z* 155). UVPD-MS^3 at 270 nm of (b) $\mathbf{P^{+\bullet}}$ and (d) $\mathbf{Z^{+\bullet}}$.

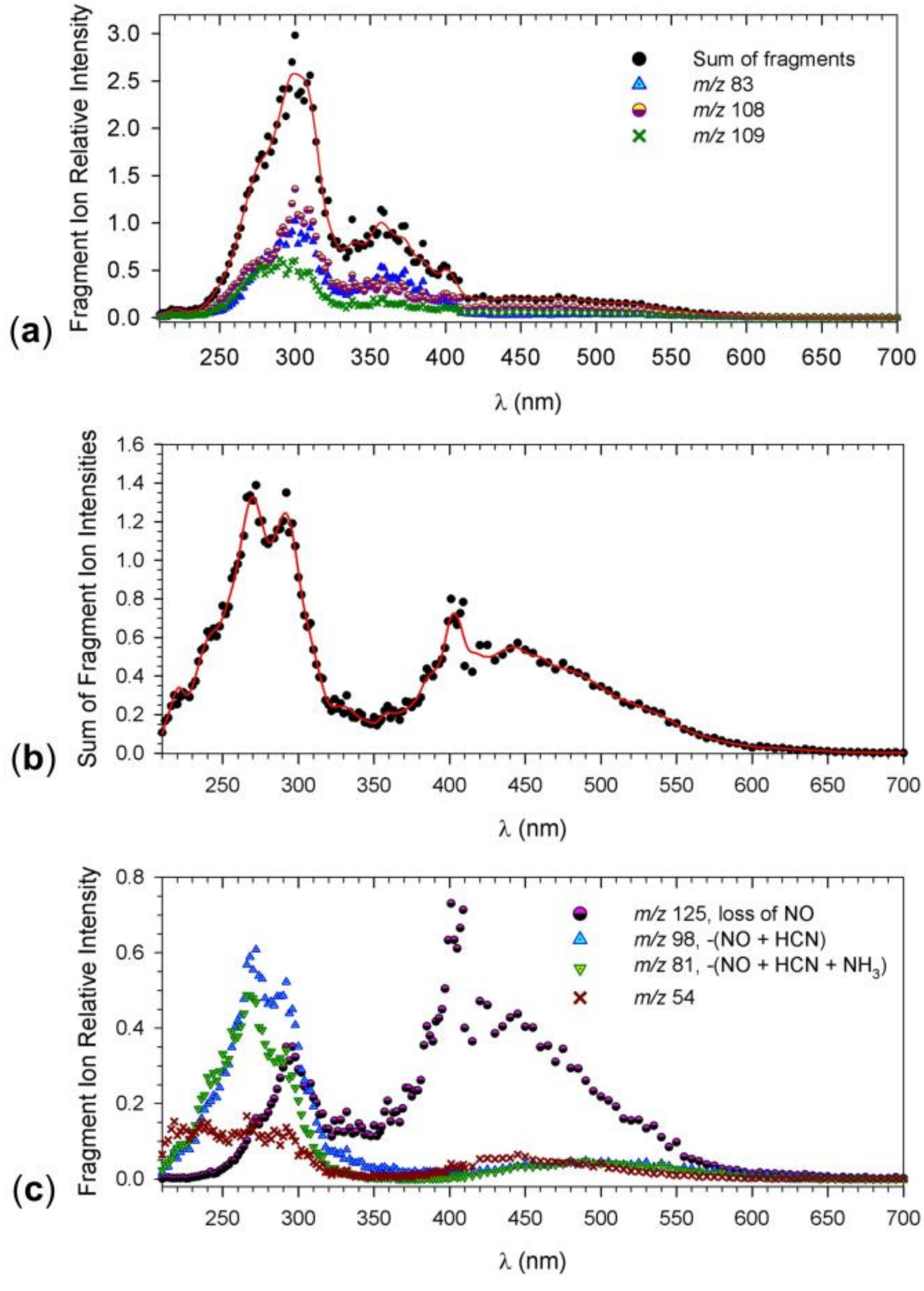

Figure 3. (a) UVPD action spectrum of **P**$^{+\bullet}$ showing all photofragment ion channels. UVPD action spectra of **Z**$^{+\bullet}$ showing (b) the sum of photofragment fragment ion relative intensities and (c) individual photofragment ion channels.

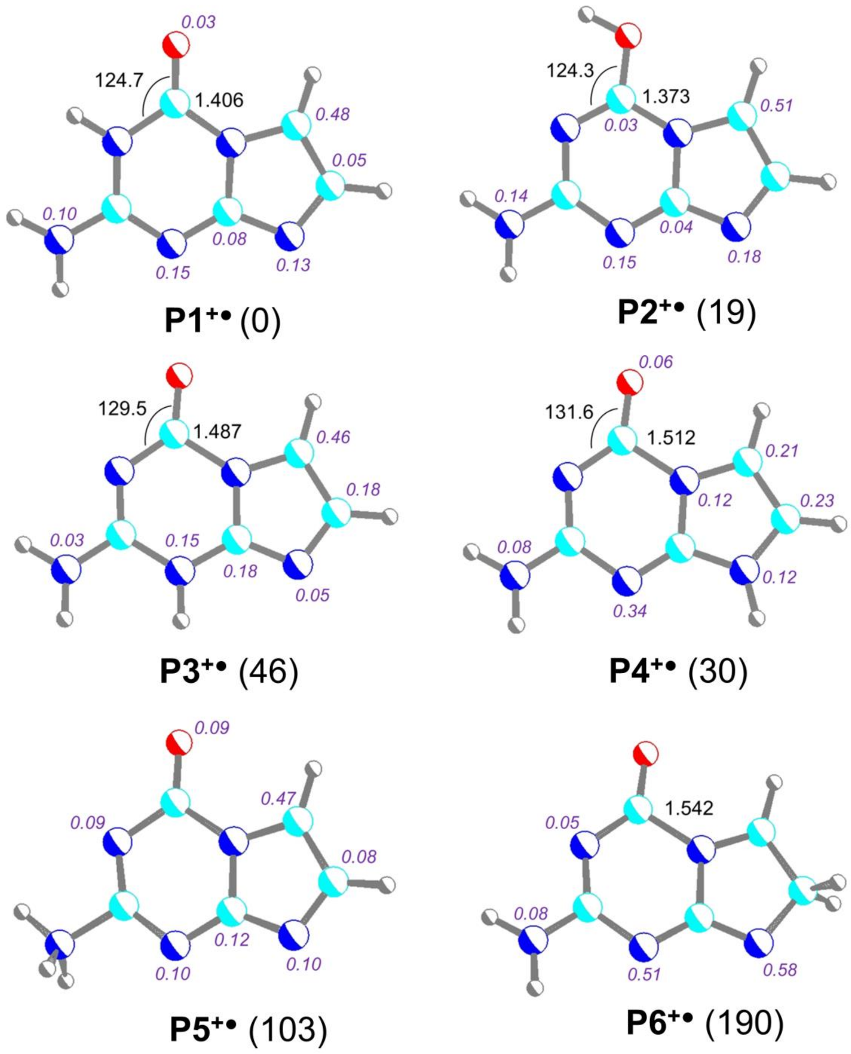

P1$^{+\bullet}$ (0)

P2$^{+\bullet}$ (19)

P3$^{+\bullet}$ (46)

P4$^{+\bullet}$ (30)

P5$^{+\bullet}$ (103)

P6$^{+\bullet}$ (190)

Figure 4. M06-2X/6-31+G(d,p) optimized structures of low-energy **P$^{+\bullet}$** isomers. Atom color coding is as follows: cyan = C, blue = N, red = O, gray = H. Bond lengths are in Ångstrøms, bond angles in degrees. Atomic spin densities from natural population analysis are shown as purple italics. Relative energies (kJ mol^{-1} in parentheses) are from CCSD(T)/CBS + ZPVE calculations referring to 0 K.

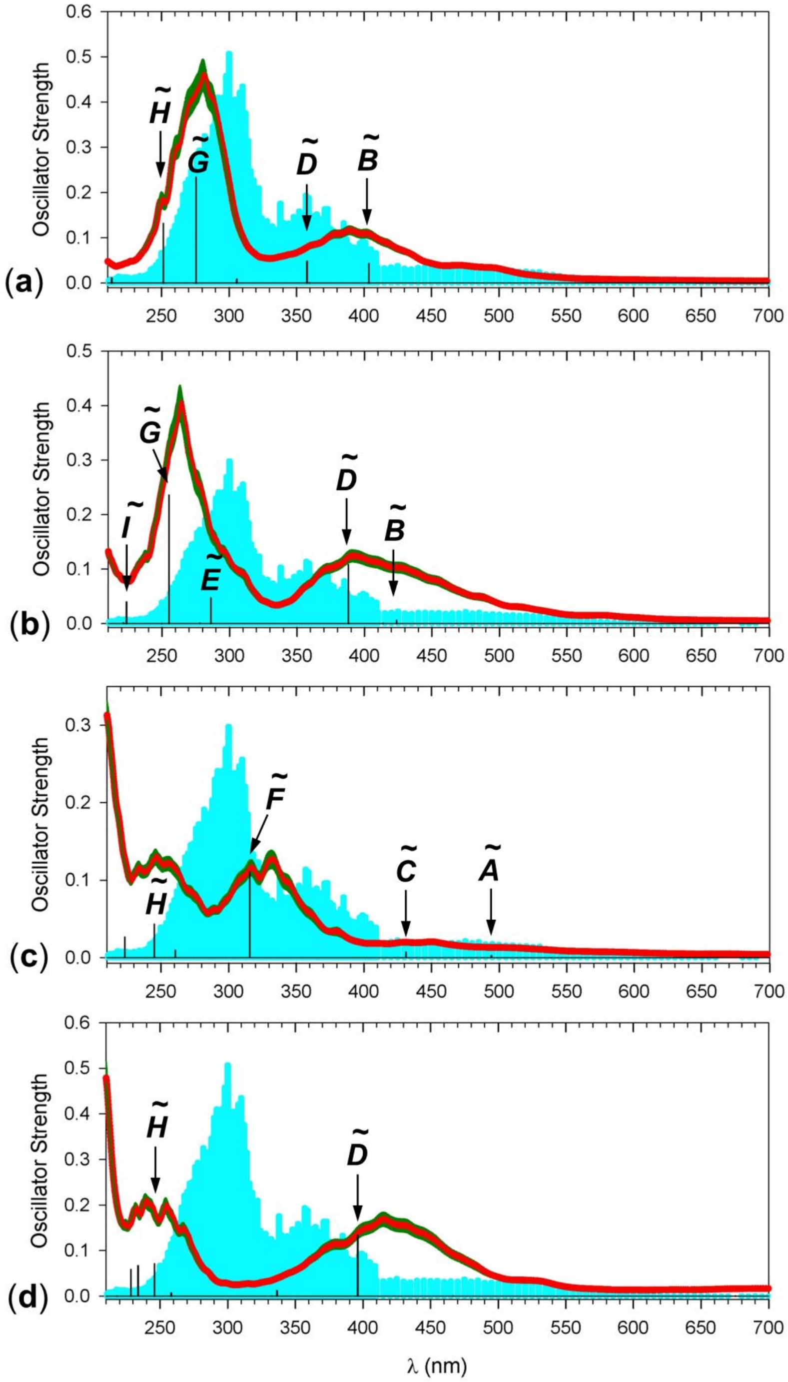

Figure 5. M06-2X/6-31+G(d,p) TD-DFT vibronic spectra of (a) **P1**$^{+\bullet}$, (b) **P2**$^{+\bullet}$, (c) **P3**$^{+\bullet}$, and (d) **P4**$^{+\bullet}$. Vertical bars denote the electron transitions. Cyan background shows the action spectrum of **P**$^{+\bullet}$ scaled to fit the plot.

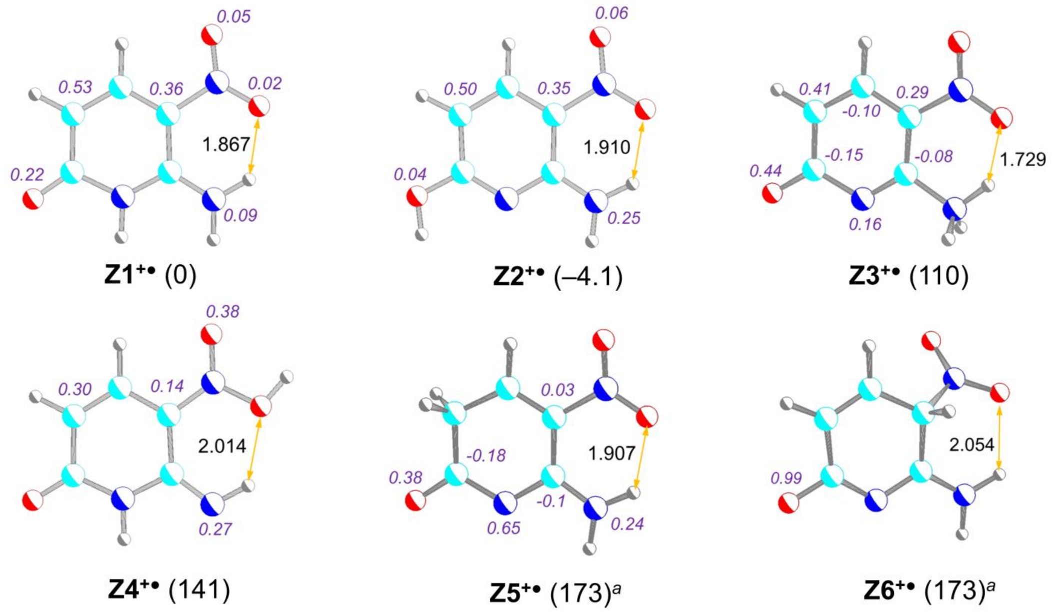

Z1$^{+\bullet}$ (0) **Z2**$^{+\bullet}$ (–4.1) **Z3**$^{+\bullet}$ (110)

Z4$^{+\bullet}$ (141) **Z5**$^{+\bullet}$ (173)^{a} **Z6**$^{+\bullet}$ (173)^{a}

Figure 6. M06-2X/6-31+G(d,p) optimized structures and atomic spin densities of low-energy **Z**$^{+\bullet}$ isomers. Structure description and relative 0 K energies are as in Figure 4. Relative energies are from CCSD(T)/CBS + ZPVE calculations, except for **Z5**$^{+\bullet}$ and **Z6**$^{+\bullet}$ which are from M06-2X calculations.^{a}

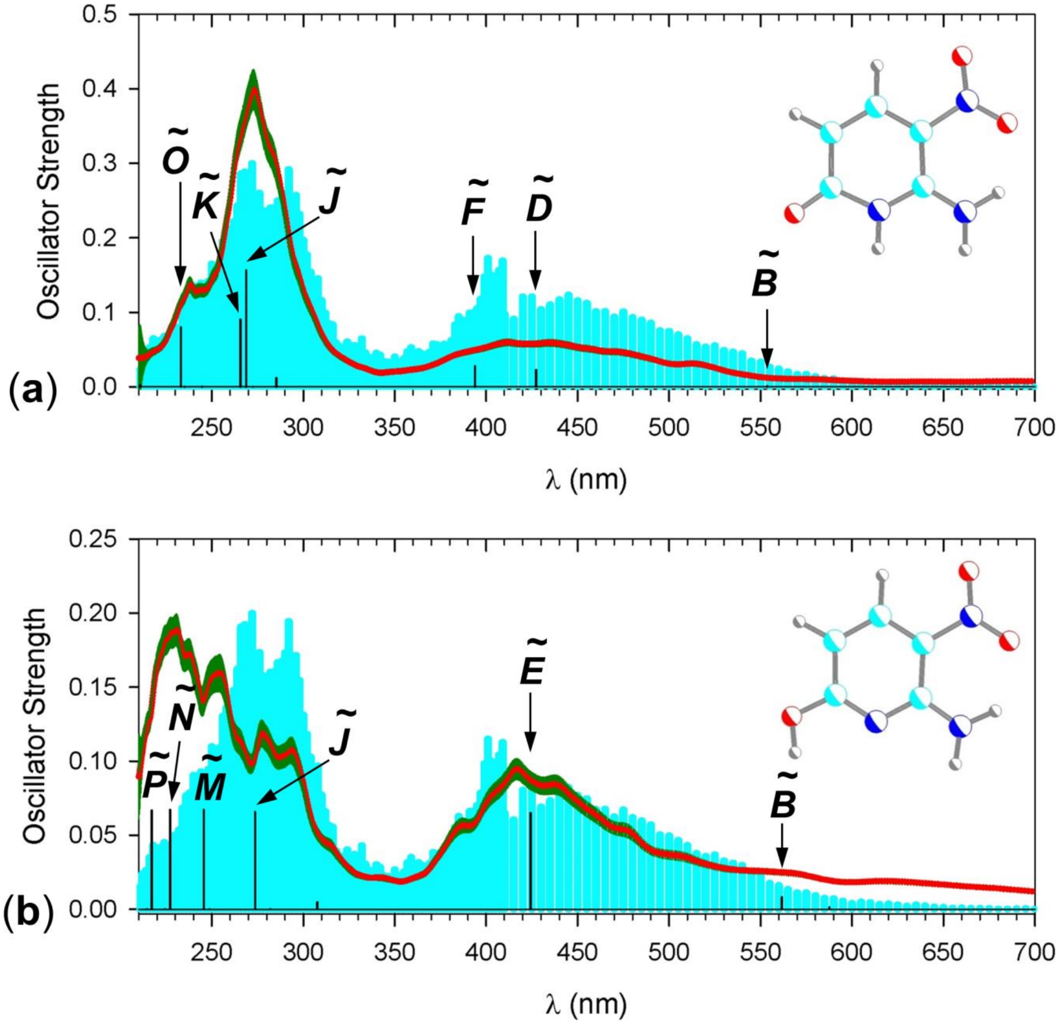

Figure 7. M06-2X/6-31+G(d,p) TD-DFT vibronic spectra of (a) **Z1$^{+\bullet}$** and (b) **Z2$^{+\bullet}$**. Vertical bars denote the electron transitions. Cyan background shows the action spectrum of **Z$^{+\bullet}$** scaled to fit the plot.

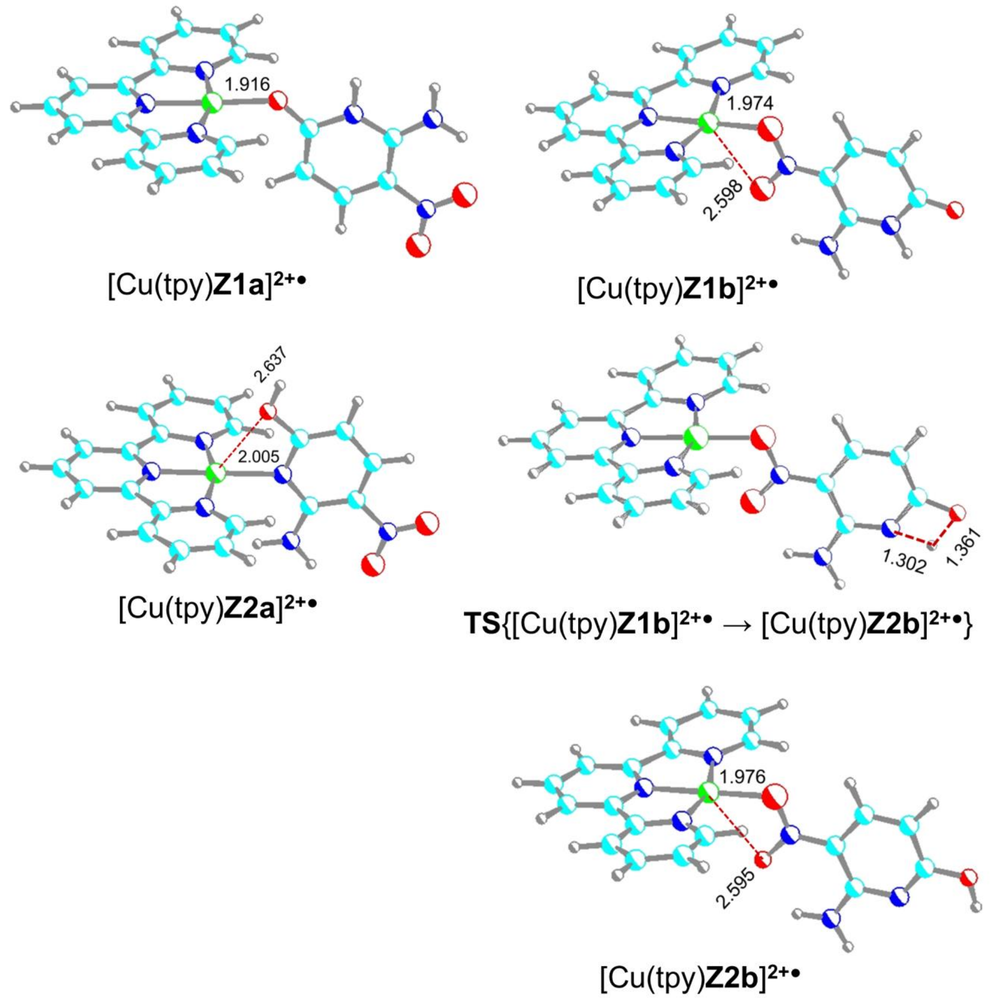

[Cu(tpy)**Z1a**]$^{2+\bullet}$ [Cu(tpy)**Z1b**]$^{2+\bullet}$

[Cu(tpy)**Z2a**]$^{2+\bullet}$ **TS**{[Cu(tpy)**Z1b**]$^{2+\bullet}$ → [Cu(tpy)**Z2b**]$^{2+\bullet}$}

[Cu(tpy)**Z2b**]$^{2+\bullet}$

Figure 8. CAM-B3LYP/6-311+G(2d,p) optimized structures of [Cu(tpy)**Z**]$^{2+\bullet}$ complexes

Chapter 6—UV-Vis Photodissociation Action Spectroscopy Reveals Cytosine-Guanine Hydrogen Transfer in DNA Tetranucleotide Cation Radicals upon One-Electron Reduction

Reproduced in part with permission from S.R. Huang, Y. Liu, F. Tureček, *J. Phys. Chem. B*, **2020**, 124, 3505-3517, DOI: 10.1021/acs.jpcb.0c01693.

6.1. Abstract

We report the generation and spectroscopic study of hydrogen-rich DNA tetranucleotide cation radicals $(GATC+2H)^{+\bullet}$ and $(AGTC+2H)^{+\bullet}$. The radicals were generated in the gas phase by one-electron reduction of the respective dications $(GATC+2H)^{2+}$ and $(AGTC+2H)^{2+}$, and characterized by collision-induced dissociation and photodissociation tandem mass spectrometry, and UV-Vis photodissociation action spectroscopy. Among several absorption bands observed for $(GATC+2H)^{+\bullet}$, the bands at 340 and 450 nm were assigned to radical chromophores. Time-dependent density functional theory calculations including vibronic transitions in the visible region of the spectrum were used to provide theoretical absorption spectra of several low-energy tetranucleotide tautomers having cytosine, adenine, and thymine-based radical chromophores that did not match the experimental spectrum. Instead, the calculations indicated the formation of a new isomer with the 7,8-H-dihydroguanine cation-radical moiety. The isomerization involved hydrogen migration from the cytosine N-3-H radical to the C-8 position in N-7-protonated guanine that was calculated to be 87 kJ mol^{-1} exothermic and had a low-energy transition state. Although the hydrogen migration was facilitated by the spatial proximity of the guanine and cytosine bases in the low-energy $(GATC+2H)^{+\bullet}$ intermediate formed by electron transfer, the reaction was calculated to have a large negative activation entropy. Rice-Ramsperger-Kassel-Marcus (RRKM) and transition state theory kinetic analysis indicated that the isomerization occurred rapidly in hot cation-radicals produced by electron transfer with the population-weighed rate constant of $k = 8.9 \times 10^{3}$ s^{-1}. The isomerization was calculated to be too slow to proceed on the experimental time scale in thermal cation-radicals at 310 K.

6.2. Introduction

Ionization of DNA by high-energy particles generates transient cation radicals that undergo subsequent chemical reactions.[1] Among those, reactions involving electron transfer along the DNA double strand have been investigated most frequently by experiments that focused on the kinetics and downstream analysis of radical products formed by reactions with solvent or other components in the reaction mixture.[2-6] In contrast to electron transfer, proton transfer between an ionized and neutral nucleobase has been considered to occur in guanine–cytosine (G–C) and adenine–thymine (A–T) Watson–Crick pairs. Experimental studies of oligonucleotides tagged with oxidizable groups have revealed rapid deprotonation of guanine cation radicals.[7,8] Proton transfer between base pairs has been investigated in solution[9-11] and studied in silico by density functional theory (DFT) calculations to indicate the proton recipient position.[12-18] In a gas-phase study of the G–C cation radical complex, O'Hair and co-workers have utilized infrared multiphoton dissociation action spectroscopy to assign the ion structure as resulting from a proton transfer between the nucleobases.[19] However, there have been few reports addressing the possibility of proton transfer along the DNA strand in cation radicals.[13]

Recently, we have generated several dinucleotide cation radicals in the gas phase and studied their structure and reactivity using UV–vis photodissociation (UVPD) action spectroscopy in combination with tandem mass spectrometry and time-dependent DFT calculations.[20-22] In our approach, the cation and radical moieties were generated on separate nucleobases in the form of the respective proton and hydrogen atom adducts. The nucleobase radicals have been found to have specific spectroscopic signatures when studied by UVPD action spectroscopy that allowed us to assign the position of the hydrogen atom determining the radical site. One feature that has been found by our studies was interbase hydrogen atom transfer that spontaneously occurred in $(AA+2H)^{+\bullet}$ and $(GG+2H)^{+\bullet}$ dinucleotide cation radicals within milliseconds of their formation.[20,21] We observed that, while interbase hydrogen transfer from $(C+H)^{\bullet}$ to $(G+H)^{+}$ was substantially exothermic and therefore thermodynamically favored, it occurred to a different extent in dinucleotide cation radicals $(CG+2H)^{+\bullet}$ and $(GC+2H)^{+\bullet}$ because of kinetic constraints imposed by the backbone conformation.[21] This raised the question of the thermodynamics, kinetics, and mechanism of hydrogen atom migration in larger oligonucleotide cation radicals. Here, we report the generation and spectroscopic investigation of tetranucleotide cation radicals containing combinations of all four DNA nucleobases, as in $(GATC+2H)^{+\bullet}$ and $(AGTC+2H)^{+\bullet}$. We wish to show that these large and complex systems are amenable to detailed structural analysis by UV–vis action spectroscopy and electronic structure calculations.

6.3. Experimental

6.3.1. Materials and Methods

DNA tetranucleotides GATC and AGTC were custom-synthesized by Integrated DNA Technologies (Coralville, IA) and used as received. Mass spectra were measured on a modified Bruker amaZon Speed 3D ion trap mass spectrometer equipped with an auxiliary ion source for electron transfer dissociation (ETD) and coupled to a laser.[23] The tetranucleotides were dissolved in 50:50:1 acetonitrile–water–acetic acid at 10–20 μM concentrations and electrosprayed into the ion trap. The doubly charged ions, $(GATC+2H)^{2+}$ or $(AGTC+2H)^{2+}$, were selected by mass and subjected to one-electron reduction by ion–ion reactions with fluoranthene anion radicals at a 150 ms reaction time. The resulting cation radicals were again selected by mass in the ion trap and probed by laser photodissociation. The laser beam was provided by an EKSPLA NL301G Nd:YAG laser (Altos Photonics, Bozeman, MT, USA) working at 20 Hz frequency and 3–6 ns pulse width. The photon pulses were treated by a PG142C unit (AltosPhotonics, Bozeman, MT, USA) which incorporated a third harmonic generator and optical parametric oscillator coupled with an optional second harmonic generator to enable wavelength tuning in the range of 210–700 nm. The laser beam (6 mm diameter) exiting the PG142C unit was aligned and focused into the ion trap. The laser pulse energies were measured at each experimental wavelength using an EnergyMax-USB J-10MB energy sensor (Coherent Inc., Santa Clara, CA, USA) to calibrate the action spectra. The measured photofragment ion intensities were normalized to the number of photons per pulse.

6.3.2. Calculations

Precursor $(GATC+2H)^{2+}$ dication structures were obtained for 18 combinations of protomers in which protons were placed in the basic positions on different nucleobases, which were N-7 on G, N-1 or N-3 on A, O-2 or O-4 on T, and N-3 or O-2 on C. Conformation analysis of the dications was performed by Born–Oppenheimer molecular dynamics (BOMD) calculations using the semiempirical all-valence-electron PM6 method[24] supplemented with corrections for dispersion and hydrogen bonding interactions, PM6-D3H4,[25] and run by MOPAC[26] under the Cuby4 platform,[27] as described previously.[22] BOMD trajectories were run for 20 ps at 410–610 K using the Berendsen thermostat algorithm.[28] Selected low-energy conformers from the BOMD runs of each protomer were reoptimized by density functional theory (DFT) calculations using the B3LYP,[29] ωB97X-D,[30] and M06-2X[31] hybrid functionals. The B3LYP calculations of dications were performed with the 6-31G(d,p) basis set to provide harmonic frequencies that were used to calculate ion enthalpies and entropies at the ion trap temperature (310 K). The ωB97X-D and M06-2X calculations were carried out with the 6-31+G(d,p) basis set to provide the electronic terms. The combined electronic, enthalpy, and entropy terms were combined to produce free energies that were used to rank conformers of each protomer. In addition, solvation energies in water were calculated with ωB97X-D/6-31+G(d,p) using the polarizable continuum model.[32] The lowest-free-energy gas-phase ions in each group were used for the selection of protomers in the charge-reduced tetranucleotide cation radicals. Cation radical structures were optimized by B3LYP and M06-2X calculations with the 6-31+G(d,p) basis set that were run within the spin unrestricted formalism. Single-point energies were calculated with M06-2X/6-311++G(2d,p) on the M06-2X/6-31+G(d,p) optimized geometries. Atomic spin densities were calculated using the natural population analysis[33] of the M06-2X/6-31+G(d,p) wave functions.

Based on our previous benchmarks,**[34]** we selected UM06-2X/6-31+G(d,p) for time-dependent DFT calculations**[35]** of an extensive set of vertical and vibronic transitions in the cation radicals. Vertical excitations were calculated for 90–145 excited states to probe transitions within the experimentally studied region of 210–700 nm. To calculate vibronic excitations, we used 300 Boltzmann-ranked ground-state configurations that were generated by the Newton X program(36) from the B3LYP/6-31+G(d,p) calculated harmonic normal modes of each cation radical at 310 K and submitted for TD-DFT calculations. The number of excited electronic states in these vibronic TD-DFT calculations (12–13) was chosen to include excitations with wavelengths down to ca. 270 nm, covering the structurally characteristic part of the experimental wavelength range of 210–700 nm. All of the electronic structure calculations were performed with the Gaussian 16 (revision A.03) suite of programs.**[37]** Rice–Ramsperger–Kassel–Marcus calculations**[38]** were run with a QCEP program**[39]** that was recompiled for Windows 7.**[40]** The calculations were performed in the 88–795 kJ mol^{-1} energy range with 2.092 kJ mol–1 (0.5 kcal mol^{-1}) steps and with a direct count of quantum states for the 387 and 386 normal modes in the reactant and transition state, respectively. Rotations were treated adiabatically, and the microcanonical k(E,J,K) rate constants were Boltzmann-averaged over the population of rotational states at 310 K. Transition state theory calculations used the standard formula with the M06-2X/6-311++G(2d,p) activation energy and partition functions based on B3LYP/6-31+G(d,p) normal-mode vibrational analysis.

6.4. Results & Discussion

6.4.1. Ion Formation

Cation radicals $(GATC+2H)^{+\bullet}$ and $(AGTC+2H)^{+\bullet}$ were generated from the tetranucleotides, as shown for $(GATC+2H)^{+\bullet}$ in Scheme 1. Electrospray ionization (ESI) of the tetranucleotide solutions produced the respective dications, $(GATC+2H)^{2+}$ and $(AGTC+2H)^{2+}$, as the dominant ion species at m/z 587.5 (Figure S1a,b, Supporting Information). The dications were isolated by mass and partially reduced by electron transfer in ion–ion reactions with fluoranthene anions. These reactions yielded (GATC+2H)$^{+\bullet}$ and (AGTC+2H)$^{+\bullet}$ cation radicals at m/z 1175 as the main products (Figure 1a,b), that were accompanied by fragment ions by loss of water (m/z 1157) and backbone cleavage (m/z 965). The cation radicals were isolated by mass and interrogated by MS^3 collision-induced dissociation (CID) and UVPD spectra.

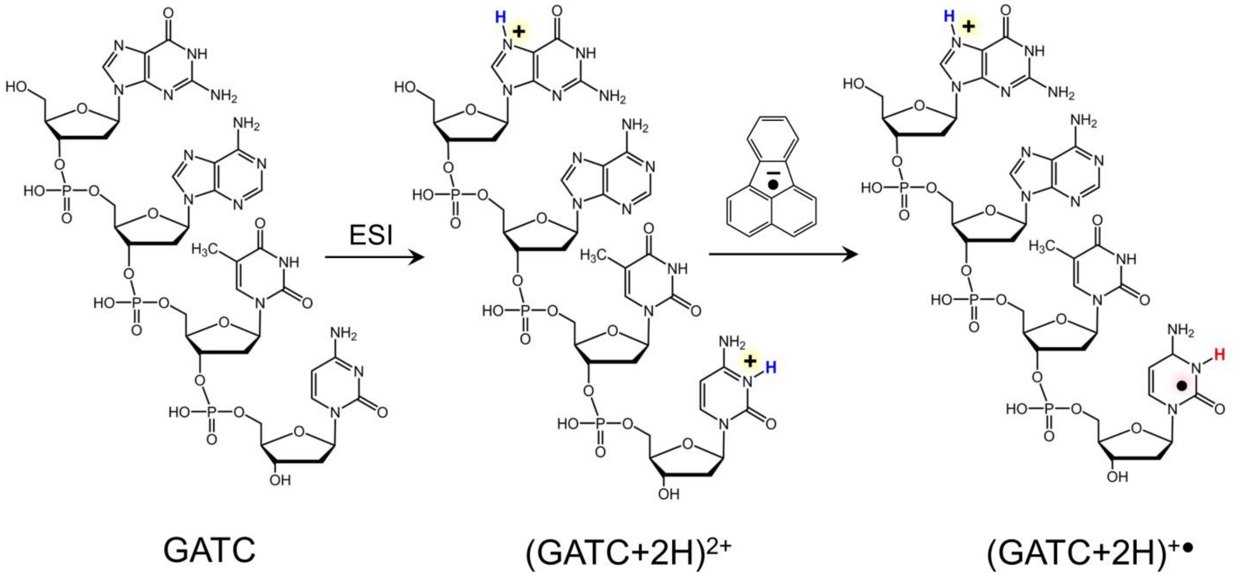

Scheme 1. Formation of (GATC+2H)$^{+\bullet}$.

CID of both (GATC+2H)$^{+\bullet}$ and (AGTC+2H)$^{+\bullet}$ (Figure 2a,b) proceeded with elimination of the dehydrocytidine radical moiety ($C_9H_{12}N_3O_3$, 210 Da) from the 3'-terminus, producing the dominant even-electron fragment ions at m/z 965 that were also observed to form spontaneously upon electron transfer (Figure 1a,b). This dissociation was analogous to the standard backbone cleavage and formation of d_3 ions upon fragmentation of even-electron nucleotide cations.[41,42] Loss of neutral 3'-cytosine (m/z 1064) and 5'-guanine (m/z 1024) nucleobases was observed as minor dissociations of (GATC+2H)$^{+\bullet}$ (Figure 2a), whereas loss of terminal nucleobases (A and C) from (AGTC+2H)$^{+\bullet}$ was negligible (Figure 2b). Consecutive dissociations of the d_3 ions were investigated by further CID-MS3 (Figure S2a,b, Supporting Information) and MS^4 (Figure S3a,b). These spectra revealed a loss of guanine (m/z 814) from both d_3 (GAT)$^+$ and d_3 (AGT)$^+$, whereas loss of adenine (m/z 830) was significant only from the

5’-position in d_3 (AGT)$^+$. The loss of the 5’-terminal nucleobase was followed by an elimination of the 3’-phosphoric acid, giving fragment ions at m/z 716 and 732 from d_3 (GAT)$^+$ and d_3 (AGT)$^+$, respectively. The nucleobase positions in these cations clearly affected the dissociations, with the 5’-base dissociating more readily.

6.4.2. Photodissociation and Action Spectra

UVPD of (GATC+2H)$^{+\bullet}$ was first investigated at 245 nm, where regular DNA[43-45] as well as DNA gas-phase ions have absorption bands.[20] The spectrum (Figure 3a) showed a dominant fragment ion at m/z 716 which we assigned to a secondary elimination of guanine and H_3PO_4 from the d_3 ion. Another possibility, the isobaric (z_3-C)$^+$ ion with the same theoretical $C_{25}H_{32}N_{17}O_{14}P_2$ composition, was less likely because of the absence in the spectrum of its z_3 precursor at m/z 827. The pulse-dependent measurement (inset in Figure 3a) showed a complete depletion of the (GATC+2H)$^{+\bullet}$ precursor ion after >6 laser pulses at 245 nm. The UVPD spectrum of (AGTC+2H)$^{+\bullet}$ (Figure 3b) was different, showing a dominant d_3 fragment ion at m/z 965 but little further dissociation by loss of nucleobases or H_3PO_4. A prominent fragment ion at m/z 412 can be assigned to the consecutive elimination of guanine and H_3PO_4 from the d_2^+ ion (m/z 661). The similarity of the CID and UVPD spectra is remarkable. Despite the different excitation modes and energetics, the spectra displayed the same type of dissociations that involved backbone cleavages and phosphoester eliminations. This indicated that the excited electronic states in the radicals accessed by UVPD were rapidly converted to vibrationally hot ground electronic states to drive the dissociations. This is analogous to the ultrafast internal conversion of excited electronic states in nucleobases and nucleosides, as studied in solution[46,47] and the gas phase.[48-51]

The fragment ions identified by single-wavelength UVPD were then used to monitor the action spectra of (GATC+2H)$^{+\bullet}$ and (AGTC+2H)$^{+\bullet}$ in the 210–700 nm range. The action spectrum of (GATC+2H)$^{+\bullet}$, when expressed as a sum of photofragment ion channels (Figure 4a), displayed several bands with maxima at 220, 250, 270, 290, 340, 450, and what appeared as a very weak band at 575 nm. The main contribution to the 220 nm band was from the d3+ fragment ion channel (Figure 4b) that also showed maxima at 280, 340, and 450 nm. The other major channel, represented by the m/z 716 ion, showed band maxima at 220, 270, 330, and 450 nm, The m/z 814 channel, assigned as $(d_3\text{-G})^+$, showed bands with maxima at 250, 300, 330, and 450 nm (Figure 4b).

The action spectrum of $(\text{AGTC+2H})^{+\bullet}$ (Figure 5a) displayed bands with maxima at 220, 255, 280, 330, and 570 nm, the last pertaining to a broad band stretching between 520 and 620 nm. The individual photofragment channels were represented by the d_3^+ ion (m/z 965) with maxima at 220, 270, 290, 335, and 570 nm, and the m/z 412 ion appearing at 260 and 320 nm (Figure 5b). Overall, the action spectra of $(\text{GATC+2H})^{+\bullet}$ and $(\text{AGTC+2H})^{+\bullet}$ displayed differences in both the intensities of the bands in the visible region of the spectrum and the contributions of individual fragmentation channels to bands at 260 and 340 nm. In particular, the channels represented by consecutive dissociations, such as those of $(d_3\text{-G})^+$ and $(d_3\text{-G-}H_3PO_4)^+$, were more intense with $(\text{GATC+2H})^{+\bullet}$.

The action spectra of $(\text{GATC+2H})^{+\bullet}$ and $(\text{AGTC+2H})^{+\bullet}$ were substantially different from the gas-phase absorption spectra of neutral adenine and guanine that have been reported by Clark et al. to display major bands with maxima at 252 and 274 nm, respectively.[45] The spectra of gas-phase thymine and cytosine have not been reported although calculations by Sapunar et al. have suggested absorption bands with maxima at 253 nm for thymine and 292 and 235 nm for cytosine.[43] Thus, the 250-280 nm bands in the action spectra of the cation radicals may indicate absorption by neutral nucleobases. In contrast, the long-wavelength bands at $\lambda > 300$ nm can be unequivocally assigned to radical chromophores produced by electron transfer. We also obtained reference action spectra of singly and doubly protonated GATC and AGTC (Supporting Figure S4a,b and Figure S5a,b, respectively) that were quite similar to the action spectra of dinucleotide mono- and dications reported previously.[20] In particular, the spectra of both $(GATC+2H)^{2+}$ and $(GATC+H)^{+}$ showed composite bands with maxima at 265 nm, another intense band below 210 nm, but no absorption above 300 nm (Figure S4a,b).

6.4.3. Precursor Dication Structures

To interpret the action spectra of the cation radicals and assign structures, we undertook a systematic computational study of precursor dications and cation radicals produced upon one-electron reduction. First, we addressed the question of protonation sites in the tetranucleotides to assess the energetically favorable dication protomers and their conformations in the gas phase. The energetically favored protonation sites in nucleobases and nucleosides have been studied previously by experiment and theory.[51-61] The standard numbering of ring positions in DNA nucleobases is shown in Scheme 2.

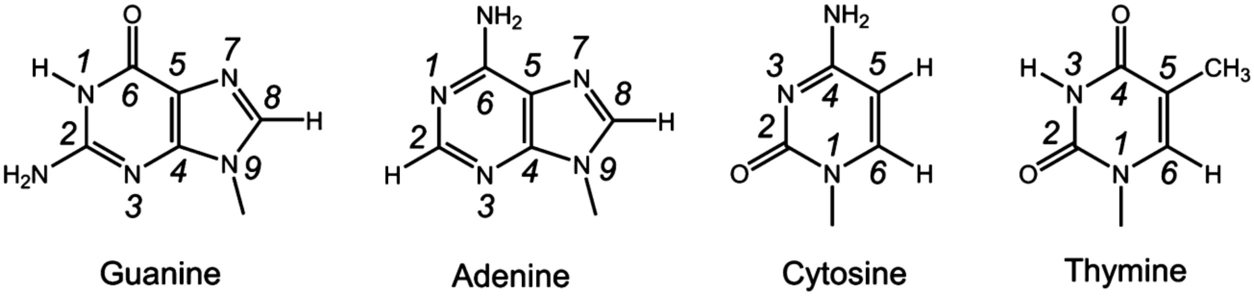

Scheme 2. Ring-Position Numbering in DNA Nucleobases.

Adenine is known to favor protonation at N-1, with N-3 and N-7 being the other possible protonation sites.[51,52,54,55] Guanine favors protonation at N-7 and, to a lesser extent, O-6.[52,53,56,57] Cytosine is promiscuous in that it favors protonation at N-3 and O-2 to a very similar extent.[58–61] Thymine, which is the least basic DNA nucleobase,[62] favors protonation at O-2 and O-4.[60] By combining these protonation sites for placing two protons in different nucleobases in $(GATC+2H)^{2+}$, we generated 18 theoretical protomers. These were labeled according to the proton positions; for example, G7C3 refers to the structure protonated at guanine N-7 and cytosine N-3. For each protomer, we generated several initial ad hoc conformations that were subjected to BOMD calculations yielding 20 ps trajectories at 310 K. After selecting 200 conformers at 100 fs intervals from each trajectory, the structures were fully gradient-optimized with the goal of identifying the lowest energy conformers. Selected low-energy structures from this round of geometry optimizations were further reoptimized with B3LYP to provide harmonic frequencies and identify local energy minima. One hundred B3LYP structures were used for the final rounds of optimizations that were performed with ωB97X-D and M06-2X and the 6-31+G(d,p) basis set. Single-point M06-2X energies and ωB97X-D solvation energies in water were also obtained, and the dications were ranked by free energy (Table 1). The M06-2X/6-311++G(2d,p) relative energies are discussed in the text. The Table 1 data indicated that the energetically favored protonation motifs in the order of increasing free energies were G7C3, G7A1, G7A3, A1C2, A1C3, and A3C2 that had at least one conformer within 30 kJ mol^{-1} of the G7C3 global minimum. The structures of the lowest-energy conformers of each protonation motif are shown in Figure 6. Since the dications were formed by protonation in electrospray microdroplets and then transferred to the gas phase containing the solvent vapor, relative free energies in both solution and the gas phase can play a role in determining the tautomer formation.

The lowest free-energy dication structure in both the gas phase and aqueous environment (G7C3a) had a zwitterionic structure in which a phosphoester proton moved to the adenine N-3 position (Figure 6). This structure showed two very short hydrogen bonds, one at 1.436 Å for adenine N3-H…O-P and the other at 1.471 Å for guanine N7-H…O-P. In contrast, the only internucleobase hydrogen bond in G7C3a was between C-N3-H and T-O2. The ωB97X-D-optimized structure of G7C3a (Figure S6, Supporting Information) showed slightly longer N3-H…O-P and N7-H…O-P H-bonds but overall was very similar to that from M06-2X. This indicated that the tight H-bonding of 5’-guanine to the phosphate and the 3’-OH contributed to a folded structure in which the guanine and cytosine nucleobases were in proximity. Such a folding of nucleotide dications, as presented by G7C3a, is unprecedented. For example, low-energy conformers of (GC+2H)$^{2+}$ and (CG+2H)$^{2+}$ have been found to prefer extended structures, minimizing Coulomb repulsion between the charged nucleobases. Evidently, increasing both the size of the dication and the number of intramolecular hydrogen bonds in tetranucleotides overcomes charge repulsion interactions to allow low-energy folded structures to develop.

The pairing of the formally distant protonated 5’-G and neutral 3’-C was also indicated for the second lowest energy gas-phase structure G7A1a (Figure 6). This ion showed two G-C hydrogen bonds, and the conformation was further buttressed by H bonding between the adjacent A and T, resulting in separated G-C and A-T pairs. Hydrogen bonding between protonated and neutral nucleobases occurred to various extents in the other low-energy dication isomers. Strong G–C hydrogen bonds were found in structures G7A3, A1C2, A1C3a, G7A1b, A1C3b, and A3C2b. Structure A1C3b, which was substantially stabilized by solvation in water, showed G-T and C-T hydrogen bonds, whereas the protonated adenine ring was not internally solvated. Other combinations of internucleobase hydrogen bonding were G-A and C-T in G7C3b and G-T in A3C2a (Figure 6).

6.4.4. Cation Radical Structures Following Electron Attachment

The structures of low-energy dications served as starting points for the geometry optimization and conformational analysis of cation radicals. Attachment of an electron to $(GATC+2H)^{2+}$ dications of the G7C3 type resulted in several cation radicals from which we selected two lowest-energy conformers, G7rC3a and G7rC3b (Figure 7, Table 2). Radical G7rC3a had a high spin density in the reduced cytosine ring, as indicated by the calculated NPA spin populations.[33] Interestingly, the structural features that were characteristic of the precursor dication (G7C3a), which were the G-C hydrogen bonds and the A-N-3-H^{+}…$^{-}$O-P zwitterion dipole, were largely conserved in G7rC3a. In contrast, electron attachment leading to G7rC3b triggered substantial conformation changes. This cation radical also had a reduced cytosine ring, which, however, was not H-bonded to the other nucleobases. Instead, G7rC3b developed hydrogen bonds between the protonated guanine and neutral thymine and adenine bases, resulting in a globular conformation (Figure 7) that was disfavored against G7rC3a by low entropy.

The low-energy cation radical produced from dications of the G7A1 type (G7A1rT) had a more unusual structure, showing a radical site in a thymine hydrogen adduct (Figure 8). This was likely created by intramolecular proton transfer from G-N-7-H to an intermediate thymine anion radical formed by electron capture. Related zwitterionic intermediates with protonated G and A and anion-radical T were obtained as local energy minima but were at substantially higher energies than G7A1rT. Cation radical G7A1rT displayed a large number of internucleobase hydrogen bonds, resulting in a globular structure of low entropy.

Electron attachment to dications of the G7A3 type produced adenine radicals with only minor changes of the conformation relative to the precursor dication G7A3, as illustrated with G7rA3 (Figure 8), which was the lowest-energy conformer in this group. Reduction of dications of the A1C2, A1C3, and A3C3 type yielded cytosine radicals, as illustrated by the respective lowest-energy conformers within each group, A1rC2, A1rC3, and A3rC3 (Figure 7). Finally, reduction of A3C2 dications placed the electron in the adenine ring in low-energy cation radicals such as rA3C2 (Figure 8). Overall, the cation radicals of different protonation types showed a larger spread of relative energies than did the respective dications.

To assign the experimental action spectrum of $(GATC+2H)^{+\bullet}$, we first obtained electronic excitation energies and absorption band intensities for 60–100 excited states of low-energy $(GATC+2H)^{+\bullet}$ cation radicals to cover the experimental wavelength range down to below 210 nm. The excited states were calculated by TD-DFT M06-2X/6-31+G(d,p) that we have previously benchmarked on equation-of-motion coupled cluster calculations of nucleobase cation radicals.[34] The calculated spectra of all of the cytosine-based radicals (G7rC3a, G7rC3b, A1rC3, A3rC3, and A1rC2 (Figure S7a–e, Supporting Information) as well as the thymine-based radical G7A1rT (Figure S7f) showed very weak bands at $\lambda > 300$ nm that were incompatible with the action spectrum of $(GATC+2H)^{+\bullet}$. The adenine-based radicals G7rA3 and rA3C2 showed weak bands in the 480–560 nm interval (Figure S7g,h) but again no significant absorption in the

300–380 nm range that could match the band in the action spectrum. The calculated electronic transitions are summarized in Supporting Tables S1–S11.

6.4.5. Cytosine-Guanine Isomerization

The above-described results indicated that the GATC cation radicals did not retain the expected primary cytosine or adenine radical units after being generated by electron transfer to the protonated nucleobases. To interpret the experimental data, we considered other chromophores formed by isomerization of the lowest-energy charge-reduced structures. Cation radical G7rC3a had a close interaction between the protonated guanine and radical-carrying cytosine rings that led to a low-energy transition state (TS_{mig}) for cytosine N-3-H migration to the C-8 position in guanine (Scheme 3). The optimized geometry of TS_{mig} indicated that it was an early transition state that was only 68 kJ mol^{-1} above the G7rC3a reactant (Table 2). The isomerization was exothermic (ΔH_0 = -87 kJ mol^{-1}, Table 2), yielding 7,8-dihydroguanine cation radical rG78a (Scheme 3). Another dihydroguanine cation radical conformer of ΔH_0 = −51 kJ mol^{-1} (rG78b, Table 2) could also be formed exothermically from G7rC3a. It is noteworthy that the isomerization within the G-C system also resulted in a proton transfer from adenine N-3-H to the proximate phosphate anion, collapsing the zwitterion and reforming the neutral adenine base (Scheme 3). An alternative isomerization of G7rC3b by cytosine hydrogen migration to adenine C-8 was also substantially exothermic to form radical G7rA8 (ΔH_0 = -72 kJ mol^{-1}, Table 2). However, an interaction between the 3'-terminal cytosine and internal adenine rings to allow N-3-H atom migration would require a substantial reorganization of the ion conformation to reach the transition state. In particular, the TS for the H-migration favored a near linear arrangement of the involved C-8…H…N-3 atoms which was 154° in TS_{mig} (Scheme 3). Such an arrangement was difficult to achieve for the C → A migration where it was expected to result in an interruption of multiple hydrogen bonds in G7rC3b, which would be associated with a substantial increase of potential energy and a higher-energy transition state.

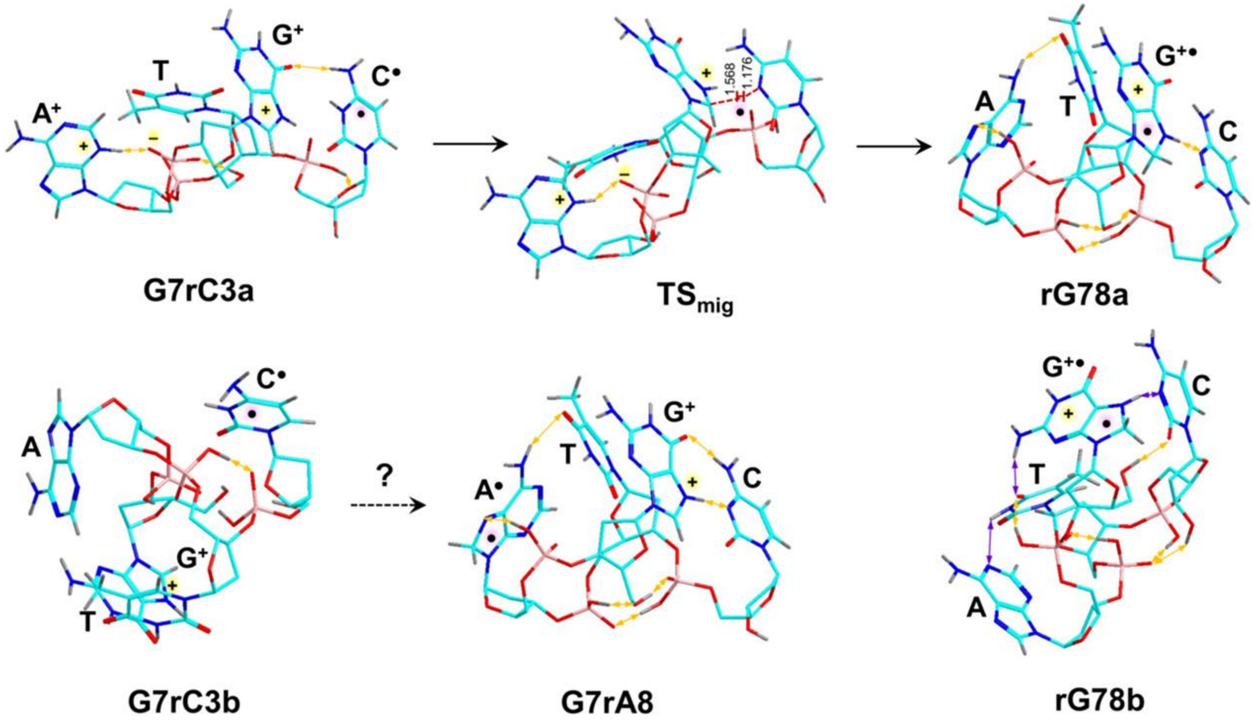

Scheme 3. Isomerization of (GATC+2H)$^{+\bullet}$ Cation Radicals.

TD-DFT absorption spectra were calculated for rG78a, rG78b, and G7rA8, including vibronic transitions for 12-13 excited states (Figure 9a-c). The limited number of excited states in these calculations was dictated by the large number of vibrational configurations (300) in the ground-state cation radicals to be considered for TD-DFT vertical excitations in these rather large open-shell systems of 1773 basis functions (2964 primitive gaussians). All three spectra showed transitions in the 300-400 nm region that were vibronically broadened beyond 450 nm for rG78a and G7rA8, and even beyond 550 nm for rG78b. The effect on the vibronic spectra of the ion conformation in rG78a and rG78b was remarkable, and it can be attributed to an enhancement of transition moments to the dark ***B*** (for rG78a) and ***B*** and ***C*** (for rG78b) states in thermal ions (Supporting Tables S9-S11). The low (***A***-***D***) excited states corresponded to π → π* transitions within the dihydroguanine moiety, as shown for rG78a (Figure 10). No G → T* charge-transfer excitation was indicated for the low excited states that could have been facilitated by the thymine proximity and electron affinity.**[62]** This can be explained by the unfavorable orientation of the interacting dipoles that are nearly perpendicular due to the position of the guanine and thymine rings in rG78a (Scheme 3). On the basis of spectra match and isomerization feasibility, we assigned rG78a as the dominant component of $(GATC+2H)^{+\bullet}$ cation radicals produced by electron transfer.

6.4.6. Energetics and Kinetics of $(GATC+2H)^{+\bullet}$ Formation

The observation of nondissociating cation radicals upon electron-transfer reduction of $(GATC+2H)^{2+}$ and (AGTC+2H)2+ raised the question of the electron transfer energetics and the cation radical stability. Previous studies of DNA dinucleotides and RNA dinucleotide chimeras have reported extensive dissociation of cation radicals upon electron transfer.[20,21] In contrast, hexanucleotide cation radicals have been reported to be stable when produced by electron transfer to the corresponding dications.[63] The energetics of the cation radical formation was evaluated from the enthalpies of the ion–ion reactions for $(GATC+2H)^{2+}$ (eq. 1):

$$(GATC+2H)^{2+} + \text{fluoranthene}^{-\bullet} \rightarrow (GATC+2H)^{+\bullet} + \text{fluoranthene} \qquad \text{(eq. 1)}$$

A previous study of the electron transfer energetics concluded that electron detachment from the anion forms the fluoranthene molecule in its ground (S_0) electronic state.[64] Thus, the energy balance in eq 1 (ΔH_{rxn}) can be expressed by the enthalpy terms for the ground states of the reactants and products, according to eq 2, where ΔH_f are the pertinent enthalpies of formation at the experimental temperature, RE < 0 is the adiabatic recombination energy of $(GATC+2H)^{+\bullet}$, and EA > 0 is the electron affinity of fluoranthene.[64]

$$\Delta H_{rxn} = \Delta H_f(\text{fluoranthene}) + \Delta H_f(GATC+2H)^{+\bullet} - \Delta H_f(\text{fluoranthene})^{-\bullet} - \Delta H_f(GATC+2H)^{2+}$$
$$= RE(GATC+2H)^{+\bullet} + EA(\text{fluoranthene}) \qquad \text{(eq. 2)}$$

The $RE(GATC+2H)^{+\bullet}$ was calculated as -562 kJ mol^{-1}, which was combined with the calculated EA(fluoranthene) = 82 kJ mol^{-1} to give ΔH_{rxn} = -486 kJ mol^{-1}. Note that, in this estimate, we used the calculated EA(fluoranthene) rather than the reported experimental value (61 kJ mol^{-1})**[65]** in an effort to in part compensate the inaccuracies of DFT calculated energies. The ΔH_{rxn} is partitioned between the reaction products to increase their internal energy. We presumed that the partitioning proceeded by the relative vibrational and rotational heat capacities in (GATC+2H)$^{+\bullet}$ (68.5 J mol^{-1} K^{-1}) and fluoranthene (10.6 J mol^{-1} K^{-1}), providing an initial vibrational excitation in (GATC+2H)$^{+\bullet}$ as ΔE_{ET} = 486 × 68.5/(68.5 + 10.6) = 412 kJ mol^{-1} (Figure 11). The total energy of (GATC+2H)$^{+\bullet}$ was then obtained as a convolution of the ET excitation energy and the internal (vibrational) energy distribution in the (GATC+2H)$^{2+}$ precursor dication that was based on the vibrational state count at 310 K. This gave the maximum of the internal energy distribution in (GATC+2H)$^{+\bullet}$ formed by electron transfer as E_{max} = 604 kJ mol^{-1} with the distribution shown in Figure 11.

The internal energy distribution was used to calculate the distribution-weighed RRKM rate constant (k_{isom}) for the exothermic isomerization of G7rC3a to rG78a (eq 3), where k(E) is the RRKM rate constant. The calculated RRKM rate constants are shown in Figure 11.

$$k_{isom} = \int_{E_{TS}}^{\infty} k(E)P(E)dE \qquad \text{(eq. 3)}$$

Using the shifted P(E) function from Figure 11, one obtains $k_{isom} = 8.9 \times 10^{3}$ s^{-1}, indicating >99% isomerization within 1 ms and a complete isomerization on the experimental time scale of 150 ms. However, because of the He buffer gas in the ion trap, the hot ions formed by ET are expected to undergo collisional cooling that can be expressed as a competitive first order process**[64]** (eqs. 4-7) where in brackets are the time-dependent mole fractions and k_{cool} is the cooling rate constant.

$$-\frac{[G7rC3a]_{hot}}{dt} = -(k_{isom} + k_{cool})[G7rC3a]_{hot} \qquad \text{(eq. 4)}$$

$$\frac{d[rG78a]}{dt} = k_{isom}[G7rC3a]_{hot} \qquad \text{(eq. 5)}$$

$$\frac{d[G7rC3a]_{cool}}{dt} = k_{cool}[G7rC3a]_{hot} \qquad \text{(eq. 6)}$$

$$x(\mathrm{G7rC3a}) = [\mathrm{G7rC3a}]_{hot} + [\mathrm{G7rC3a}]_{cool} \qquad \text{(eq. 7)}$$

Solution of eqs 4–6 gave the mole fraction of isomerized rG78a, as shown in eq 8:

$$x_{\mathrm{G7rC3a}} = \int_{E_{TS}}^{\infty} \frac{k_{isom}(E)}{k_{isom}(E)+k_{cool}} \left\{1-e^{-(k_{isom}(E)+k_{cool})t}\right\} P(E)dE \qquad \text{(eq. 8)}$$

Since we do not know the energy dependence of the cooling rate, we considered a typical range of 100-500 s-1.**64** According to eq 8, this gave x_{rG78a} = 0.986-0.935, indicating that >93% of the primary $(\mathrm{GATC+2H})^{+\bullet}$ radicals can be expected to isomerize to the more stable rG78a. In contrast, following thermalization to 310 K, the calculated transition-state-theory rate constant (k_{therm} = 0.049 s^{-1}) would allow only 0.7% isomerization on the 150 ms time scale of the measurement (Supporting Table S12). The isomerization was substantially slowed down by a negative entropy change in the TS, ΔS_{TS} = -49.5 J mol^{-1} K^{-1} at 310 K. Likewise, RRKM calculations for k_{isom}, when averaged over the vibration state distribution in G7rC3a at 310 K (k_{isom} = 0.031 s^{-1}), indicated negligible (0.5%) isomerization. These results strongly suggested that the isomerization was driven by vibrational excitation acquired upon electron transfer.

The threshold energy for the dissociation of rG78r to the d_3 fragment ion and the dehydrocytidine radical $w1^{\bullet}$ (Scheme 4) was calculated as 159 kJ mol^{-1}, which provided the lower limit for the transition-state energy. We note that the cytosine radical $w1^{\bullet}$ was not the lowest-energy neutral fragment, as the ribose-C-4 radical isomer $w1'^{\bullet}$ was 30 kJ mol^{-1} more stable (Scheme 4). We did not attempt to computationally locate the transition states and intermediates for the potentially complicated backbone cleavage involving a phosphoester elimination. The fact that the dissociation proceeded to ca. 30% over 150 ms (Figure 1a) indicated an effective rate constant of ca. 2.5 s^{-1}. The dissociation was expected to exhibit a substantial kinetic shift (ΔE_{kin}).**66** Figure 10 shows that the kinetic shift for the G7rC3a → rG78a isomerization was 233 kJ mol^{-1} to give k_{isom} = 2.5 s^{-1}.

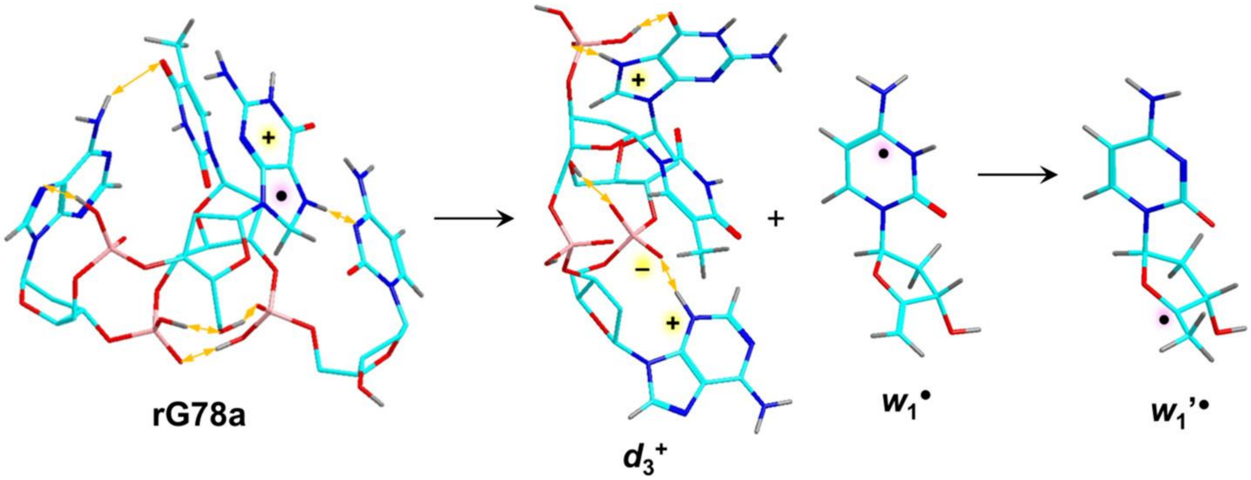

Scheme 4. Dissociation of rG78a.

Considering a similar kinetic shift for the dissociation and combining it with the estimated excitation energy from ET (412 kJ mol^{-1}), one can estimate the TS energy for the d$_3$ ion formation at ca. 200 kJ mol^{-1}.

6.5. Conclusions

The results of this combined experimental and computational study allow us to arrive at the following conclusions. Stable tetranucleotide DNA cation radicals are formed by electron transfer to dications generated by electrospray ionization. UV–vis photodissociation of the mass-selected cation radicals follows fragmentations that are similar to those induced by collisional activation. This indicates that the excited electronic states accessed by photon absorption undergo fast internal conversion to highly excited vibrational states of the ground electronic state. The de-excitation of the cation radicals is probably analogous to the ultrafast internal conversion of excited electronic states in nucleobases, as previously studied by fast spectroscopy in solution. Interpretation of the UV–vis action spectra by TD-DFT vibronic analysis indicated that the cytosine-based radicals that were initially formed by electron transfer underwent fast rearrangement by hydrogen migration, forming low-energy 7,8-dihydroguanine cation radicals. The rearrangement was facilitated by the proximity of the cytosine and guanine nucleobases in the charge-reduced cation radicals and proceeded via a low-energy transition state that was characterized computationally and by reaction kinetics analysis. The present results further indicate that the structure and properties of simpler systems, such as dinucleotide radicals, cannot be readily extrapolated to larger, more complex, oligonucleotides with more intricate networks of intramolecular interactions between the nucleobases. The tetranucleotide cation radicals studied here represent the current limit of size and complexity that is amenable to computational analysis of vibronic UV–vis absorption spectra. Further research with larger DNA oligonucleotide radicals, including those produced from DNA duplexes, is likely to rely on experimental action spectroscopy and empirical assignment of radical-related chromophores.

6.6. References

1. Kanvah, S.; Joseph, J.; Schuster, G. B.; Barnett, R. N.; Cleveland, C. L.; Landman, U. Oxidation of DNA: Damage to Nucleobases. *Acc. Chem. Res.* **2010**, 43, 280-287, DOI:10.1021/ar900175a
2. Murphy, C. J.; Arkin, M. R.; Jenkins, Y.; Ghatlia, N. D.; Bossmann, S. H.; Turro, N. J.; Barton, J. K. Long-Range Photoinduced Electron-Transfer through a DNA Helix. *Science* **1993**, 262, 1025-1029, DOI:10.1126/science.7802858
3. Giese, B.; Amaudrut, J.; Kohler, A.-K.; Spormann, M.; Wessely, S. Direct Observation of Hole Transfer through DNA by Hopping between Adenine Bases and by Tunneling. *Nature* **2001**, 412, 318-320, DOI:10.1038/35085542
4. Shao, F.; Augustyn, K.; Barton, J. K. Sequence Dependence of Charge Transport through DNA Domains. *J. Am. Chem. Soc.* **2005**, 127, 17445-17452, DOI:10.1021/ja0563399
5. Takada, T.; Kawai, K.; Fujitsuka, M.; Majima, T. Direct Observation of Hole Transfer through Double-Helical DNA over 100 A. *Proc. Natl. Acad. Sci. U. S. A.* **2004**, 101, 14002-14006, DOI:10.1073/pnas.0402756101

6. Lewis, F. D.; Daublain, P.; Cohen, B.; Vura-Weis, J.; Wasielewski, M. R. The Influence of Guanine on DNA Hole Transport Efficiency. *Angew. Chem., Int. Ed.* **2008**, 47, 3798-3800, DOI:10.1002/anie.200705903
7. Kobayashi, K.; Tagawa, S. Direct Observation of Guanine Radical Cation Deprotonation in Duplex DNA Using Pulse Radiolysis. *J. Am. Chem. Soc.* **2003**, *125*, 10213-10218, DOI: 10.1021/ja036211w
8. Kobayashi, K.; Yamagami, R.; Tagawa, S. Effect of Base Sequence and Deprotonation of Guanine Cation Radical in DNA. *J. Phys. Chem. B* **2008**, *112*, 10752– 10757, DOI: 10.1021/jp804005t
9. Ghosh, A. K.; Schuster, G. B. Role of the Guanine N1 Imino Proton in the Migration and Reaction of Radical Cations in DNA Oligomers. *J. Am. Chem. Soc.* **2006**, *128*, 4172– 4173, DOI: 10.1021/ja0573763
10. Choi, J.; Tojo, S.; Ahn, D.-S.; Fujitsuka, M.; Miyamoto, S.; Kobayashi, K.; Ihee, H.; Majima, T. Proton Transfer Accompanied by the Oxidation of Adenosine. *Chem. - Eur. J.* **2019**, *25*, 7711– 7718, DOI: 10.1002/chem.201900732
11. Choi, J.; Cho, D. W.; Tojo, S.; Fujitsuka, M.; Majima, T. Structural Study of Various Substituted Biphenyls and Their Radical Anions Based on Time-Resolved Resonance Raman Spectroscopy Combined with Pulse Radiolysis. *J. Phys. Chem. A* **2015**, *119*, 851– 856, DOI: 10.1021/jp511229t
12. Kumar, A.; Sevilla, M. D. Influence of Hydration on Proton Transfer in the Guanine-Cytosine Radical Cation ($G^{\bullet+}$-C) Base Pair: A Density Functional Theory Study. *J. Phys. Chem. B* **2009**, *113*, 11359– 11361, DOI: 10.1021/jp903403d
13. Rodriguez-Santiago, L.; Noguera, M.; Bertan, J.; Sodupe, M. Hydrogen Bonding and Proton Transfer in Ionized DNA Base Pairs, Amino Acids and Peptides. In *Quantum Biochemistry*; Matt, C. F., Ed.; Wiley-VCH: Weinheim, Germany, 2010; pp 219– 242

14. Bertran, J.; Oliva, A.; Rodriguez-Santiago, L.; Sodupe, M. Single versus Double Proton-Transfer Reactions in Watson-Crick Base Pair Radical Cations. A Theoretical Study. *J. Am. Chem. Soc.* **1998**, *120*, 8159– 8167, DOI: 10.1021/ja9804417

15. Colson, A. O.; Besler, B.; Sevilla, M. D. Ab initio Molecular Orbital Calculations on DNA Base Pair Radical Ions: Effect of Base Pairing on Proton-Transfer Energies, Electron Affinities, and Ionization Potentials. *J. Phys. Chem.* **1992**, *96*, 9787– 9794, DOI: 10.1021/j100203a039

16. Hutter, M.; Clark, T. On the Enhanced Stability of the Guanine-Cytosine Base Pair Radical Cation. *J. Am. Chem. Soc.* **1996**, *118*, 7574– 7577, DOI: 10.1021/ja953370+

17. Li, X. F.; Cai, Z. I.; Sevilla, M. D. Investigation of Proton Transfer within DNA Base Pair Anion and Cation Radicals by Density Functional Theory (DFT). *J. Phys. Chem. B* **2001**, *105*, 10115– 10123, DOI: 10.1021/jp012364z

18. Li, X. F.; Cai, Z. I.; Sevilla, M. D. Energetics of the Radical Ions of the AT and AU Base Pairs: A Density Functional Theory (DFT) Study. *J. Phys. Chem. A* **2002**, *106*, 9345– 9351, DOI: 10.1021/jp021322n

19. Feketeova, L.; Chan, B.; Khairallah, G. N.; Steinmetz, V.; Maitre, P.; Radom, L.; O’Hair, R. A. J. Watson-Crick Base Pair Radical Cation as a Model for Oxidative Damage in DNA. *J. Phys. Chem. Lett.* **2017**, *8*, 3159– 3165, DOI: 10.1021/acs.jpclett.7b01251

20. Korn, J. A.; Urban, J.; Dang, A.; Nguyen, H. T. H.; Turecek, F. UV-Vis Action Spectroscopy Reveals a Conformational Collapse in Hydrogen-Rich Dinucleotide Cation Radicals. *J. Phys. Chem. Lett.* **2017**, *8*, 4100– 4107, DOI: 10.1021/acs.jpclett.7b01856

21. Liu, Y.; Korn, J. A.; Dang, A.; Turecek, F. Hydrogen-Rich Cation Radicals of DNA Dinucleotides. Generation and Structure Elucidation by UV-Vis Action Spectroscopy. *J. Phys. Chem. B* **2018**, *122*, 9665– 9680, DOI: 10.1021/acs.jpcb.8b07925

22. Liu, Y.; Korn, J. A.; Turecek, F. UV-Vis Action Spectroscopy and Structures of Hydrogen-Rich 2′-Deoxycytidine Dinucleotide Cation Radicals. A Difficult Case. *Int. J. Mass Spectrom.* **2019**, *443*, 22– 31, DOI: 10.1016/j.ijms.2019.05.016
23. Dang, A.; Korn, J. A.; Gladden, J.; Mozzone, B.; Tureček, F. UV-Vis Photodissociation Action Spectroscopy on Thermo LTQ-XL ETD and Bruker amaZon Ion Trap Mass Spectrometers: A Practical Guide. *J. Am. Soc. Mass Spectrom.* **2019**, *30*, 1558– 1564, DOI: 10.1007/s13361-019-02229-z
24. Stewart, J. J. P. Optimization of Parameters for Semi-Empirical Methods V: Modification of NDDO Approximations and Applications to 70 Elements. *J. Mol. Model.* **2007**, *13*, 1173– 1213, DOI: 10.1007/s00894-007-0233-4
25. Řezáč, J.; Fanfrlík, J.; Salahub, D.; Hobza, P. Semi-Empirical Quantum Chemical PM6Method Augmented by Dispersion and H Bonding Correction Terms Reliably Describes Various Types of Noncovalent Complexes. *J. Chem. Theory Comput.* **2009**, *5*, 1749– 1760, DOI: 10.1021/ct9000922
26. Stewart, J. J. P. *MOPAC 16*; Stewart Computational Chemistry: Colorado Springs, CO, 2016.
27. Řezáč, J. Cuby: An Integrative Framework for Computational Chemistry. *J. Comput. Chem.* **2016**, *37*, 1230– 1237, DOI: 10.1002/jcc.24312
28. Berendsen, H. J.; Postma, J. V.; van Gunsteren, W. F.; DiNola, A. R. H. J.; Haak, J. R. Molecular Dynamics with Coupling to an External Bath. *J. Chem. Phys.* **1984**, *81*, 3684– 3690, DOI: 10.1063/1.448118
29. Becke, A. D. Density-Functional Exchange-Energy Approximation with Correct Asymptotic Behavior. *Phys. Rev. A: At., Mol., Opt. Phys.* **1988**, *38*, 3098– 3100, DOI: 10.1103/PhysRevA.38.3098

30. Chai, J. D.; Head-Gordon, M. Long-Range Corrected Hybrid Density Functionals with Damped Atom-Atom Dispersion Corrections. *Phys. Chem. Chem. Phys.* **2008**, *10*, 6615– 6620, DOI: 10.1039/b810189b

31. Zhao, Y.; Truhlar, D. G. The M06 Suite of Density Functionals for Main Group Thermochemistry, Thermochemical Kinetics, Noncovalent Interactions, Excited States, and Transition Elements: Two New Functionals and Systematic Testing of Four M06-Class Functionals and 12 Other Functionals. *Theor. Chem. Acc.* **2008**, *120*, 215– 241, DOI: 10.1007/s00214-007-0310-x

32. Tomasi, J.; Mennucci, B.; Cammi, R. Quantum Mechanical Continuum Solvation Models. *Chem. Rev.* **2005**, *105*, 2999– 3093, DOI: 10.1021/cr9904009

33. Reed, A. E.; Weinstock, R. B.; Weinhold, F. Natural Population Analysis. *J. Chem. Phys.* **1985**, *83*, 735– 746, DOI: 10.1063/1.449486

34. Dang, A.; Liu, Y.; Tureček, F. UV-Vis Action Spectroscopy of Guanine, 9-Methylguanine and 2′-Deoxyguanosine Cation Radicals in the Gas Phase. *J. Phys. Chem. A* **2019**, *123*, 3272– 3284, DOI: 10.1021/acs.jpca.9b01542

35. Furche, F.; Ahlrichs, A. Adiabatic Time-Dependent Density Functional Methods for Excited State Properties. *J. Chem. Phys.* **2002**, *117*, 7433– 7447, DOI: 10.1063/1.1508368

36. Barbatti, M.; Ruckenbauer, M.; Plasser, F.; Pittner, J.; Granucci, G.; Persico, M.; Lischka, H. Newton-X: A Surface-Hopping Program for Nonadiabatic Molecular Dynamics. *Wiley Interdiscip. Rev.: Comput. Mol. Sci.* **2014**, *4*, 26– 33, DOI: 10.1002/wcms.1158

37. Frisch, M. J.; Trucks, G. W.; Schlegel, H. B.; Scuseria, G. E.; Robb, M. A.; Cheeseman, J. R.; Scalmani, G.; Barone, V.; Petersson, G. A.; Nakatsuji, H.; *Gaussian 16*, revision A03; Gaussian, Inc.: Wallingford, CT, 2016.

38. Gilbert, R. G.; Smith, S. C. *Theory of Unimolecular and Recombination Reactions*; Blackwell Scientific Publications: Oxford, U.K., 1990; pp 52– 132.

39. Zhu, L.; Hase, W. L. *Quantum Chemistry Program Exchange*; Indiana University: Bloomington, IN, 1994; Program no. QCPE 644

40. Gregersen, J. A.; Tureček, F. Mass-Spectrometric and Computational Study of Tryptophan Radicals (Trp + H)$^\bullet$ Produced by Collisional Electron Transfer to Protonated Tryptophan in the Gas Phase. *Phys. Chem. Chem. Phys.* **2010**, *12*, 13434– 13447, DOI: 10.1039/c0cp00597e

41. Murray, K. K. DNA Sequencing by Mass Spectrometry. *J. Mass Spectrom.* **1996**, *31*, 1203– 1215, DOI: 10.1002/(SICI)1096-9888(199611)31:11<1203::AID-JMS445>3.0.CO;2-3

42. McLuckey, S. A.; Van Berkel, G. J.; Glish, G. L. Tandem Mass Spectrometry of Small, Multiply Charged Oligonucleotides. *J. Am. Soc. Mass Spectrom.* **1992**, *3*, 60– 70, DOI: 10.1016/1044-0305(92)85019-G

43. Sapunar, M.; Domcke, W.; Doslic, N. UV Absorption Spectra of DNA Bases in the 350–190 nm Range: Assignment and State Specific Analysis of Solvation Effects. *Phys. Chem. Chem. Phys.* **2019**, *21*, 22782– 22793, DOI: 10.1039/C9CP04662C

44. Tataurov, A. V.; You, Y.; Owczarzy, R. Predicting Ultraviolet Spectrum of Single Stranded and Double Stranded Deoxyribonucleic Acids. *Biophys. Chem.* **2008**, *133*, 66– 70, DOI: 10.1016/j.bpc.2007.12.004

45. Clark, L. B.; Peschel, G. G.; Tinoco, I., Jr. Vapor Spectra and Heat of Vaporization of Some Purine and Pyrimidine Bases. *J. Phys. Chem.* **1965**, *69*, 3615– 3618, DOI: 10.1021/j100894a063

46. Crespo-Hernandez, C. E.; Cohen, B.; Hare, P. M.; Kohler, B. Ultrafast Excited-State Dynamics in Nucleic Acids. *Chem. Rev.* **2004**, *104*, 1977– 2020, DOI: 10.1021/cr0206770

47. Doorley, G. W.; Wojdyla, M.; Watson, G. W.; Towrie, M.; Parker, A. W.; Kelly, J. M.; Quinn, S. J. Tracking DNA Excited States by Picosecond-Time-resolved Infrared Spectroscopy: Signature Band for a Charge-Transfer Excited State in Stacked Adenine-Thymine Systems. *J. Phys. Chem. Lett.* **2013**, *4*, 2739– 2744, DOI: 10.1021/jz401258n
48. Luhrs, D. C.; Viallon, J.; Fischer, I. Excited-State Spectroscopy and Dynamics of Isolated Adenine and 9-Methyladenine. *Phys. Chem. Chem. Phys.* **2001**, *3*, 1827– 1831, DOI: 10.1039/b101191j
49. Ullrich, S.; Schulz, T.; Zgierski, M. Z.; Stolow, A. Direct Observation of Electronic Relaxation Dynamics in Adenine via Time-Resolved Photoelectron Spectroscopy. *J. Am. Chem. Soc.* **2004**, *126*, 2262– 2263, DOI: 10.1021/ja030532q
50. Kang, H.; Jung, B.; Kim, S. K. Mechanism for Ultrafast Internal Conversion of Adenine. *J. Chem. Phys.* **2003**, *118*, 6717– 6719, DOI: 10.1063/1.1566438
51. Marian, C.; Noliting, D.; Weinkauf, R. The Electronic Spectrum of Protonated Adenine: Theory and Experiment. *Phys. Chem. Chem. Phys.* **2005**, *7*, 3306– 3316, DOI: 10.1039/b507422c
52. Podolyan, Y.; Gorb, L.; Leszczynski, J. Protonation of Nucleic Acid Bases. A Comprehensive Post-Hartree-Fock Study of the Energetics and Proton Affinities. *J. Phys. Chem. A* **2000**, *104*, 7346– 7352, DOI: 10.1021/jp000740u
53. Colominas, C.; Luque, F. J.; Orozco, M. Tautomerism and Protonation of Guanine and Cytosine. Implications in the Formation of Hydrogen-Bonded Complexes. *J. Am. Chem. Soc.* **1996**, *118*, 6811– 6821, DOI: 10.1021/ja954293l
54. Tureček, F.; Chen, X. Protonated Adenine: Tautomers, Solvated Clusters, and Dissociation Mechanisms. *J. Am. Soc. Mass Spectrom.* **2005**, *16*, 1713– 1726, DOI: 10.1016/j.jasms.2005.06.010

55. Hud, N. V.; Morton, T. H. DFT Energy Surfaces for Aminopurine Homodimers ad Their Conjugate Acid Ions. *J. Phys. Chem. A* **2007**, *111*, 3369– 3377, DOI: 10.1021/jp065786n
56. Halder, A.; Bhattacharya, S.; Datta, A.; Bhattacharyya, D.; Mitra, A. The Role of N7 Protonation of Guanine in Determining the Structure, Stability and Function of RNA Base Pairs. *Phys. Chem. Chem. Phys.* **2015**, *17*, 26249– 26263, DOI: 10.1039/C5CP04894J
57. Wu, R. R.; Yang, B.; Berden, G.; Oomens, J.; Rodgers, M. T. Gas-Phase Conformations and Energetics of Protonated 2-Deoxyguanosine and Guanosine: IRMPD Action Spectroscopy and Theoretical Studies. *J. Phys. Chem. B* **2014**, *118*, 14774– 14784, DOI: 10.1021/jp508019a
58. Yao, C.; Tureček, F.; Polce, M. J.; Wesdemiotis, C. Proton and Hydrogen Atom Adducts to Cytosine. An Experimental and Computational Study. *Int. J. Mass Spectrom.* **2007**, *265*, 106– 123, DOI: 10.1016/j.ijms.2007.01.013
59. Filippi, A.; Fraschetti, C.; Rondino, F.; Piccirillo, S.; Steinmetz, V.; Guidoni, L.; Speranza, M. Protonated Pyrimidine Nucleosides Probed by IRMPD Spectroscopy. *Int. J. Mass Spectrom.* **2013**, *354-355*, 54– 61, DOI: 10.1016/j.ijms.2013.05.016
60. Salpin, J.-Y.; Guillaumont, S.; Tortajada, J.; MacAleese, L.; Lemaire, J.; Maitre, P. Infrared Spectra of Protonated Uracil, Thymine and Cytosine. *ChemPhysChem* **2007**, *8*, 2235– 2244, DOI: 10.1002/cphc.200700284
61. Bakker, J. M.; Salpin, J.-Y.; Maitre, P. Tautomerism of Cytosine Probed by Gas Phase IR Spectroscopy. *Int. J. Mass Spectrom.* **2009**, *283*, 214– 221, DOI: 10.1016/j.ijms.2009.03.014
62. Lias, S. G.; Bartmess, J. E. Gas-Phase Ion Thermochemistry. In *NIST Chemistry WebBook*; Linstrom, P. J., Mallard, W. G., Eds; NIST Standard Reference Database Number 69; National Institute of Standards and Technology: Gaithersburg, MD, http://webbook.nist.gov (retrieved July 2019).

63. Hari, Y.; Leumann, C. J.; Schurch, S. What Hinders Electron Transfer Dissociation (ETD) of DNA Cations?. *J. Am. Soc. Mass Spectrom.* **2017**, *28*, 2677– 2685, DOI: 10.1007/s13361-017-1791-z
64. Pepin, R.; Tureček, F. Kinetic Ion Thermometers for Electron Transfer Dissociation. *J. Phys. Chem. B* **2015**, *119*, 2818– 2826, DOI: 10.1021/jp510244d
65. Michl, J. Electronic Spectrum of Fluoranthene. *J. Mol. Spectrosc.* **1969**, *30*, 66– 76, DOI: 10.1016/0022-2852(69)90236-7
66. Lifshitz, C. Time-Resolved Appearance Energies, Breakdown Graphs, and Mass Spectra: The Elusive Kinetic Shift. *Mass Spectrom. Rev.* **1982**, *1*, 309– 340, DOI: 10.1002/mas.1280010402

6.7. Appendix

Table 1. Relative Free Energies of dGATC Dications

	Relative Free Energy[a,b]		
Ion	ωB97X-D[c]	M06-2X[d]	ωB97X-D(*aq*)[e]
G7C3	0	0	0
G7A1a	12	0.2	37
G7A3	26	10	22
A1C2	44	13	66
A1C3a	18	17	22
G7C3b	29	24	42
G7A1b	29	26	50
A3C2a	46	29	22
A1C3b	43	30	3
A3C2b	49	36	22

[a] In kJ mol^{-1}. [b] Including B3LYP/6-31+G(d,p) zero-point energies and 310 K enthalpies and entropies. [c] Based on ωB97X-D/6-31+G(d,p) optimized structures. [d] Based on M06-2X/6-31+G(d,p) optimized structures. [e] Including polarizable continuum model solvation energies in water dielectric.

Table 2. Relative Free Energies of dGATC Cation Radicals

		Relative Energy^{a,b}
Ion^{c}	Radical Sites^{d}	M06-2X^{e,f}
G7rC3a	C4,6	0 (0)
G7rC3b	C4,6	3 (16)
G7A1rT	T4,6	8 (35)
G7rA3	A2,6	45 (49)
A1rC3	C4,6	45 (49)
A3rC3	C4,6	55 (55)
rA3C2	A2,6	74 (70)
A1rC2	C4,6	91 (93)
G7rA8	A9,2,6	–72 (–55)
rG78a	G7,5,9	–87 (–72)
rG78b	G7,5,9	–51 (–29)
TS		68
rG78a → $\boldsymbol{d_3^+ + w_1^\bullet}$		159 (75)
rG78a → $\boldsymbol{d_3^+ + w_1'^\bullet}$		132 (47)

[a] In kJ mol^{-1}. [b] Including B3LYP/6-31+G(d,p) zero-point energies and referring to 0 K. [c] rA, rC, rG, and rT refer to the nucleobase harboring the additional hydrogen atom at the indicated ring position. [d] Sites of highest atomic spin densities in nucleobases. [e] Single-point M06-2X/6-311++G(2d,p) energies on M06-2X/6-31+G(d,p) optimized structures. [f] Relative free energies at 310 K in parentheses.

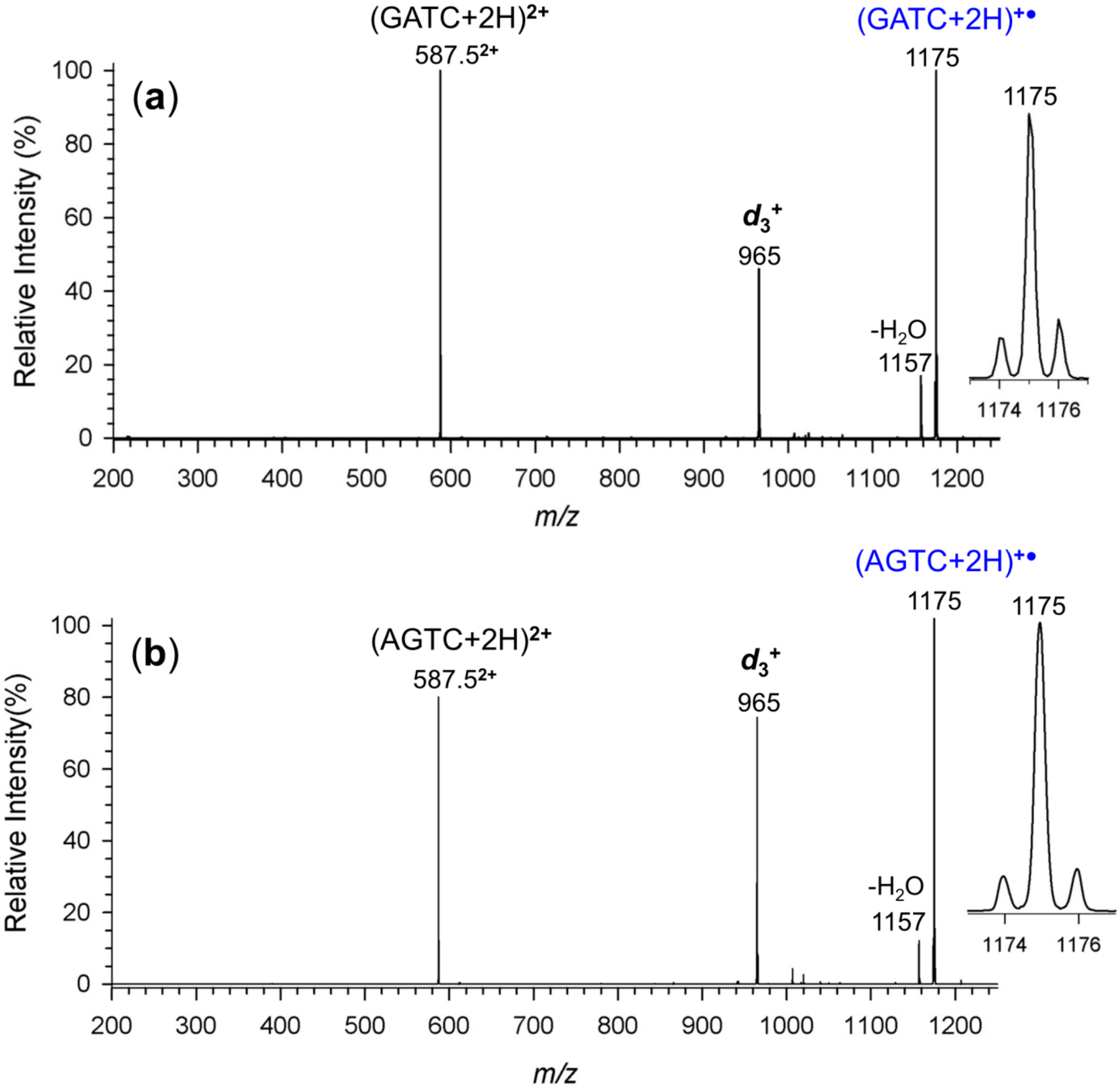

Figure 1. ETD-MS2 spectra of (a) (dGATC+2H)$^{2+}$ and (b) (dAGTC+2H)$^{2+}$ ions at m/z 587.5. Insets show the charge reduced ions at m/z 1175.

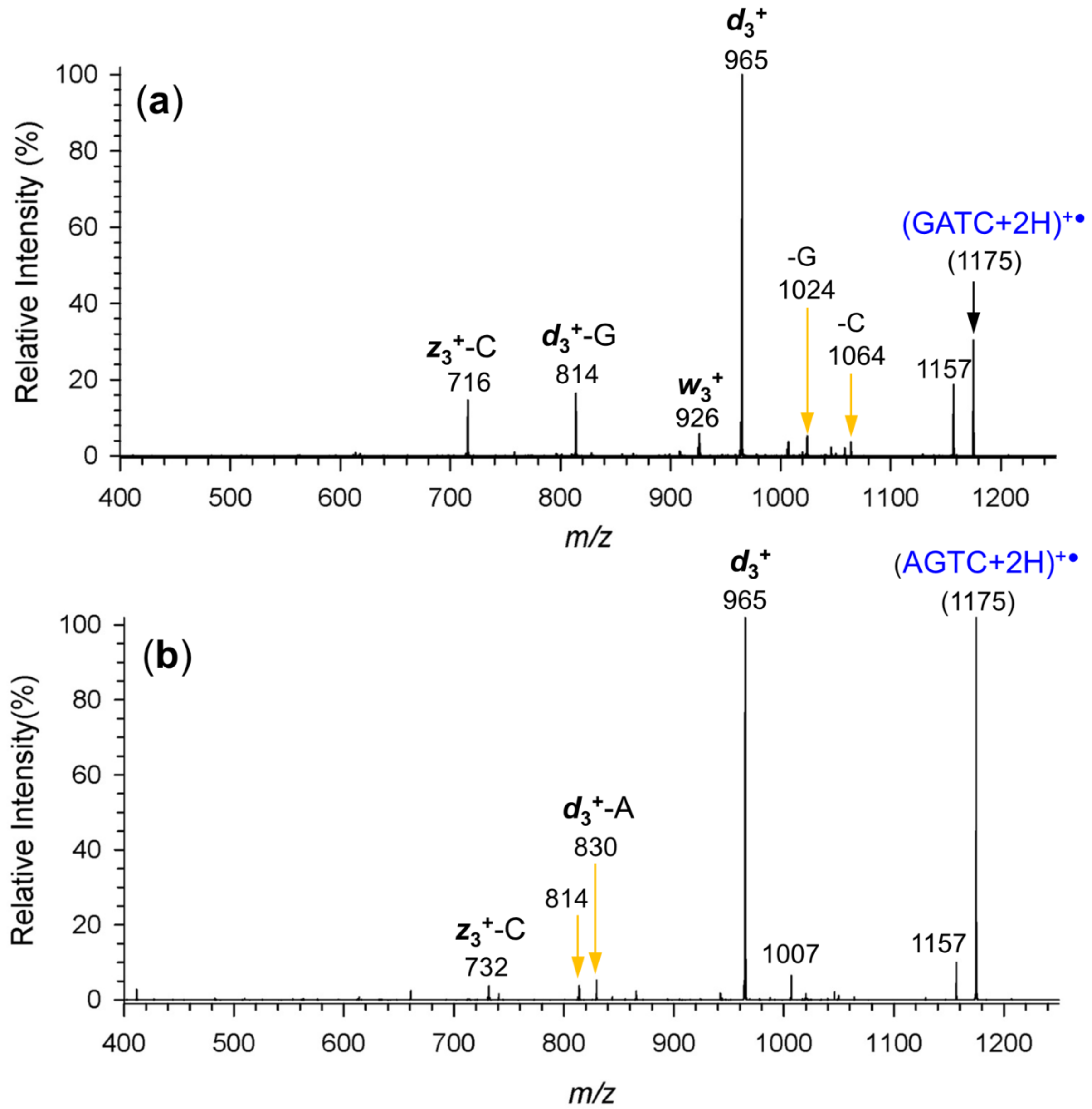

Figure 2. CID-MS3 spectra of (a) (GATC+2H)$^{+\bullet}$ and (b) (AGTC+2H)$^{+\bullet}$ ions at m/z 1175.

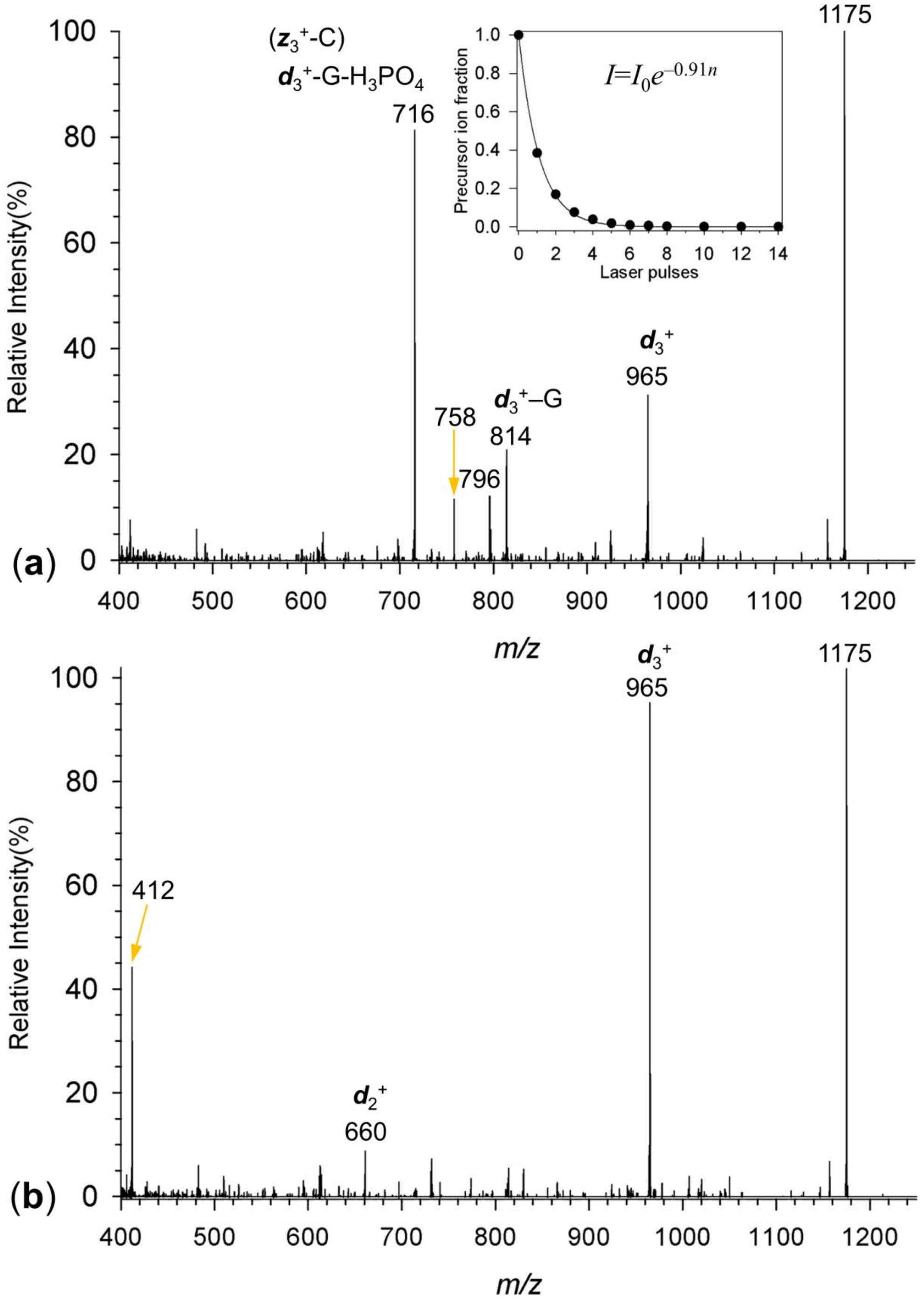

Figure 3. UVPD spectra (245 nm, 2 laser pulses) of (a) $(GATC+2H)^{+\bullet}$ and (b) $(AGTC+2H)^{+\bullet}$ ions at m/z 1175. Inset in Figure 3a shows the dependence of precursor ion relative intensity on the number of laser pulses.

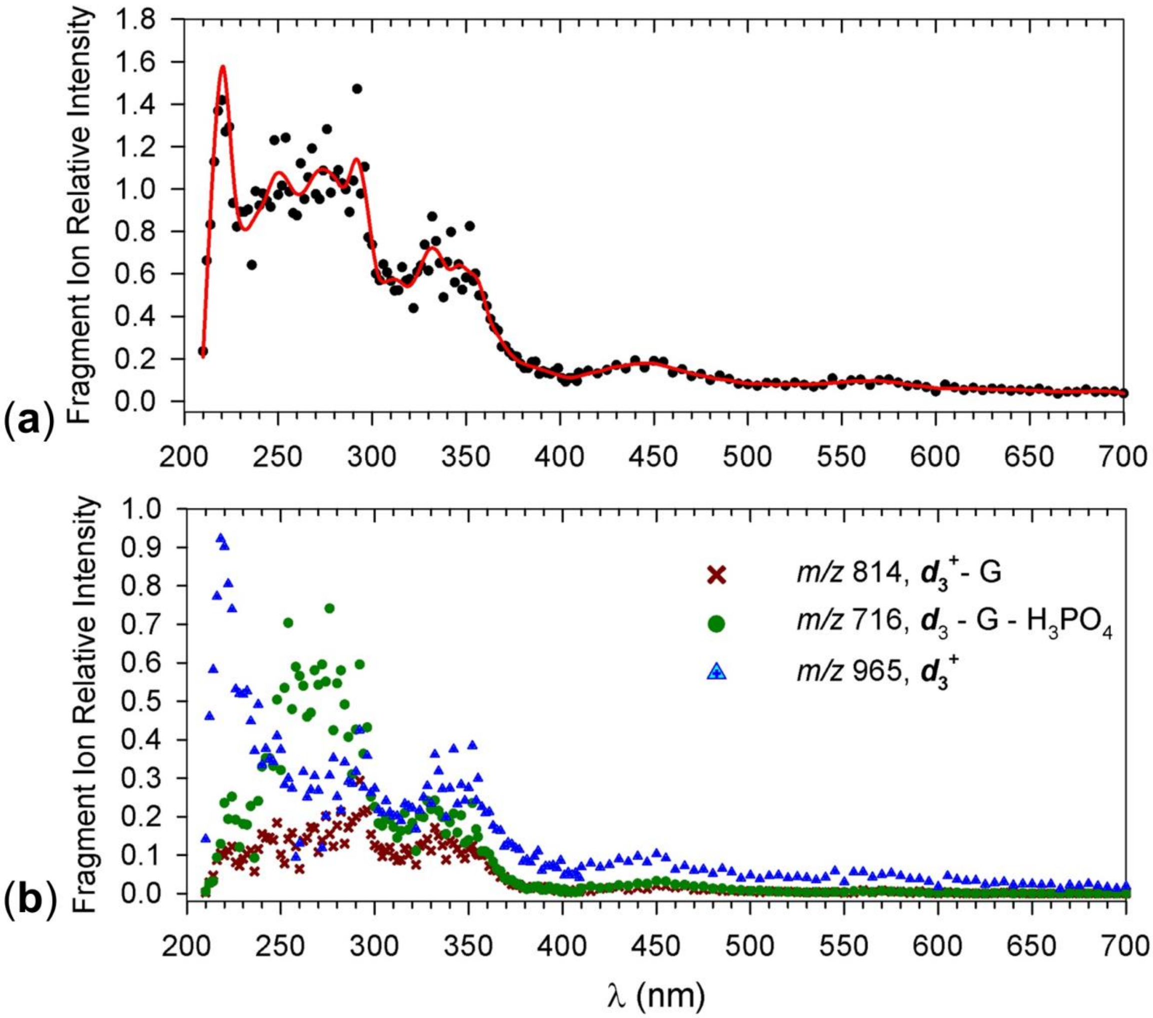

Figure 4. UVPD action spectra of (GATC+2H)$^{+\bullet}$ ploted as (a) sum of fragment ion intensities, (b) mass resolved photodissociation channels.

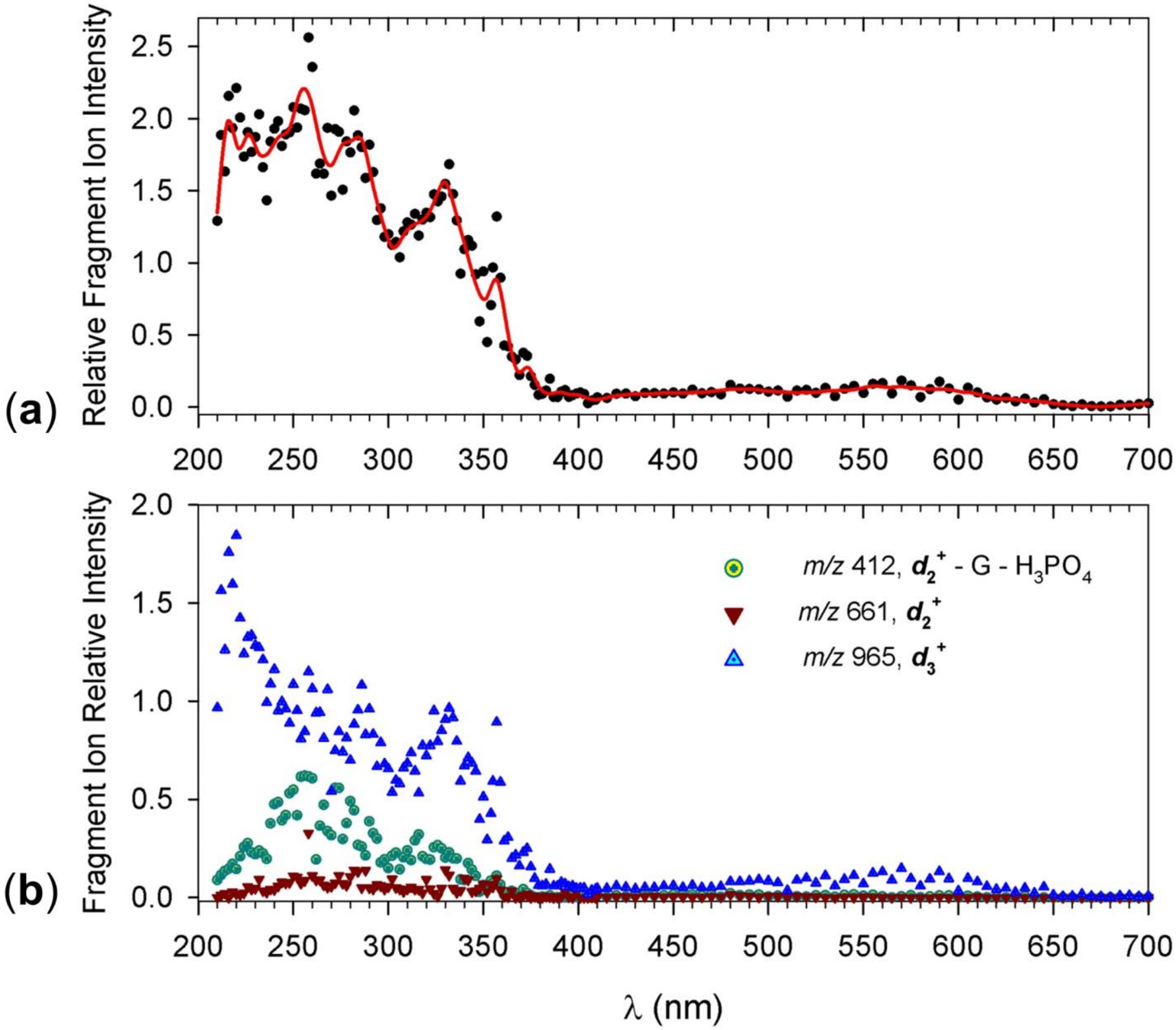

Figure 5. UVPD action spectra of $(AGTC+2H)^{+\bullet}$ plotted as (a) sum of fragment ion intensities and (b) mass resolved photodissociation channels.

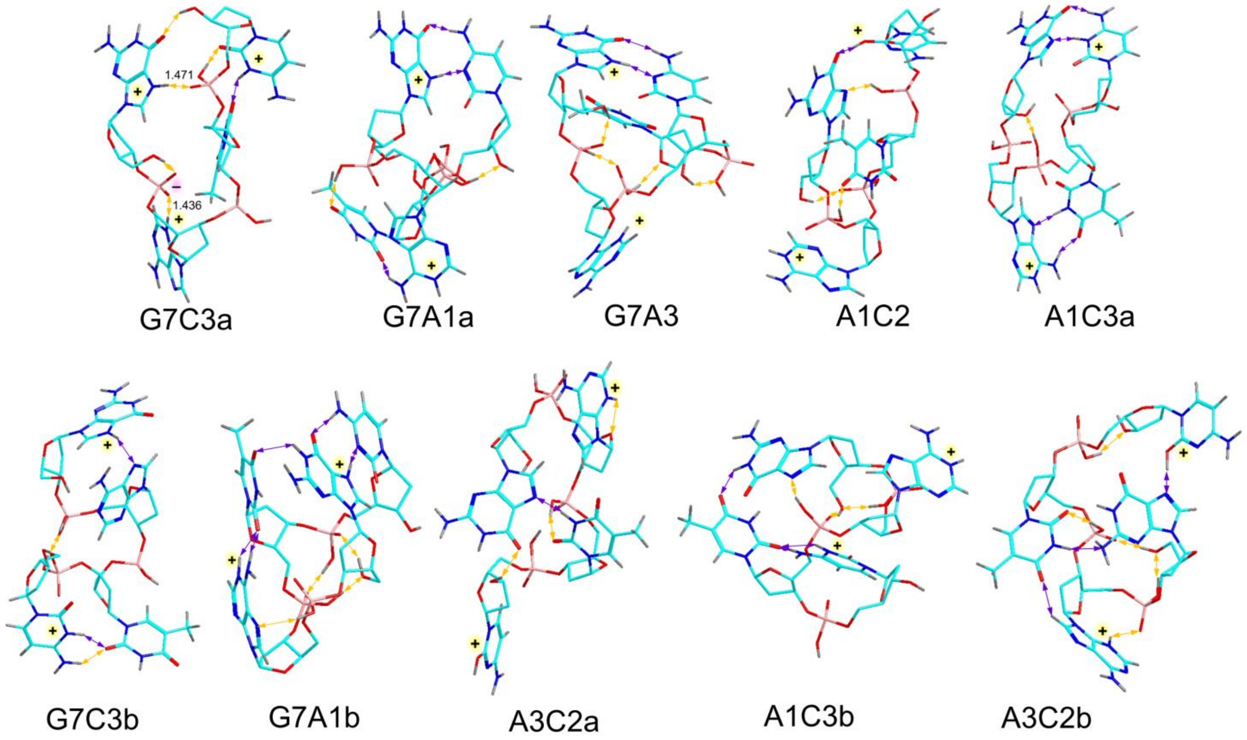

G7C3a G7A1a G7A3 A1C2 A1C3a

G7C3b G7A1b A3C2a A1C3b A3C2b

Figure 6. M06-2X optimized structures of low-energy (GATC+2H)$^{2+}$ ions. The atom color coding is as follows: cyan = C, blue = N, red = O, bronze = P, gray = H. The deoxyribose hydrogen atoms are not shown. Hydrogen bonds are indicated by double-headed arrows, purple for those between the nucleobases and yellow for the others.

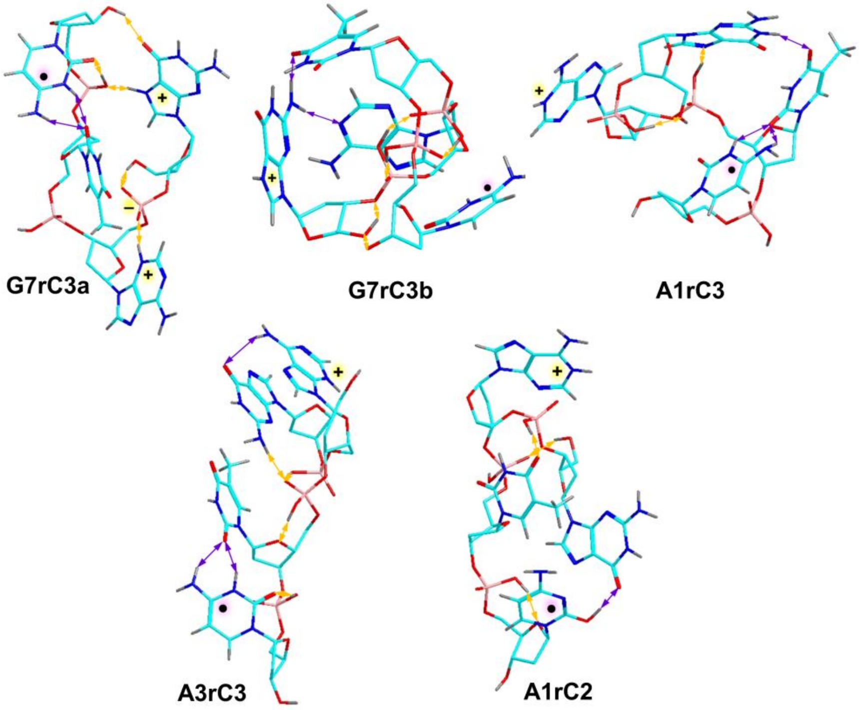

G7rC3a **G7rC3b** **A1rC3**

A3rC3 **A1rC2**

Figure 7. M06-2X optimized structures of low-energy cytosine-based radicals. The atom color coding is as in Figure 6.

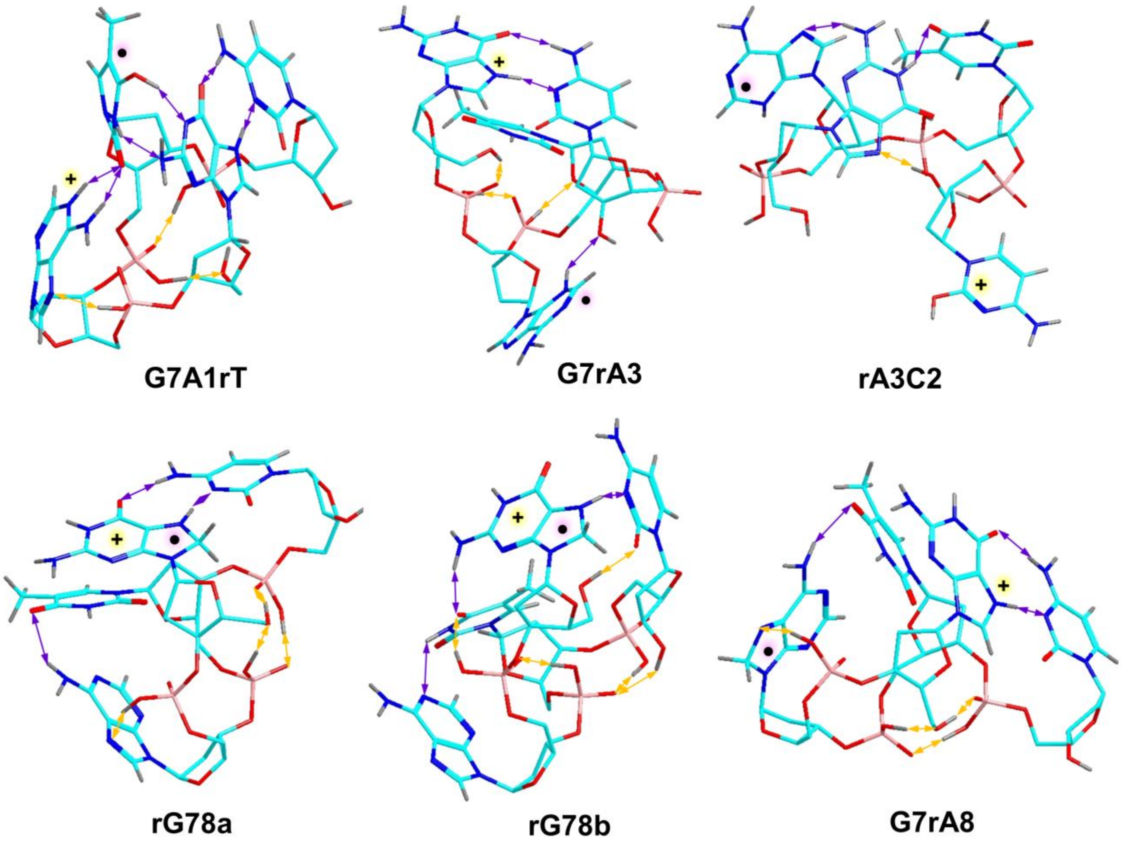

G7A1rT G7rA3 rA3C2

rG78a rG78b G7rA8

Figure 8. M06-2X optimized structures of low-energy thymine-, adenine-, and guanine-based radicals. The atom color coding is as in Figure 6.

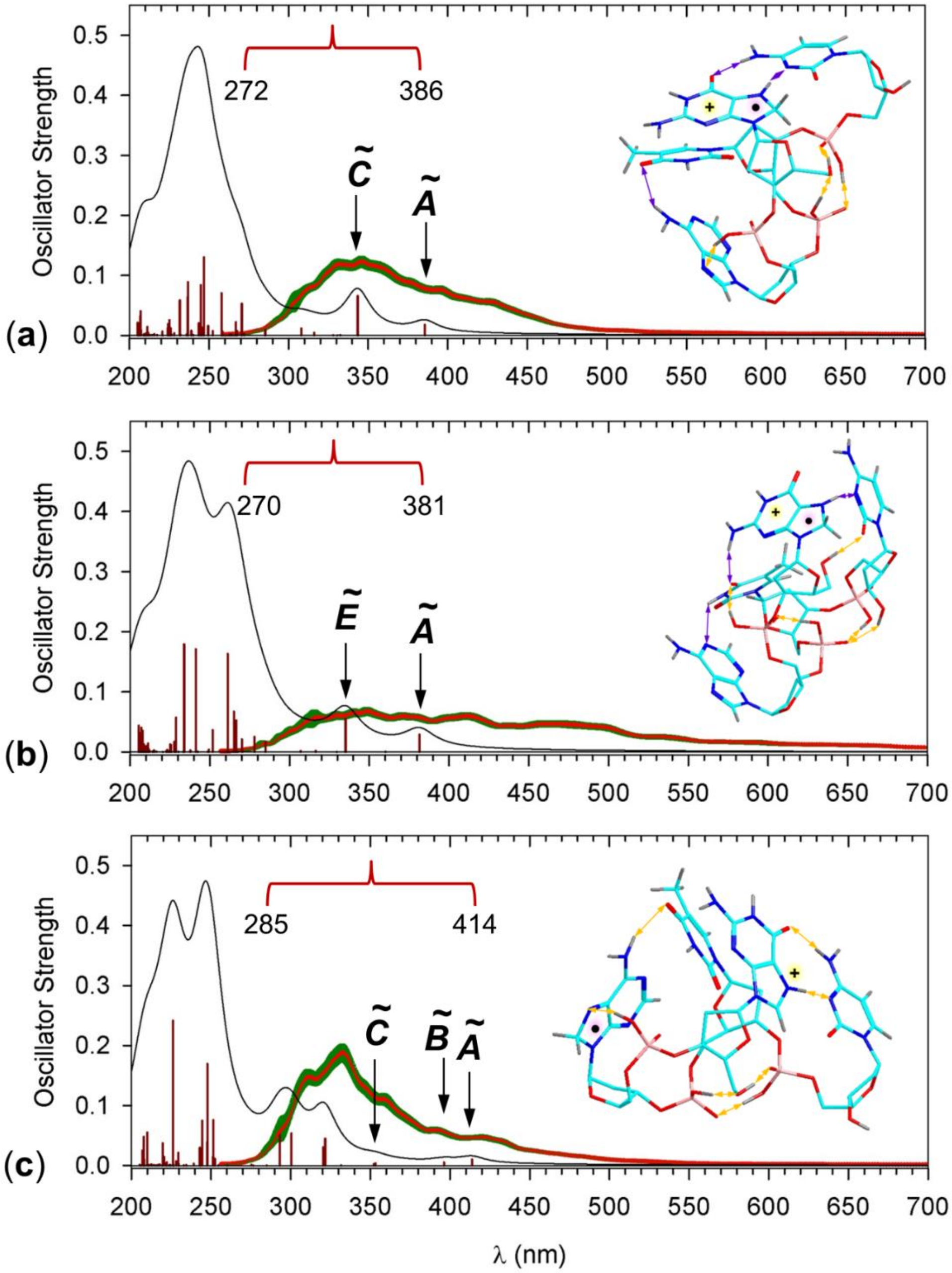

Figure 9. M06-2X/6-31+G(d,p) TD-DFT spectra and optimized structures of (a) rG78a, (b) rG78b, and (c) G7rA8. The black-line band shapes are from artificial broadening of the calculated excitation lines by convolution with Lorentzian peak shapes at 10 nm full width at half-maximum. The red-line band shapes are from 300 vibronic calculations of 12–13 excited states in the wavelength range shown by brackets. Green bars show the errors in the calculated oscillator strength.

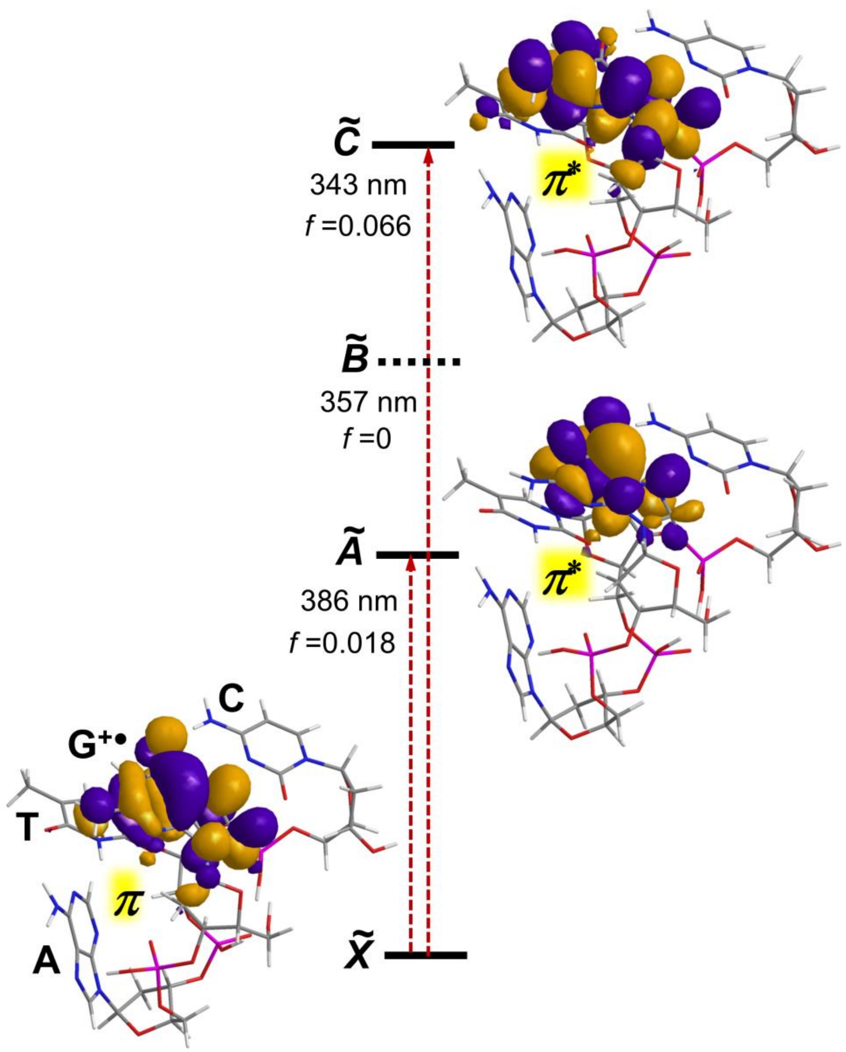

Figure 10. M06-2X/6-31+G(d,p) molecular orbitals representing the ground (X) and low excited electronic states in G78ra. Excitation wavelengths and oscillator strengths (*f*) are also shown.

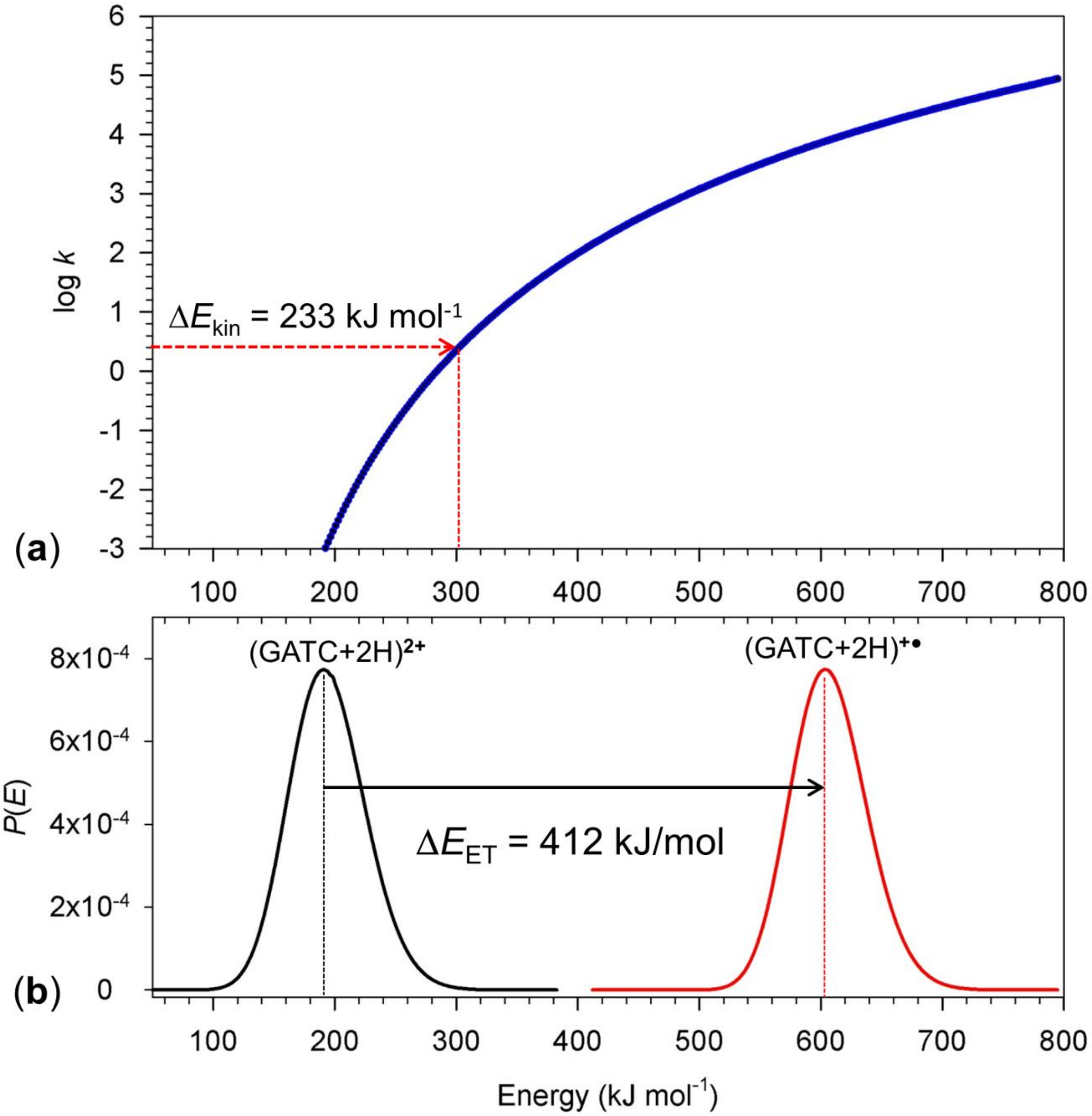

Figure 11. Top panel: RRKM rate constants for the G7rC3a → rG78a isomerization. Bottom panel: calculated vibrational energy distributions in the G7C3a dication at 310 K and G7rC3a after electron transfer.

Chapter 7—Conclusions and Outlook

This dissertation presented spectroscopy and mass spectrometry investigations on ionized DNA nucleobases and related radical intermediates. Utilizing tandem mass spectrometry, these radical intermediates were first generated with either collision-induced dissociation or electron transfer dissociations, then a UV/Vis laser was used to probe the photodissociation channels and to investigate its related chemical properties of these transient radicals via computations. More broadly speaking, collision-induced dissociation and electron-transfer dissociation were used to mimic the suspected direct and indirect mechanism of DNA ionization, respectively. More importantly, each chapter in this dissertation provides a piece of insight into the spectroscopy and the chemical nature of these individual DNA nucleobase radicals and, ultimately, becomes a scaffold to which future investigations on more complex DNA radical systems to build upon.

Moving forward, we, as the Tureček group, will use this systematically approach, that we have developed based on sound and high-quality science, to investigate more complex DNA radical systems. For example, the investigation of the tetranucleotide DNA cation radical, GATC, was initially an expansion on the dinucleotide series. Now that we understand the interaction between the cytosine radical and the guanine nucleobase a bit more, we have began the investigation on trinucleotide DNA cation radicals, as they relate to cellular replication processes like translation and transcription; and we have also began the investigation on heptanucleotide and longer sequences, as they code for one or two key amino acids in proteins. Another example, our targeted synthesis to seek and experimentally generate the more thermodynamically-stable, at least based on our calculations, the elusive 9-methylene-(1H)-adenine tautomer presents a challenging but possible experimental pathway to generate other thermodynamically-stable non-canonical ionized DNA tautomers. To provide a big picture perspective, this dissertation and our fundamental and mass spectrometry approach, as the Tureček group, aims to elucidate the intrinsic and chemical properties of these DNA transient radical species. And this research, as well as future upcoming projects, aims to achieve a better understand on the complex process of DNA ionization damage, like a single jigsaw in a thousand-piece puzzle.